MICROCOPY RESOLUTION TEST CHART
NATIONAL BUREAU OF STANDARDS-1963-A

AD-A155 927

REPORT DOCUMENTATION PAGE		READ INSTRUCTIONS BEFORE COMPLETING FORM
REPORT NUMBER ARO 17826.19-PH	2. GOVT ACCESSION NO. N/A	3. RECIPIENT'S CATALOG NUMBER N/A
TITLE *(and Subtitle)* ELECTRONIC STRUCTURE AND LATTICE DYNAMICS OF DIMENSIONALLY CONSTRAINED AND DISORDERED SOLIDS		5. TYPE OF REPORT & PERIOD COVERED FINAL REPORT 9/1/81 - 2/28/85
		6. PERFORMING ORG. REPORT NUMBER
AUTHOR*(s)* RUBIN BRAUNSTEIN		8. CONTRACT OR GRANT NUMBER*(s)* DAAG 29-81-K-0164
PERFORMING ORGANIZATION NAME AND ADDRESS		10. PROGRAM ELEMENT, PROJECT, TASK AREA & WORK UNIT NUMBERS
CONTROLLING OFFICE NAME AND ADDRESS U. S. Army Research Office Post Office Box 12211 Research Triangle Park, NC 27709		12. REPORT DATE 2/28/85
		13. NUMBER OF PAGES
14. MONITORING AGENCY NAME & ADDRESS*(if different from Controlling Office)*		15. SECURITY CLASS. *(of this report)* Unclassified
		15a. DECLASSIFICATION/DOWNGRADING SCHEDULE

16. DISTRIBUTION STATEMENT *(of this Report)*

Approved for public release; distribution unlimited.

JUN 26 1985

A

17. DISTRIBUTION STATEMENT *(of the abstract entered in Block 20, if different from Report)*

NA

18. SUPPLEMENTARY NOTES

The view, opinions, and/or findings contained in this report are those of the author(s) and should not be construed as an official Department of the Army position, policy, or decision, unless so designated by other documentation.

19. KEY WORDS *(Continue on reverse side if necessary and identify by block number)*

Surface Plasmons
Tungstate Glasses
Order-Disorder in Metal Alloys
Infrared Wavelength Modulation
Deep Levels in Semiconductors

20. ABSTRACT *(Continue on reverse side if necessary and identify by block number)*

The techniques of infrared wavelength modulation, Raman scattering, and photo-induced transients were utilized to study bulk and surface electronic and vibrational properties of metals, insulators, and semiconductors. Results are reported on: optical properties of the surface plasmons of n^+ silicon and copper-Raman and Brillouin scattering and luminiscence studies of alkali borate tungstate glasses-wavelength modulation studies of order-disorder effects on the band structure of metal alloys, bulk and surface impurities

DD $_{1\ JAN\ 73}^{FORM}$ 1473 EDITION OF 1 NOV 65 IS OBSOLETE

20. ABSTRACT CONTINUED

in alkali halide and alkaline earth fluorides, and deep levels in semiconductors.

A-1

Electronic Structure and Lattice Dynamics of

Dimensionally Constrained and Disordered Solids

Final Report

Rubin Braunstein

February 28, 1985

U.S. Army Research Office

DAAG 29-81K-0164

University of California, Los Angeles

Table of Contents

A. Statement of the Problem Studied

As metals, semiconductors, and insulators are utilized in constrained geometries to realize large scale device integration it is increasingly important to understand the electron structure and lattice dynamics of quasi-two dimensional structures. It was the purpose of the present program to develop and exploit non-destructive techniques to study the intrinsic and extrinsic electronic properties of these materials. The techniques of infrared wavelength modulation, Raman scattering, and photo-induced transients were utilized in these studies and reveal new bulk and surface electronic and vibrational properties of the metals, insulators, and semiconductors studied.

The specific areas of research activity pursued were:

Optical Properties of the Surface Plasmons of n^+ Silicon and Copper

Raman and Brillouin Scattering and Luminescence Studies
of Alkali Borate Tungstate Glasses

Development of an Infrared Wavelength Modulated Spectrometer
for the Spectral Regions 0.2-20 Microns with a Sensitivity
to Measure Changes in Absorption of a Part in 10^5.

Wavelength Modulation Studies of:

a) Order-Disorder Effects on the Band Structure of Metal Alloys

b) Bulk and Surface Impurities in Alkali Halides and Alkaline
Earth Fluorides

c) Optical Detection of Deep Levels in Semiconductors

d) Utilization of Photo-induced Transients for the Detection
of Deep Levels

B.   Summary of Results

The following are the problems studied and the conclusions reached. The reference numbers after each topic are to the publications referenced in the Publication List, reprints and preprints are included in the Appendix.

1. Surface Plasmons on Metals and Semiconductors (1,2)

The optical properties of copper and n^+ silicon were experimentally determined using attenuated total reflection (ATR) techniques and used to calculate the complex frequency dispersion curve of these materials. In copper the dispersion curve shows the characteristic vector divergence of the surface plasmon resonance, while the complex-k dispersion curve exhibits the characteristic back-bending. The resonance is shifted due to d-band Fermi level transition causing a large shift in the location of the real frequency excitation resulting in the true resonance to occur in the complex frequency plane. The surface plasmon resonance of n^+ Silicon is highly damped causing the ATR dispersion curve calculated on the real frequency axis to exhibit back-bending for its complex frequency solution; in contrast the theoretical dispersion curve exhibits the standard wave vector dispersion at the surface plasmon frequency. The discrepancy was rectified by converting the optical properties of n^+ silicon into functions in the complex frequency plane allowing the location of the complex resonance was obtained.

2.   Alkali Borate Tungstate Glasses (3,16)

We have previously published result of studies on a series of bulk transparent tungstate glasses which exhibit electrochromic and photochromic behavior and have potential use for solid state display devices. In addition these glasses serve as a prototype system to study small polaron transport,

percolation transport as well as ionic transport. To further elucidate the microscopic structure of this glass system, a series of Raman, Brillouin, and luminescence studies were completed. The Raman spectra show that for low concentration, WO_3 is incorporated into the glass as tetrahedral $WO_4^=$. As the concentration of WO_3 increases, the concentration of $WO_4^=$ also increases: however, new species become apparent such as $WO_3 \cdot H_2O$ and polymeric tungstate. Both species contain octahedral WO_3 groups. The simplest polymeric tungstate present is $W_2O_7^=$. Luminescence data provide evidence for $W_2O_7^=$ and defects of WO_3 octahedra being present even at low WO_3 concentrations. The photochromic structures are $WO_4^=$, $WO_3 \cdot H_2O$ and possibly defects of WO_3. Brillouin scattering measurements indicate that there are large changes in the elastic constant of $Li_2O \cdot (B_2O_3)_2$ with small concentrations of WO_3. The above glasses in the composition $(Li_2B_4O_7)_{1-x}(WO_3)_x$ with $x < 0.33$ which exhibit reversible electrochromic behavior when ions of H, Li and Na are transported into and out of these glasses. We have now found another glass-forming region for $x \geq 0.44$ which results in a permanent blue coloration. This concentration limit appears to be a percolation threshold where the fast diffusion of lithium decorates the WO_6-tree once it is in the glass matrix.

3. Wavelength Modulation Studies (4 - 15)

We have improved our wavelength modulation apparatus in the visible and ultra-violet region and developed a new system that covers the spectral region from 0.2 - 20 microns that is capable of measuring a charge in absorption or reflection of a part in 10^S. These systems were utilized to study the intrinsic and extrinsic optical properties of metals, insulators, and semiconductors. The results of these studies are as follows:

a) Order-Disorder Effects on the Band Structure of Metal Alloys (9,10,11)

Our wavelength modulation techniques were used to study the alloy systems: $\beta' - Cu_x Zn_{1-x}$ at the $\beta' \rightleftarrows \alpha + \beta'$ phase transition, $\alpha - Ag_{0.7} Zn_{0.3}$, and $\beta' -$ AuZn. These studies measured the positions of the critical points and the line shapes of interband transitions out of the free carrier Drude background. These parameters were used to compare various band calculations of these metal alloys and yielded accurate parameters for future band calculations. The details of these studies have been published reprints, of which are included in the Appendix.

b) Bulk and Surface Impurities in Alkali Halides and Alkaline Earth Fluorides (7)

Our infrared wavelength modulation system was developed and used to investigate the low-level absorption of a number of alkali halides and alkaline earth fluorides of interest for high power laser windows. These studies revealed rich absorption structure which enabled an indentification of surface and bulk impurities; for the first time, we measured the complete spectral distribution from 2.5 - 12.0 microns of the absorption at levels of $10^{-4} cm^{-1}$. These results have a direct bearing on the use of these materials for high power laser windows and fiber optic light guiding systems which require extremely low level of absorption.

c) Deep Level Derivative Spectroscopy of Semiconductors by Modulation Techniques (6,7,8,12,13,14,15)

Our infrared wavelength modulation absorption spectrometer was employed in a detailed study of deep levels in semi-insulating GaAs, surface layers on Si, GaAs, and HgCdTe, oxygen complexes in floating-zone Si, and the determination of strain in ion-implanted layers. We have shown that our system is a sensitive non-destructive techniques for study defects in semiconductors that have a direct bearing on the performance of mi·ro-electric devices. It was possible to detect defects that have not been observed by other techniques. The details of these studies are contained in the preprints in the Appendix.

d) Photo-induced Transients for the Detection of Deep Levels

Using photo-induced-transient spectroscopy on semi-insulating liquid-encapsulated Czochralski-grown GaAs, we have detected a number of deep levels and studied the effects of heat treatment.

4. Proposal for Future Work

The optical techniques of wavelength modulation and light scattering that we have developed during these studies have a sensitivity to study properties of 1/100 of a monolayer of adatom on a surface. Our understanding of dimensionally constrained solids would be more complete if we were able to follow the evolution of the morphology, electronic structure, and molecular vibrations as growth layers proceed from the initial nucleation process of the adsorbed atoms or molecules to the two-dimensional phase transition which

signals the completion of growth of the first layer. Such studies have been

performed using various electron spectroscopies such as LEED, Auger, and ESCA

techniques. However, they have a limited energy resolution so that it is not

possible to observe changes in the vibrational modes of the adsorbed species.

In the final phase of this program, we assembled a UHV surface analytical

facility combining the electron spectroscopies of LEED, Auger, and ESCA and the

high resolution and sensitivity of our wavelength modulation techniques with

University funds. This unique system will enable studies of physisorption,

chemisorption, and epitaxial growth.

C. List of Publications

1) "Optical Properties of the Surface Plasmon of n^+ Silicon," P. F. Robusto and R. Braunstein, Phys. Stat. Solidi (b) 107, 127 (1981).

2) "Optical Measurements of the Surface Plasmon of Copper," P. F. Robusto and R. Braunstein, Phys. Stat. Solidi (b) 107, 443 (1981).

3) "Raman and Luminescence Studies of Alkali Borate Tungstate Glasses," D. Deal, M. Burd, and R. Braunstein, Journ. of Non-Crystalline Solids 54, 207 (1983).

4) "Fully Electronic Servocircuitry for Wavelength-Modulation Spectroscopy," R. Stearns, J. Steele, and R. Braunstein, Rev. Sci. Instr. 54(8), 984 (1983).

5) "De-Correlation Technique for Separation of Drude Parameters from Wavelength Modulation Spectroscopy Data," M. Burd, R. Stearns, and R. Braunstein, Phys. Stat. Sol. (b) 117, 101 (1983).

6) "Derivative Absorption Spectroscopy of Ga As: Cr; R. Braunstein, R. K. Kim. D. Matthews, and M. Braunstein" Physica 117 and 118B 163 (1983).

7) "Infrared Wavelength Modulation Spectroscopy of Some Optical Material," R. K. Kim and R. Braunstein, Appl. Optics 23(8), 1166 (1984).

8) "Deep Level Derivative Spectroscopy of Semiconductors by Wavelength Modulation Techniques," R. Braunstein, S. M. Eetemadi, and R. K. Kim. (to appear in the Proceedings of the SPIE 1985 Los Angeles Technical Syymposium: Spectroscopy Characterization Technique for Semiconductor Technology II).

9) "Optical Properties of β'-AuZn by Wavelength-Modulated Derivative Spectroscopy," R. Stearns, R. Braunstein, and L. Muldawer [to appear in

Phys. Stat. Solidi (b)].

10) "Wavelength Modulated Spectra of α-$Ag_{0.7}Zn_{0.3}$ Near the Optical Absorption Edge," R. Stearns, R. Braunstein, and L. Muldawer [submitted to Phys. Stat. Solidi (b)].

11) "Wavelength-Modulated Spectra of the Optical Properties of β'-Cu_xZn_{1-x} from 1.5 to 5.1 eV of the $\beta' \rightarrow \alpha + \beta'$ Phase Transition." R. Stearns. R. Braunstein, and L. Muldawer" [submitted to Phys. Stat. Solidi (b)].

12) "Wavelength Modulation Absorption Spectroscopy of Deep Levels in Semi-Insulating GaAs," S. M. Eetemadi and R. Braunstein (to appear in J. Appl. Phys.).

13) "Deep Levels in Semi-Insulating, Liquid-Encapsulated Czochrolski-Grown GaAs," M. R. Burd and R. Braunstein (submitted to J. Appl. Phys.).

14) "Re-examination of the Wavelength Modulation Photoresponse Spectroscopies," S. M. Eetemadi and R. Braunstein (submitted to J. Appl. Phys.).

15) "Measurement of the EL2 and Chromium Concentration in Semi-Insulating GaAs." S. M. Eetemadi and R. Braunstein (submitted to J. Appl. Phys.).

16) "Permanent Blue Coloration of $(Li_2B_4O_7)_{1-x}(WO_3)_x$-Glasses," Ch. Ruf, K. Bärner, and R. Braunstein (to appear in Solid State Commun.).

[8] P. F. Robusto. Ph.D. Thesis. Univ. of California. Los Angeles 1978.
[9] A. A. Kucharskii and V. K. Subashiev. Soviet Phys. — Semicond. 4. 234 (1970).
[10] W. G. Spitzer and H. Y. Fan. Phys. Rev. 108. 2. 268 (1957).
[11] S. M. Sze. Physics of Semiconductor Devices. John Wiley & Sons. New York 1969.
[12] P. F. Robusto and R. Braunstein. phys. stat. sol. (b) 107. No. 2 (1981).
[13] E. Burstein and F. DeMartini. Proc. I Taormina Research Conf. Structure of Matter.
      Pergamon Press. New York 1972.

Table 4

Comparison of the Drude dielectric function as a function of real and complex frequencies

L (μm)[a]	$\varepsilon_1(\omega')$[b]	$\varepsilon_1(\omega)$[c]	$\varepsilon_2(\omega')$[d]	$\varepsilon_2(\omega)$[e]
2	10.4351	10.4348	0.155894	0.154283
3	3.9062	3.90199	0.516484	0.501147
4	6.35776	6.32434	1.15758	1.10091
5	4.37016	4.16524	2.25844	1.76509
5.5	2.98949	2.50169	2.95223	1.73513
5.9	1.32975	0.91369	3.5686	0.67388
6.66	− 0.486703	− 1.91911	5.00156	0.90968
6.7	− 0.612146	− 2.04816	5.08339	1.17191
6.8	− 0.927106	− 2.32911	5.29124	1.90725
7	− 1.56256	− 2.82691	5.72098	3.16219
7.5	− 3.1795	− 4.216	6.37692	5.19277
8.5	− 6.50066	− 7.33573	9.53347	8.46068
9	− 8.18639	− 8.96977	11.0292	10.1071
10	−11.5672	−12.2899	14.338	13.606
11	−11.5623	−13.6069	20.0286	17.4264

[a]) Wavelength (in μm) for the real frequency ω' and for complex frequency $L = 2\pi c/\omega_1$.

[b]) Real part of dielectric function as a function of real frequency ω'.

[c]) Real part of dielectric function as a function of complex frequency $\omega = \omega_1 - i\omega_2$ as defined in equation (6a), that is, $\varepsilon_1(\omega) = \varepsilon_1(\omega_1, \omega_2)$.

[d]) Imaginary part of dielectric function as a function of real frequency ω'.

[e]) Imaginary part of dielectric function as a function of complex frequency $\omega = \omega_1 - i\omega_2$ as defined in equation (6b), that is, $\varepsilon_2(\omega) = \varepsilon_2(\omega_1, \omega_2)$.

frequency plane does not exhibit the surface plasmon resonance; whereas the theoretical dispersion relationship yields the resonance.

Consequently, for this n+ silicon material which has a relatively high damping the surface plasmon will not exhibit a resonance in the real frequency spectrum when coupling is performed using the ATR experimental technique of fixing incident angle and varying frequency. By using the complex frequency analysis either through the theoretical dispersion relationship or using our developed complex frequency dependent optical constants and analyzing the ATR minima in the complex frequency plane the location of the complex frequency resonance can be obtained.

A comparison of the real and imaginary parts of the Drude dielectric function for n+ silicon for both real and complex frequencies shows that they numerically deviate the largest in the area of the surface plasmon and approach one another in value at high frequencies.

References

[1] A. Otto. Z. Phys. 219. 227 (1969).
[2] A. Otto. Z. Phys. 216. 398 (1968).
[3] N. Marschall and B. Fischer. Phys. Rev. Letters 28. 13. 811 (1972).
[4] R. A. Ferrell. Phys. Rev. 111. 1214 (1958).
[5] R. W. Gammon and E. D. Palik. J. Opt. Soc. Amer. 64. 3. 350 (1974).
[6] C. O. Salzberg and J. J. Villa. J. Opt. Soc. Amer. 48. 579 (1957).
[7] W. C. Dunlap and R. L. Walters. Phys. Rev. 92. 116 (1953).

the surface plasmon resonance ($\lambda = 6.66 \mu m$) is quite large. The wave vector solutions of the surface plasmon dispersion relationship (equation (1)) in the region between $\varepsilon(\omega) = -1$ and $\varepsilon(\omega) = 0$ are imaginary and are not surface modes in the fact that they are uncoupled modes between the incident light and the surface active medium. The complex frequency dielectric functions shown in Fig. 6 and 7 have extrapolated lines covering this region. Also in the region close to $\varepsilon(\omega) = -1$ the complex ω solutions are very difficult to obtain due to the nature of the resonance, that is, the solutions occur in a very narrow valley with a step fall-off on both sides of the valley and can be easily missed by the computer procedure [8]. The surface plasmon resonance point was determined and is marked by an $\times$ on the dielectric function plots.

In Table 4 a comparison is made of the dielectric functions obtained for real and complex frequency. The dielectric functions approach one another at high frequencies and deviate the largest in the area of the surface plasmon resonance. Solutions are shown in the region where $\varepsilon(\omega) > 0$ and $\varepsilon(\omega) < -1$; where for $\varepsilon(\omega) > 0$ the dispersion analysis yields solutions for Brewster modes [13], and for $\varepsilon(\omega) < -1$ solutions are surface polariton modes (Fano modes) [13]. The surface plasmon resonance occurs

Table 3

Comparison of the real part of the complex-ω dielectric functions $\varepsilon_1(\omega)$ and $\varepsilon_2(\omega)$ versus the dielectric function for real frequency ω'

$L(\mu m)$ a)	Re ε_1 b)	$\varepsilon_1(\omega')$ c)	$\Delta\varepsilon_1$ c)	Re ε_2 d)	$\varepsilon_2(\omega')$	$\Delta\varepsilon_2$ e)
2	10.4351	10.4351	0	0.155894	0.155894	0
3	3.90629	3.90623	0.00006	0.516462	0.516484	0.00002
4	6.35904	6.35778	0.001	1.19291	1.19358	0.0007
5	4.39236	4.37016	0.023	2.2433	2.25844	0.015
5.5	3.09752	2.98949	0.108	2.87194	2.95223	0.080
5.9	2.31265	1.32975	0.419	3.20381	3.5886	0.385
6.66	0.229251	$-$ 0.486703	0.716	4.34137	5.00156	0.660
6.7	0.0409945	$-$ 0.812146	0.853	4.4731	5.08339	0.608
6.3	$-$ 0.43728	$-$ 0.927106	0.4898	4.8232	5.29124	0.468
7	$-$ 1.23267	$-$ 1.56256	0.2799	5.44094	5.72098	0.280
7.5	$-$ 3.06521	$-$ 3.1795	0.114	6.73068	6.87892	0.126
3.5	$-$ 6.48159	$-$ 6.50066	0.039	9.48172	9.53347	0.052
9	$-$ 3.15996	$-$ 3.18639	0.026	10.990	11.0292	0.039
10	$-$11.5531	$-$11.5672	0.014	14.3139	14.338	0.024
11	$-$16.5556	$-$16.5623	0.007	20.0136	20.0286	0.015

a) Wavelength of the incident light (in μm) and for the complex frequencies is $L = 2\pi c/\omega_1$.

b) Real part of the complex dielectric function $\varepsilon_1(\omega) = \varepsilon_1(\omega_1 + i\omega_2)$; $\varepsilon_1(\omega_1, \omega_2) = \mathrm{Re}\,\varepsilon_1 - i\,\mathrm{Im}\,\varepsilon_1$.

c) $\Delta\varepsilon_1 = |\mathrm{Re}\,\varepsilon_1(\omega_1, \omega_2) - \varepsilon_1(\omega')|$ where ω_1 and ω_2 are the real and imaginary parts of the complex frequency ω, and ω' is the real frequency.

d) Imaginary part of the complex dielectric function $\varepsilon_2(\omega) = \varepsilon_2(\omega_1 + i\omega_2)$; $\varepsilon_2(\omega_1, \omega_2) = \mathrm{Re}\,\varepsilon_2 - i\,\mathrm{Im}\,\varepsilon_2$.

e) $\Delta\varepsilon_2 = |\mathrm{Re}\,\varepsilon_2(\omega_1, \omega_2) - \varepsilon_2(\omega')|$.

when $\omega_1 = \omega_s$ and $\omega_2 = -1/2\tau$ where τ is the electron relaxation time. Solutions for the Brewster modes [13] show that the bulk plasmon frequency is also complex and occurs at $\omega_1 = \omega_p$ and $\omega_2 = -1/2\tau$.

5. Conclusions

It can be concluded from analyzing the surface plasmon of n^+ silicon that the dispersion relationship obtained from plotting the ATR minima obtained in the real
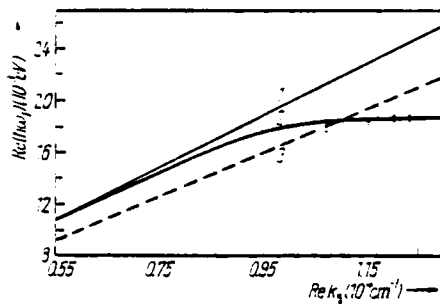
Fig. 5. Same diagram as in Fig. 3 with the inclusion of the ATR minima points calculated using the complex frequency dependent dielectric functions as defined in equations (4a to c). Error bars show the range within which the minima were determined (1) $k_0 = \omega/c$ (light line); (2) $k_{11} = (\omega/c)\,(\varepsilon(\omega)/(\varepsilon(\omega) - 1))^{1/2}$. (3) $k_{||} = (\omega/c)\,n_p \sin(A0)$: $A0 = 57.1°$. $n_p = 1.4$

ATR analysis shows a definite resonance. The error bars indicate the range of uncertainty that the ATR minima were obtained. The deviation at lower values of wave vector is due to the way that the ATR dispersion curve was generated, that is, with fixing the angle of incidence and varying the frequency of the input light. This type of ATR analysis tends to ride along valleys or ridges of the dispersion at lower wave vectors.

Using the complex frequency dependent dielectric function [1] the surface plasmon obeys the following resonance condition:

where

$$\varepsilon(\omega_1, \omega_2) = -1 ,$$
$$\varepsilon_1(\omega_1, \omega_2) = \operatorname{Re} \varepsilon_1 - \operatorname{Im} \varepsilon_2 = -1 ,$$
$$\varepsilon_2(\omega_1, \omega_2) = \operatorname{Re} \varepsilon_2 + \operatorname{Im} \varepsilon_1 = 0 .$$

(10)

The real and imaginary parts of the complex frequency dependent Drude dielectric function are shown in Fig. 6 and 7. As can be readily seen, the deviation of the real and imaginary parts of the dielectric function becomes large near the surface plasmon resonance point. In Table 3 there is a comparison of the values of the real part of $\varepsilon_1(\omega)$ which is a function of complex frequency and $\varepsilon_1(\omega)$ calculated from Drude model for real frequencies. As can be seen from Table 3, the difference in the region close to
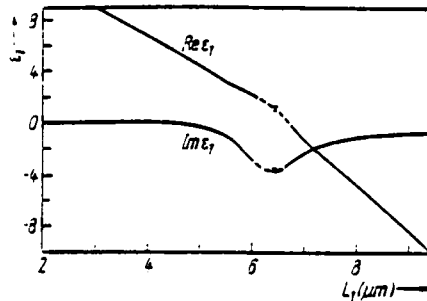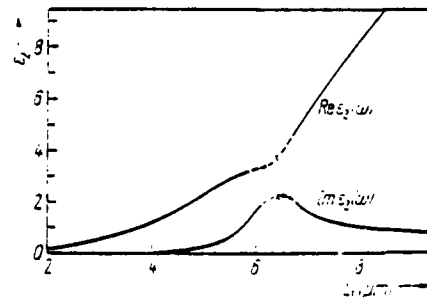

Fig. 6

Fig. 7

Fig. 6. Real and imaginary parts of complex frequency dependent ε_1 versus wavelength L_1 for n⁻ silicon; where $\varepsilon_1(\omega_1, \omega_2) = \operatorname{Re} \varepsilon_1 + i \operatorname{Im} \varepsilon_1$ and is not redefined as in equations (6) and where $L_1 = 2\pi c/\omega_1$. × resonance point. — — — extrapolated region

Fig. 7. Real and imaginary parts of complex frequency dependent ε_2 versus wavelengths L_1 for n⁻ silicon; where $\varepsilon_2(\omega_1, \omega_2) = \operatorname{Re} \varepsilon_2 + i \operatorname{Im} \varepsilon_2$ and is not redefined as in equations (6) and where $L_1 = 2\pi c/\omega_1$. × resonance point. — — — extrapolated region

By redefining the dielectric function in this way, we show that the effect of the complex frequency is to mix the old relationship of ε_1 and ε_2. That is, now the real part of the dielectric function is affected by ε_2 through its imaginary part. Also by the definition of the complex frequency that as $\omega_2 \to 0$, the imaginary parts of $\varepsilon_1(\omega)$ and $\varepsilon_2(\omega)$ both go to zero and we have the original relationship in the real frequency plane. With the dielectric function as defined in (6a) and (6b), we can use the standard relationships between the optical constants n and k and the dielectric function $\varepsilon_1(\omega)$ and $\varepsilon_2(\omega)$ in the complex frequency plane which is

$$n = n(\omega_1, \omega_2) = \{\tfrac{1}{2}[(\varepsilon_1^2 + \varepsilon_2^2)^{1/2} + \varepsilon_1]\}^{1/2}, \tag{7a}$$

$$k = k(\omega_1, \omega_2) = \{\tfrac{1}{2}[(\varepsilon_1^2 + \varepsilon_2^2)^{1/2} - \varepsilon_1]\}^{1/2}, \tag{7b}$$

$$N = n + ik. \tag{7c}$$

Consequently the complex index of refraction of the medium (N) is a function of complex frequency and may be used directly in determining the ATR reflectivity in the complex frequency plane. This is done by redefining the Fresnel reflection coefficient for p-polarized light as

$$\frac{N_2 \cos\theta_3 - N_3 \cos\theta_2}{N_2 \cos\theta_3 + N_3 \cos\theta_2} = \frac{N_2(\omega_1, \omega_2)\cos\theta_3 - N_3(\omega_1, \omega_2)\cos\theta_2}{N_2(\omega_1, \omega_2)\cos\theta_3 + N_3(\omega_1, \omega_2)\cos\theta_2}, \tag{8}$$

where N_3 is the complex index of refraction of the surface active medium, which in this case is silicon, and N_2 is the complex index of refraction of the material between the prism and the surface active medium, which is air in this case study, and θ_2 and θ_3 are the incident angles for medium 2 and 3, respectively.

The complex frequency dependence of the real and imaginary parts of the index of refraction N can also be obtained using a different procedure. This method is more difficult to solve and involves substituting (4b) and (4c) into (7a) and (7b) and finally redefining the complex index of refraction as

$$N = n + ik, \tag{9a}$$

where

$$n = n(\omega_1, \omega_2) = \operatorname{Re} n - \operatorname{Im} k, \tag{9b}$$

$$k = k(\omega_1, \omega_2) = \operatorname{Re} k + \operatorname{Im} n. \tag{9c}$$

Implementing this procedure, the optical constants of n^+ silicon were expressed as functions of complex frequency and used to calculate the ATR dispersion curve. The calculations were done by using a high-speed computer program [8]. The general procedure was to first obtain a set of ω_1 and ω_2 values as determined from calculating the complex frequency–real wave vector dispersion curve (equation (1)); that is, by solving the imaginary part of the dispersion relationship a value for ω_2 was obtained for each ω_1 value. This set of ω_1 and ω_2 values was used to calculate the real and imaginary parts of ε_1 and ε_2 from (2) and (4); and then using these values in (6a) and (6b) to obtain $\varepsilon_1(\omega_1, \omega_2)$ and $\varepsilon_2(\omega_1, \omega_2)$; which then are used in (7a) and (7b) to obtain the complex frequency dependent optical constants. These complex frequency optical constants and Fresnel reflection coefficients were used to calculate the ATR dispersion curve in the same way as done in the real frequency spectrum; but now the ATR minimum is found by fixing the angle of incidence and by scanning through ω_1 the real part of the surface plasmon frequency. The ATR dispersion curve minima are plotted in Fig. 5 along with the damped surface plasmon dispersion curve. There is no discrepancy between the ATR dispersion curve calculated in complex frequency plane and the theoretical dispersion curve. The complex frequency

occur by probing the complex-k response which is experimentally achieved by fixing the excitation frequency and by varying the angle of incidence. The complex-ω response measurements will only allow moderate coupling which is achieved by riding on the ridges and valleys of the surface plasmon excitation in the real frequency plane.

Table 2
Analysis of ATR calculated dispersion curve for n⁻ silicon [a]

$\Delta\theta$ [b]	L_0 [c] (μm)	D_0 [c] (μm)	$k_{\parallel}^{exp}$ [d] (10^4 cm^{-1})	$k_{\parallel}^{exp}/k_0$ [e]
23.3°	468.9	400.9	1.35×10^{-2}	1.00886
47.4°	1074.4	11.4	1.08×10^{-2}	1.839
49.2°	1164.6	10.97	1.02×10^{-2}	1.894
53.1°	1376.7	10.34	9.126×10^{-3}	1.9997
57.1°	1685.4	10.11	7.825×10^{-3}	2.099
61.08°	2117.5	10.24	6.493×10^{-3}	2.188
66.38°	3195.7	11.182	4.519×10^{-3}	2.279

[a] Input Drude parameters: $\varepsilon_\infty = 11.7$, $\tau = 5.62 \times 10^{-15}$ s. $N/m^* = 3.58 \times 10^{20}$ electrons/cm³.

[b] Angle of incidence with respect to the prism base where $n_p = 2.5$.

[c] L_0 and D_0 are the wavelength at the minimum and the air gap, respectively, to obtain a p-polarized reflectivity of 90%.

[d] This is the experimental wave vector at the minimum where $k_{\parallel}^{exp} = (2\pi/L_0) n_p \sin(\Delta\theta)$.

[e] This is the ratio of the experimental wave vector to the wave vector of light ($k_0 = \omega/c = 2\pi/L_0$).

4. ATR Analysis in the Complex Frequency Plane and Complex Frequency Optical Properties of n⁺ Silicon

Due to the discrepancy between the theoretical damped surface plasmon dispersion relationship which shows a definite resonance, and the ATR minima dispersion curve which shows back-bending which is calculated using real frequency dependent optical constants, an approach was made to calculate the ATR reflection spectrum in the complex frequency plane. In order to calculate the ATR spectrum in the complex frequency plane, the optical constants of the surface active medium and the Fresnel reflectance coefficient must be redefined to be functions of complex frequency. Since the frequency is complex, then the real ($\varepsilon_1(\omega)$) and imaginary ($\varepsilon_2(\omega)$) parts of the dielectric functions are themselves complex as given by

$$\varepsilon(\omega) = \varepsilon_1(\omega) + i\varepsilon_2(\omega) , \tag{4a}$$

where

$$\varepsilon_1(\omega) = \operatorname{Re}\varepsilon_1(\omega) + i\operatorname{Im}\varepsilon_1(\omega) , \tag{4b}$$

$$\varepsilon_2(\omega) = \operatorname{Re}\varepsilon_2(\omega) + i\operatorname{Im}\varepsilon_2(\omega) , \tag{4c}$$

where ω is the complex frequency defined by $\omega = \omega_1 + i\omega_2$. If one substitutes (4b) and (4c) into (4a) and regroups into real and imaginary parts, one obtains

$$\varepsilon(\omega) = [\operatorname{Re}\varepsilon_1(\omega) - \operatorname{Im}\varepsilon_2(\omega)] + i[\operatorname{Re}\varepsilon_2(\omega) + \operatorname{Im}\varepsilon_1(\omega)] . \tag{5}$$

Now using the standard definition of $\varepsilon_1(\omega)$ and $\varepsilon_2(\omega)$ to be equal to the real and imaginary parts of the dielectric function, respectively, as given in (5), we obtain

$$\varepsilon_1(\omega) = \varepsilon_1(\omega_1, \omega_2) = \operatorname{Re}\varepsilon_1(\omega) - \operatorname{Im}\varepsilon_2(\omega) , \tag{6a}$$

$$\varepsilon_2(\omega) = \varepsilon_2(\omega_1, \omega_2) = \operatorname{Re}\varepsilon_2(\omega) + \operatorname{Im}\varepsilon_1(\omega) . \tag{6b}$$

a measurement of electrical resistivity (1.32×10^{-3} Ωcm) and using the resistivity
versus impurity concentration listed in Sze [11]; this agreement is reasonable and the
difference is probably due to different sample mobilities. Kukharskii and Subashiev
[9] obtained a relaxation time of 11.27×10^{-15} s for an n-type silicon of carrier
concentration 5.5×10^{19} electrons/cm^3. They also obtained a value of $\omega_p \tau = 2.69$
which is in agreement with the present results.

3.2 Dispersion analysis

The value of $\omega_p \tau = 2.69$ as determined from the Drude optical parameters (Table 1)
shows that the surface plasmon resonance of n$^+$ silicon is fairly highly damped. The
complex frequency–real wave vector solution of the theoretical dispersion curve of
equation (1) is shown in Fig. 3 and 4. The complex frequency solutions exhibit the
the standard behavior of the surface plasmon resonance: namely, $\omega_1 \rightarrow \omega_s$ and
$\omega_2 \rightarrow -1/2\tau$ as the wave vector $k_{||} \rightarrow \infty$.

   The ATR surface plasmon dispersion curve is found by plotting the energy and
wave vector at the minimum reflectivity point in the ATR spectrum. The ATR mini-
mum point is taken when the reflectivity of p-polarized light is at 90%. The general
computer procedure has been previously explained [12], and the results of the analysis
are shown in Table 2. In this table, you can see that as the angle $\Delta 0$ (angle with
respect to the prism base) is increased, the wavelength at the minimum (L_0) increases
to longer wavelengths and smaller experimental wave vectors ($k_{||}^{exp}$) are achieved.
This analysis shows that as the incident angle is decreased, the ATR dispersion curve
approaches the light line, as can be seen by studying the last column which gives the
ratio of the wave vector generated by the prism ($k_{||}^{exp}$) to the wave vector of light in air
($k_0 = \omega/c$). That is, the experimental ratio ($k_{||}^{exp}/k_0$) approaches unity as you go higher
in energy. This is equivalent to the complex-k behavior of the surface plasmon
resonance where the dispersion relationship stays close to the light line and then
back-bends going into Brewster modes where $k_{||} < \omega/c$ [13]. Therefore, the ATR
determined dispersion shows no resonance as is achieved by the theoretical dispersion
relationship. Since $\omega_p \tau = 2.69$, there is no physical explanation why there is no
resonance present in the ATR dispersion curve obtained using real frequencies. Con-
sequently, the only true coupling to the surface plasmon resonance of n$^+$ silicon will

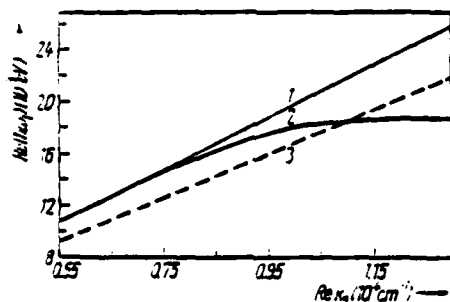Fig. 3   Fig. 4

Fig. 3. Theoretical dispersion curve (equation (1)) of the surface plasmon of n$^+$ silicon plotted
as the real part of the complex energy $\hbar\omega_1$ versus real wave vector $k_{||}$. Also shown is the light line
($k = \omega/c$) along with the energy–wave vector light line (dashed line) generated by the ATR con-
figuration shown in Fig. 1b. The theoretical dispersion curve is plotted from the parameters given
in Table 1. (1) $k_0 = \omega/c$ (light line); (2) $k_{||} = (\omega/c)(\varepsilon(\omega)/(\varepsilon(\omega) + 1))^{1/2}$; (3) $k_{||} = (\omega/c)\, n_p \sin(\Delta 0)$,
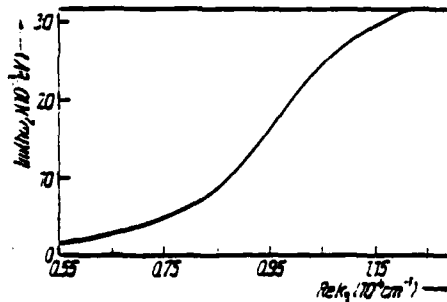$\Delta 0 = 57°$, $n_p = 1.4$

Fig. 4. Imaginary part of the complex energy ($\hbar\omega_2$) versus real wave vector for the surface
plasmon of n$^+$ silicon

large due to the bowing of the silicon chip and the need to add the extra aluminum spacer pads. The deviation in the region of the minimum for the curve fit in Fig. 1b is possibly indicative of the need to include a frequency-dependent collision time. A similar deviation was obtained by Kukharskii and Subashiev [9] when they curve-fitted a Drude model to n⁺ silicon. They corrected this deviation by using a frequency-dependent relaxation time. There exist other problems in this part of the spectral region where the Drude model should be corrected. Namely, as shown by Salzberg and Villa [6], ε_∞ increases from ≈ 11.7 at 6 μm to ≈ 11.82 at 2.5 μm. This is due to the dispersion of the index of refraction when the band edge is approached. Spitzer and Fan [10] have shown that this is a small absorption band in the range of 1.5 to

Table 1

Experimentally determined Drude free-carrier parameters for n⁺ silicon

ε_∞ [a]	N/m^* (10^{29} electrons/cm³)	τ (10^{-15} s)	m^* [b]	N (10^{19} electrons/cm³)	μ_{opt} (cm²/Vs)
11.7	3.58	8.62	0.26	9.31	58.3

[a] Input parameter for calculation.
[b] Fraction of electron rest mass obtained from Spitzer and Fan [10].

5 μm which is dependent on the carrier concentration. Corrections for these effects were not included due to the relatively large experimental error and in the region $\lambda > 5$ μm the region where the surface plasmon exists the curve fits were good enough and should accurately reproduce the surface plasmon response.

The experimentally determined Drude free-carrier parameters are shown in Table 1 along with the optical mobility $\mu = e\tau/m^*$ and the electron carrier concentration N. The overall accuracy of this least-squares fitting procedure can be seen by viewing Fig. 2 where each parameter is varied by 15% (higher values) from the best fit which is also plotted with it. A value of $N = 7 \times 10^{19}$ electrons/cm³ was determined from
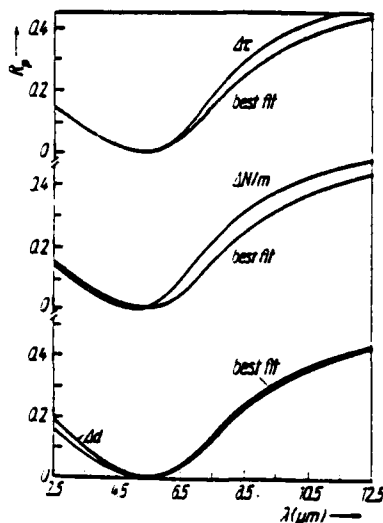

Fig. 2. ATR reflectivity spectrum of n⁺ silicon where each of the best-fit parameters τ, N/m^*, and d are changed to 15% higher values. Best-fit parameters: $\varepsilon_\infty = 11.7$, $\tau = 8.122 \times 10^{-15}$ s, $N/m^* = 3.64 \times 10^{29}$ electrons/cm³, $d = 0.2105$ μm
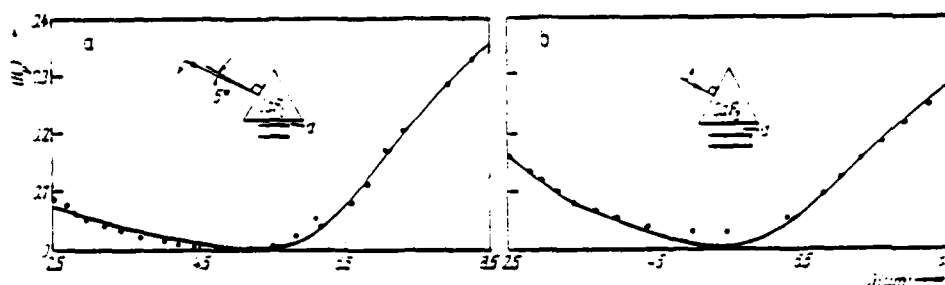
Fig. 1. Normalized ATR reflection spectrum of n⁺ silicon plotted as normalized p-polarized reflectivity versus wavelength. Solid points are the data points corrected for effects of the aluminum spacer. Solid curve is the best-fit least-squares curve with the best-fit parameters shown in the blocked region. Shown in the insert is the ATR geometry used with the angle of incidence of the input beam is a) $5°$ ($\delta = 8.17 \times 10^{-3}$, $\tau = 9.11 \times 10^{-15}$ s, $N/m^* = 3.318 \times 10^{29}$ electrons/cm³, $d = 0.1667$ μm. b) $0°$ ($\delta = 9.16 \times 10^{-3}$, $\tau = 8.12 \times 10^{-15}$ s, $N/m^* = 3.64 \times 10^{29}$ electrons/cm³, $d = 0.2105$ μm); $\varepsilon_\infty = 11.7$

where the data points are corrected for the effects of the aluminum spacers. The optical properties of the n⁺ silicon were determined by doing a least-squares curve fit of the Drude parameters N/m^* and τ, and the air gap d. The high-frequency dielectric constant ε_∞ used in the Drude model (equation (2)) was taken to be equal to $\varepsilon_0 = 11.7$ — the dielectric constant of silicon at zero frequency in the absence of free carriers. Since silicon is homopolar, the dielectric constant of silicon is equal to ε_0 in the absence of free carriers from zero frequency up to the first interband transition. The dielectric constant $\varepsilon_0 = 11.7$ was determined by Salzberg and Villa [6] on measuring the refractive index of a prism made of single crystal silicon. This dielectric constant also agrees with the value measured at radio frequencies on intrinsic silicon by Dunlap and Walters [7].

The parameters N/m^* and τ were varied along with the air gap d to obtain the best-fit least-squares parameter δ defined as

$$\delta = \left\{ \frac{\sum_i [(R_p)^i_{theory} - (R_p)^i_{exp}]^2}{M} \right\}^{1/2} ,$$

where the sum over i is for all data points and M is the total number of data points. The curve fitting program [8] was based on choosing an air gap d and finding the parameters N/m^* and τ which had a best fit of the measured reflection. The air gap d is used almost like an independent parameter, that is, for a particular d the best-fit parameters are determined, then d is varied and a set of new best-fit parameters is determined, and the total set with the smallest δ is chosen as the best fit. The total percentage area of aluminum covering the silicon was $(7.6 \pm 2.7)\%$. The input beam was masked to hit only the uniform air gap area, and it was impossible to measure exactly the total area of aluminum that was blocking the beam from hitting the silicon. Therefore, the ATR computer calculations were calculated for different percentages of aluminum present within the 2.7% change as given above: and the best fit was determined by the lowest least-squares deviation. The best-fit Drude reflectivities are plotted on the same graphs as the reflectivity data.

3. Results and Discussion

3.1 Optical properties

The Drude free-electron model of the dielectric function fits satisfactorily to the ATR spectra curves as shown in Fig. 1a and b. The experimental error is relatively

ions and to diffuse the phosphorous ions into the bulk of the sample and remove the high concentration of ions left on the surface. The samples were then deglazed in a $10:1$ solution of H_2O and HF for 5 min for the purpose of removing any grown oxide on the silicon surface. The final resistance of the diffused layer was 6 Ω/square.

The initial wafers had a bow of 0.115 mils and a taper of 0.03 mils across the 2 in. diameter. The processed wafers were scribed and broken into ATR sample sizes of 450×300 sq. mils. Aluminum spacers were electron beam evaporated onto two corners of the silicon and nine ≈ 20 mil diameter aluminum spots were evaporated between the two corners. The silicon wafers were mounted with double backed tape onto optical flats ($1/2''$ thick). With the silicon die mounted on the optical flat as they were compressed against the base of the prism, bowing of the wafer would take place when only the two corners of the die were coated with aluminum. Consequently, the addition of the ≈ 20 mil diameter spots across the center region reduced the bowing significantly and allowed a reasonably uniform air gap to exist between the prism base and the silicon.

2.2 Experimental measurements and data analysis

Initial investigations of the optical properties of n⁺ silicon were done by measuring the near normal incidence reflectivity of silicon versus gold. These measurements were not absolute but were done for the purpose of finding the plasma edge and minimum. The minimum appeared to be at ≈ 4.5 μm and consequently ATR spectrum runs were performed in the range of 3 to 9 μm. ATR measurements were performed by measuring the ratio of the reflected intensity of p-polarized light (R_p) with the sample pressed against the ATR prism to that with the sample removed. The Otto ATR method of exciting surface plasmon modes was used where the surface plasmon was for an air–Si interface. A CaF_2 prism ($57.1°–65.6°$ (apex)–$57.3°$) was used for all measurements; it has an average index of 1.45 and it transmits out to 9 μm. The prism base was flat to greater than a tenth of a wave (0.5461 μm) and the uniformity of the air gap was determined by viewing Newton interference fringes for angles less than the critical angle and by viewing the surface plasmon resonance of aluminum which appears in the visible spectrum for angles greater than the critical angle, uniformity of this color absorption was adjusted. Good uniformity of the air gap across the whole silicon surface was impossible to obtain due to its natural bow; consequently, the input beam was masked to hit only the approximately uniform section. Due to this bowing problem, uniform air gaps could be obtained only for small spacings between the silicon sample and the prism base. The probable reason for this reduction of bowing at small spacings is that both high points on the silicon and dust particles are present between the prism base and silicon surface which act as a natural spacer.

The globar light source was focused down (beam divergence 5°) and optical alignment of the beam could be seen by viewing the output beam of the prism assembly with a mirror. The reflection spectra were taken on a Perkin-Elmer model 301 far-infrared spectrometer operated in a single-beam mode with the addition of appropriate gratings and filters. The 13 Hz chopped signal from the thermocouple detector was digitized and then computer averaged. The wire grid polarizer was placed in the p-polarizing position and placed before the input beam to the prism.

2.3 Optical constants and ATR curve fitting

The ATR reflection spectra were taken at room temperature and displayed in Fig. 1a and b. The spectra are plotted as normalized reflectivity ratio R_p versus wavelength

where $k_{\parallel}$ is the magnitude of the surface plasmon wave vector which is parallel to the interface, ω the surface plasmon frequency, c the speed of light, and $\varepsilon(\omega)$ the frequency-dependent bulk dielectric function of silicon which for this study will be of the form of the Drude free-electron model which is

$$\varepsilon(\omega) = \varepsilon_1(\omega) - i\varepsilon_2(\omega)$$
$$= \varepsilon_\infty \left(1 - \frac{\omega_p^2 \tau^2}{1 + \omega^2\tau^2}\right) + i\varepsilon_\infty \left(\frac{\omega_p^2 \tau}{\omega(1 + \omega^2\tau^2)}\right), \tag{2}$$

where ε_∞ is the high-frequency dielectric function, $\omega_p = (4\pi N e^2/\varepsilon_\infty m^*)^{1/2}$ the bulk plasma frequency, m^* the electron effective mass, N the electron concentration, e the electronic charge, and τ the electronic relaxation time.

For a damped surface oscillation the complex frequency–real wave vector solution of the dispersion relationship given by (1) is solved by the methods of Gammon and Palik [5]. The wave vector $k_{\parallel}$ is assumed real, while the frequency of the excitation is complex and equal to

$$\omega = \omega_1 + i\omega_2, \tag{3}$$

where ω_1 is the surface plasmon frequency, and ω_2 is related to the surface plasmon damping. A plot of ω_1 versus $k_{\parallel}$ yields the surface plasmon dispersion curve. Briefly, Gammon and Palik [5] methods involve substituting (2) and (3) into (1) and solving for a ω_2 value for a particular ω_1 value such that the imaginary part of (1) is equal to zero. With these values of ω_1 and ω_2 the real part of (1) is solved for the real wave vector $k_{\parallel}$. Repeating this produces a set of ω_1, ω_2, and $k_{\parallel}$ values are obtained from which the dispersion curve is obtained. The complex wave vector–real frequency solutions of the surface plasmon dispersion relationship (equation (1)) will not be discussed in this study.

The Otto ATR technique [1] is a method for coupling incident electromagnetic waves to surface polaritons. By computer curve fitting the ATR spectra to the Drude dielectric function (equation (2)) the optical properties of the surface active medium are obtained. Using these optical constants the dispersion relation of the surface plasmon on the real frequency axis is obtained from the computer calculated minima. Each minimum is obtained by fixing the incident angle and varying the frequency, where the reflected intensity of p-polarized light is greater than 90% at the minimum.

Section 2 contains the experimental details of sample preparation and surface plasmon resonance measurements. Section 3 gives the results of the optical measurements and discusses the dispersion of the surface plasmon on the real frequency axis. In Section 4 we discuss the ATR analysis in the complex frequency plane and the complex frequency optical properties of n⁺ silicon. In Section 5 we summarize our results.

2. Experiment

2.1 Sample preparation

The n⁺ silicon samples were obtained by diffusing phosphorus into a 5 Ωcm n-type silicon wafer. The initial wafers were 2 in. in diameter and 18 mils thick and were polished on both sides. The samples were prepared at the Micro-Electronics Production Laboratory at Hughes Aircraft Company in Carlsbad. The wafers were initially prefurnace cleaned in a 50:50 mixture of H_2SO_4 and H_2O_2 to remove any oxide on the surface and to take off any wax left from the polishing. The samples were then diffused at 925 °C in phosphine (PH_3) gas for 20 min with a pre-heat and post-heat for 10 min in N_2/O_2. After the n⁺ deposition, the samples were heated at 1000 °C in pure nitrogen for 180 min. The purpose was to both electrically activate the phosphorous

Department of Physics, University of California, Los Angeles[1])

Optical Properties of the Surface Plasmon of n⁻ Silicon[2])

By

P. F. Robusto[3]) and R. Braunstein[4])

The optical properties of the surface plasmon of n⁻ silicon are determined by a least-squares curve fit of the Drude intraband model to the ATR reflection spectra. The surface plasmon resonance of n⁻ silicon is highly damped ($\omega_p \tau = 2.69$), and causes the ATR dispersion curve calculated on the real frequency axis to exhibit back-bending for its complex frequency-like solutions; whereas the theoretical dispersion curve exhibits the standard wave vector divergence at the surface plasmon frequency. This discrepancy is rectified by converting the optical properties of n⁻ silicon into functions of complex frequency, and using them to calculate the ATR dispersion curve in the complex frequency plane. A comparison of the Drude dielectric function as a function of real and complex frequencies is analyzed. The comparison shows that the difference between their values is small at high frequencies and deviate the largest in the region near the surface plasmon resonance.

Die optischen Eigenschaften des Oberflächen-Plasmons von n⁺- Silizium werden bestimmt, indem für das Drude-Intraband-Modell die Methode der kleinsten Quadrate für das Verfahren der stochastischen Kurvenermittlung an die abgeschwächten Totalreflexions-Spektren benutzt wird. Die Oberflächen-Plasmonresonanz von n⁺- Silizium ist stark gedämpft ($\omega_p \tau = 2.69$) und bewirkt, daß die auf der wirklichen Frequenzachse berechnete, abgeschwächte Totalreflexions-Dispersionskurve eine Zurückbiegung für deren komplexe frequenzartige Lösungen aufweist, wohingegen die theoretische Dispersionskurve die Standard-Wellenvektor-Divergenz bei der Oberflächen-Plasmonfrequenz aufweist. Diese Unstimmigkeit wird korrigiert, indem die optischen Eigenschaften von n⁺-Silizium in Abhängigkeit von der komplexen Frequenz umgewandelt werden, und indem diese benützt werden, um die Kurve der abgeschwächten Totalreflexion in der Ebene der komplexen Frequenz zu berechnen. Ein Vergleich der dielektrischen Funktion nach Drude in Abhängigkeit von wirklichen und komplexen Frequenzen wird analysiert. Der Vergleich ergibt, daß der Unterschied zwischen den Werten bei hohen Frequenzen niedrig ist, und daß die Werte am meisten im Bereich nahe der Oberflächen-Plasmonresonanz abweichen.

1. Introduction

The dispersion relationship of surface polaritons of metals [1, 2] and semiconductors [3] has been extensively studied for materials where the damping of the surface polariton oscillation is small. It is the aim of this study to investigate the optical properties of the surface plasmon of n⁺ silicon for which the oscillation is highly damped. The general dispersion relationship for surface plasmons for an air–material interface is [4]

$$k_{\parallel} = \frac{\omega}{c} \left(\frac{\varepsilon(\omega)}{\varepsilon(\omega) + 1} \right)^{1/2}, \tag{1}$$

E. APPENDIX

D.   Participating Scientific Personnel:

R. Braunstein	Principal Investigator
B. Bobbs	Ph.D. candidate
M. Burd	Ph.D. received Dec. 1984
D. Deal	Ph.D. received March 1982
B. Dorfman	Post Doctoral Fellow
S. M. Eetemadi	Ph.D. received Dec. 1984
R. K. Kim	Ph.D. received Sept. 1983
R. Martin	Ph.D. candidate
A. Melo	Post Doctoral Fellow
R. Stearns	Ph.D. received March 1982
J. Stevens	Ph.D. candidate

Department of Physics, University of California, Los Angeles[1])

Optical Measurements of the Surface Plasmon of Copper[2])

By

P. F. Robusto[3]) and R. Braunstein[4])

The optical properties of the noble metal copper are determined by computer fitting the experimentally obtained attenuated total internal reflection (ATR) spectra of its surface plasmon in the visible spectral region (0.42 to 0.63 μm). The dispersion curves of the surface plasmon resonance of copper are determined; they show that the resonance exists on the steep absorption edge of ε_2 at 2.16 eV. This absorption edge, which is due to the d-band to Fermi level transition, causes the large shift in the location of the surface plasmon excitation from $\varepsilon_1(\omega_s) = -1$ to $\varepsilon_1(\omega_s) = -4.7$ and causes the true resonance to occur in the complex frequency plane.

Die optischen Eigenschaften des Edelmetalls Kupfer werden durch Computer-Anpassung an die experimentell erhaltenen inneren Totalreflexionsspektren (ATR) des Oberflächenplasmons im sichtbaren Spektralbereich (0,42 bis 0,63 μm) ermittelt. Die Dispersionskurven der Oberflächenplasmonresonanz von Kupfer werden bestimmt; sie zeigen, daß an der steilen Absorptionskante von ε_2 eine Resonanz bei 2,16 eV vorhanden ist. Die Absorptionskante, die auf den Übergang vom d-Band zum Fermi-Niveau zurückzuführen ist, verursacht die große Verschiebung in der Lage der Oberflächenplasmonanregung von $\varepsilon_1(\omega_s) = -1$ auf $\varepsilon_1(\omega_s) = -4,7$ und bewirkt, daß die echte Resonanz in der komplexen Frequenzebene auftritt.

1. Introduction

The optical constants of copper have been measured since the time of Drude. Copper is known to exhibit interband transitions throughout the visible region of the spectrum starting with a d-band to Fermi level transition at ≈ 2.1 eV. However, copper is known not to exhibit a bulk plasma resonance. The general explanation of this is that due to the d-states the positive contribution of the bound part of the dielectric function ε_1^b comes in a frequency region where the negative contribution of the free-electron part of the dielectric function ε_1^f is of too large a magnitude for ε_1 to reach zero. It is the aim of this study to determine the optical properties of copper using attenuated total internal reflection (ATR) techniques [1, 2] and to determine if a surface plasmon resonance exists in the visible region.

Section 2 contains the experimental details of sample preparation and surface plasmon resonance measurements and analysis. In Section 3 we give the results of the optical measurements, namely the optical properties of copper and the dispersion of its surface plasmon. This study is concluded with a summary in Section 4.

2. Experiment

2.1 Sample preparation

The copper films were prepared by thermal evaporation in a high-vacuum deposition system. All films were prepared on the same day that the experimental measurements were performed, so as to reduce the effects of oxide forming on the surface. The deposition was done from an Al_2O_3 coated evaporation boat with 99.999% pure copper. The evaporation was performed in a diffusion pumped liquid nitrogen trapped deposition system with the pressure prior to growth $\approx 2 \times 10^{-4}$ Torr. The substrates were fused silica front surface mirror substrates (7.75 mm dia. × 4.00 mm) polished to better than 1/10 wave flatness at 0.5461 μm over the center 6 mm portion. The deposition rate was 150 Å/min and was monitored during evaporation with a Sloan Omni 11A rate and thickness monitor. The total thickness of the Cu films was 3000 Å as measured by a Sloan Ångstrometer. The prepared films had a bright metallic luster and visually appeared to be optically smooth and homogenous.

2.2 Experimental measurements

The Otto ATR method [1, 2] of exciting surface plasmons was used where the surface plasmon was for an air–Cu interface. The ATR measurements were performed by measuring the ratio of the intensities of p-polarized light (R_p) to that of s-polarized light (R_s) with the sample pressed against the base of the ATR prism and normalized to the reflectivity with the sample removed. The prism used for optical measurements was a (45.0°–89.9° (apex)–45.1°) light flint prism which was flat to greater than a tenth of a wave at 0.5461 μm. The air gap was obtained by using either evaporated spacers or natural dust particles. The uniformity of the air gap was adjusted by observing the uniformity of the surface plasmon resonance of copper at angles greater than the critical angle of total internal reflection. Beautiful colors of red, green, and blue could be visually seen for p-polarized light depending on the viewing angle and the air gap thickness. These colors could be seen for the largest viewing angle possible, therefore indicating the wave vector divergence of the resonance condition. At angles less than the critical angle, Newton interference colors were not visible due to the smallness of the air gap used ($d \approx 1000$ Å). The reflection spectra were taken on a Perkin-Elmer model 301 far-infrared spectrometer modified to operate in the single-beam mode in the visible with the addition of 1440 lines/mm grating, appropriate filters, and use of tungsten light source and EMI photomultiplier No. 9592B. The data collection system consisted of locking in on the 13 Hz chopped signal with a PAR model 124A lock-in amplifier. The data were digitized and punched on paper tape and a PDP 11/20 computer averaged the data and generated a plot of normalized reflectivity versus wavelength. A digital controller was used to sequence a stepping motor for changing for both polarizations and for stepping the wavelength drive through the visible spectrum [3]. All experimental data were obtained by fixing the angle of incidence of the input light and by varying its frequency; that is, the complex frequency behavior of the surface plasma resonance was analyzed.

2.3 Optical constant determination

The ATR experiments were performed with a constant air gap and incident angle; the reflectivity ratio (R_p/R_s) was measured as a function of wavelength. All optical measurements were taken at room temperature and are plotted as normalized reflectivity ratio (R_p/R_s) versus wavelength, as shown in Fig. 1 a and b.

To theoretical curve fit an experimental ATR curve the wavelength dependent optical constants n and k need to be determined along with the wavelength indepen-
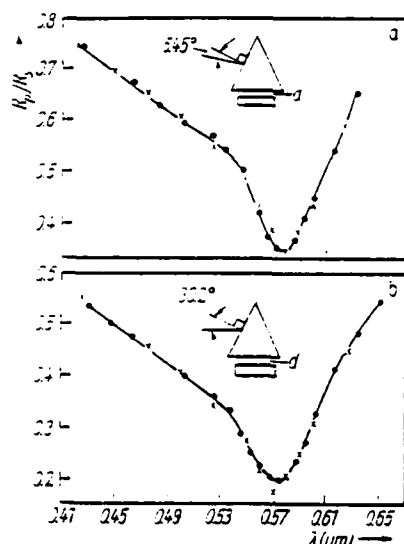
Fig. 1. Attenuated total internal reflection spectrum of copper plotted as the normalized value of the reflectivity ratio (R_p/R_s) versus wavelength. Solid points denote the experimental data with a solid line drawn through them for clarity. The ×'s are the computer fitted values. The best-fit air gap value (d) is in a) 1400 Å and in b) 480 Å. The angle of incidence of the incoming light with respect to the input side of the light flint prism is shown in the ATR diagram in the insert. × computer, ● experimental

dent air gap d. For each ATR spectrum the wavelength dependent normalized reflectivity ratio (R_p/R_s) was measured giving us one set of values for two unknown wavelength-dependent values (n and k) and wavelength-independent value of d. Consequently, it is impossible to determine the optical constants and the air gap directly from the experimentally obtained data. The method that was chosen was to use the experimentally determined optical constant k obtained in the spectral region of 0.44 to 0.55 μm by Schultz [4]. He obtained accurate values of k from normal-incidence transmission measurements, which is more sensitive for determining k-values than reflectance measurements. The spectral region of 0.44 to 0.55 μm was chosen for two reasons, the first being that the relative change of k is nearly flat on the low-energy side and slopes off slightly on the high-energy side; the second being that this region is at higher energy than the surface plasmon minimum and therefore will have a small effect on the optical constants determined in this region.

The optical constants in the 0.44 to 0.55 μm region were determined by using Schultz's [4] k-values and the experimentally obtained R_p/R_s values for two experimental curves. The procedure used was to pick an arbitrary air value d_1 for experimental curve 1 and then to calculate from the R_p/R_s and k-values a set of n-values. With this set of n- and k-values, curve 2 was computed and compared to the experimental curve. The air gap for the second curve d_2 was varied until an optimum fit was obtained. This procedure was performed several times by varying the air gap d_1 until the best fit for curve 2 was obtained. The k-values of Schultz [4] were accurate to $\pm 2\%$ and therefore they were varied within this range to optimize the fit. Once this procedure was completed, a set of n- and k-values was determined for the spectral range 0.44 to 0.55 μm and the best-fit air gaps d_1 and d_2 were determined. The final stepping interval for d was ± 5 Å whereas the n-values were determined to 0.0002 for each curve. Once the air gaps d_1 and d_2 were determined, the experimental reflectance data could be used directly to obtain both n and k in the surface plasmon region. The procedure for this region was to pick a k-value and to find the set of n-values which would fit the experimental curves. The constraint used in this part of the spectral range was that the k-values should vary smoothly in this interval and that

the error be displayed in the n-values. The reason for this will be explained in the results section. Computer programs [3] were written using the Fresnel reflection coefficients and the three-media multilayer reflectance formula to theoretically computer fit the experimental data. The computer fits are shown by ×'s on the same graphs as the reflectivity data in Figs. 1 a and b.

3. Results of the Optical Measurements of the Surface Plasmon of Copper

3.1 Optical properties

The ATR determined optical constants n and k are shown in Fig. 2 a and b, while the dielectric functions $\varepsilon_1(\omega)$ and $\varepsilon_2(\omega)$ are shown in Fig. 3 a and b, respectively along with the calculated normal-incidence reflectivity in Fig. 4. The error in determining the optical constants is difficult to estimate. The average percentage error in the determined index of refraction as shown in Fig. 2a was 1.38%. The average experimental error was $\leq 1\%$ which gives an error of $\approx \pm 2\%$ for the index of refraction values, while an error of 2% in the k-values yields an $\approx 3.5\%$ error in n. Combining all the error producing terms yields an approximate error of 8% for the n-values and 4% for the k-values. The determined optical constants are quite adequate for determining the optical properties of the surface plasmon dispersion which is the main purpose of this investigation. By evaluating the imaginary part of the dielectric function ε_2, we obtain a strong absorption edge at 2.15 eV which is attributed to the d-band to Fermi surface transitions $\Delta_5 \rightarrow \Delta_1(E_F)$ and $L_3(Q-) \rightarrow E_F(L_2)$; the band nomenclature is due to Mueller and Phillips [5]. The rapid rise in ε_2 is due to the flatness of the L_3 d-band, which permits a large number of interband transitions to the Fermi surface within a narrow energy range. The first peak in ε_2 is seen at ≈ 2.18 eV and corresponds to the transition $L_3(Q-) \rightarrow E_F(L_2^1)$. These values agree well with those obtained by Welkowsky and Braunstein [6] which were 2.18 and 2.53 eV.

Fig. 2   Fig. 3
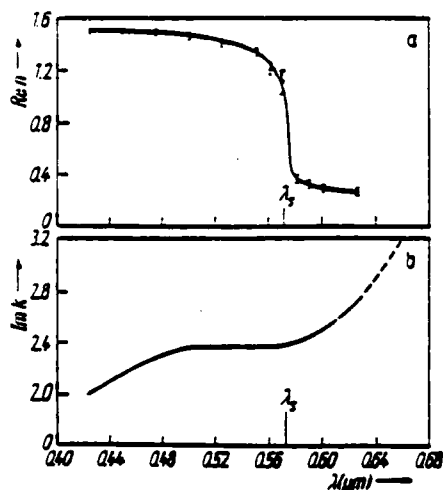
Fig. 2. Plot of the a) real and b) imaginary part of the refractive index of copper versus wavelength for the computer fitted data of Fig. 1 a and b. Also shown is the location of the surface plasmon resonance (λ_s)
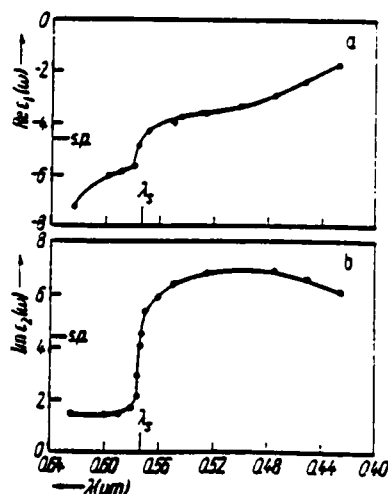
Fig. 3. Plot of the a) real and b) imaginary part of the dielectric function of copper versus wavelength for the computer fitted data of Fig. 1 a and b. Also shown is the location of the surface plasmon resonance (λ_s)

3.2 Dispersion analysis

The experimental dispersion of the surface plasmon resonance can be seen by noting the shift of the minimum for two different incidence angles in Fig. 1 a and b. The ATR experimental minima must be corrected for the effects of the prism. These effects are essentially eliminated by using only the minima obtained when the minimum reflectivity for p-polarized light is greater than $\approx 90\%$. The dispersion curve for the ATR analysis is accomplished by plotting the value of the energy at the minimum of each ATR curve obtained for different incident angles (different wave vectors $k_{\parallel}$) for continuous changes in the frequency of the incident light. The ATR computed [3] dispersion curve is shown in Fig. 5 where the error bars signify that minima were determined within ± 10 Å at low values of wave vector and ± 1 Å at high wave vector points. The dispersion curve shows the characteristic surface plasmon resonance, that is, $k_{\parallel} \rightarrow \infty$ at $\omega = \omega_s$. The computed and experimental ATR spectra had less than 10% absorption for s-polarized light as expected theoretically. The resonance value for the plotted wave vectors is at 2.163 eV. The energy wave vector light line generated by the prism for the experimental runs of Fig. 1 a and b are shown on the dispersion curve plot in Fig. 5.

The experimental ATR minima shown in Fig. 1 a and b occur at lower energy due to the prism and the large amount of overcoupling ($\approx 75\%$ absorption of incident light); the minimum is partly governed by the resonance condition $\varepsilon_1(\omega) = -n_p^2$ which causes the resonance to shift to a frequency where $\varepsilon_1(\omega)$ is more negative. The location of the surface plasmon resonance is shown in the plots of the optical constants n and k in Fig. 2 a and b and on the dielectric function plots of ε_1 and ε_2 in Fig. 3a and b. In the region of the surface plasmon resonance, the error bars for determining the index of refraction is large, as shown in Fig. 2a. This error is mainly due to the effects of very thin oxide layers on the copper surface which cause the resonance condition to shift. This is the reason why the arbitrary criteria of fixing the values of k to lie on a smooth curve was chosen as explained in the previous section for determining the optical constants. As seen from Fig. 3, the surface plasmon resonance
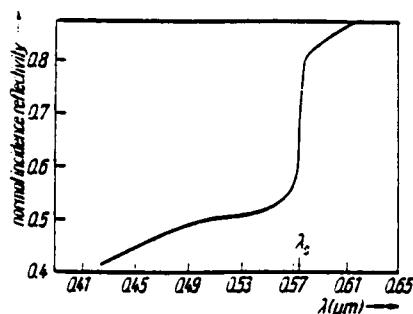

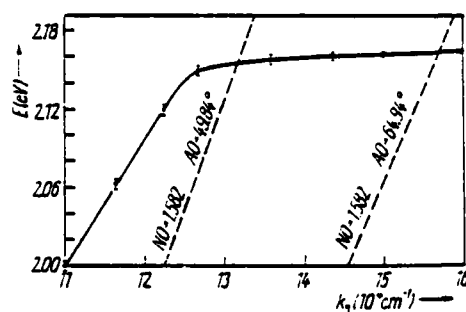Fig. 4   Fig. 5

Fig. 4. Plot of the calculated normal-incidence reflectivity of copper using the average optical constants obtained from the computer fitting of Fig. 1a and b. Also shown is the location of its surface plasmon resonance (λ_s) on the steep reflectivity edge

Fig. 5. Dispersion curve of the surface plasmon of copper (solid line). Range bars indicate that the minima were determined within ± 10 Å for low wave vector and ± 1 Å for high values of wave vector. Also shown is the energy–wave vector light line generated by the prism for the experimental spectra of Fig. 1a and b where the low wave vector line corresponds to Fig. 1a and the high wave vector line to Fig. 1b. The angle (AO) is with respect to normal to the prism base
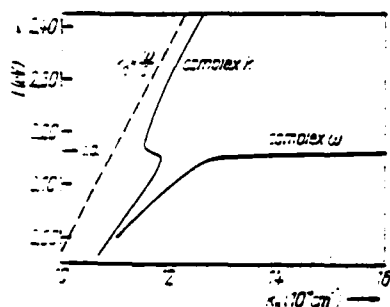
Fig. 6. Complex-ω and complex-k dispersion curves of the surface plasmon of copper along with a plot of the energy-wave vector relation for light in air

occurs at $\varepsilon_1(\omega) = -4.7$ which is a large deviation from the normal condition $\varepsilon_1(\omega) = -1$. This deviation is due to the relatively large value of $\varepsilon_2(\omega) = 4.4$ which causes the resonance to be damped and the true resonance to occur in the complex frequency plane at $\varepsilon(\omega = \omega_s) = -1$. It should also be noticed that the resonance occurs on the steep absorption edge of the d-band to Fermi level transitions.

Shown in Fig. 4 is the location of the surface plasmon resonance (λ_s) on the normal-incidence reflectivity curve. This resonance should be barely visible in high-resolution normal-incidence reflectivity spectra on copper which has a rough surface. The rough surface acts as a grating coupler and permits coupling between the incident transverse light and longitudinal surface plasmon resonance [7].

Steel [8] has done a study on the characteristics of the energy loss function (L) for Au and Ag. He used a Drude-Lorentz model for characterizing the dielectric functions of Au and Ag and varied the free-electron plasma frequency and relaxation time and studied their relationship to peaks in the energy loss function. He determined that "the presence of the absorption band causes the structure in (L) to change from the single free-electron peak to two peaks: a comparatively weak low-energy peak (LEP) below the absorption band and also a strong high-energy peak (HEP) above ω_{to}"; where ω_{po} is the bulk plasma frequency. The surface plasmon resonance of copper as obtained in this study is equivalent to the surface plasmon resonance associated with the (LEP) as discussed by Steel [8]; but there is no peak in the energy loss function at these low energies where the energy loss function for the surface plasmon resonance is defined at $L = -\mathrm{Im}\,[1/(\varepsilon - 1)]$. The probable reason for this is that the damping is larger in Cu than it is for both Ag and Au and that the resonance is truly a function of complex frequency. It can be easily seen that the location of the surface plasmon resonance in Fig. 4 is in the region of the steep drop in normal-incidence reflectivity. This reflectivity drop is normally attributed to the copper interband transition, but from this study we can see that reflectivity drop may also be partially caused by the normal decrease in reflectivity as the frequency ω goes through the surface plasmon frequency and approaches the bulk plasmon frequency. The existence of the bulk plasma frequency is still questionable and, if it exists, it will occur in the complex frequency plane.

It was of interest to see if back-bending of the complex-k dispersion curve occurred. The results of the analysis are shown in Fig. 6 where the real part of the complex wave vector (k_1) is plotted versus energy. The plot of the complex-ω behavior is also shown. It can be seen that the back-bending of the complex-k dispersion curve occurs when the complex-ω curve diverges, therefore having the desired characteristics of the surface plasmon resonance.

4. Summary

Experimental results show that the surface plasmon resonance of copper exists in the visible spectral region at 2.163 eV. The optical properties of copper have been experimentally determined by ATR methods and used to calculate the complex frequency dispersion curve which shows the characteristic wave vector divergence of the surface plasmon resonance, while the complex-k dispersion curve exhibits the characteristic back-bending. The location of the resonance is on the steep absorption edges of ε_2 which is due to the d-band to Fermi level transitions. These transitions cause the large shift in the location of the real frequency excitations and for the true resonance to occur in the complex frequency plane. The color of the noble metal of copper may be partially attributed to the steep decrease in reflectivity which is caused by the normal decrease in reflectivity as the excitation frequency ω goes through the surface plasmon frequency and approaches the bulk plasmon frequency and to the numerous copper interband transitions. The existence of the bulk plasma frequency is still questionable and if it exists it will occur in the complex frequency plane.

References

[1] A. Otto, Z. Phys. 219. 227 (1969).
[2] A. Otto. Z. Phys. 216. 398 (1968).
[3] P. F. Robusto. Ph. D. Thesis. Dept. of Phys., Univ. of Calif., Los Angeles 1978.
[4] L. G. Schultz. J. Opt. Soc. Amer. 44. 357 (1954).
[5] F. M. Mueller and J. C. Phillips. Phys. Rev. 157. 600 (1967).
[6] M. Welkowsky and R. Braunstein. Solid State Commun. 9. 2139 (1971).
[7] N. Marschall. B. Fischer. and H. J. Queisser. Phys. Rev. Letters 27, 95 (1971).
[8] M. R. Steel. J. Opt. Soc. Amer. 63. 69 (1973).

RAMAN AND LUMINESCENCE STUDIES OF ALKALI BORATE TUNGSTATE GLASSES

D. DEAL, M. BURD and R. BRAUNSTEIN

University of California, Los Angeles, California 90024, USA

Raman and luminescence spectroscopy were used to determine the structure of alkali borate tungstate glasses: $M_2O(B_2O_3)_2 \cdot xWO_3$, M = Li or Na ($0 < x < 1$). Raman scattering results showed the dominant tungstate species in these photochromic glasses to be tetrahedral WO_4^-. At high concentrations of WO_3, $WO_3 \cdot H_2O$, and $W_2O_7^-$ are also present. Luminescence measurements provided evidence for an octahedral WO_3 structure not identified by the Raman results. The results also revealed a possible change in the structure of the glasses similar to that observed in alkali borate glasses and associated with the "borate anomaly". In addition, preliminary measurements are reported on the variation of the band gap, density, index of refraction, and the elastic coefficient C_{11} determined by Brillouin scattering with composition.

1. Introduction

The preparation of glasses with the composition $M_2O \cdot (B_2O_3)_2 \cdot xWO_3$ (M = Li, Na; $0 < x < 1$) has recently been reported [1]. The glasses were shown to exhibit a variety of interesting properties including photochromism and electrochromism [1], dipole correlation behavior [2], and space-charge injection [3]. The discovery of the photochromism and the unusual dielectric properties of these glass systems has led us to study the glass structure. An identification of the tungstate structures would be helpful in determining the species responsible for the properties mentioned.

In this work, we report on the tungstate structures in the glasses as identified by Raman and luminescence spectroscopies. The photochromism is ascribed to specific tungstate structures. In addition, the effect of added WO_3 on the borate structures, as determined by Raman, index of refraction, density, band edge, and Brillouin measurements, is discussed.

2. Experimental

The glasses were prepared as previously described from WO_3 and alkali borates [1]. The $M_2O \cdot (B_2O_3)_2 \cdot xWO_3$ glasses were also prepared by the same technique from M_2WO_4 and B_2O_3. Crystalline $M_2W_2O_7$ was also prepared by the same technique from M_2WO_4 and WO_3.

The Raman scattering data were collected with an apparatus consisting of a Spectra-Physics 165 argon ion laser, a Spex 1400-II double monochromator, an ITT FW 130 photomultiplier tube, and a photon-counting system. The 5145 Å laser line was used most often, but the 4880 Å line was also employed as a check for spurious plasma lines and luminescence. The polarization of the spectra was determined with the use of a polarizing prism after the samples.

Luminescence spectra were recorded with a Spex Fluorolog Spectrometer employing a mercury lamp for excitation and a photomultiplier as the detector. Emission and excitation spectra were taken on the solid samples in the front face configuration at both 300 K and 77 K. The 77 K spectra were performed by immersing the sample in liquid N_2 contained in a quartz glass dewar.

The samples studied were tested for photochromic behavior by the method described previously [1]. The tests confirmed that all samples for which structures were determined exhibited some photochromism. Samples of pure crystalline tungstates were also tested for photochromism in order to determine the structures responsible for the phenomenon. The UV and visible band edges were determined with a Cary 239 spectrometer in the spectral range of 200–600 nm using air as a reference. Densities were measured with a pycnometer, using methanol as the reference liquid. Refractive indices were measured with Cargille certified refractive index liquids and a Unitron microscope. Samples were illuminated with 4880 Å light and their refractive indices were obtained by bracketing the Becke line. Preliminary Brillouin scattering measurements were obtained using a Burleigh 5-pass Fabry-Perot. The scattering light from a 4880 Å incident laser beam was detected by an RCA photomultiplier and analyzed by a CAMAC LSI 11/2 computer system.

3. Results and discussion

The Raman spectra for the range of alkali borate tungstate glasses are shown in figs. 1 and 2; the spectra of $Li_2O \cdot (B_2O_3)_2$ glass and WO_3 powder are shown in fig. 3 for comparison. Glassy or amorphous WO_3 has not been studied by Raman scattering, but the spectrum is probably similar to the powder spectrum with broader peaks.

The pure lithium borate glass ($x = 0$) spectrum shown in fig. 3 displays the characteristic peaks found in alkali borate glasses with an alkali concentration greater than 16 mol% [4–6]. The peak at 770 cm^{-1} has been attributed to a tetraborate structure with a 4-coordinated boron atom. Production of non-bonding oxygen by adding alkali oxide is thought to be responsible for the tetraborate structure [4]; B_2O_3 without added alkali oxide produces a Raman peak at 807 cm^{-1} due to a triborate structure.

As shown in fig. 1, the addition of a small amount of WO_3 ($x = 0.08$) produces a Raman spectrum that differs little from that of pure lithium diborate. This is interesting in the light of the large changes seen in the elastic coefficients (fig. 4) and band edge (fig. 5). The only apparent change in the
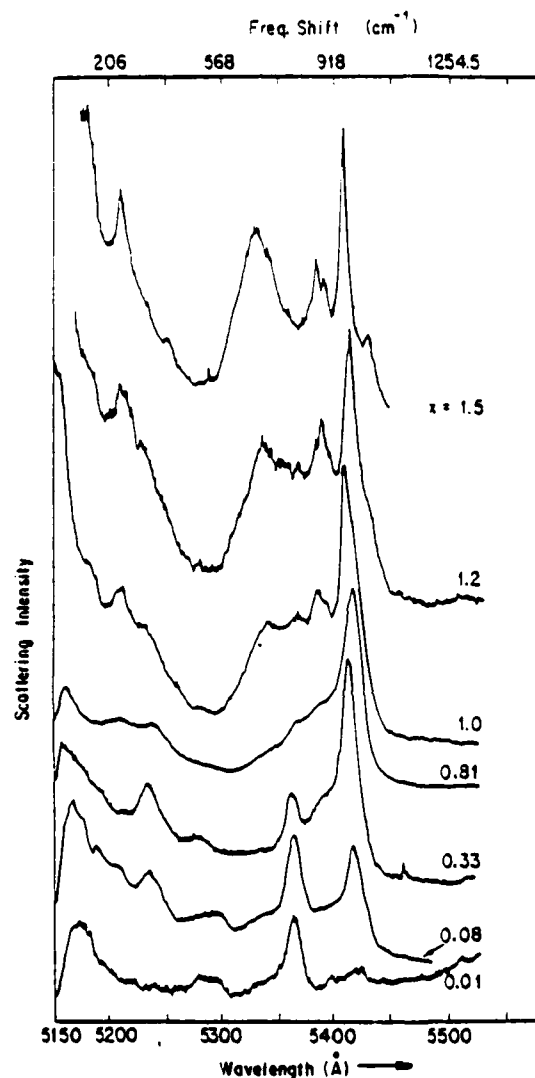
Freq. Shift (cm⁻¹)

Fig. 1. Raman scattering spectra for $Li_2O \cdot (B_2O_3)_2 \cdot xWO_3$ glasses using the 5154 Å argon ion laser line.

Raman spectrum is a small increase in scattering in 950 cm⁻¹ peak. As the WO_3 concentration increases, new peaks build up at 325, 820–860, and 945 cm⁻¹. The peaks associated with borate structure appear little changed, although there is a possibility the 770 cm⁻¹ peak has shifted to a slightly higher energy.

The Raman peaks at 325, 820–860, and 945 cm⁻¹ for low WO_3 concentration glasses are apparently due to tungstate species. Comparison of these peaks to

Freq. Shift   (cm⁻¹)
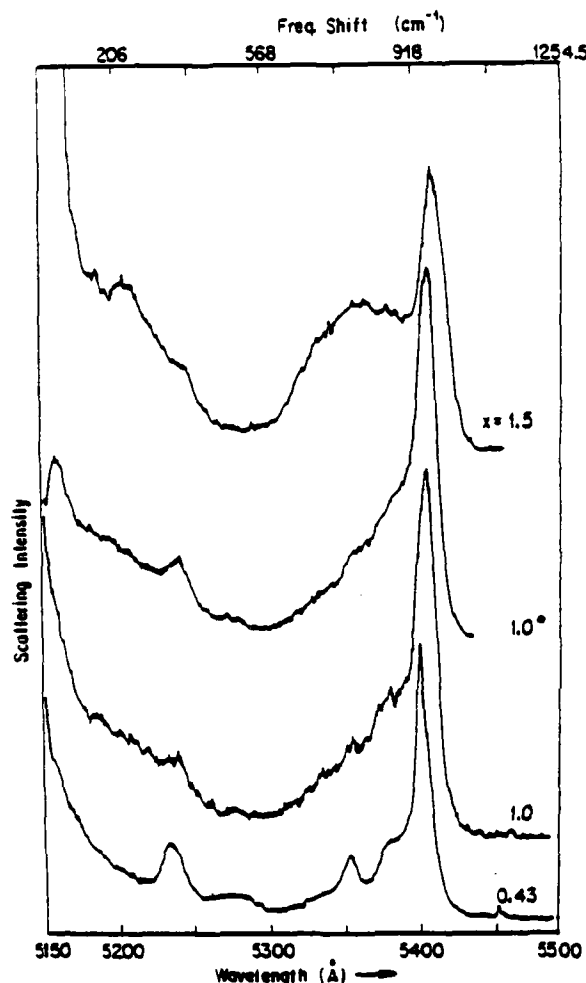
Fig. 2. Raman scattering spectra for $Na_2O \cdot (B_2O_3)_2 \cdot xWO_3$ glasses using the 5145 Å argon ion laser line. *: Glass made from Na_2WO_4 and B_2O_3.

the spectrum of crystalline WO_3 (fig. 3) reveals that they are not due to octahedral WO_3 but, instead, are characteristic of tetrahedrally coordinated tungsten [7,8]. Comparison with the Raman spectra for Li_2WO_4 (solid line) and Na_2WO_4 powders (fig. 6) clearly confirms the presence of WO_4^- in the glasses. Although the peaks in the glasses are broader, the position and relative intensities of the peaks match well with the corresponding peaks of Li_2WO_4 and Na_2WO_4. The broadness of the glass peaks can be attributed to the amorphous arrangement of the tungstates in the glass system.

Raman scattering results on Li_2WO_4 and Na_2WO_4 melts have been reported which corroborate the identification of amorphous WO_4^- in the glasses studied
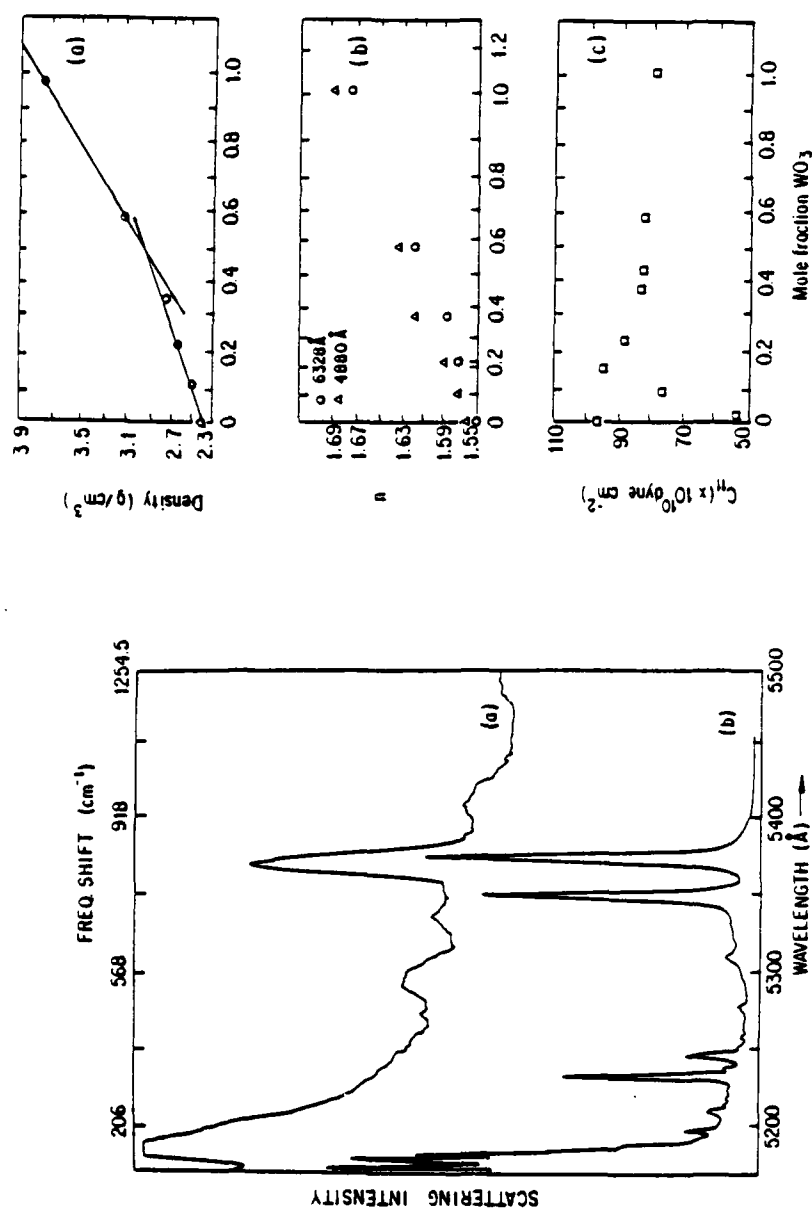
Fig. 3. Raman scattering spectra. (a) $Li_2O \cdot (B_2O_3)_2$ glass. (b) Crystalline WO_3 powder.

Fig. 4. (a) Density vs composition of $Li_2O \cdot (B_2O_3)_2 \cdot xWO_3$ glasses. (b) Index of refraction versus composition: $\triangle = 4880$ Å line, $O = 6328$ Å line. (c) Elastic coefficients obtained from Brillouin scattering for range of $Li_2O \cdot (B_2O_3)_2 \cdot xWO_3$ glasses.
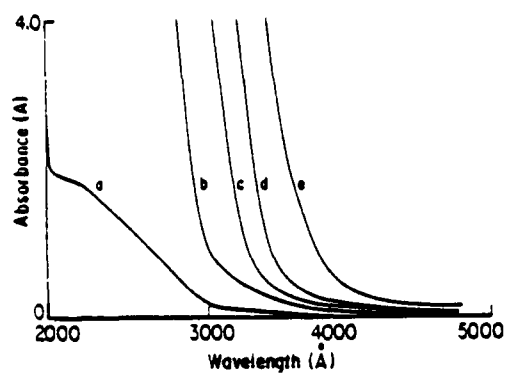
Fig. 5. Band edge measurements for $Li_2O \cdot (B_2O_3)_2 \cdot x WO_3$ glasses. (a) $x = 0$, (b) $x = 0.09$, (c) $x = 0.35$, (d) $x = 0.58$, (e) $x = 1.0$. Sample thickness = 1 mm.
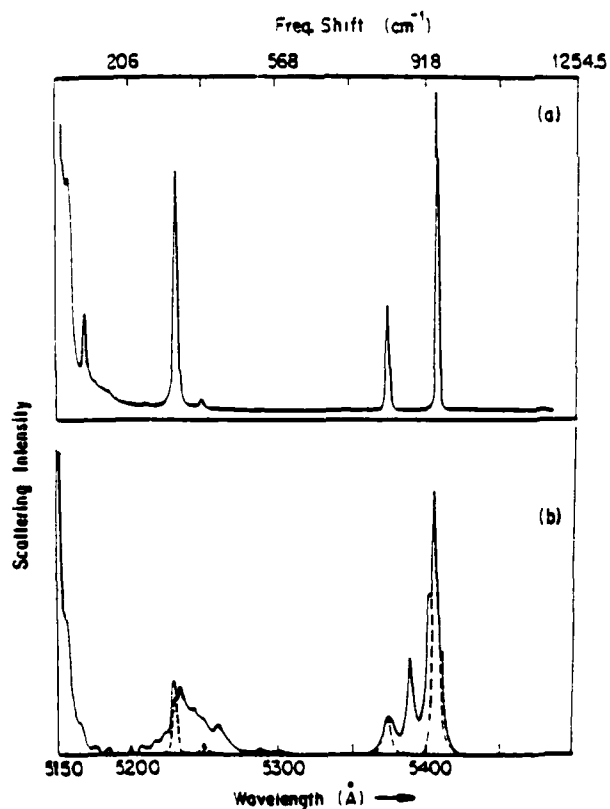
Fig. 6. Raman spectra for M_2WO_4 crystalline powders. (a) Na_2WO_4, (b) Li_2WO_4. Full curve obtained from this laboratory; dashed curve theoretical spectrum (ref. [7]).

here [8]. The authors found peaks similar to the ones reported here for the sodium and lithium tungstates. Spectra of WO_4^- melts showed the broad Raman peaks associated with amorphous materials and found in the glasses studied here.

The high energy 938 cm^{-1} peak for a melt consisting of K_2WO_4 and Li_2WO_4 is reported to be due to an A_{1g} symmetric stretching mode [8]. In both the WO_4^- melts and the glasses studied here, the A_{1g} mode was found to be polarized, while the other tungstate peaks were unpolarized.

Several literature reports also suggest the presence of tetrahedral WO_4^- [9,10] and MoO_4^- [11] in glassy systems. Glasses of the composition $Li_2WO_4 \cdot xWO_3$ have been made using a splat cooling technique and the structure identified by X-ray diffraction. Both WO_4^- and $W_2O_7^-$ were found in these glasses [9]. These rapidly quenched glasses form thin flakes and not bulk glasses of the present work.

For both the lithium and sodium glasses, reported in this work, the Raman peaks due to WO_4^- remain broad and increase in intensity as the concentration of WO_3 increases up to about $x = 0.8$. The tungstate peaks for the sodium glasses may be slightly lower in energy than the lithium peaks; however, the broadness of the peaks makes an accurate determination of such a shift difficult. The relative positions of the sodium and lithium tungstate peaks agree with literature findings [8].

As the concentration of WO_3 approaches and passes $x = 1.0$, the Raman spectra reveal the growth of new bands at 250 cm^{-1} and in the region from 600–800 cm^{-1} for both the lithium and sodium glasses. This evidence for new structures is expected as the WO_3 concentration becomes greater than the concentration of alkali oxide. Bands associated with WO_4^- become narrower and the 940cm^{-1} band begins to lose its polarization. This indicates the glasses
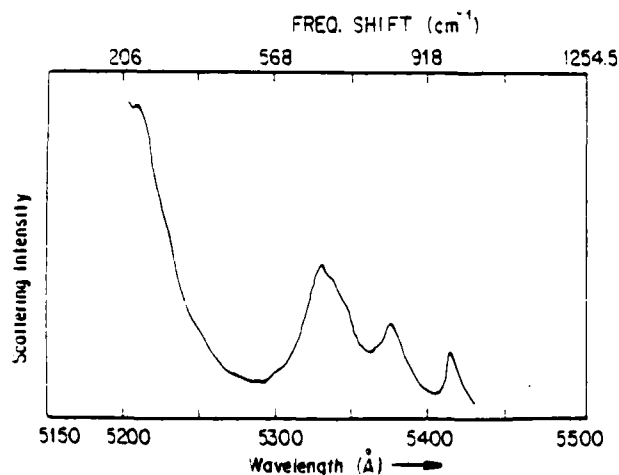

Fig. 7. Raman spectrum of $WO_3 \cdot H_2O$ powder.

Department of Physics, University of California, Los Angeles[1])

De-Correlation Technique for Separation of Drude Parameters from Wavelength Modulation Spectroscopy Data[2])

By

M. Burd, R. Stearns[3]), and R. Braunstein

Separation of bound- and free-electron contributions to the dielectric function is necessary for an accurate analysis of interband transitions. A technique for doing this separation which does not require low energy data is presented. The technique makes use of the fact that the functions which describe the contributions of each part are sufficiently uncorrelated, allowing the construction of a correlation function which uses the Drude effective mass and Drude relaxation time as adjustable parameters. The technique is shown to properly separate a test function and to yield reasonable results from experimental data.

Une analyse rigoureuse des transitions entre bandes nécessite une séparation entre les contributions des électrons libres et celles des électrons liés. Nous présentons ici une technique pour effectuer une telle séparation qui n'exige pas de données à basse energie. La technique en question utilise le fait que les fonctions décrivant les deux types de contributions sont suffisemment non corrélées. Cela permet de construire une fonction de corrélation en faisant de la masse éffective de Drude et du temps de relaxation de Drude des paramètres ajustables. Nous montions que cette technique sépare proprement une fonction test et fournit des résultats raisonnables à partir de données experimentales.

1. Introduction

The dielectric function, $\varepsilon(\omega)$, contains important information about the optical properties of solids. It is defined as the response of a crystal to an electromagnetic field,

$$\boldsymbol{D}(\omega) = \varepsilon(\omega)\,\boldsymbol{E}(\omega)\ . \tag{1}$$

The dielectric function is sensitive to the electronic band structure of the material, and the determination of the dielectric function by optical spectroscopy is an important tool for investigating the overall band structure.

The broad bands found in solid state spectroscopy are convolutions of a number of contributions which emerge when derivatives of the reflectance are taken. A number of modulation techniques are available, which include temperature [1, 2], electric field [3, 4], pressure or uniaxial stress [5, 6] modulation. Wavelength modulation is employed in these studies because of the unambiguous lineshapes which emerge [7 to 11]. Transitions are strongest at points where the lower and upper bands are parallel, i.e., at frequencies which satisfy

$$\nabla_{\boldsymbol{k}}[E_{c}(\boldsymbol{k}) - E_{v}(\boldsymbol{k})] = 0\ , \tag{2}$$

where E_c and E_v are the energies of the upper and lower bands, respectively. At these critical points in $\boldsymbol{k}$-space, which are the van Hove singularities [12], the joint density

---

[1]) Los Angeles, California 90024, USA.

[2]) Work supported in part by U.S. Army Research Office, Durham, North Carolina, and by the Air Force Office of Scientific Research.

[3]) Current address: TRW Technology Research Center, El Segundo, CA 90245, USA.

[9] B. Batz, Solid State Commun. 4, 241 (1965).
[10] C. N. Berglund, J. Appl. Phys. 37, 301 (1966).
[11] I. Balslev, Phys. Rev. 143, 636 (1966).
[12] G. Bonfiglioli and P. Brovetts, Appl. Opt. 3, 1417 (1964).
[13] R. E. Drews, Bull. Am. Phys. Soc. 12, 384 (1967).
[14] M. Welkowsky and R. Braunstein, Rev. Sci. Instrum. 43, 399 (1972).

[15] Perkin-Elmer Corp., Costa Mesa, CA 92626.
[16] M. Welkowsky, Ph.D. thesis, University of California at Los Angeles, 1971.
[17] National Semiconductor Ltd., Plattsburgh, NY 12901.
[18] RCA Electronic Components, Harrison, NJ 07029.
[19] EG & G Princeton Applied Research, Princeton, NJ 08540.

one-half of the rotation time of the mirror, 38.5 ms. It is used to determine which channel, sample or background, is being gated at any particular time. When one-shot B ends its period it starts one-shot C. One-shot C starts one-shot D and is also used to center the sample and background periods in their respective time windows. This sequence then provides the delay signal for timing the starts of the gates. One-shot D sets flip flop F, which controls the feedback network sampling time, that is, the width of the gates. D also starts one-shot E. The starting of one-shot E sets flip flop G, which is used to start the gate time of the output circuits.

When the signal from flip flop F is added to signals B and B inverse, signals K and L are formed. These are the actual gating signals which control the active feedback networks. The signal from flip flop G, when added to B and B inverse, forms signals I and J, which control the output switches. Signal M controls the impedance of the amplifier during the transition of the chopper between sample and background. It is the complement of F from the same flip flop.

All of the logic was implemented in CMOS, using CD4047's for the one shots and 74C74's for the flip flops. NAND gates are 74C00's and inverters are 74C04's.

The output signals are sent to a PAR Model 124 A Lock-In Amplifier with a PAR Model 116 Differential Preamplifier.[19] The sample and background signals are differentially amplified, with the 124A in the high dynamic range with a Q of 1.

The differential derivative circuit was constructed with conventional point-to-point wiring in a double NIM module. All power is obtained from the NIM bin. For convenience in checking and calibrating the unit, a 217-Hz reference oscillator was constructed in the same module.

II. SYSTEM SENSITIVITY

The critical test of the system is its ability to eliminate signals which are due to sharp structure in the source. Figure 6 shows the structure from the line at 4193 Å in the spectrum
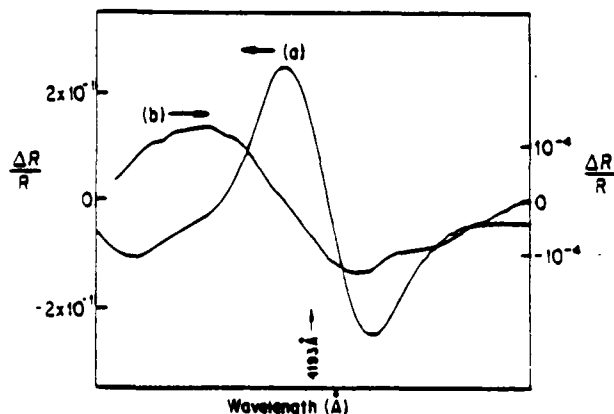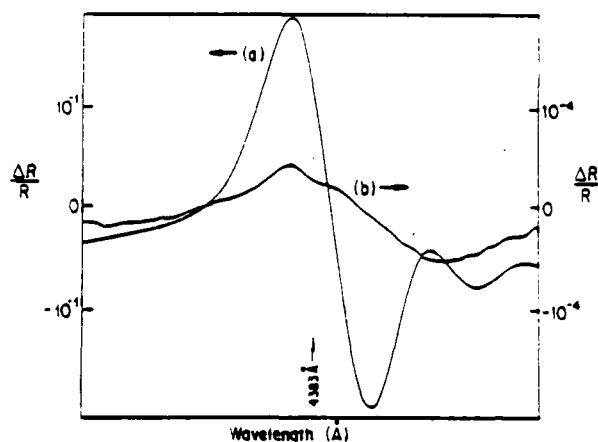

FIG. 7. Comparison of balanced (b) and unbalanced (a) scans of the Xe line at 4383 Å. Note the scale change between the two curves. The wavelength scale extends to approximately 100 Å on either side of the 4383 Å line.

of a 150-W Hanovia Xenon arc lamp which is the source for the violet and ultraviolet regions. The figure shows the results for both the modulated signal (a) which has not been processed by the differential derivative circuitry and also the signal (b) when this spectra line has been balanced by the system. Note that the balancing by the system reduces the signal by three orders of magnitude. The signal level of the balanced line of Fig. 6 represents a maximum sensitivity of $\Delta R/R = 1.3 \times 10^{-4}$; this is the worst case result. In practice, sensitivities of better than 10^{-4} and down to 10^{-5} are routinely obtained in regions of the spectrum without sharp lines in the source. Figure 7 shows the structure at 4383 Å in the same source spectrum. Here the improvement is much better than three orders of magnitude with the best $\Delta R/R$ being 9×10^{-5}.

ACKNOWLEDGMENTS

FIG. 6. Comparison of balanced (b) and unbalanced (a) scans of the Xe line at 4193 Å. Note the scale changes between the two curves. The wavelength scale extends 100 Å on either side of the 4193 Å line.

[a] Current address: TRW Technology Research Center, El Segundo, CA 90245.
[b] Current address: Litton Industries, Woodland Hills, CA 91304.
[1] L. Van Hove, Phys. Rev. 89, 1189 (1953).
[2] M. Cardona, Modulation Spectroscopy (Academic, New York, 1969).
[3] B. Batz, Ph.D. thesis, Université Libre de Bruxelles, 1967.
[4] F. Wooten, Optical Properties of Solids (Academic, New York, 1972).
[5] W. E. Engeler, H. Fritzsche, M. Garfinkel, and J. J. Tiemann, Phys. Rev. Lett. 14, 1069 (1965).
[6] G. W. Gobeli and E. O. Kane, Phys. Rev. Lett. 15, 142 (1965).
[7] B. O. Seraphin and R. B. Hess, Phys. Rev. Lett. 14, 138 (1965).
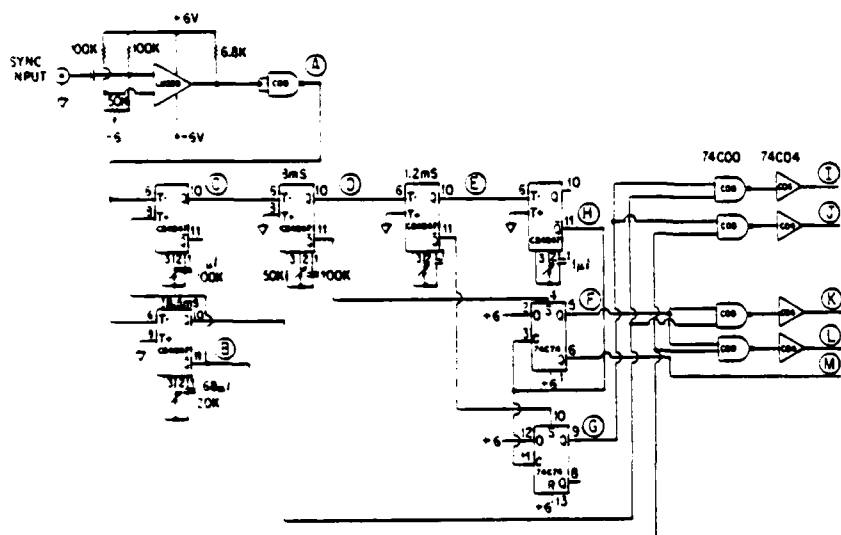[8] M. Cardona, K. L. Shaklee, and F. H. Pollak, Phys. Rev. 154, 696 (1967).

FIG. 4. Logic circuit. This circuit generates the switching signals which drive the feedback networks of Fig. 3.

plier tube is the direct input to the inverting terminal of a National Semiconductor LM308A operational amplifier[17] (OA1 in Fig. 3). This op amp is connected in the current-to-voltage configuration and has three switched feedback networks. Each network is switched into the circuit during a different portion of the rotation period of the chopping mirror. These networks function to make the output voltage of the op amp (OA1) equal to a reference voltage, which is the reference level of Fig. 2(b), chosen to be 200 mV. These networks serve to replace the mechanical servomotors used in the original design of a wavelength-modulation system.[14,16]

Each feedback network consists of a 2N4360 field effect transistor, an RCA CD4066 CMOS analog switch,[18] and another LM308A op amp connected as an integrator. The CMOS switches are marked S1 through S5 in Fig. 3. The LM308A integrator uses the integrated value of the difference between the output of OA1 and the reference voltage to control the source-to-drain resistance of the 2N4360 FET. This brings the 13-Hz component of the output of OA1 equal to the reference voltage. The output of the LM308A integrator is coupled to the gate of the FET with a 30K resistor and a 10-μF capacitor so that the 217-Hz modulation signal will have no effect on the source-to-drain resistance to the FET. An integration time of 1 s has been found to be adequate in this system.

The output circuit for each signal, sample and background, is a DC4066 CMOS switch (marked S6 and S7) coupled with a 1-μF capacitor to the output BNC connector. The 1-μF capacitor charges to the referee voltage and only the 217-Hz modulation component of the signal appears at the output. This produces the output signals in Fig. 2(c).

The remainder of the discussion deals with the switching signals which drive the feedback networks. These signals synchronize the system to the rotation of the chopping mirror and time the onsets and widths of the gate for the feedback circuits. These signals are timed by a synchronization trigger, derived from a photodiode located on the rotating mirror, which drives a set of one-shot multivibrators and flip flops. This circuitry is shown in Fig. 4 and the timing signal

which is produced is given in Fig. 5. Figure 5 also shows the signals from Fig. 2 for reference.

The synchronization trigger signal is squared in an LM399A comparator (Fig. 4) with positive feedback and buffered with a CMOS band gate stage to form the trigger signal (A in Figs. 4 and 5). Trigger signal A starts one-shots B and C, which are CD4047's. One-shot B is timed to run for
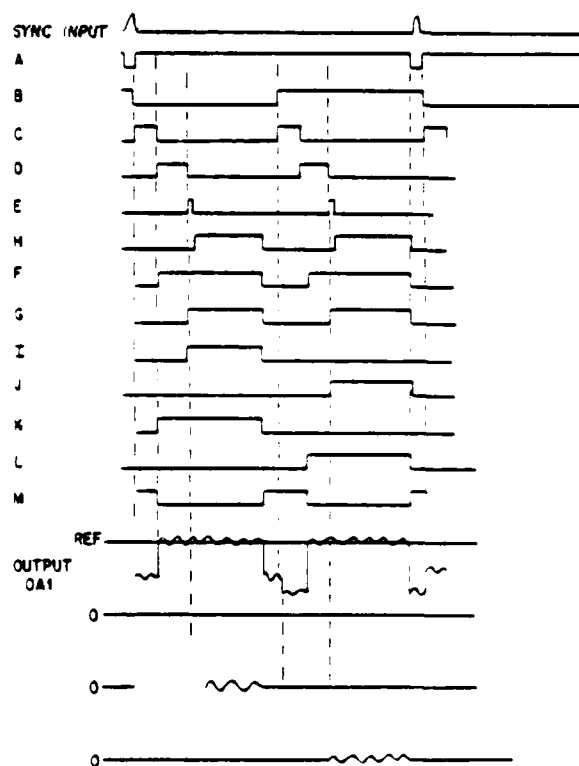

FIG. 5. Timing diagram. The timing of each signal in Figs. 3 and 4 are given in relationship to each other. Parts of Fig. 2 are reproduced at the lower parts of this figure for reference.

nal I reflected from the sample is

$$I(\lambda) = R(\lambda) I_0(\lambda), \qquad (8)$$

where R is the reflectivity and I_0 is the signal incident on the sample. The wavelength derivative of Eq. (8), which is denoted by prime, is

$$I' = R' I_0 + R I_0'. \qquad (9)$$

The second term in Eq. (9) is what causes the difficulty in wavelength modulation experiments with respect to other modulation techniques. In other methods, where only sample is modulated, this term is zero. However, when the wavelength is modulated, this term contains the derivative of the incident beam, which includes wavelength-dependent information about the light source, optical path, atmospheric absorption, and detector response. $R I_0'$ is, more often than not, on the same order as $R' I_0$ and, as is the case of a light source with sharp line structure, may be orders of magnitude larger than $R' I_0$. A means of subtracting this contribution to the total derivative signal is essential if meaningful wavelength modulation data are to be obtained.

If Eq. (9) is divided by Eq. (8) and the terms are rearranged, we get

$$\frac{R'}{R} = \frac{I'}{I} - \frac{I_0'}{I_0}. \qquad (10)$$

This is the quantity which we wish to extract from the experiment. We choose to keep the signal level in each term equal, so that the subtraction may be easily done electronically. Rearranging Eq. (10), we now have

$$\frac{R'}{R} = \frac{1}{I}(I' - kI_0'), \qquad (11)$$

where $k = I/I_0$. A qualitative description of how R'/R is determined will be given first, and then the new electronic system will be described.

The double-beam optical system is shown in Fig. 1. The signal from a Perkin–Elmer 99G monochromator[15] is modulated at 217 Hz by a vibrating mirror.[14,16] The signal reflected from the sample when the chopping mirror, which rotates at 13 Hz, does not block the beam will be called the sample channel. The signal reflected from the chopping mirror during the other half cycle will be called the background

FIG. 2. Wavelength-modulation waveforms: (a) Chopper cycle of the raw signal from the photomultiplier. The higher level is the background channel; the lower level is the sample channel. (b) The raw signals have been gated and servoed to a predetermined reference level. (c) The servoed and gated signals have been separated into their own output channels and ac coupled to eliminate the 13-Hz component.

channel. Figure 2 shows how we would like to process the signal. Figure 2(a) is the raw signal from the photomultiplier tube. The higher level is I_0 and the lower level is I, because the aluminum chopping mirror will be more reflective than the sample. In Fig. 2(b) we have gated a portion of each channel and amplified it to a reference level, which will be kept constant. Thus we have brought the signal channel to a constant level which is our new level for I and also made I_0 equal to I. The constant k in Eq. (11) now represents the fact that different gains are needed in the sample and background channels to bring them to the reference level. The 217-Hz components in the sample and reference channels are now proportional to kI_0' and I' and are shown by signals B and A, respectively, in Fig. 2(c). We can now run these to a differential lock-in amplifier, and the difference between the two signals will now be proportional to $I' - kI_0'$.

This new electronic circuit is designed to make the source to output gain at the 13-Hz chopping frequency the same for both the sample and background channels. The differential derivative and logical circuits are shown in Figs. 3 and 4, respectively. The current output of the photomulti-

FIG. 1. Double-beam signal detector optical system. Light from the Perkin–Elmer 99G monochromator is modulated at 217 Hz. The chopper C rotates at 13 Hz.

FIG. 3. Differential derivative circuitry. Signals K, L, and M are from the logic circuit (Fig. 4).

Fully electronic servocircuitry for wavelength-modulation spectroscopy

R. Stearns,[a] J. Steele,[b] and R. Braunstein

Department of Physics, University of California, Los Angeles, California 90024

Electronic circuits have been developed to replace the mechanical servos and lock-in amplifiers customarily used in a wavelength-modulated derivative spectrometer. The result is a faster response and wider range of gain while maintaining a constant photomultiplier-tube voltage.

INTRODUCTION

The identification of Van Hove Singularities[1] in optical absorption or reflection spectra can be difficult, since singularities are usually superimposed on a broad structureless background. In the case of metals, this background is the Drude intraband spectrum, and interband singularities can be small compared to this background. This problem is especially acute in the case of three dimensions as Van Hove singularities do not produce infinite peaks, but only changes in the slope of the optical properties. Broadening mechanisms reduce the optical structure in all cases.

The optical structure associated with critical points can be greatly enhanced by the use of derivative, or modulation, spectroscopic methods. The dielectric function near a three-dimensional critical point may be written as[1-4]

$$\epsilon(\omega) = b\,(\omega - \omega_g)^{1/2} + \text{constant}, \qquad (1)$$

$\hbar\omega$ is the photon energy and $\hbar\omega_g$ is the transition energy at the critical point. The constant in Eq. (1) represents the background contribution, which may be larger than the singular part. Thus, observation of the critical structure may be lost in the background. Therefore, it would be most advantageous to measure, not ϵ directly, but the derivative of ϵ with respect to some parameter x. Since the background does not vary rapidly, it would essentially be eliminated from the spectrum. This leads to

$$\frac{d\epsilon}{dx} = \frac{b}{2}(\omega - \omega_g)^{-1/2}\frac{d(\omega - \omega_g)}{dx} + \frac{db}{dx}(\omega - \omega_g)^{1/2}. \qquad (2)$$

The first term in Eq. (2) diverges at the critical point $\omega = \omega_g$ and is, therefore, easily detectable in a derivative spectrum. The second term in Eq. (2) is generally negligible near $\omega = \omega_g$ since b can vary slowly. There are two obvious possibilities for the differentiation parameter x. The first is the energy of the incident radiation $\hbar\omega$ and the second is the critical point transition energy $\hbar\omega_g$.

Techniques which modulate the energy critical point transition avoid experimental complications which will be found in frequency (wavelength) modulation experiments, but have the analytical problem of ambiguous interpretation of line shapes. Possible parameters which modulate the energy gap include hydrostatic pressure and uniaxial stress,[5,6] electric field,[7,8] and temperature[9,10] modulation. The ambiguity of these methods can be seen when Eq. (2) is reduced to

$$\frac{d\epsilon}{dx} \propto (\omega - \omega_g)^{-1/2}\frac{d\omega_g}{dx}. \qquad (3)$$

Detailed analysis of the lineshapes of Van Hove singularities is not possible unless one already has knowledge of the contribution from $d\omega_g/dx$. Thus, the theory of internal modulation experiments depends not only on the theory of the optical properties, but also on the effect of the perturbation parameter x on those optical properties.

When a frequency-modulated light beam[11-14] is used, Eq. (2) reduces to

$$\frac{d\epsilon}{d\omega} = \frac{b}{2}(\omega - \omega_g)^{-1/2}. \qquad (4)$$

Thus, there are no theoretical ambiguities in the interpretation of data. If the dependence of the frequency of the modulated beam is

$$\omega = \omega_0 + (\Delta\omega)\cos\Omega t, \qquad (5)$$

where $\Delta\omega$ is the depth of modulation and Ω is the modulation frequency, then we have

$$\epsilon = \epsilon(\omega_0) + \Delta\epsilon\cos\Omega t. \qquad (6)$$

If $\Delta\epsilon$ is measured, the derivative of the dielectric function may be found from

$$\frac{d\epsilon}{d\omega} = \lim_{\Delta\omega \to 0}\frac{\Delta\epsilon}{\Delta\omega}. \qquad (7)$$

However, $\Delta\epsilon$ is generally not measured directly. Instead, the modulation of the reflectivity ΔR or the transmission ΔT is measured. Great accuracy and sensitivity can be achieved in the measurement of ΔR or ΔT by means of phase sensitive detection with a lock-in amplifier.

A double-beam, single-detector optical system with its associated electronics for obtaining wavelength-modulated derivative spectra was previously reported.[14] This system eliminated problems due to background derivative structure caused by source, detectors, optics, and atmospheric absorption. We now report electronic circuitry which has been designed to replace the system of mechanical servos and lock-in amplifiers which is normally used.[14] This new system has the advantage of faster response times and wider ranges of gains while maintaining a constant voltage to the photomultiplier tube.

I. WAVELENGTH MODULATION

Wavelength-modulation derivative spectroscopy has experimental difficulties, which may be overcome, compared to other types of modulation as may be seen in the following.

In conventional reflection measurements, the total sig-

plest polymeric tungstate present is $W_2O_7^-$.

Luminescence data provide evidence for $W_2O_7^-$ and defect WO_3 octahedra being present even at low WO_3 concentrations. The photochromic structures are WO_4^-, $WO_3 \cdot H_2O$ and possibly defect WO_3.

There is some evidence for structural changes of the borate groups as seen by Raman spectroscopy and trends seen in the density, reference index, and elastic properties.

References

[1] R. Braunstein, Sol. St. Commun. 28 (1978) 839.
[2] R. Braunstein and K. Bärner, Sol. St. Commun. 28 (1978) 847.
[3] R. Braunstein and K. Bärner, Sol. St. Commun. 33 (1980) 941.
[4] W.L. Konijnendijk, Phys. Chem. Glasses 17 (1976) 205.
[5] T. Furukawa and W.B. White, Phys. Chem. Glasses 21 (1980) 85.
[6] W.B. White, S.B. Brewer, T. Furukawa and G.J. McCarthy, in Borate Glasses – Structure, properties, Applications, ed. L.D. Pye (Plenum Press, 1978), p. 281.
[7] F.A. Cotton and R.M. Wing, Inorg. Chem. 4 (1965) 867.
[8] T.W. Cape, V.A. Maroni, P.T. Cunningham and J.B. Bates, Spectrochim. Acta 32A (1981) 1219.
[9] M. Tatsumisago, I. Sakono, T. Minami and M. Tanaka, J. Non-Crystalline Solids 46 (1981) 119.
[10] V.T. Maltzer and V.L. Volkov, Russ. J. Inorg. Chem. 20 (1975) 1217.
[11] M. Yamone and Y. Nakoa, Yogyo-Kyokai-Shi 87 (1979) 327.
[12] M.L. Freedman, J. Amer. Chem. Soc. 81 (1959) 3834.
[13] V.E. Schwarzmann and O. Glemser, Ann. Anorg. Allgem. Chem. 312 (1961) 45.
[14] L.Y. Chang and S. Sachdev, J. Amer. Ceram. Soc. 58 (1975) 267.
[15] K. Nassau, A.M. Glass, M. Grasso and D.H. Olson, J. Electrochem. Soc. 127 (1980) 2743.
[16] F. Knee and R.A. Condrate, J. Phys. Chem. Sol. 40 (1975) 1145.
[17] C. Rocchiccioli-Deltcheff, R. Thouvenot and R. Franck, Spectachimica Acta 32A (1976) 587.
[18] Von Panier Mattes, H. Bierbusse and J. Fuchs, Ann. Anorg. Allgem. Chem. 385 (1971) 230.
[19] F. Kröger, Some Aspects of the Luminescence of Solids (Elsevier, New York, 1948).
[20] R. Grasser and J. Scharmann, J. Luminescence 12 (1976) 473.
[21] C. Sunseri, F. DiQuatro and A. DiPialo, J. Appl. Electrochem. 10 (1980) 669.
[22] R. Hurditch, Elect. Lett. 11 (1975) 142.
[23] P. Schlotter and L. Pickelmann, J. Electron. Mat. 11 (1982) 207.

that a study of the density and refractive index with WO_3 concentration might provide a clue to changes in the borate structure. The graphs of these two properties versus composition are shown in fig. 4. The density data show what appears to be a slope change in the region $x = 0.5$ to $x = 0.6$. The index of refraction data, however, does not show such behavior. The elastic coefficient versus concentration shows a peak at $x = 0.2$ (fig. 4c). Of particular interest is the discontinuity between pure $Li_2O \cdot (B_2O_3)_2$ and when a small concentration of WO_3 is present. Since these data were obtained from Brillouin scattering, which couples to acoustic phonons, they therefore sample large regions of the glass matrix as opposed to Raman scattering data which examine local molecular bonds. This sudden change in the elastic coefficients with added WO_3 indicates surprising modifications in the long range borate structure of the glasses. More work needs to be done, but there appears to be some evidence for changes in the borate structure as WO_3 is added to the glasses.

Tungstate structures identified in the glasses were checked for photochromic properties by a method previously described [1]. Pure crystalline or powder samples of these species were immersed in trichloracetic acid and methanol solutions, illuminated with UV light and observed for color changes. Under these conditions, H_2WO_4 and M_2WO_4 (M = Li, Na) were found to be photochromic. The coloring process for H_2WO_4 under other conditions has been studied extensively [21,22], while recent work has also observed the coloring of M_2WO_4 [9]. Crystalline Li_2WO_7 was found to be only slightly photochromic under our experimental conditions. However, recent work has indicated that amorphous $Li_2W_2O_7$ is electrochromic [9].

The photochromism in these bulk glasses is in contrast to work on the structure of photochromic WO_3 films [23]. In that work evidence was provided showing that coloring occurs in amorphous WO_3 films, due primarily to the presence of water and structural voids which allow ion movement. The structure of the present bulk alkali borate tungstate glasses permits ion diffusion for the photochromic process without the porous nature of thin films.

4. Conclusions

A series of alkali borate tungstate glasses which exhibit photochromism has been studied by Raman and luminescence spectroscopies in order to determine structures. The Raman work has confirmed the amorphous nature of the glasses at concentrations of WO_3 less than $x = 1.0$. At concentrations above $x = 1.0$ the amorphous nature is gradually lost resulting in a ceramic at $x = 1.2$ and $x = 1.5$ for the lithium and sodium glasses, respectively.

The Raman spectra show that at low concentrations the WO_3 is incorporated into the glass as tetrahedral WO_4^-. As the concentration of WO_3 increases, the concentration of WO_4^- also increases; however, new species become apparent. The other species have been identified as $WO_3 \cdot H_2O$ and polymeric tungstates. Both species contain octahedral WO_3 groups. The sim-

peaks which is virtually identical to the glasses and Li_2WO_4 (figs. 12, 13). The emission peak at 535 nm found in $CdWO_4$ was attributed to WO_3 imperfections.

Analysis of the borate structures is of interest in the light of the Raman work performed on alkali borate glasses [4–6]. It has been found that as alkali oxide is added to B_2O_3 the Raman line at 807 cm^{-1} for pure borate gradually weakens while a peak at 770 cm^{-1} grows until at 16 mol% alkali the 807 cm^{-1} has totally disappeared. The Raman data have been explained in terms of the added alkali introducing non-bonding oxygens. This procedures a tetraborate structure which contains tetrahedrally bonded boron. The 770 cm^{-1} peak has been assigned to tetraborate [4]. It is theorized that only trigonally bonded boron is contained in pure B_2O_3 which produces the 807 cm^{-1} peak.

All the glasses studied here contain the some mol% of alkali compared to borate. This composition contains borate as tetraborate as shown by the 770 cm^{-1} Raman peak (fig. 3). The addition of WO_3, however, may have some effect on the borate structure.

Since WO_3 is incorporated into the glass as WO_4^-, the possibility arises that the WO_3 is counteracting the effect of the alkali oxide on the borate structure by removing non-bonding oxygen. If one assumes that each WO_3 molecule complexes with an alkali oxide and effectively keeps that alkali oxide from affecting the borate structure, then one can calculate a theoretical WO_3 concentration at which there would be a 16 mol% alkali oxide concentration with respect to the borates. At and above the calculated concentration, the Raman should show a shift from the tetraborate 770 cm^{-1} peak to the triborate 807 cm^{-1} peak.

Our calculations show that a significant shift in the borate Raman structure should occur at a WO_3 concentration of $x = 0.62$. The Raman data shown in figs. 1 and 2 are unfortunately somewhat ambiguous. In the samples in which the pertinent borate peak is still resolved, there appear to be only minor shifts in the peak. At WO_3 concentrations near and above $x = 0.62$, the Raman peaks of the tungstates tend to mask the borate peaks. However, the $x = 0.81$ and $x = 1.0$ lithium glass Raman spectra do show a peak at 797 cm^{-1} (fig. 1) which could be due to a triborate structure. In addition, one sample of devitrified sodium glass of composition $x = 1.5$ yielded some evidence for the switch in borate structure. A strong peak at 800 cm^{-1} was seen, which indicates the presence of triborate in the glass.

If the borate structure is transformed by the addition of WO_3, then effects similar to the "borate anomaly" of alkali borate glasses may be seen. The "borate anomaly" is the name given to the phenomenon observed in alkali borate glasses which shows abrupt changes in density, refractive index, and other properties with increasing alkali content with the change occurring at 16 mol% alkali. A satisfying explanation for the effect is still forthcoming, but the anomaly seems to correlate with a change in the borate structure as determined by Raman scattering.

The relevance of the "borate anomaly" to the present work is the suggestion
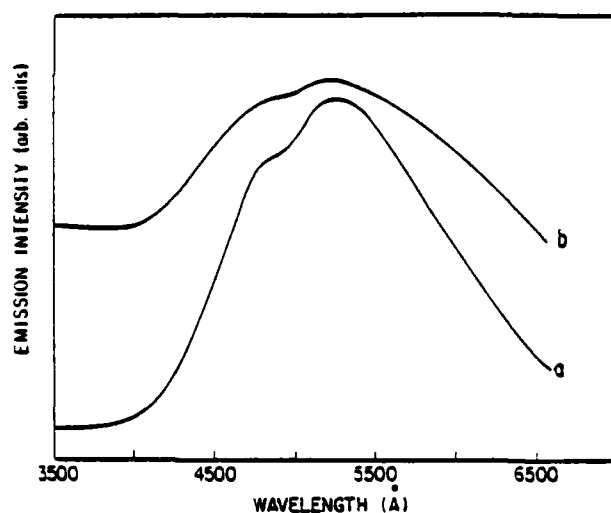
Fig. 13. Room temperature emission spectra of crystalline Li_2WO_4 powder. Excitation wavelength = (a) 2700 Å. (b) 2850 Å.

to the WO_4^- species should have only one broad emission centered at 470 nm [19]. The Raman spectrum of the unpurified Li_2WO_4 powder used in the emission experiment shows many peaks other than those due to normal WO_4^- vibrations (dotted line, fig. 6). The extra Raman peaks provide evidence for defect tungstate structures of polymeric structure probably responsible for the 550 nm luminescence. The 99.999% Na_2WO_4 shows only the WO_4^- Raman peaks and does not emit at 550 nm. The possibility of impurities not related to the tungstates causing the luminescence may be discounted. The crystalline WO_3 and $Li_2O \cdot (B_2O_3)_2$ used in making the glasses do not luminescence by themselves in the region between 400–600 nm. This indicates luminescent impurities are not being introduced directly by the glasses constituents. The formation of MoO_4^- is possible if MoO_3 is introduced with the WO_3; however, MoO_4^- has an extremely weak emission [19] and produced no discernible emission when Li_2MoO_4 powder was tested. The most compelling evidence for eliminating impurities as a cause of the emission peaks is the results for the $Na_2O \cdot (B_2O_3)_2 \cdot 1WO_3$ glass. This glass was made from $Na_2B_4O_7$ and WO_3 and from Na_2WO_4 and B_2O_3; yet both produced the same emission spectrum. This strongly indicates that impurities are not the cause of the luminescence seen.

Corroboration for assigning the 550 nm emission to a WO_3 defect or polymeric structure comes from work recently reported on $CdWO_4$ luminescence [20]. It was found that certain samples of $CdWO_4$ produce an emission spectrum with twin peaks. The two emission peaks are similar in relative size and position to those found for impure Li_2WO_4 and the glasses studied here. In addition, the $CdWO_4$ study revealed an excitation dependence of the emission

in line shape, the wavelength of the emissions (400–600 nm), and the excitation wavelengths [19] (< 300 nm). Since most pure tungsten oxide compounds have an emission consisting of one broad peak [19], the presence of two or more different emission lines in the glasses indicates the presence of two or more species of tungstates.

The emission of Li_2WO_4 has been reported as having a maximum at 450 nm [19]. The peak at 470 nm in the lithium glasses can be assigned to that species. Kröger's [19] inability to detect any emission from Na_2WO_4 was apparently due to less sensitive equipment since an emission spectrum of 99.999% Na_2WO_4 powder (fig. 11) shows an emission at 480 nm. This corresponds to an emission peak in the sodium glasses.

$Li_2W_2O_7$ and $Na_2W_2O_7$ emit in the region between 500 and 530 nm as reported in the literature [19] and confirmed in the present work. At low concentrations of WO_3, the lower energy emission in glasses fails within this region. The 520 nm emission remains as a shoulder even at high WO_3 concentrations and can be assigned to the $W_2O_7^-$ ion.

The other species of tungstate identified by Raman spectrum of $WO_3 \cdot H_2O$ do not luminesce, at least not in its crystalline form. It is suggested, therefore, that the 550 nm emission is due either to a defect octahedral tungstate species or one of the longer polymeric tungstates. This can be supported by several observations. The emission of unpurified Li_2WO_4 (fig. 11) reveals the presence of two peaks which are similar in size, shape, and position to the peaks found for the high WO_3 concentration glasses. However, the expected spectrum due
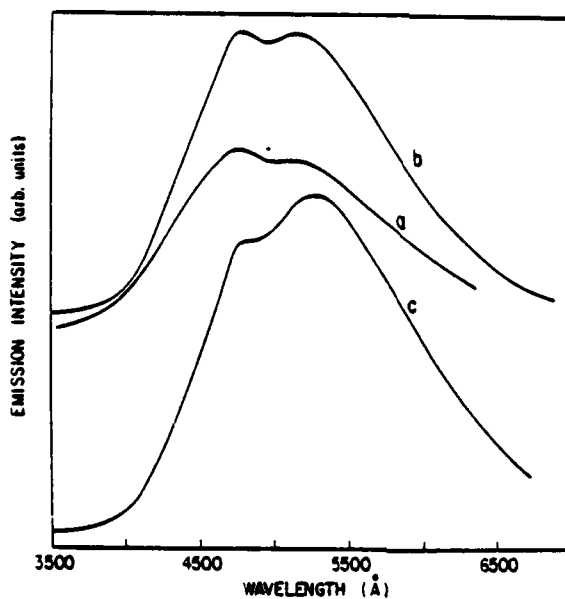
Fig. 12. Room temperature emission spectra of $Li_2O \cdot (B_2O_3)_2 \cdot 0.08WO_3$ glass. Excitation wavelength = (a) 2500 Å, (b) 2700 Å, (c) 3000 Å.
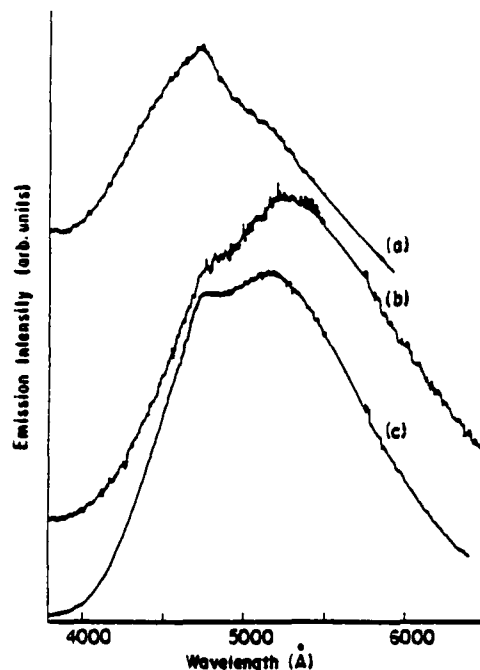
Fig. 11. Room temperature emission spectra of pure tungstates. Excitation wavelength = 2850 Å. (a) Na_2WO_4 powder (99.999% pure), (b) Li_2WO_4 powder (unpurified), (c) $Na_2W_2O_7$.

$W_2O_7^-$ spectrum. Peaks at 220 and 225 cm^{-1} of $W_2O_7^-$ fall in a region of a peak due to H_2WO_4. However, in the $x = 0.9$ lithium glass, the borate peak appears to be resolved into two peaks at 220 and 250 cm^{-1}. At this composition, H_2WO_4 may not be sufficiently concentrated to mask the $W_2O_7^-$ peaks.

Other polymeric tungstates are also possible, but absolute identifications have not been made. The peak at 1000 cm^{-1} for the $Li_2O \cdot (B_2O_3)_2 \cdot 1.2WO_3$ ceramic falls in a region indicative of a polymeric tungstate with multiple WO_3's [17,18]. However, samples of Na_2WO_4 with various concentrations of WO_3 added produced ceramics which showed Raman peaks due only to WO_4^- and $W_2O_7^-$.

Luminescence data obtained at room temperature for the glasses are shown in figs. 9 and 10. Spectra were also obtained at liquid N_2 temperatures. The only apparent difference between the spectra taken at the two temperatures is more intense emissions at lower temperature. The trend of the emission spectra with increasing WO_3 concentration should be noted. Two emission peaks are seen at low concentrations of WO_3. The lower energy emission peak at 525 nm increases in intensity relative to the higher energy peak at 470 nm and tends to develop an asymmetry on the lower energy side of the peak.

The luminescence of the glasses is characteristic of tungsten oxide emission
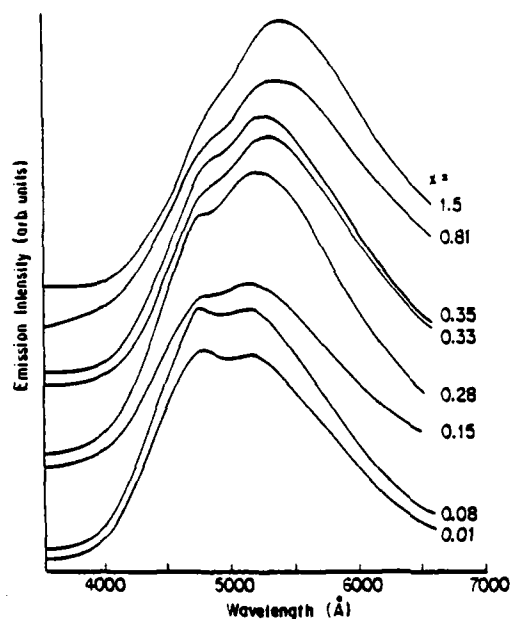
Fig. 9. Room temperature emission spectra of $Li_2O \cdot (B_2O_3)_2 \cdot xWO_3$ glasses. Excitation wavelength = 2850 Å.

by Raman very difficult. However, the parts of the spectrum which can be analyzed provide evidence for the presence of $W_2O_7^=$. The two peaks in the glass spectra and 840 and 885 cm^{-1} correlate well with the peaks present in the
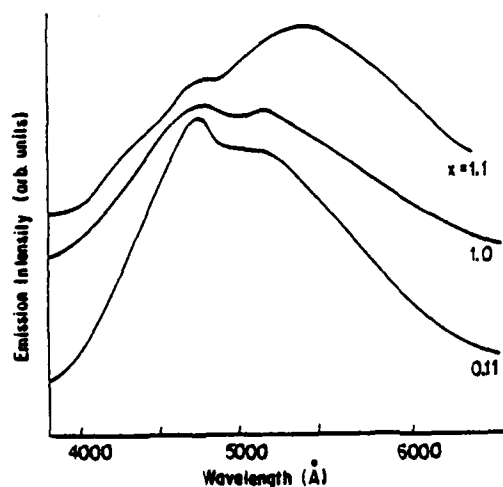
Fig. 10. Room temperature emission spectra of $Na_2O \cdot (B_2O_3)_2 \cdot xWO_3$ glasses. Excitation wavelength = 2850Å.

FREQ. SHIFT (cm⁻¹)
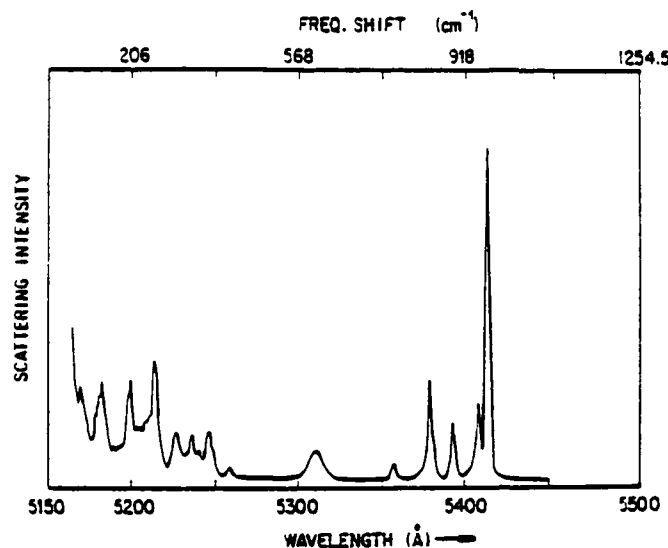
Fig. 8. Raman spectrum of Na₂W₂O₇.

are beginning to devitrify as the WO_3 concentration increases above $x = 1.0$. The samples appear glassy (transparent) until $x = 1.2$ for the Li glasses and $x = 1.6$ for the Na glasses, while above these concentrations opaque ceramics are formed.

Because the glasses were made under atmospheric conditions, the possibility of water being involved in any tungstate structures was investigated. Water is known to coordinate with WO_3 to form the compounds $WO_3 \cdot H_2O$ and $WO_3 \cdot 2H_2O$ [12,13], both of which are thought to contain octahedral WO_3. The spectrum of H_2WO_4 powder ($WO_3 \cdot H_2O$), shown in fig. 7, correlates with the new peaks seen in the higher concentration glasses. The peaks match in broadness, position, and relative size the 225 and 600–700 cm^{-1} bands found in the high concentration glasses. The 950 cm^{-1} peak in H_2WO_4 would be masked by the WO_4^- A_{1g} peak in the glasses.

The presence of H_2WO_4 does not explain all the peaks found in the glasses with WO_3 concentration ≥ 1.0. At these concentrations the glasses resemble the $Li_2WO_4 \cdot xWO_3$ crystalline systems studied by a number of investigators [9,14,15]. These systems have been found to contain polymeric tungstates with the general formula $M_2O \cdot xWO_3$, where x is an integer. As mentioned previously, the system can be made into a glass with the proper quenching procedure [9]. The most common of the polymeric tungstates is $W_2O_7^-$ which consists of the tetrahedral WO_4^- group with an octahedral WO_3 group.

A Raman spectrum of pure $Na_2W_2O_7$ is shown in fig. 8. The spectrum obtained here agrees with the spectrum published recently [16]. Most of the dominant Raman peaks of $W_2O_7^-$ fall in the regions which overlap with the peaks of WO_4^- and H_2WO_4. This makes the identification of $W_2O_7^-$ exclusively

of states is singular. These critical points dominate the interband structure of the reflectivity spectrum. With the proper experimental feedback, band-to-band energy differences can be calculated with an accuracy of 0.1 eV. Energy band calculations are usually adjusted to fit the results of optical determinations of interband transition energies.

It is necessary to find the real and imaginary parts of the dielectric function, ε_1 and ε_2, and their derivatives to examine the interband structure of the material under study. However, the dielectric function may not be directly available from experimental measurements. In some experiments, the reflectivity, $R(\omega)$, is obtained by integrating the data from wavelength modulation spectroscopy; the real and imaginary parts of the dielectric function are subsequently calculated by a Kramers-Kronig analysis [13]. When the material being studied is a metal or metal alloy, however, another step is needed. The dielectric function is the sum of two parts, a contribution due to interband structure and a contribution due to intraband transitions of the electrons at the Fermi level in the partially filled conduction bands. In order to separate the interband and intraband transitions, low-energy data are required which sometimes are not readily available.

We report a new technique for separating these contributions. For continuity of presentation, Section 2 of this paper will review the classical formalism which is used to describe the intraband contribution. Section 3 will deal with the interband structure, and Section 4 will present the new method of separation.

2. Classical Drude Theory

The classical Drude theory of the electronic properties of solids is due mainly to Lorentz [14] and Drude [15]. The Lorentz model assumes that an electron bound to the nucleus of an atom may be dealt with in much the same way as a small mass bound to a large mass by a spring. A classical damped oscillator model yields the Lorentz dielectric function

$$\varepsilon = 1 + \frac{4\pi N e^2}{m} \frac{1}{(\omega_0^2 - \omega^2) - i\Gamma\omega}, \tag{3}$$

where Γ is a viscous damping coefficient, N the electron density, and $m\omega_0^2 r$ is a Hooke's law force. The Drude model for metals is derived from the Lorentz model; the conduction electrons in a metal are not bound to a nucleus so the restoring force is set equal to zero.

When ω_0 is set to zero in (3) and real and imaginary parts are taken, we have

$$\varepsilon_1 = 1 - \frac{\omega_p^2 \tau^2}{1 + \omega^2 \tau^2}, \tag{4a}$$

$$\varepsilon_2 = \frac{\omega_p^2 \tau^3}{\omega(1 + \omega^2 \tau^2)}, \tag{4b}$$

where $\omega_p = (4\pi N e^2/m)^{1/2}$ is the free-electron plasma frequency, and $\tau = 1/\Gamma$ is a relaxation due to the ordinary scattering responsible for electrical resistivity.

The Drude model provides a good fit for the optical properties of metals at energies below those of any interband transition. The experimentally derived dielectric function may be fitted to equations (4a) and (4b) where m is now replaced by an effective mass, m^*, and m^* and τ are used as adjustable curve-fitting parameters. Once this is done, the Drude dielectric function may be subtracted from the total dielectric function throughout the spectrum to yield the interband contribution.

One would expect that at energies where the photon energy is greater than the width of the actual bands in a solid, the Drude model could not be used. However, it should be remembered that the Drude model is simply a classical approximation and that the values found for m^* and τ are measures of the fitness of that approximation at the Fermi level.

3. Interband Transitions

Points in k-space for which (2) applies are van Hove singularities. These critical points form the dominant contribution to the interband part of the dielectric function. There are four types of critical points which are labelled as M_s critical points, with $s = 0, 1, 2, 3$ for the number of negative values of the effective masses associated with the band curvatures at these points. The lineshapes of the four types of critical points determined by the joint density of states, J_{cv}, without broadening are summarized in Table 1.

Table 1

J_{cv} for critical points

critical point	J_{cv}	
	$E < \hbar\omega_g$	$E > \hbar\omega_g$
M_0	0	$C_0(E - \hbar\omega_g)^{1/2}$
M_1	$C_1 - C_2'(\hbar\omega_g - E)^{1/2}$	C_1
M_2	C_2	$C_2 - C_2'(E - \hbar\omega_g)^{1/2}$
M_3	$C_3(\hbar\omega_g - E)^{1/2}$	0

The effects of phonon broadening may be included in the dielectric function by introducing a phenomenological broadening parameter, η. A dielectric function which includes broadening near an M_0 critical point can be defined by [16, 17]

$$\varepsilon - 1 \sim (\omega + i\eta)^{-2} \left[2\omega_g^{1/2} + (\omega_g - \omega - i\eta)^{1/2} + (\omega_g - \omega + i\eta)^{1/2} \right]. \qquad (5)$$

When derivative spectroscopy is being done, the derivatives of ε need to be considered. If the broadening parameter, η, is small $(\omega \ll \omega_g)$, the main contribution to the derivative of (5) is due to the $(\omega_g - \omega - i\eta)^{1/2}$ term. This term is singular in the limit $\eta \to 0$ while the other terms are well behaved. Using an M_0 critical point as an example, and defining a reduced frequency $W = (\omega - \omega_g)/\eta$, we obtained [18, 19]

$$\frac{d\varepsilon_1}{d\omega} \sim \mathrm{Re}\left[\frac{1}{2}(\omega + i\eta)^{-2}(\omega_g - \omega - i\eta)^{-1/2} \right]$$

$$= \frac{1}{2}\eta^{-1/2}[W^2 + 1]^{-1/2}[(W^2 + 1)^{1/2} - W]^{1/2}$$

$$= \frac{1}{2}\eta^{-1/2}F(-W), \qquad (6a)$$

$$\frac{d\varepsilon_2}{d\omega} \sim \mathrm{Im}\left[\frac{1}{2}(\omega + i\eta)^{-2}(\omega_g - \omega - i\eta)^{-1/2} \right]$$

$$= \frac{1}{2}\eta^{-1/2}[W^2 + 1]^{-1/2}[(W^2 + 1)^{1/2} + W]^{1/2}$$

$$= \frac{1}{2}\eta^{-1/2}F(W). \qquad (6b)$$
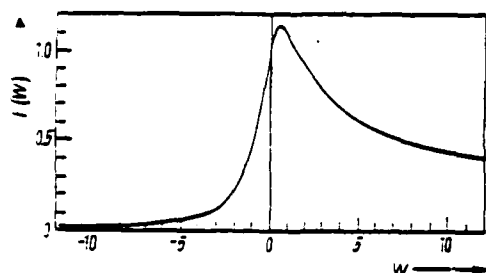
Fig. 1. Universal function derived by Batz [18]. The function $F(W) = (W^2 - 1)^{-1/2} \times$ $\times [(W^2 + 1)^{1/2} - W]^{1/2}$, where W is a normalized frequency. $\eta^{-1/2}F(W)$ becomes $(\omega - \omega_g)^{1/2}$ in the limit $\eta \to 0$. $W = (\omega - \omega_g)/\eta$

The universal function $F(W)$ was derived by Batz [18] and is illustrated in Fig. 1. It is found that the derivative spectra around other types of critical points can also be expressed in terms of this function. The results are summarized in Table 2. The function $\eta^{-1/2} F(W)$ goes to $(\omega - \omega_g)^{-1/2}$ in the limit $\eta \to 0$, as expected.

Table 2

Derivatives of critical points with broadening included in terms of $F(W)$

critical point	$2\eta^{1/2}\dfrac{d\varepsilon_1}{d\omega}$	$2\eta^{1/2}\dfrac{d\varepsilon_2}{d\omega}$
M_0	$F(-W)$	$F(W)$
M_1	$-F(W)$	$F(-W)$
M_2	$-F(-W)$	$-F(W)$
M_3	$F(W)$	$-F(-W)$

4. Separation of Bound- and Free-Electron Contributions

When experimental data exist for energies less than any interband transition, the Drude forms in (4a) and (4b) may be fit to these low-energy data in order to determine m^* and τ. The spectral range of our wavelength-modulated spectrometer is 1.5 to 5.1 eV. Since many metals and metal alloys have significant interband structure down to the lowest energies of this spectral region, the above method cannot be used. However, when the derivatives of (4a) and (4b) are compared to (6a) and (6b), it is noted that the Drude dielectric function and the interband term at the critical points are sufficiently uncorrelated to justify the method used here to separate them.

The method of separation is the use of m^* and τ as adjustable parameters in writing a trial Drude function, subtract the Drude function from the total dielectric function obtaining a difference function, and calculate the correlation of the Drude and difference functions. The de-correlation function may be written [20] as

$$C_1(m^*, \tau) = \frac{(\text{cov}\,[B_1,\, A_1 - B_1])^2}{V[B_1]\,V[A_1 - B_1]}, \tag{7a}$$

where

$$\text{cov}\,[B_1,\, A_1 - B_1] = \frac{1}{N} \sum_i (B_{ij} - \bar{B}_1)[(A_{ij} - B_{ij}) - (\bar{A}_1 - \bar{B}_1)], \tag{7b}$$

$$V[B_j] = \frac{1}{N} \sum_i (B_{ij} - \bar{B}_j)^2 . \tag{7c}$$

The function A is the derivative of the experimental dielectric function, and B is the derivative of the trial Drude function. The sums are over data points. N. the subscript $j = 1$ or 2 for the real or imaginary parts, and the bars indicate averages over all points. cov $(B_j, A_j - B_j]$ is the covariance of B_j and $A_j - B_j$. $V[B_j]$ is the variance of B_j.

A computer program has been written which. for a given τ. finds the value of m^* which best minimizes (7a) [19]. This produces two curves $m^*(\tau)$, one for $j = 1$ and another for $j = 2$. Then these two curves are plotted together: their intersection gives the physical values of m^* and τ. These are the correct values of the Drude parameters since they are the ones which simultaneously minimize the de-correlation function for both the real and imaginary part. In each de-correlation function alone there is only one independent variable, which has been chosen to be τ. When τ is fixed. there will always be some value of m^* which best minimizes $C_i(m^*, \tau)$. When values of m^* and τ are found which minimize both C_1 and C_2, we have confidence that we have found the correct physical values. Once m^* and τ are determined the Drude part of ε is subtracted leaving the interband part.

To test the method, a trial function was formed. It was the sum of Drude and interband contributions in the range from 1.5 to 5.1 eV. The Drude term was given an effective mass of 1.4 electron rest masses and a relaxation time of 1.2×10^{-15} s. These values are within the normal range found in typical metals. The interband part had an M_0 critical point at 2.5 eV and an M_3 critical point at 4.0 eV. The two parts were cal-
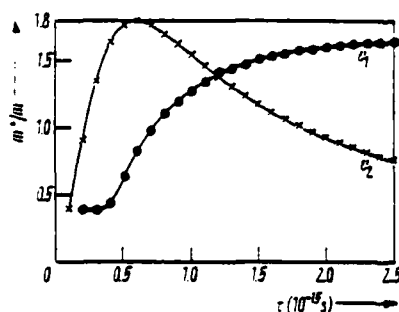
Fig. 2   Fig. 3

Fig. 2. Results of de-correlation functions for the test functions described in the text. A function, $m^*(\tau)$, is generated for each de-correlation function, C_1 and C_2. $m^*(\tau)$ is the value of the effective mass which best minimizes C_1 or C_2 for a given value of the relaxation time. τ. One curve is generated by using ε_1' in (7a) to (7c) and the other curve is from ε_2'. The point where the curves cross represents the correct physical value of m^* and τ. Test function: $m^*/m = 1.39, \tau = 1.19 \times 10^{-15}$ s
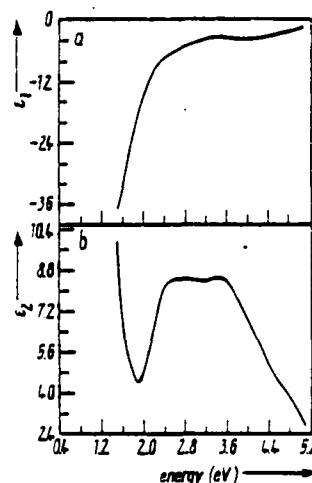
Fig. 3. Dielectric function of β'-AuZn which was used to test the de-correlation technique. a) Real part, ε_1; b) imaginary part, ε_2. The derivatives of these were used to find the Drude parameters
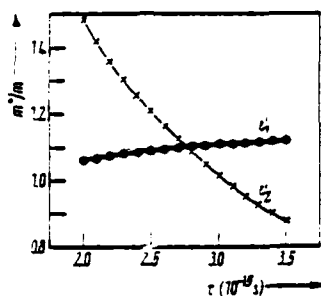
Fig. 4   Fig. 5

Fig. 4. Results of the de-correlation functions for β'-AuZn. The point where the curves cross is at $m^*/m = 1.10$ electron masses and $\tau = 2.76 \times 10^{-15}$ s
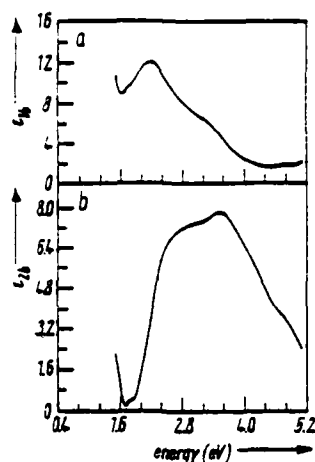
Fig. 5. Interband contribution to the dielectric function of β'-AuZn. The Drude parameters found in Fig. 4 were used in (4a) and (4b), which was then subtracted from the experimental dielectric function of Fig. 3

culated using (4a) and (4b) and Table 2. The curves for the solution of the test function are shown in Fig. 2. The values found at the intersection of the curves were $m^* = 1.39$ electron masses and $\tau = 1.19 \times 10^{-15}$ s.

Fig. 3 shows ε_1 and ε_2 for β'-AuZn obtained by integrating wavelength modulation data. The graph of the correlation minima is given in Fig. 4. The values at the intersection of the curves are $m^* = 1.10$ electron masses and $\tau = 2.76 \times 10^{-15}$ s. The value for m^* is slightly lower than previously reported [21]. Fig. 5 shows the bound parts of ε_1 and ε_2 (ε_{1b} and ε_{2b}) after the Drude terms are subtracted.

This separation technique has two shortcomings. The first is that the Drude relaxation time is not actually a constant over the entire spectrum. The value obtained is assumed to be an average value over the spectral range. However, this problem also occurs when extrapolations from low-energy data are used. The advantage in this calculation is that here the values are from the visible-ultraviolet part of the spectrum which is actually under study. Secondly, there is a small ω^{-2}-contribution to the bound parts of the dielectric function. However, if the linewidths of the interband transitions are small compared to the transition energies, these terms may be neglected [18, 22]. Such terms may cause a small error in the Drude parameters, but will not cause any change in the general lineshapes of the interband contributions to the dielectric function, which are the important results for band structure determinations.

References

[1] B. BATZ, Solid State Commun. 4, 241 (1965).
[2] C. N. BERGLUND, J. appl. Phys. 37, 3019 (1966).
[3] B. O. SERAPHIN and R. B. HESS, Phys. Rev. Letters 14, 138 (1965).
[4] M. CARDONA, K. L. SHAKLEE, and F. H. POLLACK, Phys. Rev. 154, 696 (1967).

[5] W. E. ENGELES, H. FRITZSCHE, M. GARFINKEL, and J. J. TIEMANN, Phys. Rev. Letters 14, 1069 (1965).
[6] G. W. GOBELI and E. O. KANE, Phys. Rev. Letters 15, 142 (1965).
[7] I. BALSLEV, Phys. Rev. 143, 636 (1965).
[8] G. BONFIGLIOLI and P. BROVETTO, Appl. Optics 3, 1417 (1964).
[9] R. E. DREWS, Bull. Amer. Phys. Soc. 12, 384 (1967).
[10] M. WELKOWSKY and R. BRAUNSTEIN, Rev. sci. Instrum. 43, 399 (1972).
[11] M. WELKOWSKY, Ph. D. Thesis, Univ. California, Los Angeles 1971.
[12] L. VAN HOVE, Phys. Rev. 89, 1189 (1953).
[13] J. MATHEWS and R. L. WALKER, Mathematical Methods of Physics. W. A. Benjamin, Inc., New York 1970.
[14] H. A. LORENTZ, The Theory of Electrons, Dover Publ., Inc., New York 1952.
[15] P. K. L. DRUDE, Theory of Optics, Dover, Publ., Inc., New York 1959.
[16] B. BATZ, Solid State Commun. 5, 985 (1967).
[17] O. H. F. VREHEN, Phys. Rev. 145, 675 (1966).
[18] B. BATZ, Ph. D. Thesis, Univ. Libre de Bruxelles, 1967.
[19] R. STEARNS, Ph. D. Thesis, Univ. California, Los Angeles 1982.
[20] K. A. BROWNLEE, Statistical Theory and Methodology in Science and Engineering. John Wiley & Sons, New York 1960.
[21] J. P. JAN and S. S. VISHNUBHATLA, Canad. J. Phys. 45, 2505 (1967).
[22] M. CARDONA, Modulation Spectroscopy, Academic Press, New York 1969.

DERIVATIVE ABSORPTION SPECTROSCOPY OF GaAs:Cr

R. Braunstein[a], R.K. Kim[a], D. Matthews[b], and M. Braunstein[b]

(a.) Physics Department, University of California, Los Angeles, U.S.A. 90024
(b.) Hughes Research Laboratories, Malibu, Calif., U.S.A. 90265

Infrared wavelength modulation measurements at 300K in the spectral range 0.5-1.4 eV on semi-insulating n and p-type Cr doped GaAs have revealed extensive fine structure with variations in absorption coefficient $\Delta K \sim 10^{-1}$ - $10^{-2} cm^{-1}$ out of a relatively smoothly varying background absorption of 1-2 cm^{-1}. These results can be interpreted in terms of transitions from (Cr^{3+} - Cr^{2+}) to the valence and conduction bands and excited states.

1. INTRODUCTION - EXPERIMENTAL PROCEDURES

Although the deep levels of Cr in GaAs have been extensively studied by luminescence, absorption, photoconductivity and junction techniques, there are still questions concerning the possible energy level schemes of this important deep impurity. In general, excited states are not observed by the above techniques and absorption thresholds are not easily observed. We have developed an infrared wavelength modulated spectrometer that is capable of detecting changes in absorption of a part in 10^5 out of a relatively smoothly varying background in the spectral range 0.05-5.0 eV. Consequently, our detection limit for concentrations of deep levels is 10^{12}-$10^{14}/cm^3$ which was previously only possible by DLTS techniques. It has been possible to observe absorption thresholds and excited states in highly transparent solids[1]. In the present work, we report the results of a study of semi-insulating GaAs:Cr compensated with n and p-type impurities. Structures have been resolved in previously reported smoothly varying absorption bands which we interpret in terms of the level of Cr at various lattice sites. The infrared wavelength modulation system used in our work has been previously described [1].

2. RESULTS

Figures 1 and 2 show the integrated derivative wavelength data of semi-insulating GaAs:Cr at 300K with varying degrees of shallow donor and acceptor compensations. The constants of integration were supplied by direct absorption measurements. Although data was taken in the spectral range 0.5-1.5 eV, for purposes of the present discussion, we shall discuss the data for the 0.5-1.2 eV region since the vast literature on GaAs:Cr has considered this regime. The region above 1.2 eV shows structures which can be associated with transitions from the Cr^{2+} ground state to the X and L conduction bands as well as EL2 structures. The scale of the absorption should be noted; in general the best previous absorption data have a precision of $\Delta K \sim 0.1 cm^{-1}$ (2). The present work reveals structures at levels of $K < 10^{-2} cm^{-1}$ in samples of the order of 1mm thick.

The samples were all semi-insulating and contained $\sim 10^{16}/cm^3$ Cr and where grown by horizontal Bridgman techniques. The samples in Figure 1 were highly compensated while those in Figure 2a and 2b were slightly more p and n-type respectively. Although quantitative measurements of shallow donor or acceptor compensation are difficult for such high resistivity samples, qualitative differences in n and p-type were measured by the changes in the characteristics of the space-charge limited I-V curves under illumination and in the dark.

The general features of the data exhibit clusters of lines in the 0.5-0.7, 0.8-0.95 and the 0.95-1.05 eV regions with extensive fine structure in every region, but with more pronounced structures in the 0.8-0.93 eV range. Previous conventional absorption measurements have shown a no-phonon line in the 0.82 region (2) and a broad continuum peaking at 0.9 eV for n-type material. In the 0.5-0.72 eV region, previous absorption measurements showed no fine structures but a smoothly varying free carrier absorption. A number of luminescence bands have been observed in GaAs:Cr in the range 0.57-0.81 eV, but their interpretation has been difficult (3).

The relative magnitudes and the fine details vary from sample to sample as seen in Figures 1 and 2, but the envelopes of the dominant structures tend to vary in a systematic fashion with a degree of compensation. Samples in Figure 1 show essentially the same features but the sample in Figure 1b exhibits finer structure at 0.8-0.9 eV while the bands in the 0.5-0.72 eV have somewhat the same relative intensities. These samples were from the same crystal, but different parts of a single wafer. The samples in Figure 2a and 2b were more heavily doped p and n-type respectively than the samples in Figure 1. It should be noted that the relative intensities of the 0.5-0.72 eV bands change in Figures 2a and 2b with the 0.67 band enhanced in the n-type sample while the 0.58 eV band is enhanced in the p-type sample and the general level of absorption has increased over that of Figure 1. In addition, in the p-type sample, the cluster of lines between 0.8 eV
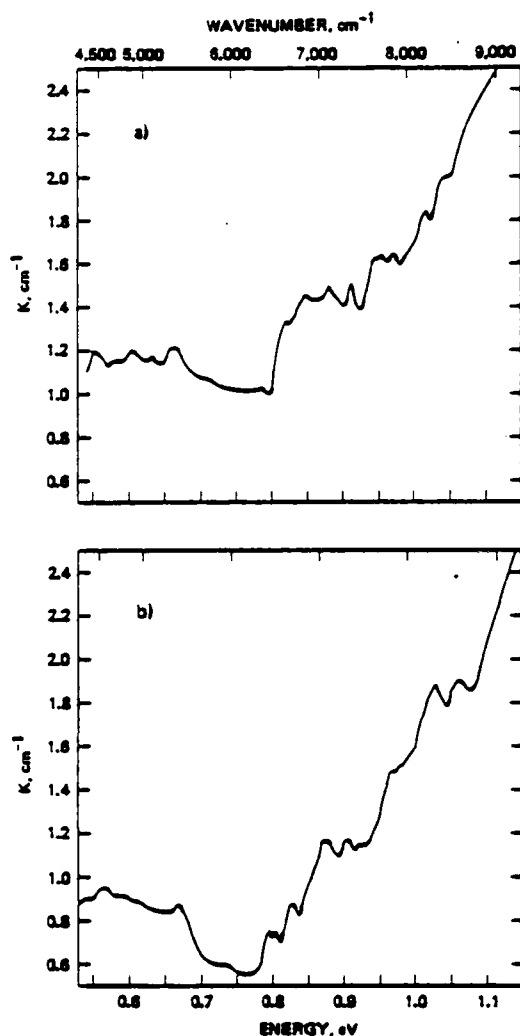
Figure 1:   a) and b)   Semi-insulating GaAs:Cr

Figure 2.   a) p-type,   b) n-type   GaAs:Cr

and 0.9 eV have suppressed while the fine structure is maintained in the n-type sample.

3. DISCUSSION

The explanation of some of the varied structures and their variation with the degree of free carrier compensation can be explained in terms of transitions between $(Cr^{3+} - Cr^{2+})$ states in a tetragonal environment and the conduction and valence bands and excited states. Figure 3 shows a level scheme of a ^5D state of Cr^{2+} placed within the energy gap of GaAs (4), we shall see that the explanation of the bands in the 0.5-0.72 eV region cannot be explained by this level scheme but is consistent with Cr^{2+} being in a C_{3v} symmetry site.

The data in the 0.8-1.05 eV region shows two main thresholds roughly around 0.8 eV and the other around 0.93 eV with fine structure in each band with the 0.8 eV threshold enhanced in the more n-type samples. We can attribute the 0.8 eV transition from the Cr^{2+} ground state to a resonant state in the conduction band: $^5B_2(^5T_2) \longrightarrow ^5A_1(^5E)$, P_1 in Figure 1 (4). The second threshold can be ascribed to the transition from the valence band to the Cr^{2+} level Cr^{2+} ($^5T_2$) (4), i.e. P_2 and P_3. The $^5T_2$ state can be split by a tetragonal Jahn-Teller distortion into a $^5B_2$ and ^5E level. The ground state can be further split by spin-orbit coupling, however these are not shown because of the scale of the resolution of our experiments. The structure seen in the

0.93 - 1.05 eV region can be associated with valence band to Cr^{3+}, P_2 and P_3, transitions. Various estimates have been made of the magnitude of the Jahn-Teller distortion for C^{2+} and these have varied from 175 cm^{-1} to 700 cm^{-1} (2). If we take the peak at 0.95 eV and the shoulder at 1.04 eV as due to the transitions from the valence band to $^5B_2(^5T_2)$, P_2, and $^5E(^5T_2)$, P_3, respectively the Jahn-Teller distortion E_{JT} ∿ 100 cm^{-1}. The transition $^5B_2-^5E$ has not been seen in absorption in GaAs:Cr despite extensive studies which merely reveal free carrier absorption in this region.
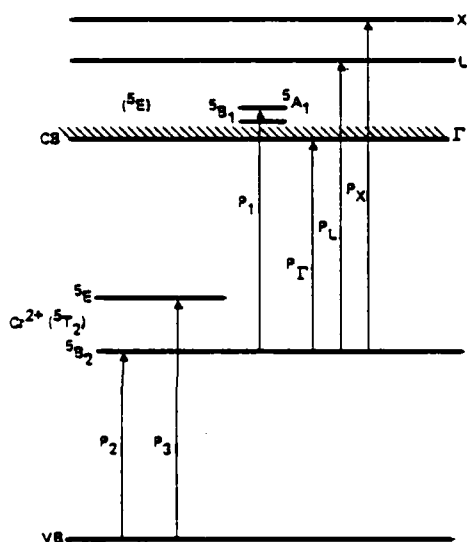
Figure 3. Energy levels of $(Cr^{3+}-Cr^{2+})$ ions in GaAs.

Although all our absorption measurements show extensive structure in the 0.8-0.93 eV - more so in n-type samples, most previous measurements show a broad peak around 0.9 eV. Recently (2) an absorption band at 0.92 eV and a no-phonon line have been resolved and have been interpreted as the interval transition $^5B_2(^5T_2)$- $^5A_1(^5E)$ of Cr^{2+}. It is of interest to note that the fine structure around 0.8 eV in Figure 1 maybe due to these no-phonon lines, although our measurements were performed at 300K while the above work was at 4K. Luminescence experiments have shown a band at 0.81 eV and a no-phonon line at 0.839 eV (5). These lines have commonly been considered to be an internal $^5E-^5T_2$ transition of Cr^{2+}, however, it has been argued that the ground splitting of the 0.83 - eV line is inconsistent with E.S.R. measurements (3).

The luminescence bands in GaAs:Cr at 0.57, 0.61, 0.64, 0.68 eV have been difficult to interpret; it has been suggested that the 0.57 and 0.61 eV bands are due to the transition from a Cr^{2+} to the valence band and from the conduction band to a Cr^{3+} (6). The 0.62 eV band is always present in n-type material while in semi-insulating or p-type GaAs:Cr the 0.57 eV is more intense, while accompanied by the 0.3 eV band and thus can be attributed to the Cr^{3+} state. Arguments have recently been advanced that dispute that the 0.839 eV and the no-phonon line as being related to a single Cr acceptor center in a tetragonal Ga site (3). It has been proposed that the 0.839 eV band and the 0.574/0.535 eV lines are due to Cr at a C_{3v} symmetry site induced by coupling of a chromium atom at an interstitial or on a Ga site to a first neighbor impurity (3). For a trigonal field, C_{3v}, this work shows that there is a reordering of the Cr levels different from the tetragonal site shown in Figure 3. For intersitial chromium at a trigonal C_{3v} site coupled to an acceptor, the ordering of the orbital levels are ^5E, ^3A, and ^5E from lower to upper. While for a substitutional chromium at C_{3v} symmetry site coupled to a donor the ordering from lower to upper is ^5E, $^5A_1$, ^5E. The 0.574 eV and its associated emission are interpreted as transitions from the ground state to the valence band.

It is strongly suggestive that the absorption bands observed in the present work are related to the luminescence bands in this spectral region. It should be noted that for the samples in Figures 2a and 2b, which have a slightly higher doping, the level of absorption is greater for these bands than in the more compensated samples of Figures 1a and 1b. In the p-type sample of Figure 2a, the 0.585 eV line is enhanced over the 0.641 eV line, while for the n-type sample the 0.671 eV line is enhanced over the 0.59, 0.62 and 0.64 eV lines. Thus it seems that these absorption bands can be the complements of the luminesence bands. The complexity of this structure is evident and if they are due to C_{3v} trigonal symmetry due to coupling with Cr to donor or acceptor complexes, the subtle changes are due to degree of compensation and consequent position of the Fermi level in these four semi-insulating samples. The level of absorption in the 0.5 - 0.72 eV and 0.85 - 1.05 eV regions would indicate that about a comparable numb. of Cr atoms are at tetragonal and trigonal sites.

References

(1) Braunstein, R., Kim, R.K., and Braunstein, M., NBS Special Publication 568, U.S. Government Printing Office.

(2) Clerjaued, B, Hennel, A.M., and Martinez, G., Solid State Comm. 33 (1980) 983–985.

(3) Picoli, G., Deveaued, B., and Galland, D., Le Journal De Physique T42, No. T (1980) 133–145.

(4) Leyral, P., Litty, F., Loualichi, S., Nouailhot, A., and Guillot, G., Solit State Comm. 38 (1981) 333–336.

(5) Lightowlers, E.C., and Penchina, C.M., J. Phys. C. Solid State Phys, 11 (1978) L405

(6) Deveaued, B., Hennel, A.M., Suzuzkiewicz, Picoli, G., Martinez, G., Revue Phys, Appl 15 (1980) 671.

Infrared wavelength modulation spectroscopy of some optical materials

Ryu K. Kim and Rubin Braunstein

Infrared wavelength modulation techniques were developed and used to investigate the low-level absorption of some optical materials such as alkali halides and alkaline earth fluorides. The results reveal rich absorption structures which enable an identification of some of the surface and bulk impurities of these materials. Those impurities are principal sources of optical absorption which limit the expected transparency of these materials in the spectral region studied (2.5–12 μm).

I. Introduction

The development of high-power laser sources has generated considerable interest in the study of very weak absorption processes difficult to detect by conventional spectroscopic methods because of the need for low absorption laser components. In recent years, extensive theoretical and experimental investigations have been conducted in an effort to determine the frequency and temperature dependence of the absorption coefficient of a number of alkali halides and alkaline earth fluorides to identify the principal mechanisms responsible for intrinsic and extrinsic absorption processes. The very low values expected of the absorption coefficient characteristic of multiphonon infrared absorption have spurred the development of various specialized measurement techniques and/or refinements of existing ones.[1]

The majority of the investigations have focused on ionic solids, especially alkali halide crystals. The latter are attractive for theoretical analysis because of their relative simplicity and the wealth of knowledge already available about many of their fundamental properties. Experimentally, alkali halides again represent relatively well-investigated materials in terms of fundamental properties as well as growth, preparation, and purification.

Deutsch[2] showed that the exponential dependence of absorption coefficient $K(\omega)$ for multiphonon processes follows the empirical law

$$K(\omega) = A_0 \exp(-A\omega), \qquad (1)$$

where A_0 and A are material dependent parameters for a wide class of materials which includes alkali halides, alkaline earth fluorides, oxides, and semiconductors. Sparks and Sham[3] developed a theory for the exponential dependence of $K(\omega)$. Duthler[4] estimated the absorption coefficients for some alkali halides in the regions of interest, particularly at the wavelength of the CO_2 laser line (10.6 μm), by assuming a Lorentzian line shape of impurities peaked at the appropriate wavelengths. The extrapolation of exponential dependence of the absorption coefficient to the spectral region of interest as laser window materials in the 2.5–12-μm region predicts the absorption coefficient to be as low as $\sim 10^{-7}$ cm^{-1}, but in practice the absorption coefficients are always higher than the predicted values, sometimes by 2 orders of magnitude and varying from sample to sample, indicating the presence of extrinsic absorption due to impurities.

To improve the ability to measure the very small values of the absorption coefficient in very high-purity materials, a laser calorimeter has been employed.[5] In this method, an incident laser beam is passed through the sample, and the temperature rise produced by absorption of the radiation is measured. By this method, values of $K(\omega)$ in the range of 10^{-4} or 10^{-5} cm^{-1} have been measured.[6] The major disadvantage of the laser calorimetry approach is that one can measure $K(\omega)$ only at those discrete frequencies at which laser radiation is available. To identify the mechanisms which limit the ultimate transparency of solids, knowledge of variations of the absorption coefficient as a function of frequencies and temperature at very low level is required.

We have developed an infrared wavelength modulation technique which has a sensitivity as low as $\sim 10^{-5}$ cm^{-1} in the spectral region between 2.5 and 12 μm and have studied intrinsic and extrinsic absorption processes in alkali halides and alkaline earth fluorides.

II. Experimental System

A. Experimental Background

Derivative optical spectroscopy as a powerful technique for enhancing weak structure immersed in a relatively smooth background spectrum is well known. Several different modulation schemes were introduced in optical derivative spectroscopy.[7] In most cases, the optical spectrum of the sample is modulated by an external ac perturbation such as electric field,[8] pressure,[9] temperature,[10] and light intensity[11] on the sample. The modulation spectrum so obtained depends intimately on how the property of the sample is affected by the external perturbation, and such knowledge is often limited.

As opposed to other modulation schemes, wavelength modulation allows one to obtain a derivative spectrum by modulating the wavelength of light incident upon a sample without any external ac perturbation to the sample. The main difficulty of the wavelength modulation scheme is the elimination of the background derivative spectra due to light source, detector, optics, and atmospheric absorption. To normalize the background, various servo systems have been employed,[7,12,13] but these are difficult to employ with photoconductive detectors with varying dark current. We developed a wavelength modulation system which eliminates the background problem numerically.

Almost always the wavelength modulation technique has been applied in the ultraviolet and visible spectral regions.[12-14] We have extended the spectral range of the wavelength modulation technique into the infrared; for absorption measurements in the spectral region of this study, 2–12 μm, the system has a sensitivity of $\Delta I/I \sim 10^{-5}$, where ΔI is the fluctuation of signal in the derivative channel.

B. Theory of Wavelength Modulation

In a conventional transmission measurement, the total signal S transmitted by the sample is

$$S(\lambda) = T(\lambda) I_0(\lambda), \tag{2}$$

where T is the sample transmission, and I_0 is the background signal, which consists of the incident light source, optics, atmospheric absorption, and detector response.

When the wavelength is swept sinusoidally across the exit slit of the monochromator at a frequency Ω, that is,

$$\lambda(t) = \lambda_0 + \Delta\lambda \cos(\Omega t), \tag{3}$$

where λ_0 is a fixed wavelength around which the sinusoidal sweeping of the wavelength is performed, and $\Delta\lambda$ is the amplitude of the sweep, the output of the monochromator becomes a function of time, that is,

$$S(\lambda_0,t) = T[\lambda_0 + \Delta\lambda \cos(\Omega t)] I_0[\lambda_0 + \Delta\lambda \cos(\Omega t)]. \tag{4}$$

Expansion of Eq. (4) in a Taylor series in powers of $\Delta\lambda \cos(\Omega t)$ and using the trigonometric identities and collecting terms, we can show that, for small $\Delta\lambda$, retaining the terms up to linear in $\Delta\lambda$,

$$S(\lambda_0,t) = S^{dc}(\lambda_0) + S^{ac}(\lambda_0) \cos(\Omega t), \tag{5}$$

where

$$S^{dc}(\lambda_0) = T_0(\lambda_0) I_0(\lambda_0), \tag{6}$$

$$S^{ac}(\lambda_0) = \Delta\lambda(T' I_0 + T I_0'). \tag{7}$$

Standard lock-in amplifiers measure the ac component of the signal at the reference frequency. Therefore, what is measured at the reference frequency of a lock-in amplifier, which is Ω in our case, is the ac component of $S(\lambda_0, t)$ at Ω. Here we note that S^{ac} contains terms of the form $T' I_0$ and $T I_0'$, that is, a term which is proportional to the first derivative of background as shown in Eq. (7).

In practice, the elimination of the derivative signal of the background is a crucial problem in wavelength modulation. This problem will be discussed in Sec. II.C. As expected, the derivative signal is proportional to the depth of modulation $\Delta\lambda$. The correction terms can be minimized by using the smallest possible $\Delta\lambda$. A convenient test for the distortion of the first derivative due to the correction terms is to measure the change in the magnitude of the signal as a function of $\Delta\lambda$ if a linear relationship is desired. For further discussion of the theory, we refer the reader to the literature[12] and references therein.

C. General Considerations

In a transmission measurement, the signal $I(\lambda)$ transmitted through the sample is given by

$$I(\lambda) = I_0(\lambda) \exp[-K(\lambda)d], \tag{8}$$

where $I_0(\lambda)$ is the background signal which consists of the incident light source, optics, atmospheric absorption, and detector response. $K(\lambda)$ and d are absorption coefficients as a function of wavelength and sample thickness, respectively.

The differentiation of Eq. (8) with respect to the wavelength gives, after a little rearrangement of terms,

$$\frac{dK(\lambda)}{d\lambda} = \frac{1}{d}\left[\frac{1}{I_0}\frac{dI_0(\lambda)}{d\lambda} - \frac{1}{I(\lambda)}\frac{dI(\lambda)}{d\lambda}\right], \tag{9}$$

or, in terms of energy,

$$\frac{dK}{dE} = \frac{1}{d}\left[\frac{1}{I_0(E)}\frac{dI_0(E)}{dE} - \frac{1}{I(E)}\frac{dI(E)}{dE}\right]. \tag{10}$$

As indicated in the theory of wavelength modulation, the measured quantity by a lock-in amplifier for the derivative signal at the preset reference frequency is of the form $\alpha(dI/dE)$, where α is a constant. But as shown in Eq. (7), the derivative signal contains the derivative of the background as well as the derivative of the transmitted intensity. To eliminate the derivative of the background, we use the sample-in and sample-out technique, which is described in a later section.

With the sample-in setting, the derivative signal is, from Eq. (7), for small $\Delta\lambda$

$$S_T^{ac} = \Delta\lambda(T' I_0 + T I_0'), \tag{11}$$

or

$$\frac{S_T^{ac}}{I} = \frac{S_T^{ac}}{T I_0} = \Delta\lambda\left(\frac{T'}{T} + \frac{I_0'}{I_0}\right). \tag{12}$$

With the sample-out setting, the derivative signal of the background is

$$S^{ac}_b \approx \Delta\lambda I_0 \qquad (13)$$

or

$$\frac{S^{ac}_b}{I_0} = \Delta\lambda \frac{I'_0}{I_0} . \qquad (14)$$

The subscripts s and b of S^{ac} refer to the sample and background, respectively.

The difference of S^{ac}_s/I and S^{ac}_b/I_0 will give the derivative of the transmitted intensity solely by the sample in principle. But in practice we encounter some difficulties; defocusing of the light beam at sample-in setting by the sample, for example. This defocusing effect by the sample, in conjunction with the nonuniformity of the active area of the photodetector surface, obscures the zero crossing of the derivative signal.

We overcome this difficulty by a number method. That is, with the measured quantities with sample-in and sample-out settings, we form the expression

$$\phi(E) = \alpha \frac{1}{I_0(E)} \frac{dI_0(E)}{dE} - \beta \frac{1}{I(E)} \frac{dI(E)}{dE} , \qquad (15)$$

where α and β are multiplicative constants independent of energy. Here we note that the first term in Eq. (15) is solely due to the background, while the second term is due to the sample in addition to the background.

To convert Eq. (15) into the form of Eq. (10), we write Eq. (15) as

$$\phi(x,E) = \alpha \left[\frac{1}{I_0(E)} \frac{dI_0(E)}{dE} - \frac{\beta}{\alpha} \times \frac{1}{I(E)} \frac{dI(E)}{dE} \right] \qquad (16)$$

and determine the ratio of proportionality constants $\gamma = \alpha/\beta$ in such a way that $\phi(x,E)$ and

$$\alpha \frac{1}{I_0(E)} \frac{dI_0(E)}{dE}$$

are not correlated for $\gamma = x$. For this particular value of γ,

$$\phi(E) = \alpha d \frac{dK}{dE} . \qquad (17)$$

This procedure is performed by a computer using a decorrelation algorithm.[15] Consider quantities a_i, b_i, and

$$c_i = a_i + \gamma b_i. \qquad (18)$$

Here, a_i is a quantity due to sample alone, b_i is a quantity due to background alone, and c_i is a quantity due to sample and background together. If we relate these quantities to our study, b_i and c_i are measured quantities, that is, signal with sample-out setting and signal with sample-in setting, respectively. And a_i is the quantity to be obtained by the decorrelation procedure. We set

$$d_i = c_i - t b_i = a_i + (\gamma - t) b_i. \qquad (19)$$

Now, we search for t, which minimizes the correlation function

$$f = \left\{ \frac{\sum_i [(d_i - \bar{d})(b_i - \bar{b})]^2}{\sum_i (d_i - \bar{d})^2 \sum_i (b_i - \bar{b})^2} \right\}^{1/2} \qquad (20)$$
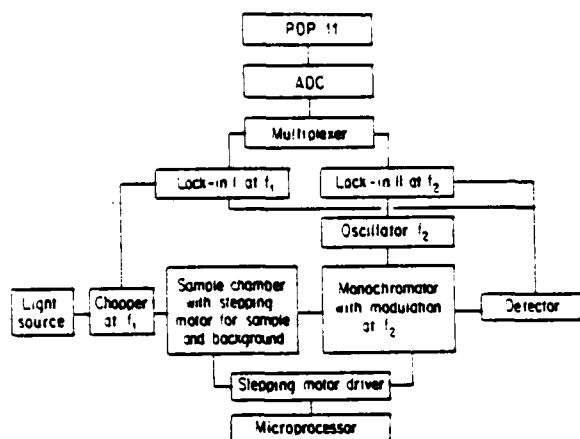
Fig. 1. Block diagram of the infrared wavelength modulated system.

when $\gamma = t$, $d_i = a_i$. Here, $d_i = a_i$ independent of b_i is assumed. If desired, Eq. (17) can be integrated numerically. In this study, the trapezoidal integration of Eq. (17) was performed.

D. Implementation and Operation of the System

1. Construction

The block diagram of the system is shown in Fig. 1. We have converted a Perkin-Elmer 301 spectrophotometer into a single beam system for improved SNR by using a sample-in and sample-out scheme. The sample-in and sample-out mechanism was accomplished with a linear translator assembly unit driven by a stepping motor. The wave-number drive was also performed by a stepping motor at preset intervals to scan the spectral regions of interest. Both stepping motors are driven by a dual-channel step motor drive unit. The intervals of stepping of sample-in and sample-out stepping motor and the wave-number driving motor as well as the data-collecting system as a whole are controlled by an on-line microprocessor (Motorola M6800 microprocessor) in a cycle for each set of data.

Sinusoidal sweeping of the light beam across the exit slit of the monochromator was accomplished by a vibrating mirror at 11 Hz. We have chosen this low frequency in spite of the $1/f$ noise in anticipation of the need of a slow detector such as a thermocouple, bolometer, or Golay cell, and most important to avoid the subharmonics of the background chopper channel, which is 39 Hz. The amplitude of modulation is adjustable through the output voltage of the scanner driver and can result in a wide range of modulation for $\Delta\lambda/\lambda \sim 10^{-2}$ to investigate the broad structures of solids in the infrared region of the spectrum.

As shown in the block diagram of the system in Fig. 1, two lock-in amplifiers are employed. Lock-in amplifier I measures the intensity of the chopped radiation at 39 Hz with sample-in and sample-out settings at a fixed wavelength. The lock-in amplifier II, which is fed with the 11-Hz reference frequency derived from the vibrating mirror, measures the derivative signal with

sample-in and sample-out settings. The sample-in and sample-out mechanism is a stepping motor coupled with a translation stage. With appropriate combinations of gratings, filters, and light sources, the system can be operated in the spectral region from ultraviolet to infrared (~12 μm). The main light sources in this study were a tungsten lamp in the visible and near infrared and a globar in the infrared. The detectors used were PbSnTe, PbS, and a silicon photodiode for appropriate spectral regions.

2. Operation

With the sample-in settings, two data points were taken; one from lock-in I, which is in the intensity of radiation transmitted by the sample, and the other from lock-in II, which is the derivative signal. The same set of data is taken with the sample-out setting yielding the equivalent for the background. Those two sets of data are fed into a multiplexer and then digitized by an ADC. The digitized result can be either punched on paper tape by a teletype or fed into the on-line computer (PDP 11/23) directly for numerical processing. By appropriate combinations of these sets of data, we can form a logarithmic derivative of intensity as a function of energy or direct transmission. A computer program was written to obtain the numerical values and graphs of derivative of the absorption coefficient, integrated result, and direct transmission as a function of energy.

All these data-taking processes are done in a sequence at one wavelength, and after a cycle the system moves to the next wavelength. This data-collecting cycle, which is controlled by a microprocessor (Motorola M6800), is operated in the following sequences. The block diagram of the data-taking cycle is shown in Fig. 2, which performs in the following cycle:

(1) The M6800 sends out pulses to the stepping motor driver which drives two stepping motors: one for the linear translator assembly unit and another one for wavelength drive.

(2) The stepping motor which is attached to the linear translator assembly unit takes the sample in or out of the path of the light beam.

(3) While the sample mount is translating, the wavelength drive is stepped by the second stepping motor.

(4) Then the system waits for a certain time before taking the first set of data. In this study, we have chosen the waiting time to be approximately three times the lock-in time constant.

(5) At the end of the waiting time, two data points are taken: one from the lock-in I, which is the intensity of the background radiation, and one from lock-in II, which is the derivative signal of the background radiation.

(6) The microprocessor sends out reverse pulses to the driver to step the stepping motor backward so the linear translator assembly unit will bring the sample mount to the sample-in position. This brings the sample in the path of the light beam.

(7) Waiting time starts.
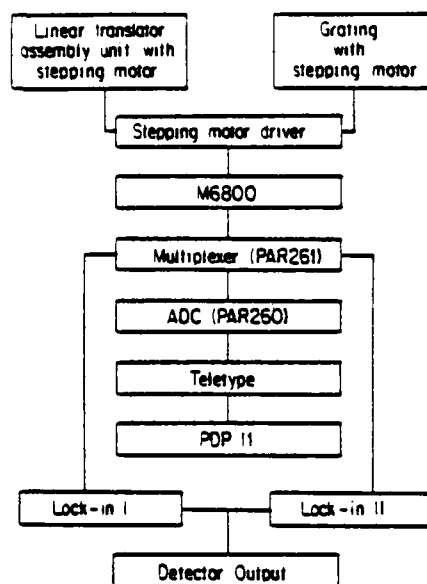
Fig. 2. Block diagram of control system for data-taking cycle.

(8) At the end of the waiting time, two similar data points are taken, except with the sample-in this time.

This completes one data-taking cycle at one wavelength. The interval of the linear translation of the sample-mount and the wavelength drive as well as the length of the waiting time can be adjusted by changing the appropriate program parameters fed to the microprocessor. The program of the microprocessor is taped on a cassette tape and played by a cassette player at the beginning of the run of the system.

III. Experimental Results and Discussions

A. Treatment of Data

Before a detailed discussion of the experimental results and the interpretation of the spectra of the individual substances measured, we shall present the method of presentation of data and the mode of analysis.

In the intrinsic spectral regions, values of the absorption coefficient were determined from transmission measurements. In the extrinsic spectral regions, that is, impurity dominating regions, the integrated derivative data were normalized to the laser calorimetry measurement at indicated discrete laser lines.[16] This representation of the data allows us to display the fine structure excursions in absorption above and below the calorimetric point. In a number of cases a second calorimetric point was measured at the other end of the spectrum. It was found that the absorption coefficient derived from this second measurement agreed with the integrated value obtained from wavelength modulation data.

To discriminate the effect of atmospheric absorption on a sample, we ran each sample in two different ambient conditions, one in atmospheric ambient, the other in dry nitrogen ambient. The latter was accomplished by flushing the whole system by dry nitrogen gas flowing

21. Ryznkova, E. M., Trapeznikova, I. I., Chelnokov, V. E., and Yakovenko, A. A., Sov. Phys. Semicond. 11, 628 (1977).

22. Braunstein, R., Kim, R. K., and Braunstein, M., Laser Induced Damage in Optical Materials: 1979, Boulder, CO, USA, 30-31 Oct. 1979 (Washington D. C., U.S.A.: NBS 1980), pp. 99-117.

23. Hrostowski, H. J., and Kaiser, R. K., Phys. Rev. 107, 966 (1957).

As shown in all of the figures, at low oxygen content the infrared absorption mechanism in the 9 μm -region is complicated. This indicates the existence of oxygen in different energy states. This is understandable if we keep in mind the fact that, although oxygen is interstitial in the sense that it does not occupy a lattice site, it can occupy slightly different positions of varying energy.[23] During growth, oxygen atoms are randomly trapped in the silicon lattice, and at room temperature thermal agitation permits the oxygen atom to occupy a number of slightly different configurations of varying energy.

In Fig. 16 the absorption is stronger than the previous samples; it appears that if the oxygen content exceeds a certain value ~ 10^{16} atoms/cm^3, the absorption mechanism at 1108 cm^{-1} dominates. This band at 1108 cm^{-1} we attribute to the form of freely dissolved Si$_2$O "quasimolecule." In the above figure we can also note a band at 1048 cm^{-1} (9.5 μm) in both seed and tail-ends; this band might be related to still another complex which can be formed if the oxygen content reaches a certain value (~ 10^{16} atoms/cm^3).

In concluding, we summarize our results:

1) Even though the use of float-zone silicon as an oxygen free reference is a common practice, our results show the float-zone silicon also contains oxygen.

2) The state of oxygen in silicon is in the form of complexes.

3) If the oxygen concentration exceeds a certain value, the oxygen in Si$_2$O "quasimolecule" starts dominating the infrared absorption mechanism at about 9 μm.

4) Different parts of the same ingot of float-zone grown silicon have different oxygen content which is responsible for infrared absorption around 9 μm.

5) Our wavelength modulation system can detect the variation in the absorption coefficient of ~ 10^{-6} cm^{-1}. If we approximate the scattering cross section of oxygen responsible for absorption at 9 μm to be ~ 10^{-18} cm^2, we have the capability of detecting oxygen at levels of ~ 10^{12} atoms/cm^3!

Summary

In this paper we have shown that infrared wavelength modulation is a sensitive and versatile spectroscopic characterization technique for a variety of semiconductor technology problems. In particular the results of a study of deep levels in semi-insulating GaAs, surface layers in Si, GaAs, and HgCdTe, oxygen complexes in floating-zone Si, as well as the determination of strain in ion implanted layers were presented.

Acknowledgments

References

1. Czanderna, A. W., editor, *Methods of Surface Analysis, Vol. 1*, Elsevier Scientific Publishing Co., Amsterdam-Oxford-New York, 1975.
2. Lang, D. V., in *Thermally Stimulated Relaxation in Solids*, edited by P. Bräunlick, Springer-Verlag, Berlin-Heidelberg, New York, 1979.
3. Willardson, R. K., and Beer, A. C., editors, *Semiconductors and Semimetals, Vol. 9*, Academic Press, New York, 1977.
4. Lagowski, J., Walukiewicz, W., Slusarczuk, M. M. G., and Gatos, H. C., J. Appl. Phys. 50, 5059 (1979).
5. Kamieniecki, E., Lagowski, J., and Gatos, H. C., J. Appl. Phys. 51, 1863 (1980).
6. T. Nishino and Y. Hamakava, Phys. Stat. Sol. (b) 50, 345 (1972).
7. Eetemadi, S. M., and Braunstein, R., to be published.
8. Kim, R. K., and Braunstein, R., Appl. Opt. 23, 1166 (1984).
9. Braunstein, R., Kim, R. K., Matthews, D., and Braunstein, M., Physica 117B and 118B (1983).
10. Clerjaud, B., Hennel, A. M., and Martinez, G., Solid State Comm. 33, 983 (1980).
11. Martin, G., Appl. Phys. Lett. 39, 747 (1981).
12. Barnowski, J. M., Allen, J. W., and Pearson, G. L., Phys. Rev. 160, 627 (1967).
13. R. W. Haisty, Appl. Phys. Lett. 7, 208 (1965).
14. Look, D. C., Chaudhuri, S., and Sizelove, J. R., Appl. Phys. Lett. 42, (a) (1983).
15. Eetemadi, S. M., and Braunstein, R., to be published.
16. Patel, J. R., in *Semiconductor Silicon*, edited by H. R. Huff, R. J. Kriegler, and Y. Takeishi, Electrochemical Society, Princeton, 1981, p. 189.
17. Kaiser, W., Phys. Rev. 105, 1751 (1957).
18. Kaiser, W., Frisch, H. L., and Reiss, H., Phys. Rev. 112, 1546 (1958).
19. Kaiser, W., Keck, P. H., and Lange, C. F., Phys. Rev. 101, 1264 (1956).
20. Malyshev, V. A., Sov. Phys. Semicond. 8, 92 (1974).

Difference wavelength modulation spectroscopy of oxygen in floating-zone silicon

The use of infrared spectroscopy to identify relative amounts of oxygen in silicon is routine.[16] Usually the concentration of dissolved oxygen is deduced from the infrared absorption at about 9 μm (1100 cm^{-1}). The relationship between the intensity of this band and the dissolved oxygen has been demonstrated reliably in experiments by comparing the absorption in samples containing the oxygen isotopes O[16] and O[18].[17,18]

It has been shown that this band is associated with interstitial oxygen and is due to an infrared-active antisymmetric type of vibration of the Si$_2$O "molecule."[19] This model has been questioned and it has been suggested[20] that the oxygen in silicon is in a bound state, forming fine second-phase SiO$_2$ particles and the absorption at 9 μm is due to this oxygen. Attempts have been made to explain the changes of optical and electrical properties of silicon after various heat treatments by the phase transitions of these second-phase particles of SiO$_2$.[20] Other workers showed that absorption spectra of silicon samples around 9 μm with relatively low oxygen concentration have a complex structure. They observed a peak at 1128 cm^{-1}, and another peak at 1135 cm^{-1}, and they attributed these peaks to dissolved oxygen in the lattice and in the second-phase SiO$_2$ particles, respectively. They suggested that other electrically inactive states of oxygen in silicon might exist, and there might be a threshold oxygen concentration which is necessary for any significant formation of SiO$_4$ complexes to occur.

Nearly all previous optical studies of oxygen in silicon were performed on silicon samples grown by the Czochralski method, which presumably have oxygen contents in the range of 10[17]-10[18] atoms/cm^3. Practically no information is available on the state of oxygen in float-zone grown silicon. The reason for this, we believe, is that float-zone grown silicon has low oxygen content (< 10[16] atoms/cm^3), and the detection limit of conventional differential absorption methods is ~ 1 × 10^{16} atoms/cm^3. Oxygen concentration in the range of ~ 10[16] atoms/cm^3 contributes ~ 0.5 cm^{-1} to the absorption coefficient at about 9 μm. In addition, the intrinsic lattice band of silicon contributes ~ 0.8 cm^{-1} to the absorption coefficient at about 9 μm. This fact clearly indicates the difficulty of the study of the samples with low oxygen content.

But we believe that the mechanism of oxygen complex formation and thermal donors can be understood better if we can understand how the oxygen complex formation is initiated for low oxygen content. In this spirit, we initiated the study of oxygen in silicon with low oxygen content (< 10[13] atoms/cm^3) using an infrared difference wavelength modulation technique. Several float-zone grown silicon samples were studied, all with oxygen content below the detection limit of conventional methods ~ 1 × 10^{16} atoms/cm^3. Measurements were made on different sections of the same ingot, that is, the seed-end and the tail-end of the dimensions ~ 2 cm in diameter and 1 cm in thickness.

Our infrared wavelength modulation technique[22] was employed to study the 9 μm absorption band of these samples at room temperature. To eliminate the absorption due to the intrinsic lattice vibration of silicon and surface effects, we used a sample-in and sample-out procedure, which enables a comparison of the derivative of the absorption of a sample with a reference sample. With this procedure, the derivative spectrum of the difference of the absorption between a sample and the reference crystal is obtained. A conventional spectrophotometer run of the reference crystal, which is a seed-end of another float-zone silicon, showed just a trace of oxygen at 9 μm; that is, at 9 μm the oxygen contributes approximately 0.15 cm^{-1} to the absorption coefficient. From this we can approximate the oxygen content of reference crystal to be ~ 10[13] atoms/cm^3. The detector used in this study was PbSnTe at liquid nitrogen temperature.

The integrated results of these derivative spectra of the difference for a series of samples are shown in Figs. 13, 14, 15, and 16. The figures show the relative variations of absorption of samples with respect to the reference crystal. Therefore, the positive side of the absorption of the sample in the figures means more absorption and negative side of the absorption means less absorption than the reference crystal at the appropriate wavenumbers. In all the figures, the upper drawing is the experimental result of the seed-end and the lower one is the result of the tail-end of the same ingot with respect to the reference crystal with ~ 10[13] oxygen atoms/cm^3.

In this study, it should be noted that since we are taking the derivative of the difference of absorption at appropriate frequencies between sample and the reference crystal, the shift or the different width of the bands of the crystals represent changes relative to the reference crystal. Consequently, it is interesting to note that because of the sensitivity of the difference derivative technique (Δk ~ 10^{-3} cm^{-1}), the subtle spectra changes introduced by various heat treatments can be studied by comparing it with the reference even though the change of spectral distribution caused by heat treatment on the sample by itself is difficult to determine!

In Fig. 13, we note that a band emerges at 1123 cm^{-1} (8.9 μm) in the tail-end (lower figure). It is not clear exactly what complex is responsible for this band. We can clearly see a shoulder at 1108 cm^{-1} (9 μm) in the tail-end (lower figure) which appears to be Si$_2$O. The results on two different ingots are shown in Figs. 14 and 15 and we can see about the same level of absorption due to Si$_2$O at 1108 cm^{-1} in both parts of the same ingot. However, we can immediately note that the spectral distribution changes even within the same ingot depending on which part of the ingot the sample is taken from. This is not unreasonable if we consider the fact that the crystals are float-zone samples and the sensitivity of our system.

4

Surface absorption

The sensitivity of our system enables us to study surface absorption. Although the primary aim of this report is to demonstrate the power of infrared wavelength modulation spectroscopy as a characterization technique for bulk semiconductors, we shall show some examples of measurements on alkali halides[a] since recently a great deal of material preparation studies have taken place to improve these materials for light guiding applications. First we shall discuss an example of measurements on KBr which reveal both surface and bulk absorption. These clean alkali halides are potentially useful insulators in MIS structures. Subsequently we describe some examples of surface absorption on semiconductor.

The absorption spectra of a typical KBr crystal obtained with a conventional double-beam spectrometer are shown in Fig. 10. This crystal was grown from material which was selectively ion filtered and reactive gas treated for purification prior to crystal growth. As can be seen, virtually no absorption structure can be seen above the noise level of the instrument, confirming the relative purity of the sample.

Figure 11a shows the integrated derivative spectra of the above KBr sample taken with the sample in the laboratory atmosphere. The richness of the observed spectra should be noted in contrast to the featureless spectral shown in Fig. 10 for the same sample. The right-hand ordinate in Fig. 11 indicates the absorption coefficient at 3.8 μm as inferred from a laser calorimeter measurement with a DF laser; the left-hand ordinate indicates the relative change of absorption obtained by integrating the wavelength modulation derivative data. The depth of the modulation of the monochromator frequency used to obtain these data was 10 cm^{-1}. The zero of the ΔK cm^{-1} wavelength modulation result is registered with the absorption calibration point of 0.4 $\times$ 10^{-5} cm^{-1} obtained by laser calorimetry. Therefore, to obtain the actual absorption coefficient at a particular wavelength, one merely adds or subtracts the appropriate ΔK value at a given frequency to the 0.4 $\times$ 10^{-5} cm^{-1} value. This type of representation of the data allows us to display the fine structure excursions in absorption above and below the calorimetric point. Successive runs on this sample reveal that the structure shown in Fig. 11 is reproducible within a mean deviation of $\Delta K \sim$ 10^{-6} cm^{-1}. Consequently, the noise level is at the level of the width of the drafting lines. The data points were taken at 5 cm^{-1} frequency intervals. The sample thickness was 4 cm.

When this sample is placed in a dry N$_2$ atmosphere, a continuous change in the spectral distribution of the absorption is observed until the spectra stabilize after the sample has been in this gaseous ambient for an hour. The dominant features of the spectra of this sample when in the laboratory atmosphere displayed in Fig. 11a are: a band near 2.5 μm with the fine structure, multiple structure between 3 to 4 μm with fine structure, a sharp strong band at 4.2 μm, a band at 5 μm, and multiple structures between 6 to 12 μm. The data shown in Fig. 11b are for this same sample in a dry N$_2$ atmosphere. Although there is a distinct change in the spectra in Fig. 11b compared to Fig. 11a, some of the original prominent features can still be recognized. The sharp peak at 4.2 μm is greatly reduced, and the band at 5 μm is gone, while some of the original structure between 5.8 and 12.0 μm is still present; however, a valley develops around 9 μm. Analysis of the observed spectra has allowed us for the first time to identify volume and surface impurities in highly pure KBr and other alkali halides.[a]

Using our infrared wavelength modulation system, we have been able to study the growth of nature oxides on freshly etched silicon surfaces. We can easily detect the 9 micron SiO absorption band in a 10 Å layer of silicon with a signal-to-noise ratio of 100/1, indicating that we have the capabilities of studying the growth of a fraction of a monolayer of adsorbed species. An example of this band is shown in Fig. 12 immediately after the silicon surface was etched with HF. Studies of oxides on GaAs and HgCdTe have enabled us to study the formation of OH in oxides on GaAs as well as the presence of TeO$_2$ on HgCdTe due to various surface treatments.

Determination of strain in layered semiconductors

In the growth of semiconductor layers by various epitaxial techniques such as M.B.E., L.P.E., and C.V.D., and the doping of layers by ion implantation and other techniques, an important technological problem is the assessment of the homogeneity of doping, alloy composition, and strain in the layers. We have used our wavelength techniques to determine shifts in various critical points as a function of doping and strain in several semiconductors.

One of the major fabrication processes used in the fabricate of n-type channel FET's on semiconducting GaAs is the utilization of ion implantation. The assessment of defects subsequent to implantation and annealing is of prime importance, especially so for shallow implanted layers - 1000 Å. We have observed the effects of ion implantation by the nondestructive methods of wavelength modulation. Local strain was observed by measuring the shift of the imaginary part of the dielectric function of GaAs in the neighborhood of the E_1 and $E_1 + \Delta$ critical point. Implants of Be, Sb, S, In, and double implanted Sb and Be were studied; the implanting fluxes were of the order of 10^{13}/cm^2, compared to ion unimplanted GaAs, positive and negative shifts of the energy of the critical point were observed, indicating that we are able to distinguish contraction or expansion of the lattice.

In addition, we found that the intensity of ϵ_2 the imaginary part of the dielectric function at the $E_1 + \Delta$ critical point decreased as a function of n-type doping. These results can be interpreted in terms of screening of the hyperbolic exciton associated with this critical point.

shown in Figs. 1 and 2, lock-in amplifier I measures the intensity of the chopped radiation at frequency f_1 at a fixed wavelength with the sample-in and the sample-out while lock-in amplifer II, at frequency f_2, measures the derivative signal also with the sample-in and sample-out. Appropriate light sources, filters and detectors are employed for a given spectral region. At the end of a data taking cycle the energy derivative of the absorption as well as its integral are calculated by a PDP 11/23 computer and the results plotted. The constant of integration is supplied by the direct measurement of the absorption in a convenient spectral region.

Derivative absorption spectroscopy of GaAs:Cr

The above infrared wavelength modulated system was employed in a detailed study of the derivative absorption of GaAs:Cr.[9] Figures 3 and 4 show the integrated derivative data of semi-insulating GaAs:Cr at 300 K with various degrees of shallow donor-acceptor compensations. All the samples were semi-insulating and contained ~ $10^{16}/cm^3$ Cr. The samples in Fig. 3 were highly compensated while those in Fig. 4 were slightly more p- or n-type, respectively. The extensive fine structures with variation in absorption coefficient of $\Delta K \sim 10^{-1}$ to 10^{-2} cm^{-1} out of a relatively smooth background absorption of 1-2 cm^{-1} should be noted. Previously reported conventional optical absorption measurements revealed a few plateau-like structures, indicating that they had only observed the envelope of the absorption in this region.[10] The detailed extensive fine structure observed can be correlated with an energy level scheme of $(Cr^{3+}-Cr^{2+})$ ions in GaAs shown in Fig. 5 and interpreted in terms of transitions from Cr-ions to the valence and conduction bands and excited states. The complexity of the spectra is due to coupling of Cr to donor or acceptor complexes, and the subtle changes are due to the degree of compensation and consequent position of the Fermi level in these four semi-insulating samples. A complete analysis indicates that a comparable number of Cr atoms are at tetragonal and trigonal sites and can explain the rapid diffusion of Cr in GaAs.[9]

Semi-insulating LEC GaAs

An extensive study was made on semi-insulating GaAs grown by the liquid encapsulated Czochralski technique (LEC). These studies were performed in the spectral region 0.3-1.5 eV and the temperature range 80-300 K. In these samples, we observed a number of structures due to EL2, other defects, and impurities. Several fine structures were observed which can be interpreted in terms of intra-center transitions between levels of impurities split by the crystal field; the data were obtained with our derivative spectrometer and the integrated results are discussed below.

Figure 6 shows the absorption of semi-insulating LEC GaAs at 300 K. The threshold at 1.4 eV is the onset of the direct band-to-band transition, while the threshold at 1.0 eV is the onset of the EL2 defect. The small structure between 0.3 and 0.5 eV and threshold at 0.5 eV should be noted. The sensitivity of our measurement allows us to give credence to changes in absorption coefficient ~ 10^{-3} cm^{-1}. As the temperature is reduced to 160 K, we note the emergence of structure shown in Fig. 7 on a vastly expanded scale. When the sample temperature is reduced to 80 K, the structure with a threshold at 1.0 eV at room temperature abruptly quenches when the sample is illuminated with band gap light; see Fig. 8. When the sample temperature is increased and the measurement performed without band gap light present, the EL2 threshold returns. The metastability of this level and its possible identification as an anti-site defect of GaAs have been previously discussed.[11]

Figure 9 shows the structure observed in Fig. 8 on a vastly expanded scale possibly by the precision of our measurement. Note should be taken of the sharp structure at 0.36 - 0.38 eV, a broad peak at 0.4 eV, structure between 0.42 - 0.5 eV, and the threshold at 0.5 eV. Similar structures are observed in the same spectral region for other undoped LEC GaAs samples, but with changes in the relative intensities of the various structures. The structures at 0.36 - 0.38 eV and the threshold at 0.5 eV seem to be correlated, indicating they are due to the same level. The structures at 0.36 - 0.38 eV are very similar to that which is observed for deliberately Fe doped in a number of semiconductors,[12] and so can be identified as an intra-center transition of Fe^{2+} in GaAs. (Estimating the oscillator strength for Fe, our samples contain ~ 10^{16} Fe/cm^3.) The threshold at 0.5 eV whose intensity scales with this intra-center transition corresponds to the transition from the valence band to the Fe levels. This is further substantiated by the fact that the position of this threshold moves with a temperature coefficient similar to the GaAs band gap; a similar observation has been made from Hall measurements.[13] The resonance-like band around 0.4 eV with its possible fine structure seems to be an intra-center transition. Photo-induced-transient spectroscopy (P.I.T.S.) electrical measurements made on the same samples as the optical measurements reveal levels at 0.4 and 0.8 eV, the latter being due to EL2. A level at 0.4 eV has been reported in semi-insulating GaAs by a number of measurements[14] which was originally ascribed to oxygen in O-doped GaAs. Recently a combination of temperature-dependent Hall-effect measurements, spark-source mass spectroscopy, and secondary ion mass spectroscopy measurements have indicated that neither oxygen nor any other impurity can account for the 0.4 eV level and consequently it is probably due to a pure defect.

Thermal annealing and quenching experiments on a range of LEC GaAs samples revealed that some of these levels are probably due to structure imperfections.[15] The subtle changes in these levels could readily be followed by our wavelength modulation technique.

2

Deep level derivative spectroscopy of semiconductors by wavelength modulation techniques

R. Braunstein, S. M. Eetemadi, and R. K. Kim

Department of Physics, University of California,
Los Angeles, California 90024

Abstract

An infrared wavelength modulated absorption spectrometer capable of measuring changes in the absorption coefficient of levels of 10^{-3} cm^{-1} in the spectral range 0.2-20 microns was employed to study bulk and surface absorption in semiconductors. The results of the study of deep levels in semi-insulating GaAs, surface layers on Si, GaAs, and HgCdTe, oxygen complexes in floating-zone silicon, and determination of strain in ion implanted layers are presented.

Introduction

The utilization of semiconductors in devices for the amplification, detection, generation, and signal processing of high frequency electromagnetic radiation in very high density configurations requires an intimate knowledge of the impurities and structure imperfections which affect device performance. It has been a scientific and technological challenge to develop nondestructive techniques to detect such imperfections and to develop a conceptual framework for understanding their microscopic electronic structure. In fashioning high density arrays of semiconductor devices, it is essential to start with well characterized, homogeneous substrates to obtain near-identical properties of individual circuit elements. Aside from knowing how to select the initial "winning" substrate, subsequent device processing can introduce unknown impurities or defects which can degrade device performance and consequently it would be desirable to have a technique which is capable of following the evaluation of a semiconductor's characteristics from its initial growth through the device processing phases.

A powerful array of electron spectroscopies[1] exist for detecting chemical impurities but these require an ultra-high-vacuum environment and are not readily adaptable to analytical procedures which can ultimately be used on the production line. There exists an immense variety of junction techniques employing some form of deep level transient spectroscopy (DLTS) to study deep level defects whose variation depends on which junction parameter is finally measured.[2] However, apart from technical details, the end result one desires to extract from these measurements are the optical and thermal emission cross sections for electrons and holes, as well as the concentration of levels. In general excited state, thresholds for transitions between levels, and intra-center transitions between levels are not easily determined using the above techniques. The presence of high electric fields at the junctions adds complications to the interpretation of the data. In addition, thermal processing of the test structures can introduce further defects. Direct optical absorption measurements yield the quantities of interest, but at the level of sensitivity of DLTS techniques, on the order of $10^{12}-10^{14}$/cm^3, it is not possible to employ conventional techniques. Consequently consideration has been given to optical modulation spectroscopies for detecting small structures out of a broad background.[3] A family of derivative spectroscopy techniques has been developed where the modulation parameter may be the electric field, stress temperature, or wavelength of the probing light beam. Recently, wavelength modulation photoresponse spectroscopies have evolved to measure photo-induced changes in voltage,[4] capacitance,[5] and current[6] from which the absorption coefficients are inferred. An examination of wavelength modulation photoresponse spectroscopies in contrast to direct wavelength modulation absorption/reflection indicates that the latter is the most suitable technique for studying deep levels since it yields unambiguous line shapes.[7]

We have developed an infrared wavelength modulated system capable of measuring changes in absorption coefficients at levels of 10^{-3} cm^{-1} out of a broad background in the spectral range 0.2-20 microns.[8] Since it is not necessary to make electrical contact to the sample one obviates possible contamination by thermal processing necessary for DLTS or photoresponse techniques. In addition, being an optical technique there are no restrictions on the resistivity of the sample. In this report we will discuss the use of this system in a number of studies concerned with characterization of semiconductors.

Infrared wavelength modulation system

The theory of operation of the infrared wavelength modulation system, its construction, and implementation has been previously reported.[9] For the purposes of the present discussion we shall indicate some general aspects of its operation. In one form of this system we have employed a Perkin-Elmer 301 spectrometer in a single beam sample-in and sample-out scheme shown in Fig. 1. The sample-in, sample-out and spectrometer wave-number positions are preset at intervals by stepping motors, these and the data collecting system are controlled by an on-line microprocessor (Motorola M6800) or a CAMAC based PDP 11/23 computer; a block diagram of the control system is shown in Fig. 2. The modulation of the wavelength is accomplished by the sinusoidal sweeping the output of the light beam across the exit slit of the monochromator by a vibrating mirror; this method of modulation is equally good for any wavelength and the amplitude can be continuously varied up to $\Delta\lambda/\lambda - 10^{-2}$. The system employes two lock-in amplifiers. As

15. M. Burd, R. Stearns, and R. Braunstein, Phys. Status Solidi (B) 117, 101 (1983).
16. The laser calorimetric measurements were performed by Robert Curran of the Hughes Laboratories.
17. M. Flannery and M. Sparks, in *Laser Damage in Optical Materials, 1977*, A. J. Glass and A. J. Guenther, Eds., NBS Spec. Publ. 509 (U.S. GPO, Washington, D.C., 1977), p. 5.
18. T. F. Deutsch, J. Electron. Mater. 4, 663 (1975).
19. M. Hass, J. A. Harrington, D. A. Gregory, and J. W. Davisson, Appl. Phys. Lett. 28, 610 (1976).
20. P. Handler and D. E. Aspnes, Phys. Rev. Lett. 17, 1095 (1966).
21. M. L. Hair, *Infrared Spectroscopy in Surface Chemistry* (Marcel Dekker, New York, 1967).
22. J. R. Howe and J. A. Harrington, J. Appl. Phys. 47, 4926 (1976).
23. A. Hordvik, Appl. Opt. 16, 2827 (1977).
24. Y. Kozirovski and M. Folman, Trans. Faraday Soc. 62, 1431 (1966).
25. J. T. Gourly and W. A. Runciman, J. Phys. C 6, 583 (1973).
26. D. W. Pohl, in *Optical Properties of Highly Transparent Solids*, S. S. Mitra and B. Bendow, Eds. (Plenum, New York, 1975).
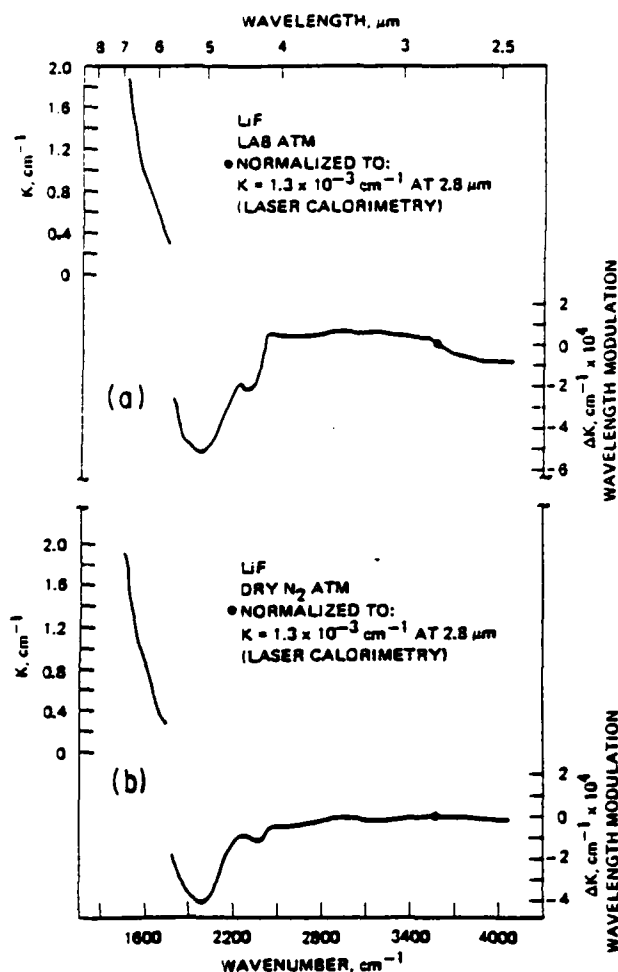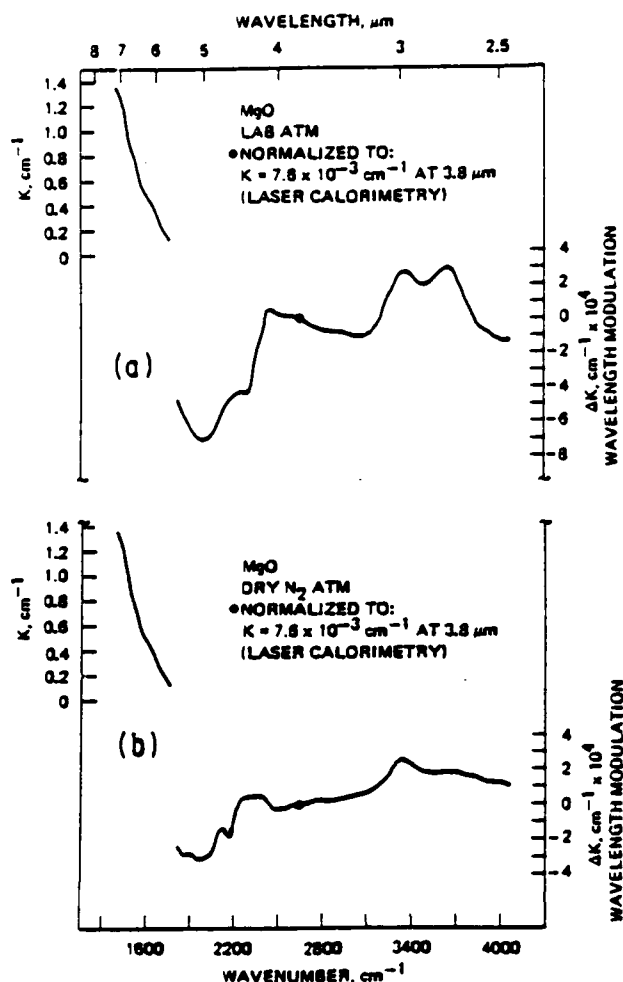
Fig. 14. Wavelength modulation absorption spectra of LiF; K is the absorption coefficient in cm^{-1}: (a) in the laboratory atmosphere; (b) in a dry N_2 atmosphere.
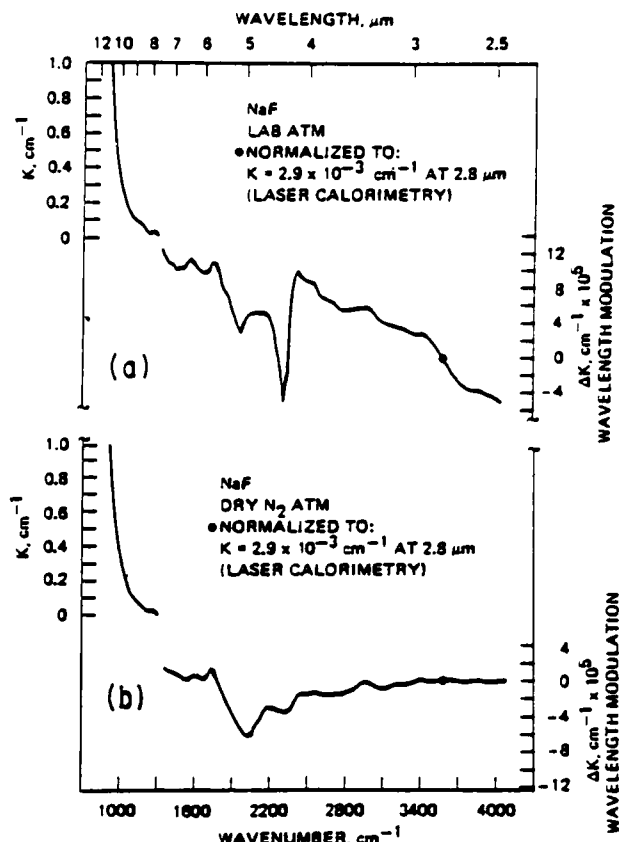

Fig. 15. Wavelength modulation absorption spectra of KCl; K is the absorption coefficient in cm^{-1}: (a) in the laboratory atmosphere; (b) in a dry N_2 atmosphere.

the visible to the further infrared using appropriate detectors. For the first time the continuous spectral distribution of extrinsic absorption at levels of 10^{-8} cm^{-1} were measured on KCl, KBr, CaF_2, LiF, NaCl, NaF, LaF_3, BaF_2, MgF_2, SrF_2, and MgO enabling an identification of physisorption, volume, and surface chemisorption of impurities. The use of the infrared wavelength modulated spectroscopy of this work can be of great utility in monitoring crystal growth and surface preparation for optical materials for high-power laser and lightguiding systems requiring extremely low absorption levels. The system is capable of detecting a hundredth of a monolayer of surface species on a single crystal surface and so can play a role in catalysis studies.

References

1. B. Bendow, in *Solid State Physics, Vol. 33*, F. Seitz and D. Turnbull, Eds. (Academic, New York, 1978), p. 249.
2. T. F. Deutsch, J. Phys. Chem. Solids 34, 2091 (1973).
3. M. Sparks and L. J. Sham, Solid State Commun. 11, 1451 (1972).
4. C. J. Duthler, J. Appl. Phys. 45, 2668 (1974).
5. M. Hass, J. W. Davisson, P. H. Klein, and L. L. Boyer, J. Appl. Phys. 45, 3959 (1974).
6. J. A. Harrington, D. A. Gregory, and W. F. Otto, Jr., Appl. Opt. 15, 1953 (1976).
7. M. Cardona, *Modulation Spectroscopy* (Academic, New York, 1969).
8. B. O. Seraphin and N. Bottka, Phys. Rev. 145, 628 (1966).
9. G. W. Gobeli and E. O. Kane, Phys. Rev. Lett. 15, 142 (1965).
10. B. Batz, Solid State Commun. 4, 241 (1966).
11. E. Y. Wang, W. A. Albers, and C. E. Bleil, in *Proceedings, II-VI Semiconducting Compounds, 1967 Conference*, D. G. Thomas, Ed. (Benjamin, New York, 1967), p. 136.
12. M. Welkowsky and R. Braunstein, Rev. Sci. Instrum. 43, 399 (1972).
13. R. Stearns, J. Steele, and R. Braunstein, Rev. Sci. Instrum. 54, 984 (1983).
14. K. L. Shaklee, J. E. Rowe, and M. Cardona, Phys. Rev. 174, 828 (1968).
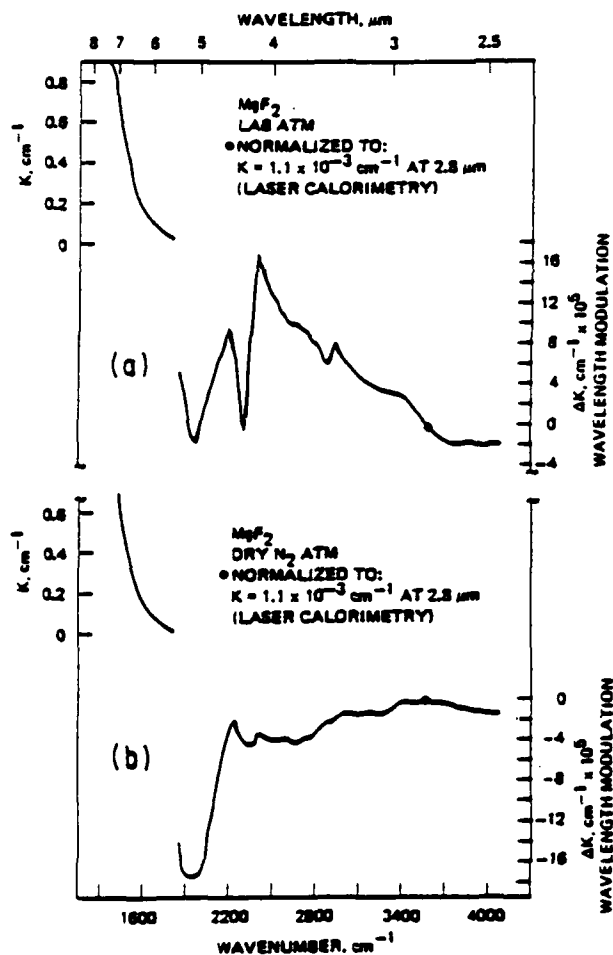
Fig. 12. Wavelength modulation absorption spectra of MgF$_2$; K is the absorption coefficient in cm^{-1}: (a) in the laboratory atmosphere; (b) in a dry N$_2$ atmosphere.

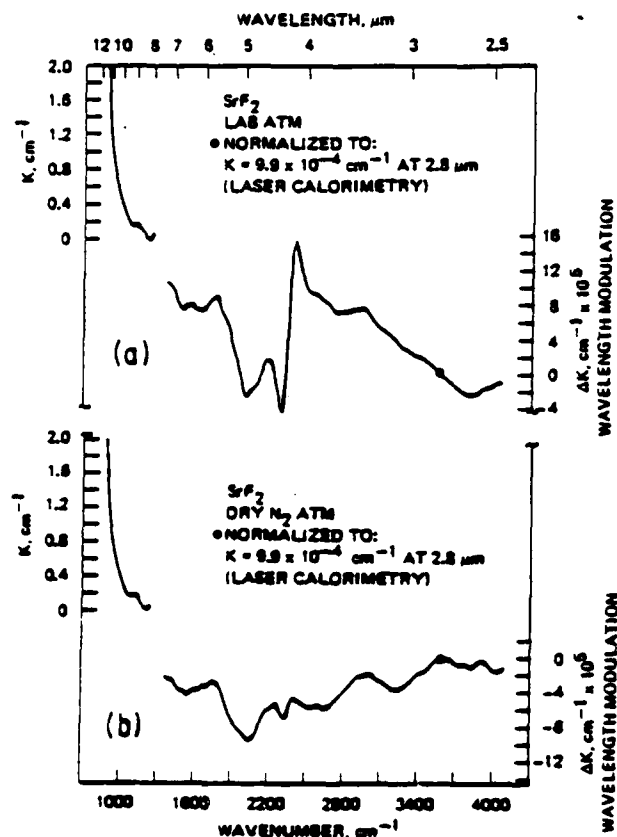Fig. 13. Wavelength modulation absorption spectra of LaF$_3$; K is the absorption coefficient in cm^{-1}: (a) in the laboratory atmosphere; (b) in a dry N$_2$ atmosphere.

possible overlay of C—H bands. The 6–9-μm bands seen in BaF$_2$ seem to be absent or are obscured by the strong water band in the 4–6-μm region. The MgF$_2$ data in dry N$_2$ atmosphere in Fig. 12(b) show a dramatic suppression of all the above bands. The remaining structure can be due to volume or chemisorbed species: the rise in the neighborhood of 2.8 and 4.8 μm can be due to OH$^-$ and liquid water, respectively.

9. Lanthanum Fluoride

The LaF$_3$ data in the laboratory atmosphere shown in Fig. 13(a) reveal the CO$_2$ band at 4.2 μm, the possible carbonates in the 6–8-μm region and OH$^-$ band near 2.8 μm. However, it should be noted that the bands in the 3–4-μm region due to C—H vibrations which have been prominent in BaF$_2$, SrF$_2$, MgF$_2$, CaF$_2$, and NaF seem to be absent or greatly suppressed. In the dry N$_2$ atmosphere data shown in Fig. 13(b), the peak near 2.8 μm possibly due to OH$^-$ is about the same height as shown in Fig. 13(a). The structure around 1200 cm^{-1} is due to chemisorbed surface contamination, tertiary alcohol, for example.

10. Lithium Fluoride

The LiF data in Fig. 14 show little structure indicating that LiF is the least surface active of all the substances studied. The absence of the 4.2-μm band, which was visible in all the substances studied, should be noted. The only band which seems to be noticeable is the 4.5-μm band in both ambients, and this can be due to water.

11. Potassium Chloride

If we examine the data of KCl shown in Fig. 15 in the light of the discussion of the identification of the bands seen in other alkali-halides (KBr, for example), similar features can be discerned. It is interesting to note that the adsorbed CO$_2$ band is markedly suppressed in KCl relative to KBr. The band around 1400 cm^{-1} can be due to the chemisorbed species of surface carbonates. The band around 1900 cm^{-1} can be due to some type of carbonyl.

IV. Summary

The infrared wavelength modulated spectrometer system that we have developed has the capabilities of detecting a change in absorption of a part in 10^6 out of a relatively smooth background in the spectral region from 2.5 to 12 μm. This sensitivity can be realized from

Fig. 10. Wavelength modulation absorption spectra of MgO; K is the absorption coefficient in cm^{-1}: (a) in the laboratory atmosphere; (b) in a dry N_2 atmosphere.
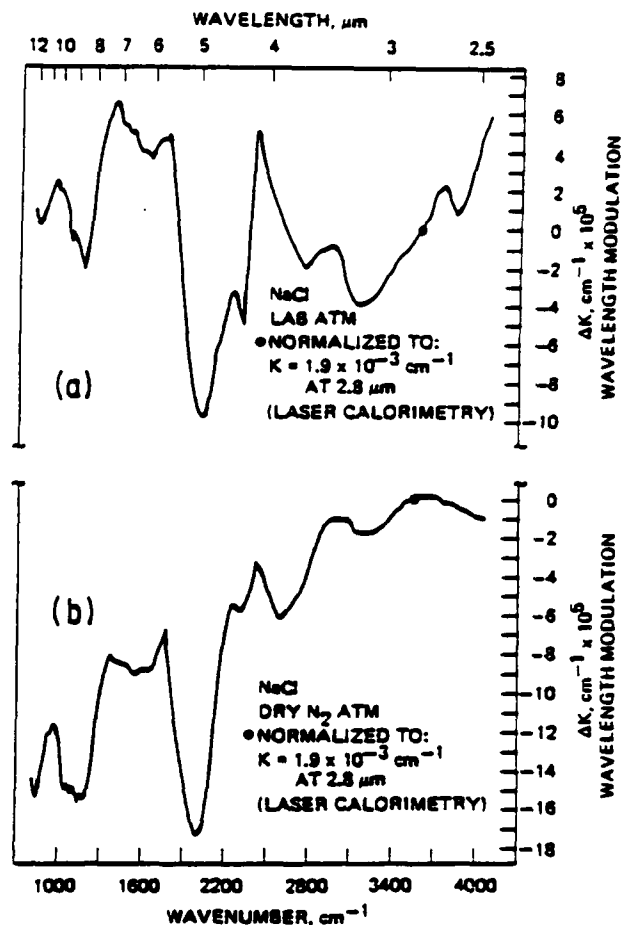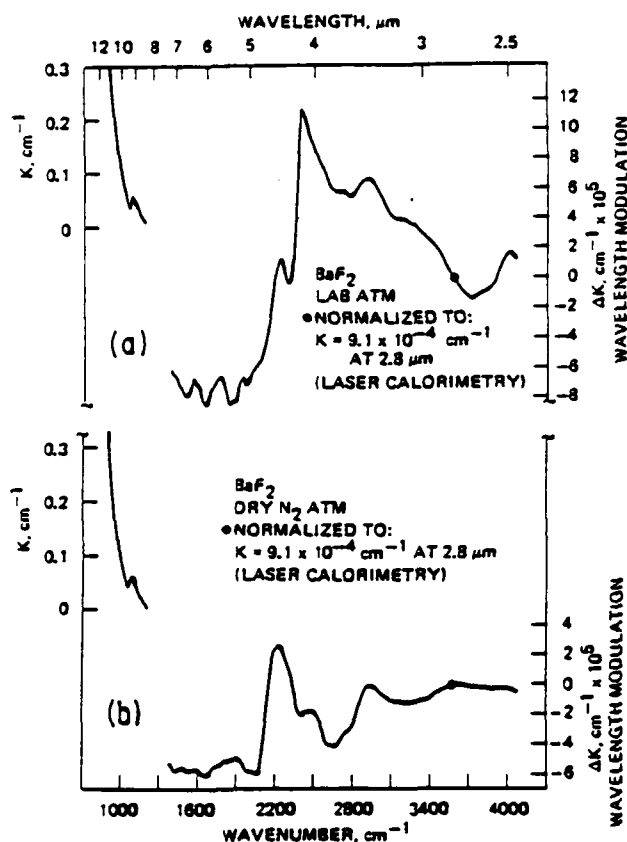

Fig. 11. Wavelength modulation absorption spectra of NaF; K is the absorption coefficient in cm^{-1}: (a) in the laboratory atmosphere; (b) in a dry N_2 atmosphere.

perturbed by the surface field, and the energy of interaction with the adsorbent is not high. The ease of removal of CO_2 on evacuation was observed.[24] It is intersting to note that the intensity of absorption due to CO_2 can be reduced by flushing alone as this study shows.

6. Magnesium Oxide

The data for MgO are shown in Fig. 10. The most prominent features seen in the laboratory ambient are a doublet in the 2.8–3.0-μm region (water and OH$^-$), some trace of a possible CO_2 at 4.2 μm, a structure in the 4–6-μm region (liquid water), and very slight structure in the 3–4-μm region (hydrocarbon). It is interesting to note that, of the doublet in the laboratory ambient, it is only the 3.0-μm band which survives dry N_2 flushings with a noticeable suppression of the 2.8-μm band. In a previous study[8] of MgO, impurity bands were observed between 3.8 and 2.7 μm. Our study clearly shows that the 3.0-μm band is due to bulk or chemisorbed OH$^-$, while the 2.8-μm band is due to physisorbed OH$^-$.

The region of intrinsic absorption in MgO shows some fluted structures in the multiphonon absorption tail. The rise ~1600 cm^{-1} agrees with the shoulder previously studied in the multiphonon spectra of MgO and was attributed to a four TO phonon process by suitably averaging over the dispersion curves.[25]

7. Sodium Fluoride

Comparison of the NaF data in Fig. 11 shows a large decrease of the band heights in the 2.5–4.0-μm region, but the familiar patterns shown in BaF$_2$, SrF$_2$, and CaF$_2$ are still apparent. The relationship between the adsorbed CO_2 and surface carbonates at 6.5 μm is clear. In both Figs. 11(a) and (b) we can observe a little break ~1100 cm^{-1}; this corresponds to the regime of three phonon spectrum.[26] But it can as well be due to surface contamination of chemisorbed species of some alcohol which is often used as surface polishing reagents—tertiary alcohol, for example.

8. Magnesium Fluoride

The MgF$_2$ laboratory atmosphere data shown in Fig. 12 reveal a cluster of bands similar to those observed in BaF$_2$. Again the ubiquitous CO_2 at 4.2 μm is evident. The 2.8-μm and 4–6-μm regions reveal the liquid water and OH$^-$ bands, while the 3–4-μm region reveals the
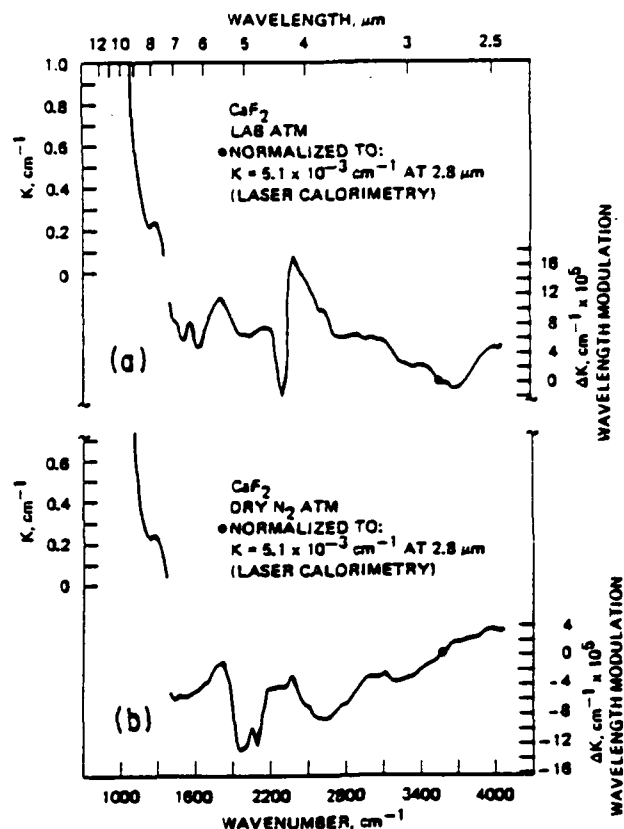
Fig. 8. Wavelength modulation absorption spectra of SrF_2; K is the absorption coefficient in cm^{-1}: (a) in the laboratory atmosphere; (b) in a dry N_2 atmosphere.

Carbonyl around 5.6 μm appears to be chemisorbed species. We note here that a band at 6.5 μm in Fig. 7(a) disappears in (b) completely. This band must be due to physisorbed carbonates. The relationship of physisorbed CO_2 and carbonates in two different ambients clearly indicates the active participation of adsorbed CO_2 in the formation of physisorbed carbonates. This is particularly clear in CaF_2, even though we can see this relationship in most of the samples studied. A structure around 8 μm is again due to the surface contamination. From Fig. 7(a) and (b) we can conclude that these are chemisorbed species. They can be surface-polishing chemical agents such as secondary and tertiary alcohol.

4. Strontium Fluoride

The SrF_2 sample used was from a press-forged RAP boule. In Fig. 8(a) we show data of SrF_2 in the laboratory atmosphere, where we can see all the main features of BaF_2 and CaF_2: hydrocarbon in the 3–4-μm region, CO_2 at 4.2 μm, liquid water around the 4.5-μm region, carbonyls around 5.6 μm, and various carbonates in the 6–7.5-μm region. In Fig. 8(a) we note the emergence of a structure around 2.8 μm. This can be due to OH^- in bulk. Judging from the dry N_2 gas atmosphere data in Fig. 8(b), C—H bonds in the 3–4 μm region must be due to chemisorbed species. In Fig. 8(b) we again see

that the disappearance of carbonate at 6.5 μm can be attributed to the suppression of physisorbed CO_2. A small structure at the tail of the intrinsic region is due to the chemisorbed species on the surface from the surface polishing chemicals.

5. Sodium Chloride

The NaCl data in both the laboratory and dry N_2 atmosphere, Figs. 9(a) and (b), respectively, show prominent structures. Although the spectral distribution is different in detail in two different ambients, we still can identify the structures: 10–11-μm ($>C=CH_2$ alcohols), 6–8-μm (carbonates), 5.6-μm (carbonyl), 4.8-μm (liquid water), the 4.2-μm (CO_2), 4-μm (C—H), and 2.8-μm (OH^-) bands. The prominence of the bands in both ambients is consistent with the greater surface activities which are expected for NaCl as compared to the other substances in this study. Comparison of Figs. 9(a) and (b) reveals the difference between chemisorbed species and physisorbed species.

A vibrational frequency of CO_2 adsorbed on NaCl shifts only slightly (4–5 cm^{-1}) with respect to the gas-phase frequency. The molecule is only weakly
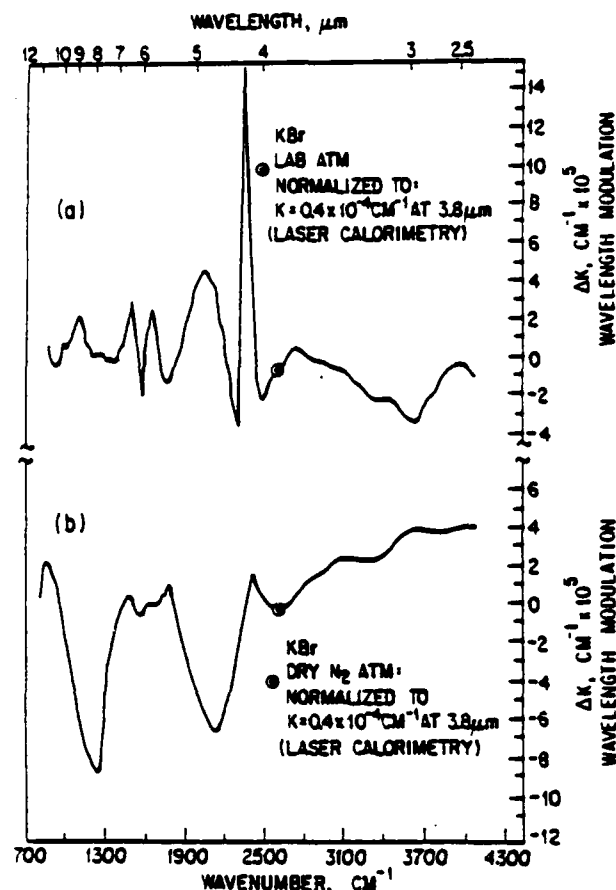
Fig. 6. Wavelength modulation absorption spectra of BaF_2; K is the absorption coefficient in cm^{-1}: (a) in the laboratory atmosphere; (b) in a dry N_2 atmosphere.

Fig. 7. Wavelength modulation absorption spectra of CaF_2; K is the absorption coefficient in cm^{-1}: (a) in the laboratory atmosphere; (b) in a dry N_2 atmosphere.

at 10.6 μm is expected to be 2×10^{-7} cm^{-1}, but our results show that, even at this region, the main mechanisms of absorption are dominated by impurities, that is, $K \sim 10^{-4}$ cm^{-1}, therefore, masking intrinsic multiphonon contribution to the absorption.

2. Barium Fluoride

By similar analysis with KBr, we can readily identify several main features of BaF_2 in Fig. 6(a). A prominent band at 4.2 μm can be associated with the physisorption of atmospheric CO_2. The bands in the 4–6-μm region can be due to atmospheric water, while the bands in the 3–4-μm region can be assigned to an overlap of hydrocarbon bands. Internal reflection spectrum of an ethylene-glycol-polished BaF_2 plate and a water-polished BaF_2 plate showed the absorption structure at 2915 cm^{-1} (3.43 μm), and it was attributed to C—H stretching absorption from residual organic material used in cutting or preparing the plates.[18] The bands in the 6–8-μm region are associated with carbonates. The fact that the bands in the 3–4-μm and 4–6-μm regions are largely due to physisorbed species is confirmed by the decrease in absorption in the dry N_2 atmosphere data shown in Fig. 6(b).

The region between 6 and 8 μm in BaF_2 shows considerable structures whose magnitudes vary only slightly with dry N_2 flushings. These structures can be

associated with the chemisorbed carbonates. The small structure at 5.6 μm can be associated with chemisorbed carbonyl. Photoacoustic measurements on BaF_2 and SrF_2 using a CO laser that was tunable to discrete lines in the 6–8-μm region have revealed a steplike structure in the surface adsorption,[23] while our results show distinct bands. A structure around 1100 cm^{-1} can be due to surface contaminations of secondary or tertiary alcohol which is commonly used as a surface polishing chemical agent, isopropyl alcohol, for example.

The relationship between physisorbed CO_2 at 4.2 μm and the formation of the carbonates CO_3^{-2} on BaF_2 can be seen if we compare the data on BaF_2 in two different ambients. Namely, higher adsorption of CO_2 at 4.2 μm gives rise to the formation of more carbonates CO_3^{-2} around 6.5 μm.

3. Calcium Fluoride

The CaF_2 data in the laboratory ambient are shown in Fig. 7(a). Here we can see the similar distribution of bands as exhibited by BaF_2: adsorbed CO_2 at 4.2 μm, overlap of various hydrocarbons in the 3–4-μm region, liquid water around 4.8 μm, carbonyls around 5.6 μm, and carbonates in the 6–7.5-μm region. Comparison of Figs. 7(a) and (b) reveals several features. The fact that the CO_2 band is suppressed in dry N_2 atmosphere confirms the nature of physisorbed CO_2 on the surface.

Fig. 5. Wavelength modulation absorption spectra of KBr; K is the absorption coefficient in cm^{-1}: (a) in the laboratory atmosphere; (b) in a dry N_2 atmosphere.

the complex superposition of the bands, it was difficult to distinguish unambiguously which bands would scale with a thickness that would identify volume absorption. The 4.2-μm band was observed with the same intensity for all thicknesses, confirming a surface origin. The continuous variation of the spectral features with the thickness of sample that remains at $\sim 10^{-6}$-cm^{-1} levels indicates that, at this level of absorption, we have a combination of volume and surface absorption or there is an inhomogeneous distribution of volume impurities.

The region between 2 and 4 μm reveals several structures, while previous measurements by laser calorimetry have indicated a peak near 2.7 μm which has usually been associated with the stretching frequency of the isolated OH^- radicals.[19] However, the laser calorimetry measurements are performed with a multiline laser at a few discrete wavelengths and so can only infer a broad band with the great possibility of missing peaks or valleys.

In this study, a prominent peak is observed at 3850 cm^{-1}, which is shifted from the peak that is observed at 3610 cm^{-1} in deliberately doped KBr.[20] It is not clear that such a large shift could occur due to different crystallographic locations of OH^- in the lattice. The

magnitude and linewidth of this peak vary from sample to sample. In addition, placing a sample in N_2 gas atmosphere results in spectral changes that indicate that part of this band may be due to surface adsorption. However, there is a shoulder in this line near 3700 cm^{-1} that persists in dry N_2 ambient and can be associated with adsorbed H_2O.

The region between 3 and 4.0 μm shows a superposition of structures that could be attributed to various C—H bonds. The origin of these groups can result from surface contaminants due to alcohol that is used to disperse the grinding compounds used in the surface polishing of the crystals. However, some of these bands may be due to volume absorption since some of the spectra scale with sample thickness. Volume absorption due to C—H bonds can be due to carbonaceous fractions, which can result from organic materials such as water-soluble alcohols that decompose on melting and are incorporated in the crystals.

A unique example of physical adsorption taking place on a surface of KBr is seen at 4.2 μm. This strong narrow band with varying intensity is observed at 2358 cm^{-1} on all samples of KBr. This is close to the gas-phase value of 2349 cm^{-1} for the CO_2 vibration. Since this band is easily suppressed by flushing with dry N_2 gas, it is readily identified as due to a physically adsorbed species. When the sample is returned to atmospheric ambient, this band returns. It was observed that the CO_2 adsorption varies from sample to sample for the laboratory ambient. It is not unreasonable to expect physical adsorption to depend on surface variations or impurities in the substrate.

The band at 4.8 μm is most likely due to surface-adsorbed liquid water as the adsorption in this region is markedly reduced in a dry N_2 ambient; some of the additional structure in the 2.7-μm region can be due to the vibrational structure of water as it is also reduced by dry N_2 flushing.

The bands between 5.5 and 8.0 μm are the most persistent of all structures seen in all the KBr samples. Measurements on thin samples still reveal these structures, which lends evidence that these are due to surface chemical adsorption. The position of these bands is consistent with the vibrational frequencies of various surface carbonate complexes.[21]

It is interesting to note that the data reveal a peak in absorption at 10.6 μm and a valley around 9 μm. It is possible to identify the 10.6-μm peak as due to the C—C vibration. It is our interpretation that the laser calorimetry data indicate a possible minimum in absorption near the CO_2 laser line at 9.27 μm.[22] The wavelength modulation data definitely establish this valley.

The absorption between 5.5 and 8.0 μm seems to be due to surface carbonates. However, the absence of absorption at 1070 cm^{-1} signals that the species are in the form of carboxylates. Therefore, we can infer the presence of chemisorbed carbonates not only by the presence of absorption in the 5.5–8.0-μm region but also by the absence of absorption at 9.27 μm. The 10.6-μm (960-cm^{-1}) region corresponds to the 7–8-phonon region for KBr; the intrinsic multiphonon absorption of KBr
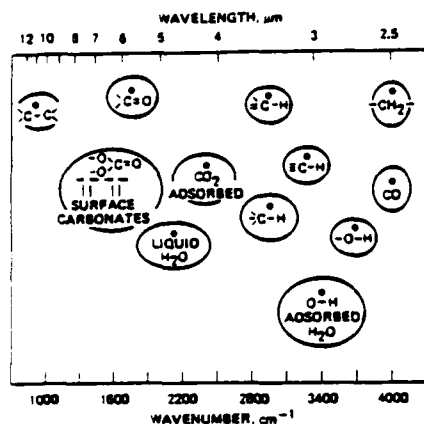
Fig. 3. Correlation chart of carbonates, C—H, O—H, and water frequency.

into the system throughout the entire run. When the sample was placed in a dry N_2 atmosphere, a continuous change in the spectral distribution of the absorption was observed until the spectra stabilized after the sample had been in this gaseous ambient for an hour.

Correlation-type charts have been published that represent a tabulation of molecular-ion vibrational frequencies as means of identifying possible surface and volume impurities in alkali-halide laser window materials.[17] If one considers a frequency overlay of possible impurities that can be present in concentration of 0.1 ppm, one finds that a quasi-continuous absorption would be expected throughout the 2.6–12-μm region due to the overlap of the Lorentzian tails of the various absorption bands. It has been felt that a heterogeneous distribution of a conglomeration of chemical compositions which can be deposited on the surface from the environment would produce a uniform absorption throughout the infrared spectral regions.[17] However, the distinct absorption bands observed in this study indicate the possibility of specifically identifying dominant absorption centers. Figure 3 shows a correlation chart of carbonates, C—H, O—H, and water frequencies which prove to be the common bulk and surface impurities encountered in this study.

B. Discussions

In Table I we show the origins of the samples used in this study.

1. Potassium Bromide

Several different reactive atmosphere process (RAP) grown samples from various sources have been studied. The dimensions of the samples varied, that is, 2.5 cm in diameter and 1–7 cm in length. The absorption spectrum of a typical KBr sample obtained with a conventional double-beam spectrometer is shown in Fig. 4. Virtually no absorption structure is present in the extrinsic spectral region above the noise level of the instrument, confirming the relative purity of the sample. Calculated values of absorption coefficients from the exponential behavior of the multiphonon processes from Eq. (1) at 10.6- and 5.3-μm wavelength regions predict

Table I. Origins of Samples Used in This Study

KBr	Naval Research Laboratory
	Oregon State University
KCl	Hughes Research Laboratories
BaF_2	Harshaw
MgF_2	Optovac
SrF_2	Hughes Research Laboratories
CaF_2	Harshaw
NaF	Optovac
LaF_3	Hughes Research Laboratories
NaCl	Hughes Research Laboratories
LiF	Meller
MgO	Optovac
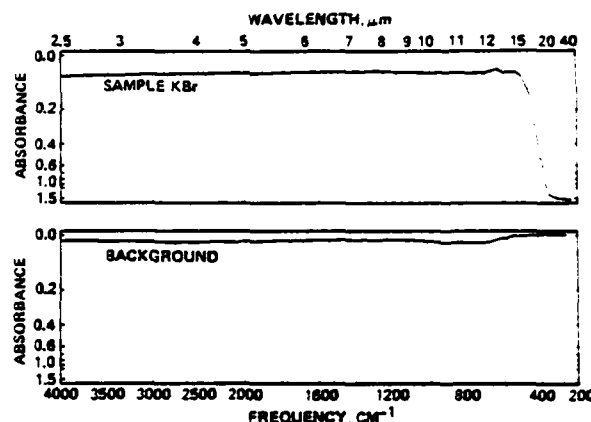
Fig. 4. Absorption spectrum of a typical KBr sample obtained by a conventional double-beam instrument.

2×10^{-7} and 8×10^{-18} cm^{-1}, respectively.[18] The actual measurements at best show 4.2×10^{-4} cm^{-1} at 10.6 μm and 2.1×10^{-4} cm^{-1} at 5.3 μm, respectively.[1] Therefore, in these spectral regions, the absorptions are mainly due to extrinsic origins.

In Fig. 5 we show a typical result of our study of KBr in two different ambients. In general, for the spectral region from 2.5 μm to 12 μm, the samples in this study show a structure around 2.5 μm, multiple structures between 3 and 4.0 μm, a sharp peak at 4.2 μm, a band centered at 4.8 μm, multiple structures between 6 and 8 μm, a valley near 9 μm, and a peak at 10.6 μm at the levels of absorption coefficient of ~10^{-5} cm^{-1}. Since the relative magnitudes of these structures differ in different samples, the indications are that these bands have extrinsic origins. Although the spectra differ in detail, the clustering of the spectral lines in similar spectral regimes indicate common origins of the spectra. The magnitudes and linewidths of some of the bands vary when the samples are in a dry N_2 atmosphere compared with a laboratory ambient, indicating that a portion of the absorption is due to surface physical adsorption. The structures that persist even when the samples are flushed in dry N_2 may be due to surface chemisorbed species or volume impurities. The surface character of some of these bands was confirmed by performing similar measurements on 1-mm thick samples. Absorption coefficients of the order of 10^{-5} cm^{-1} were observed on thick and thin samples with slight differences in the spectral distribution. Due to
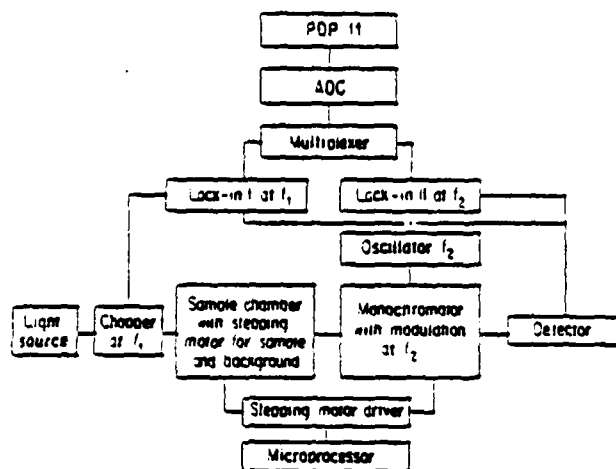
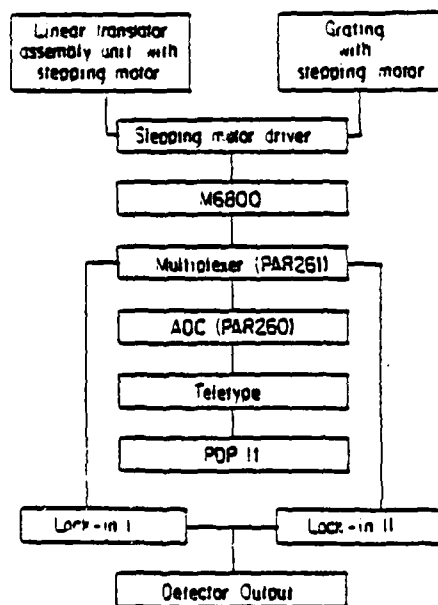Figure 1. Block diagram of the infrared wavelength modulated system.

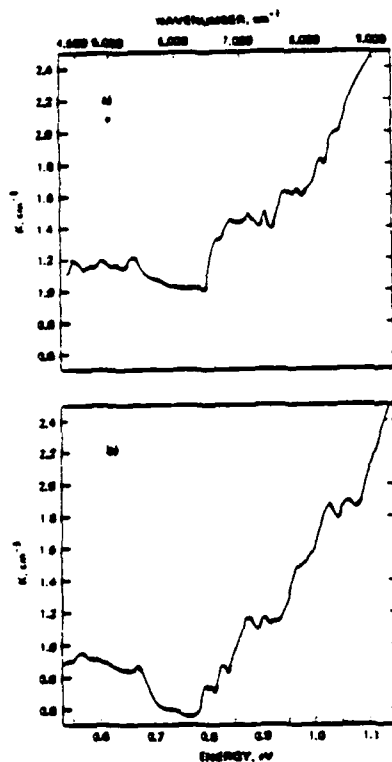Figure 2. Block diagram of control system for data-taking cycle.

7

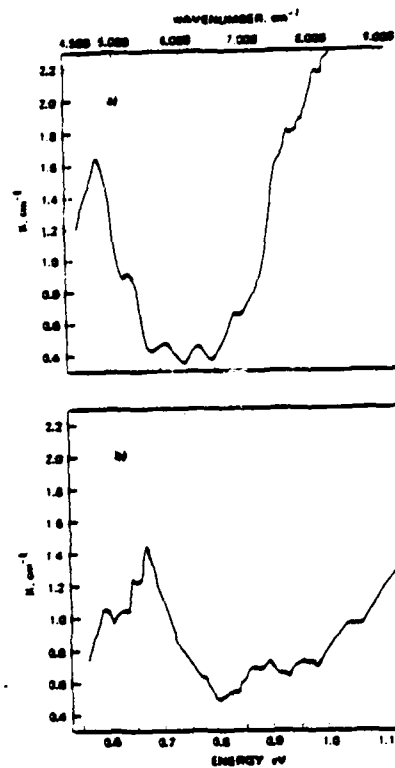Figure 3. a) and b) Semi-insulating GaAs:Cr.
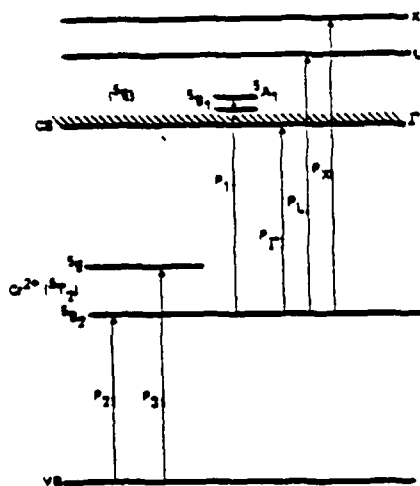

Figure 4. a) p-type, b) n-type GaAs:Cr.

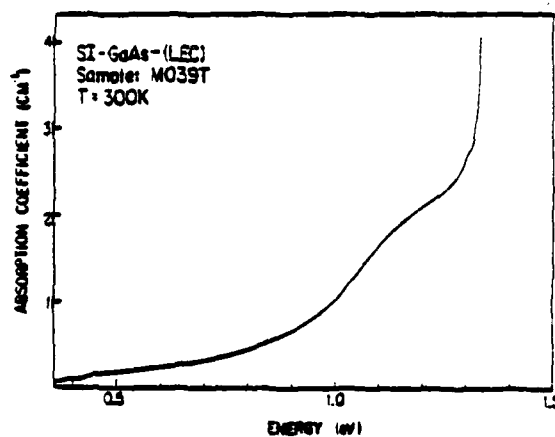Figure 5. Energy levels of $(Cr^{3+}-Cr^{2+})$ ions in GaAs:Cr.

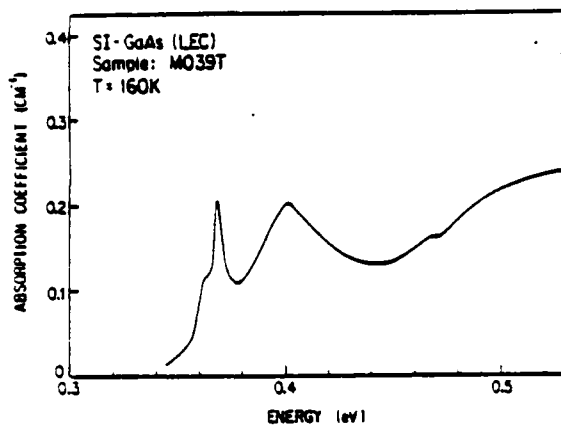Figure 6. Wavelength modulation absorption spectra of LEC-GaAs at 300 K.

8

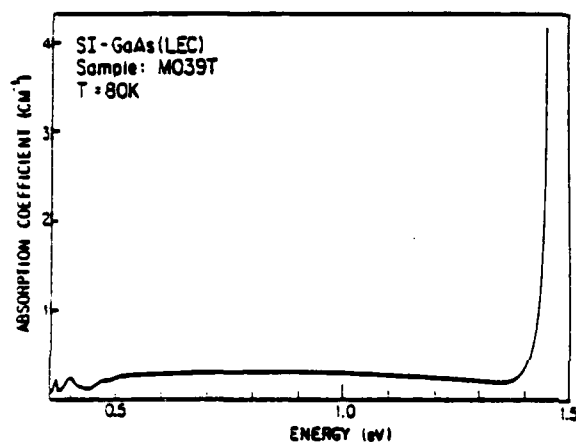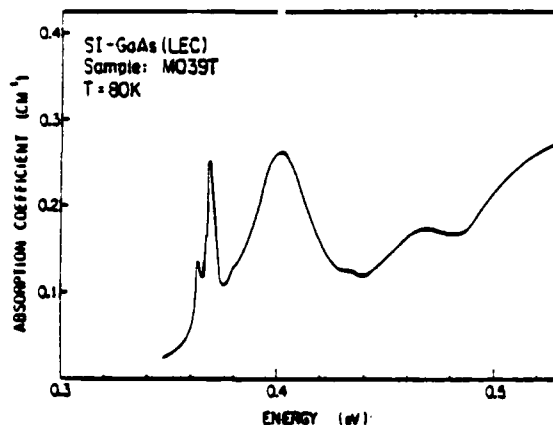Figure 7. Wavelength modulation absorption spectra of LEC-GaAs at 160 K.

Figure 8. Wavelength modulation absorption spectra of LEC-GaAs at 80 K with EL2 photo-quenched.

Figure 9. Wavelength modulation absorption spectra of LEC-GaAs at 80 K on a vastly expanded scale compared to Fig. 8.
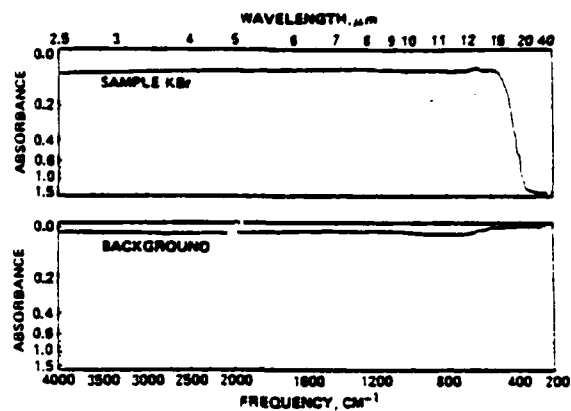
Figure 10. Absorption spectrum of a typical KBr sample obtained by a conventional double-beam instrument.
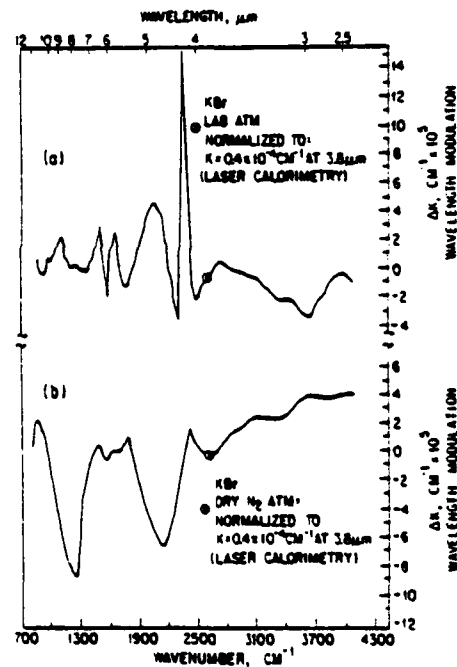
Figure 11. Wavelength modulation absorption spectra of KBr; ΔK is the change in the absorption coefficient in cm^{-1}; (a) in the laboratory atmosphere; (b) in a dry N_2 atmosphere.

9
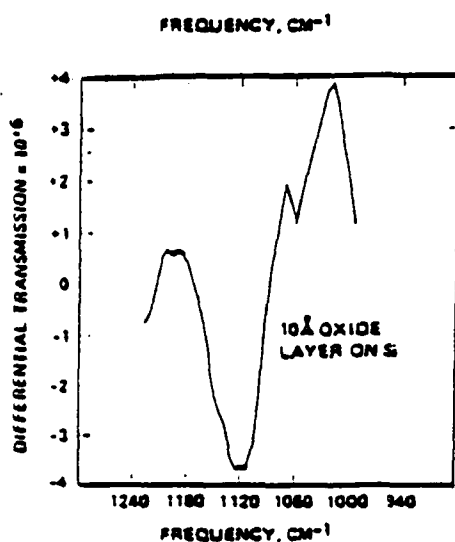
Figure 12. Wavelength modulation absorption spectra of a 10 A oxide layer of Si.
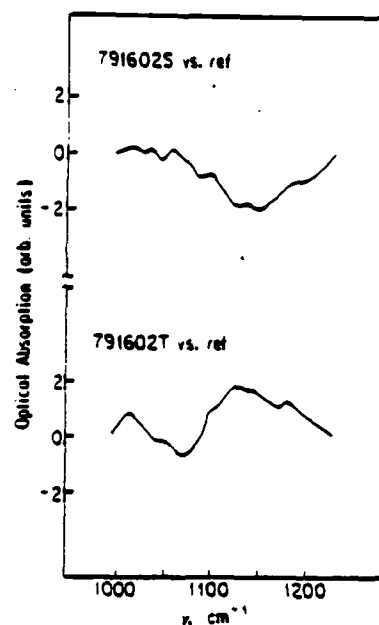
Figure 13.
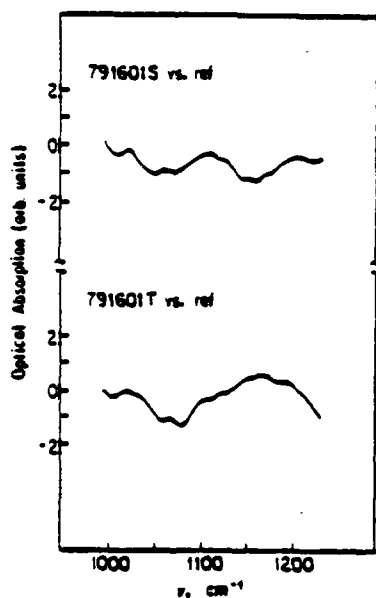
Figure 14.
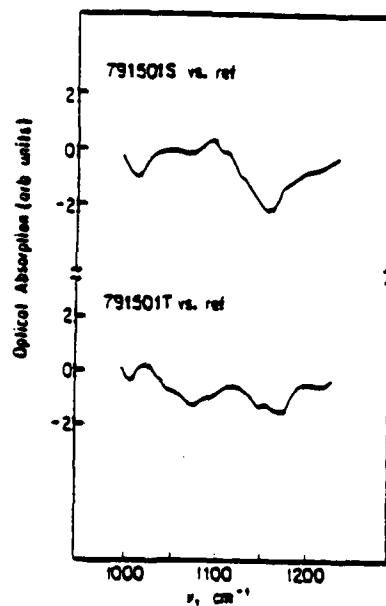
Figure 15.
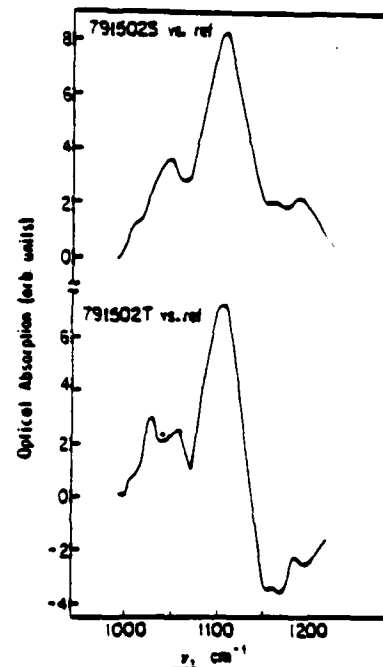
Figure 16.

Figures 13, 14, 15, 16. The relative optical absorption of the seed (top curve) and tail-end (bottom curve) of 791602, 791601, 791501, and 791502, respectively, float-zone Si ingots with respect to a Si reference containing ~ 10^{15} oxygen atoms/cm^3.

10

Subject classification 1.3, 13.1, 20.1, 21.1, 21.6

Department of Physics, University of California, Los Angeles

Optical Properties of β'-AuZn by Wavelength-Modulated Derivative Spectroscopy[1]

By

R. Stearns,[2] R. Braunstein, and L. Muldawer[3]

Derivative spectra of the optical properties of β'-AuZn have been obtained using wavelength-modulated spectroscopy between 1.5 and 5.1 eV. Assignments are made for interband transition at the M point of the Brillouin zone which fix the transition energies with an accuracy previously unattained.

Es wurden Ableitungsspektren der optischen Eigenschaften von β'-AuZn erhalten, indem wellenlängen-modulierte Spektroskopie zwischen 1.5 und 5.1 eV benutzt wurde. Für den Zwischenbandübergang am M-Punkt der Brillouin-Zone wurden Zuordnungen gemacht, welche die Übergangsenergien mit einer bisher unerreichten Genauigkeit festlegen.

[2] Current address: Newport Corporation, Fountain Valley, CA 92708.

[3] Permanent address: Temple University, Philadelphia, PA 19122.

I. Introduction

β'-AuZn is nearly a perfect prototype of the ordered alloy of the CsCl structure. The β' phase is an ordered phase of two interlocking simple cubic sublattices, one for each atomic constituent; the cube corners of each sublattice form the cube centers for the other sublattice. The principal problem in calculating the band structure of this alloy system is similar to that in other alloys, that is, the problem of specification of the potentials to give proper placement of the Au d-bands.

The best band structure calculation available places the Au d-bands with an accuracy of 0.5 eV [1]. Previous experimental studies of this alloy system [2,3] have not shed much light on this problem since they mainly dealt with the principal band edge, which does not involve the lower lying d-bands.

This current study reports the wavelength-modulated spectrum of β'-AuZn for the first time. The results which follow give specific assignment to some of the transitions involving the Au d-bands. The spectrum of $(1/R)(dR/dE)$ has been determined between 1.5 and 5.1 eV, and other optical properties have been calculated after a Kramers-Kronig analysis of the data was performed.

The ordered beta phase of AuZn is stable over a narrow range of atomic composition, bracketing the stoichiometric $\beta'Au_{50}Zn_{50}$, as shown in Figure 1. At room temperature, the boundaries of the β' phase are $Au_{48}Zn_{52}$ and $Au_{52.5}Zn_{47.5}$, with the phase boundaries widening with increasing temperature [4]. This phase has the structure of CsCl(B2) type [5], with a lattice constant a = 0.3128 nm at 49.5 atomic-% Zn [6]. It may also be noted from Figure 1 that this system has no disordered β phase at higher temperature as is seen, for example, in the CuZn alloy system [4].

II. Sample Preparation

The AuZn sample which was used in this investigation was prepared from 0.9998 pure Au and 0.99999 pure Zn. The AuZn mixture was sealed in a tube at a pressure of less than 10^{-5} mm Hg and shaken in the liquid state 5000 times before quenching to room temperature. The sample was subsequently annealed at 600°C for 24 hours in order to homogenize it and was then again quenched to room temperature. After cutting and polishing, it was given another anneal near 200°C in order to remove any cold work introduced during the finishing process. The final composition of the sample, as determined by assay for Au content by the U. S. Mint, is $\beta'-Au_{51.9}Zn_{48.1}$.

III. Experimental Method

Wavelength-modulated spectroscopy [7,8] was used because of the unambiguous lineshapes obtained by the technique and the resulting ease of interpretation of these lineshapes. The theory of wavelength-modulation spectroscopy is well detailed elsewhere [9,10]. The theory of the lineshapes near a three-dimensional critical point was given by Batz [11,12]. It is sufficient here to give the theoretical lineshapes for the sake of reference. All three-dimensional critical point lineshapes may be expressed in terms of a single function, $F(W)$, which is reproduced in Figure 2. The behavior of critical points in terms of $F(W)$ is listed in Table 1. Derivative data with a spacing of 0.02 eV between data points were taken between 1.50 and 5.10 eV. The depth of modulation, $\Delta\lambda/\lambda$, was about 1.5×10^{-3} at the Hg green line and varied in a manner that was approximately proportional to energy. Thus, the resolution of the data should be better than the spacing of the data points.

IV. Experimental Results

The logarithmic derivative of the reflectivity (Figure 3) was determined experimentally and integrated to yield the complete reflectivity spectrum from 1.5 to 5.1 eV (Figure 4). The general shape of the reflectivity curve in Figure 4 agrees with previous results [2,3], but shows shifting of major structures and has additional fine structure. The minimum at 3.2 eV and the maximum at 3.78 eV are at higher energies than in the other work. The sharp dip in the reflectivity at about 2 eV accounts for the color of the material, which could be described as a ruddy brass. This may be similar to the yellow-pink described by Jan and Vishnubhatla [3] and the "pale purple" seen by Muldawer [2].

In order to determine the other optical properties of AuZn, a Kramers-Kronig analysis of the data was undertaken. In order to perform the integration which is involved, extrapolations of the reflectivity to the infrared and ultraviolet regions of the spectrum were necessary. The data of Jan and Vishnubhatla [3] were used for the region from 5.1 to 10 eV. Contributions to the integrals from even high energies are small, due to the local nature of the integrals. A principal effect of a different choice of far uv extrapolation is the addition of a dc level to the optical constants. Muldawer and Goldman [13] found that for β-CuZn alloys, the reflectivity actually increases between 12 and 18 eV. Therefore, in order to provide a reasonable comparison with other alloys of the CsCl structure, a constant reflectivity was used for energies greater than 10 eV. In the infrared, a Hagen-Rubens [14] extrapolation to a reflectivity of 100% at zero energy was used. The extrapolations were normalized to the experimental data. These are small discontinuities at the points where the spectral regions meet.

This can cause localized anomalous structure at the end points of the data. However, due to the local nature of the Kramers-Krönig integrals, this structure will not effect the general structure of the experimental spectra.

Figure 5 shows the real and imaginary parts of the dielectric function, ϵ_1 and ϵ_2, and Figure 6 their derivatives, ϵ'_1 and ϵ'_2, which are calculated from the results of the Kramers-Krönig integral. These data are then used to find the Drude parameters, the effective mass, and relaxation time, by deconvoluting the Drude-like terms and bound terms as described elsewhere [15,16]. Figure 7 shows the curves generated from the derivatives of the dielectric functions to separate the free and bound electron contributions. Their intersection determines the values of the Drude parameters [14,15]. The Drude effective mass was found to be 1.10 times the free electron mass and the relaxation time was found to be 2.76×10^{-15} second. The value for the effective mass compares favorably with the previous value of 1.2 [3]. The relaxation time for AuZn is not given elsewhere; the value here is about 2-3 times the relaxation time for CuZn [13]. Figures 8 and 9 are the bound-electron contributions to the dielectric function, ϵ_{1b} and ϵ_{2b}, and their derivatives, ϵ'_{1b} and ϵ'_{2b}, which are obtained when the Drude parameters are used to subtract the free-electron contributions from the dielectric function.

Finally, the absorption coefficient is given in Figure 10. The general shape is the same as previously reported [3], but the maximum is at 4.1 eV instead of 3.2 eV. This also illustrates the shift in major structure noted in the discussion of the reflectivity.

V. Interband Transitions

The band structure which was previously calculated for AuZn is given in Figure 11 [1]. Assignment of interband transitions is made using the data found from the derivatives of the bound parts of the dielectric function. The proper lineshape for each transition is determined by first finding the type of critical point involved in the transition from band theory and comparing that with the lineshapes of Table 1. Finding that a transition, determined from Figure 9, has a lineshape as expected near the predicted energy lends confidence to interband transition assignments.

A. Fermi Level to Higher Bands

The band structure in Figure 11 shows that the onset of interband transitions is due to transitions from the Fermi level to higher conduction bands at the M point, that is, the (110) direction, in the Brillouin zone. The lowest energy transitions are $M_{7-} \rightarrow M_{6+}$ and $M_{6-} \rightarrow M_{6+}$. The band calculation has a critical gap of 2.0 eV for $M_{7-} \rightarrow M_{6+}$, with an onset at 1.6 eV for this transition. The $M_{6-} \rightarrow M_{6+}$ transition has a critical point energy of 2.6 eV and an onset of 1.8 eV, according to Figure 11. The experimental data yield lower values for these energies. $M_{7-} \rightarrow M_{6+}$ is at 1.67 eV. This is probably the reason why the reflectivity is rising at the low energy end of the spectrum.

$M_{6-} \rightarrow M_{6+}$ is found to be at 2.23 eV, as given by the dip in ε'_{2b} at 2.4 eV and the peak in ε'_{1b} at 2.2 eV. Both transitions involved here are shifted to a lower energy by about 0.3 eV. This leads to a conclusion at the M_{6+} conduction band should be shifted down by about that energy with respect to the Fermi level. If this is done, that would place the onset of the second transition below the experimental energy range.

The transitions from the Fermi level to the second higher conduction band occur in the intermediate part of the spectrum. The band picture predicts that the transitions $M_{7-} \rightarrow M_{7+}$ and $M_{6-} \rightarrow M_{7+}$ will be at 3.3 and 3.9 eV, respectively. The experimental data show these to be at 3.26 and 3.86 eV. These assignments give an internal consistency to the results. By subtracting transition energies, a value for the $M_{6-} \rightarrow M_{7-}$ gap may be obtained. The low and intermediate energy assignments give 0.61 and 0.60 eV, respectively, for this difference. The difference between these two values is less than the resolution of the experimental data.

B. Transitions Involving d-Bands

There is one other structure in the lower energy portion of the spectrum. This is due to transitions from the upper Au d-band to the Fermi level. The actual critical point from the highest lying M_{7+} to the M_{7-} conduction band at the Fermi level cannot be seen because the upper level is filled. However, the transition has an onset at the point where the valence band crosses the Fermi level. By inspection of the band structure of Figure 11, it is apparent that this critical point is of the M_0 (minimum) type. Figure 12 shows, in accordance with Table 1, how the lineshapes for ϵ'_1 and ϵ'_2 behave near an M_0 critical point. In this figure, ω_g is the critical point gap and ω_0 is the point of the actual onset. The dotted line shows how the transition lineshape will actually behave. Note that the structure in ϵ'_1 is quite small compared to the structure which would be observed in ϵ'_2. This behavior can actually be seen in the experimental spectrum at 2.06 eV. The observation of this transition is an illustration of the strength of modulation spectroscopy, since this observation would be very difficult in a standard reflectivity experiment.

The onset is observed at 2.06 eV, compared to 2.2 eV as predicted by the

band structure. Figure 13 shows how some of the bands might be shifted to match the observations made so far (along with some other shifts which will be discussed in the remainder of this discussion). The M_{6+} point is shifted down in energy by 0.3 eV, while M_{7+} remains the same. The M_{7-} and M_{6-} partially filled valence bands are unchanged with respect to these two bands. The M_{7+} Au d-band is shifted upward by about 0.2 eV, in accordance with the observed structure.

If the modification of the M_{6+} conduction band is correct, the transition from the second Au d-band to this upper band would be at 4.6 eV. A major structure is observed centered at 4.61 eV. Since it follows the lineshape for the M_o transition which is predicted by the band picture, this structure is assigned to the M_{6+}(d-band) $\rightarrow$ M_{6+}(cond.) transition.

Also, the M_{6+} modification, along with the proposed shift in the M_{7+} d-band, brings the $M_{7+} \rightarrow M_{6+}$ transition to almost the same energy as the $M_{7-} \rightarrow M_{7+}$ transition discussed previously. The convolution of these two critical points can be seen in the additional structure at about 3.4 eV.

The last major structure in this experimental spectrum is at 5.0 eV. A possible assignment for this structure is the d-band to conduction band transition $M_{7+} \rightarrow M_{6+}$. However, this would require breaking the degeneracy of the intermediate Au d-bands as suggested by Figure 13. An exact assignment is difficult since anomalous structure due to end point problems may have some effect on the apparent optical functions, as discussed previously.

The only transition which we would hope to see from the lowest Au d-band is to the Fermi level. Again, the actual critical point is filled, so all that will be seen is a small break in the spectrum at the point where the d-band to Fermi level transition has its onset. The band structure gives an energy of 4.8 eV for the onset of this transition. There are no breaks between the

structures at 4.6 and 5.0 eV. This transition is assigned to the small

structure at 4.4 eV. This necessitates raising the lower Au d-band as shown in

Figure 13. This structure is right at the limits allowed by the noise level in

the data, so this assignment must be regarded as tentative.

VI. Conclusions

The experimental results which have been described are summarized in Table 2.

These results should help in the placement of the Au d-bands in the AuZn alloy

system. In the band structure of Connolly and Johnson [1], the four Au d-bands

had a total width of 2.8 eV at the M point, while using the results from our

work, this same width is about 2.5 eV. This should be a more accurate result,

since the placement of the d-bands in the previous calculation was ± 0.5 eV.

These results should allow a more accurate calculation of the crystal potential

for band structure calculations.

References

[1] J. W. D. Connolly and K. H. Johnson, <u>Proceedings of the Third Material Research Symposium, Electronic Density of States</u>, Gaithersburg, MD (National Bureau of Standards, 1967).

[2] L. Muldawer, Phys. Rev. <u>127</u>, 1551 (1962).

[3] J. P. Jan and S. S. Vsihnubhatla, Canad. J. Phys. <u>45</u>, 2205 (1967).

[4] M. Hansen, <u>Constitution of Binary Alloys</u> (McGraw-Hill, New York, 1958).

[5] A. West₆ren and G. Phragmen, Phil. Mag. <u>50</u>, 311 (1925).

[6] N. V. Ageev and D. H. Shoylshet, Izvest. Sektora Fiz.-Khim. Anal. <u>13</u>, 165 (1940).

[7] M. Welkowsky and R. Braunstein, Rev. Sci. Instrum. <u>43</u>, 399 (1972).

[8] R. Stearns, J. Steele, and R. Braunstein, Rev. Sci. Instrum. <u>54(8)</u>, 984 (1983).

[9] M. Cardona, <u>Modulation Spectroscopy</u> (Academic Press, New York, 1969).

[10] M. Welkowsky, Ph.D. Thesis, University of California, Los Angeles (1971).

[11] B. Batz, Ph.D. Thesis, Univ. Libre de Bruxelles (1967).

[12] B. Batz, Sol. St. Commun. <u>4</u>, 241 (1965).

[13] L. Muldawer and H. J. Goldman, in <u>Optical Properties and Electronic Structure of Metals and Alloys</u>, F. Abeles, ed. (North Holland Publ. Co., Amsterdam, 1966), p. 574.

[14] N. F. Mott and H. Jones, <u>The Theory of the Properties of Metals and Alloys</u> (Dover Publications, New York, 1958).

[15] M. Burd, R. Stearns, and R. Braunstein, Phys. Status Solidi (b) <u>117</u>, 101 (1983).

[16] R. Stearns, Ph.D. Thesis, University of California, Los Angeles (1982).

[17] K. Gottfried, <u>Quantum Mechanics I</u> (Benjamin, Reading, Mass., 1966).

[18] F. Wooten, <u>Optical Properties of Solids</u> (Academic Press, New York, 1972).

1.0

45
50
56
63

2.8

2.5

3.2

2.2

1.1

36

40

2.0

1.8

1.25

1.4

1.6
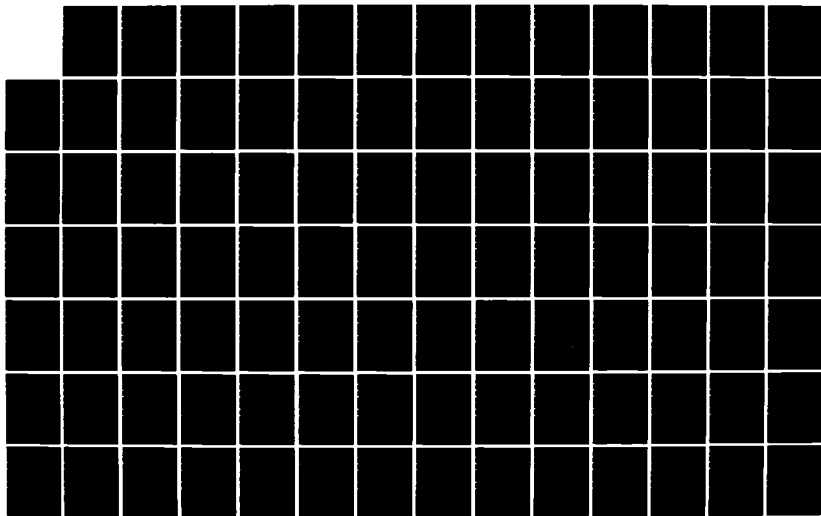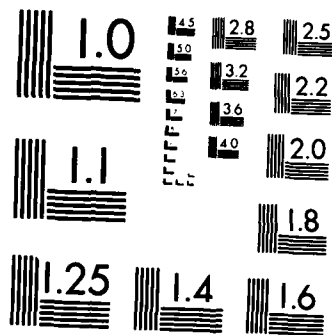
MICROCOPY RESOLUTION TEST CHART
NATIONAL BUREAU OF STANDARDS-1963-A

Figure Captions

Figure 1. Phase diagram of the $Au_{1-x}Zn_x$ alloy system. Dashed lines indicate boundaries which have not been firmly established [4].

Figure 2. Universal function, F(W), derived by Batz [11,12] for lineshapes near critical points as seen in wavelength modulation spectroscopy. $F(W) = [W^2+1]^{-1/2} [(W^2+1)^{1/2} + W]^{1/2}$, where W is the reduced frequency $(\omega-\omega_g)/\eta$. $\hbar\omega_g$ is the interband energy at the critical point and η is a phenomenological broadening parameter.

Figure 3. 1/R dR/dE for β'-AuZn. This is the direct experimental result of wavelength-modulated derivative spectroscopy.

Figure 4. Reflectivity of β'-AuZn. The reflectivity is determined by integrating the results of Figure 3.

Figure 5. Real and imaginary parts of the dielectric function, ϵ_1 (a) and ϵ_2 (b) [15]. These are determined by a Kramers-Kronig analysis of the reflectivity in Figure 4.

Figure 6. Derivatives of the real and imaginary parts of the dielectric function, ϵ'_1 (a) and ϵ'_2 (b).

Figure 7. Determination of the Drude parameters of β'-AuZn. The curves represent two functions, $m^*(\tau)$ (m^* = effective mass, τ = relaxation time), one for the real part and one for the imaginary part of ϵ'. Each function gives the value of m^* which best deconvolutes [14,15] the Drude and bound parts of the dielectric function for a given value of τ. The crossing of these functions is the point where the same values of m^* and τ minimize the decorrelation function of both ϵ'_1 and ϵ'_2. This intersection is the physical result for the Drude parameters [14,15].

Figure 8. Bound parts of the dielectric function, ϵ_{1b} and ϵ_{2b} [1S], which
result when the Drude contributions are subtracted from ϵ_1 and ϵ_2.

Figure 9. Derivatives with respect to energy of the bound parts of the
dielectric function, ϵ'_{1b} and ϵ'_{2b}. With reference to the band
structure in Fig. 11 obtained from Ref. 11, the following transitions
are identified: $M_{7-} \to M_{6+}$ (1.67 eV), $M_{7-} \to M_{7+}(E_F)$ (2.06 eV),
$M_{6-} \to M_{6+}$ (2.28 eV), $M_{7-} \to M_{7+}$ (3.26 eV), $M_{6-} \to M_{7+}$ (3.86 eV),
$M_{7+}(d) \to M_{6+}$ (4.4 eV), $M_{6+}(d) \to M_{6+}$ (4.61 eV).

Figure 10. Absorption coefficient, α, of β'-AuZn.

Figure 11. Band structure of β'-AuZn as calculated by Connolly and Johnson [1].

Figure 12. Lineshapes near an M_0 critical point as determined from Figure 2 and
Table 1. If the upper band involved in the transition is partially
filled, then the critical point itself will not be seen in
experimental spectrum since it is a filled-state to filled-state
transition. Transitions will begin at an energy, $\hbar\omega_0$, at which there
are empty final states. The dotted lines in the figure show the
expected experimental results for such a situation.

Figure 13. Adjustments of the β'-AuZn bands near the M point of the Brillouin
zone to fit the experimental results. The solid lines are reproduced
from Figure 11 and the dotted lines are the adjustments of the bands
which are suggested by the experimentally determined transition
assignments.

Table 1. Derivative of Critical Points With Broadening Included in Terms of F(W)

$$F(W) = [(W^2 + 1)^{1/2} + W]^{1/2}/(W^2 + 1)^{1/2} , \qquad W = (\omega - \omega_g)/\eta$$

Critical Point	$2\eta^{1/2} \dfrac{d\epsilon_1}{d\omega}$	$2\eta^{1/2} \dfrac{d\epsilon_2}{d\omega}$
M_0	$F(-W)$	$F(W)$
M_1	$-F(W)$	$F(-W)$
M_2	$-F(-W)$	$-F(W)$
M_3	$F(W)$	$-F(-W)$

Table 2. Summary of Experimental Results

Transition	Predicted Energy (eV) (Ref. 1)	Experimental Energy (eV) ΔE
$M_{7-} \rightarrow M_{6+}$	2.0	1.67
$M_{6-} \rightarrow M_{6+}$	2.6	2.28
$M_{7-} \rightarrow M_{7+}$	3.3	3.26
$M_{6-} \rightarrow M_{7+}$	3.9	3.86
M_{7+}(upper d) $\rightarrow$ $M_{7-}(E_F)$	2.2(onset)	2.06(onset)
M_{6+}(mid d) $\rightarrow$ M_{6+}(cond.)	5.0	4.61
$M_{7+} \rightarrow M_{6+}$	5.0	~ 5.0
M_{6+}(lower d) $\rightarrow$ $M_{7-}(E_F)$	4.8(onset)	4.4(onset)
$R_{8+} \rightarrow R_{7-}$	4.6	4.6
$R_{8+} \rightarrow R_{8+}$	4.8	5.0

Drude effective mass $m^*/m = 1.10$

Drude relaxation time $\tau = 2.76 \times 10^{-15}$ second

Fig. 1

$$W = \frac{\omega - \omega_g}{\eta}$$

Fig. 2

Fig. 3

REFLECTIVITY

ENERGY (EV)
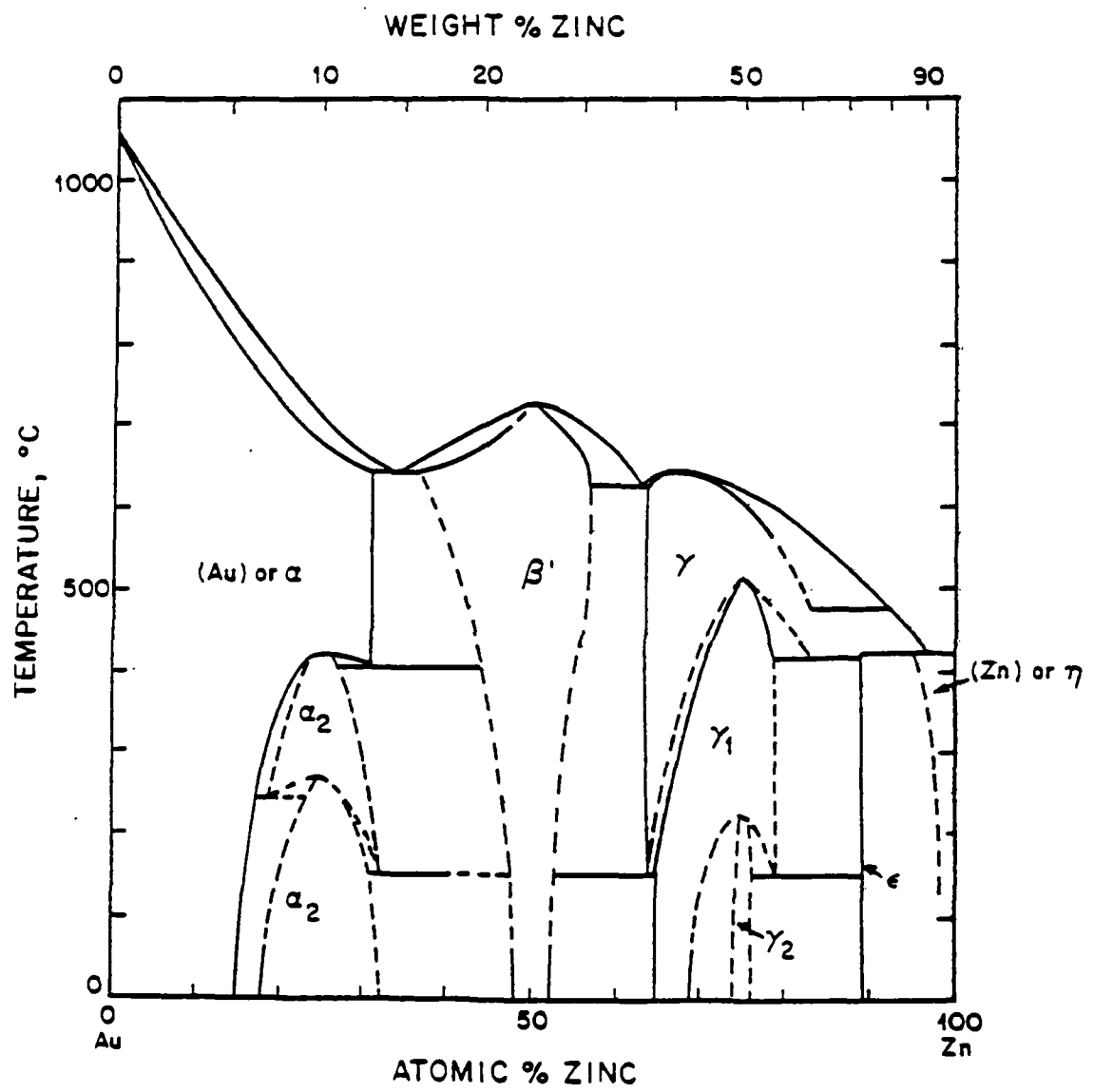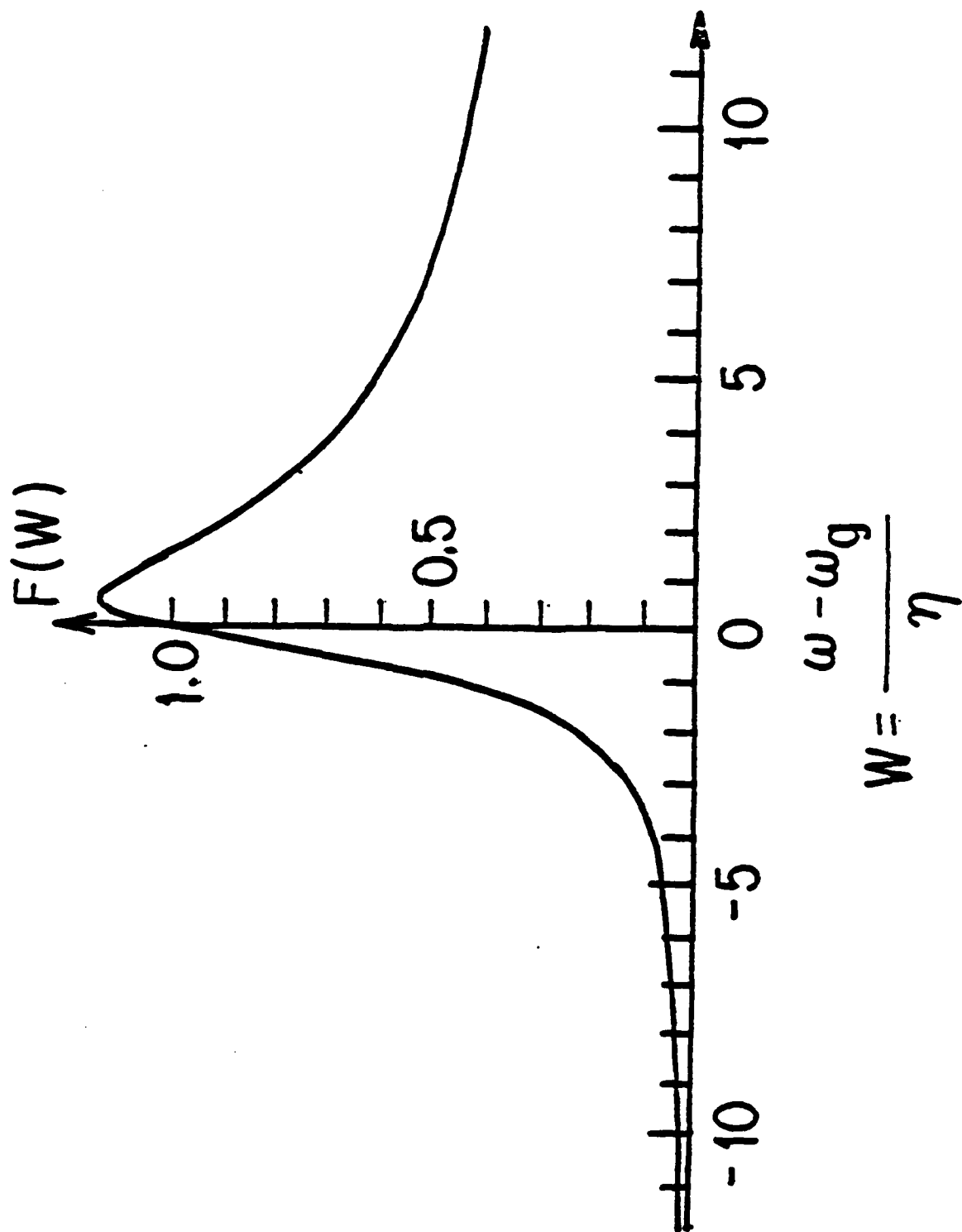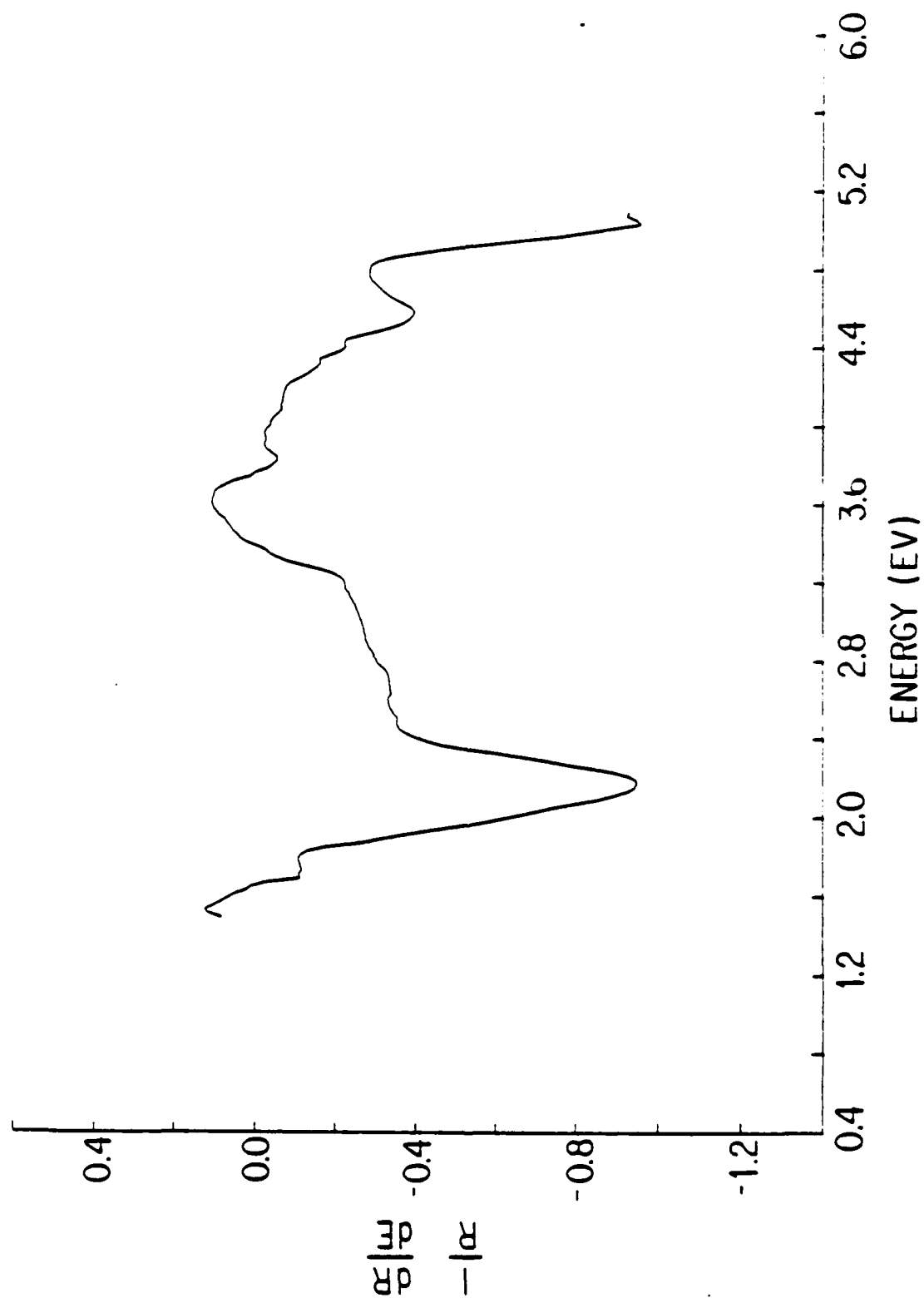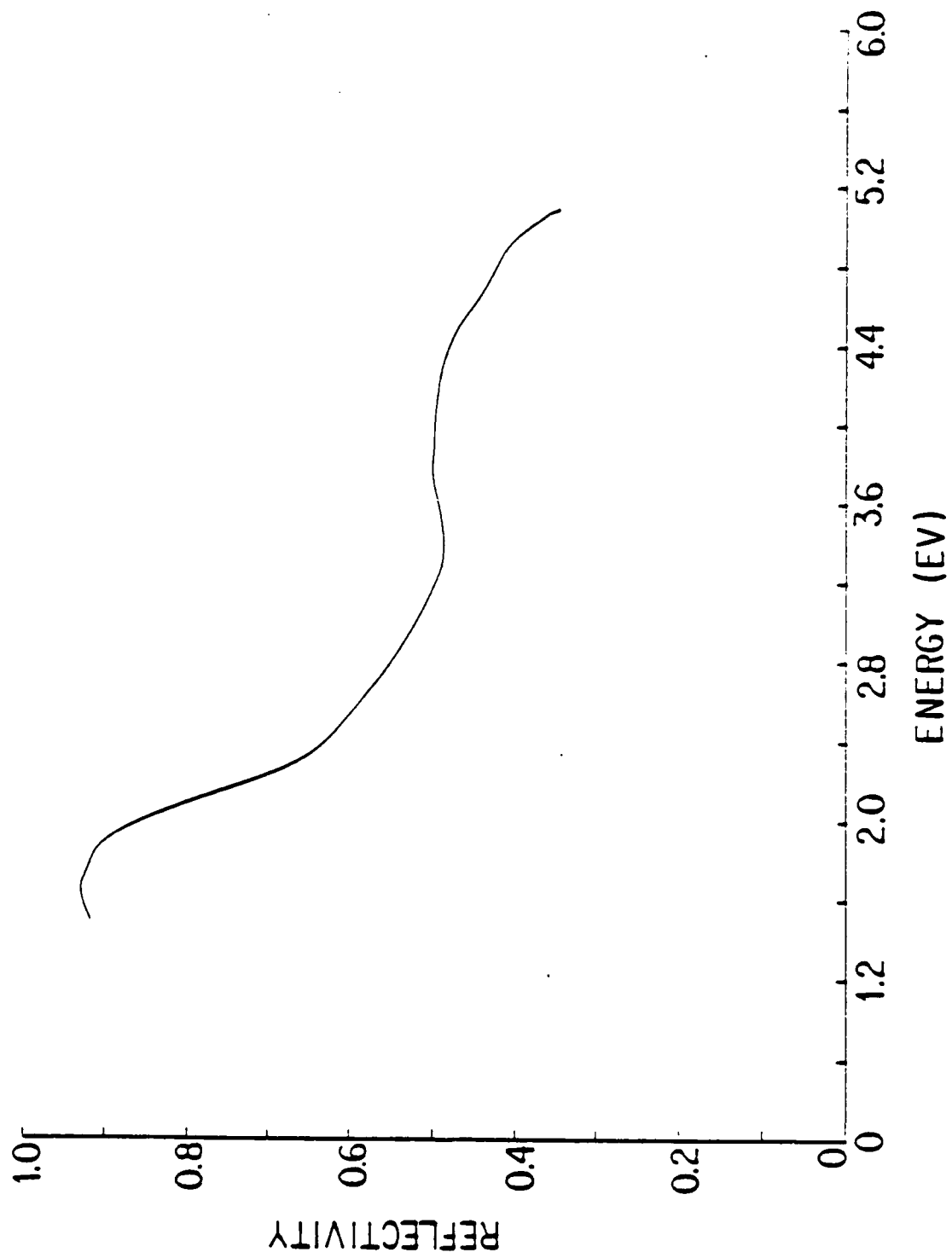
Fig. 4
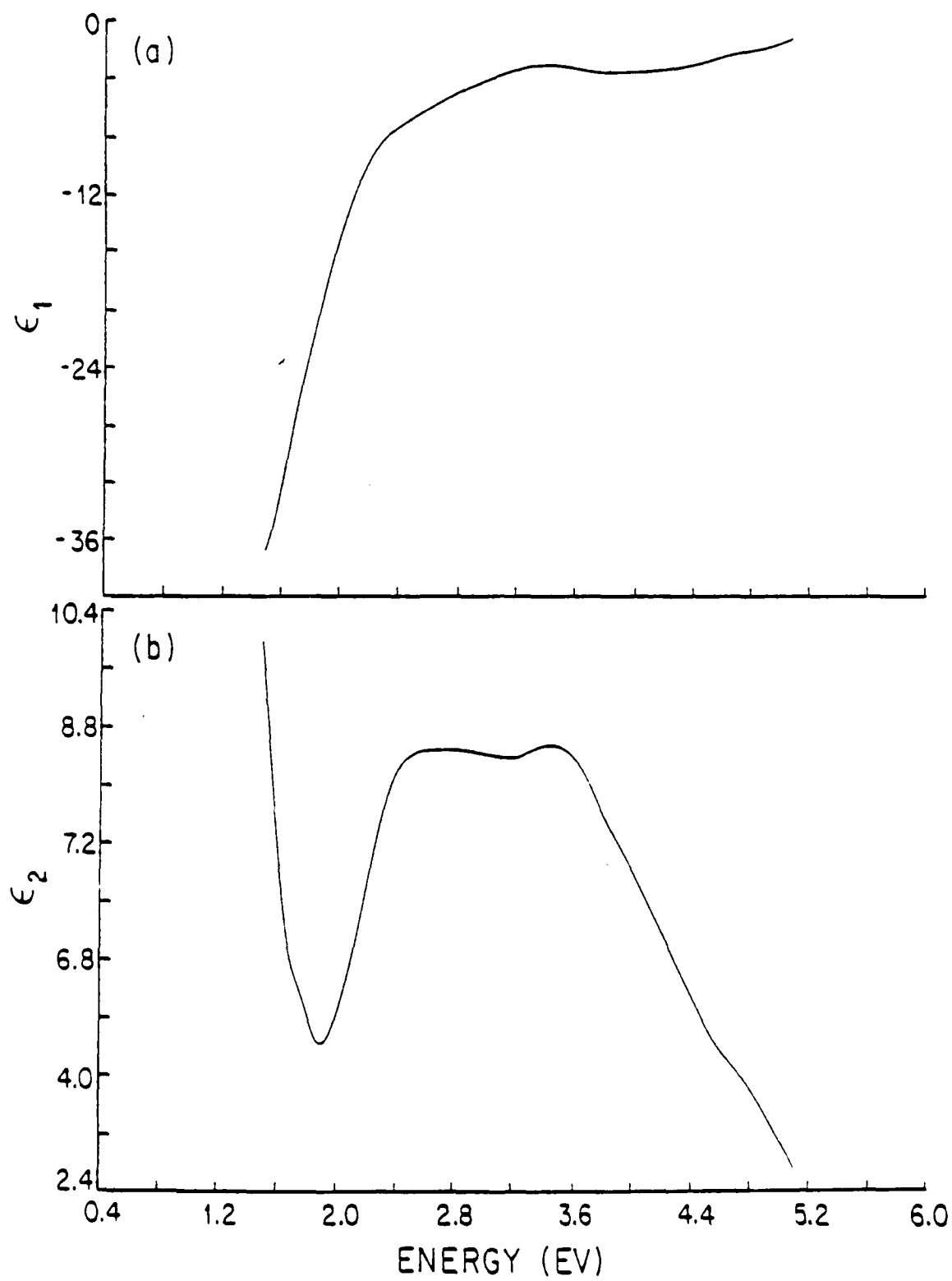
Fig. 5
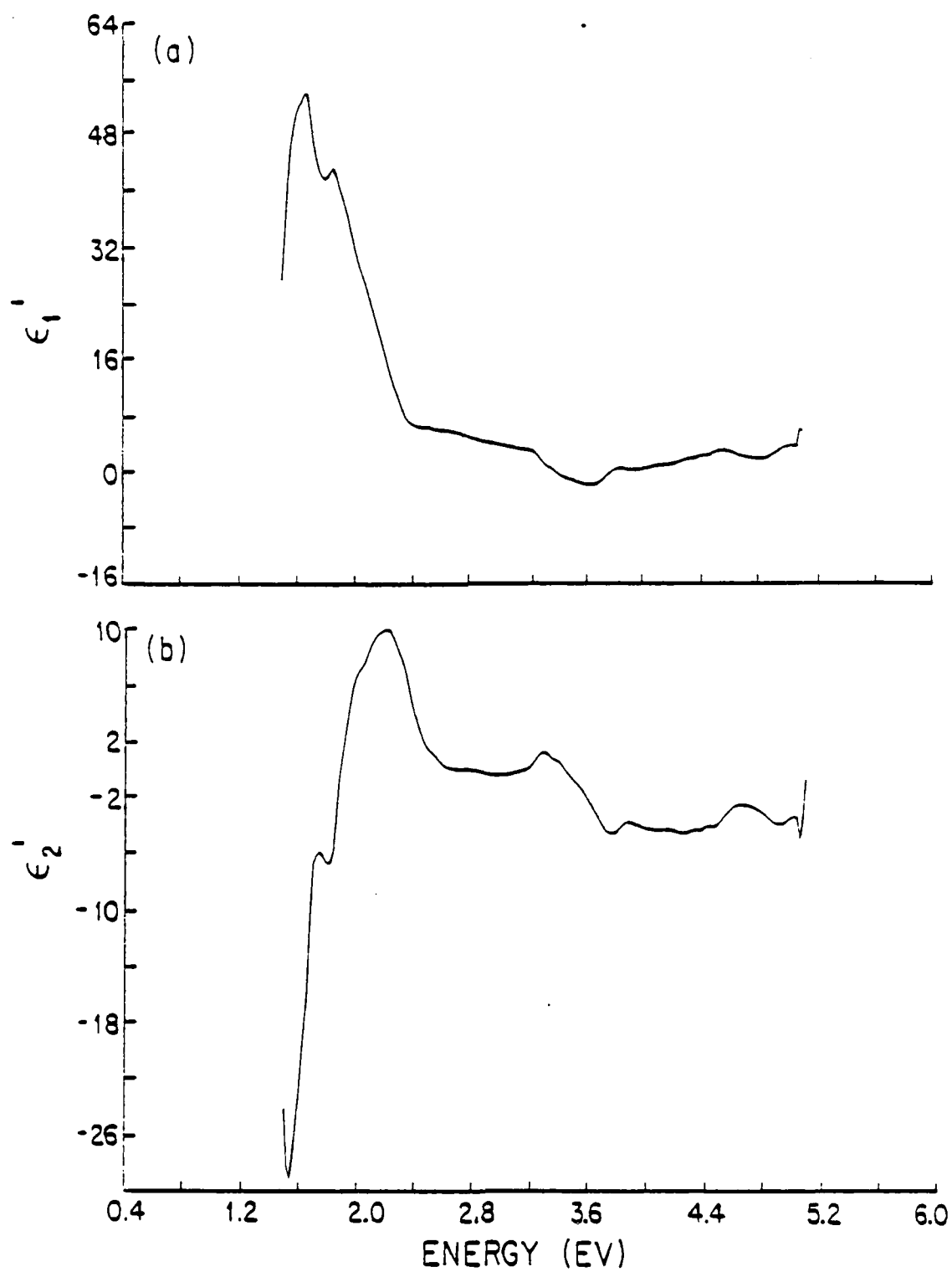
Fig. 6
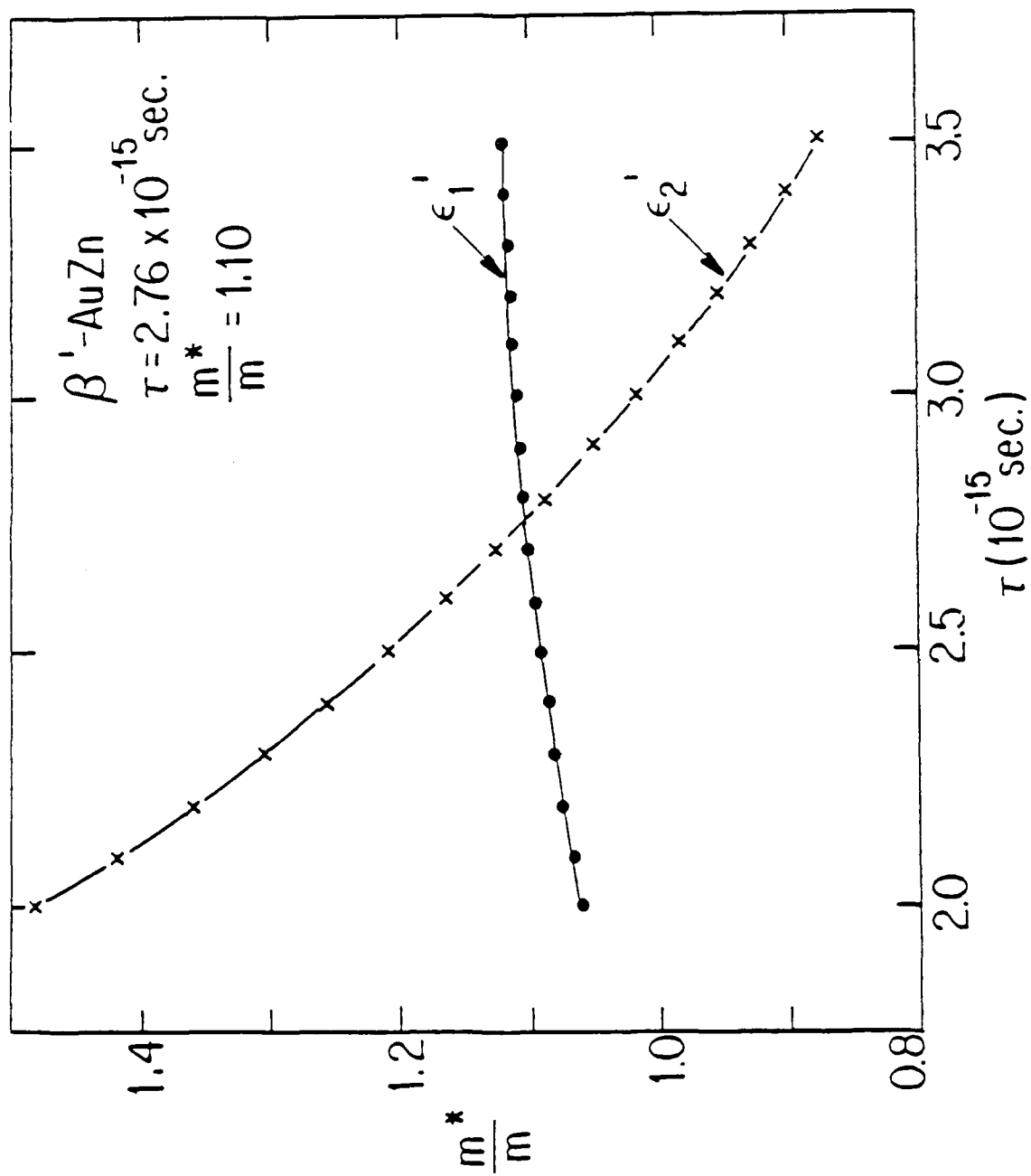
Fig. 7
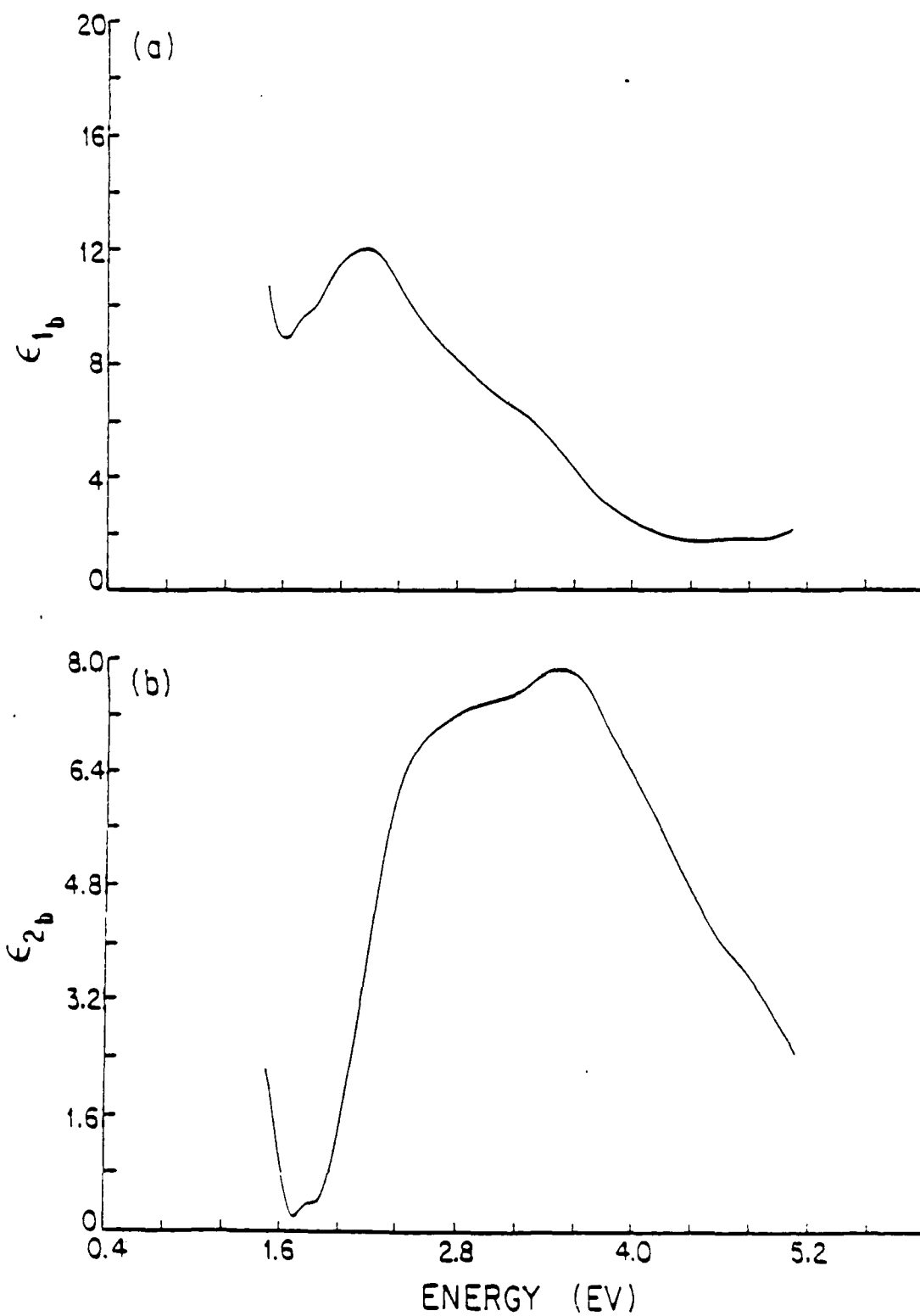
Fig. 8

VII. Discussion

The results of this study indicate that the effects of alloying in the $Ag_{0.7}Zn_{0.3}$ are actually fairly small. The shifts in the interband transitions must be on the lower end of those predicted for the α-$Cu_{0.7}Zn_{0.3}$ system by Bansil et al. [22]. If the $L_3 \rightarrow L_{2'}(E_F)$ transition has been shifted by +0.3 eV, as might be expected from the α-$Cu_{0.7}Zn_{0.3}$ study, then this transition should have an onset at about 4.2 eV in pure Ag. This value is just within the range of experimental values which have been quoted. The actual shift in α-$Cu_{0.7}Zn_{0.3}$ for the $L_{2'} \rightarrow L_1$ transition is about -0.2 eV [23,24]. Using this value would place the $L_{2'} \rightarrow L_1$ transition in pure Ag at 4.0 eV which is about the middle of the experimental values for this transition.

The following may be cited as the important results of this study:

(1) In this alloy composition, ε_1 is dampened to the point where the main Ag plasma resonance is eliminated.

(2) The Drude effective mass predicts a slight flattening of the bands. The fact that the energy difference $L_3 \rightarrow L_{2'}(E_F)$ is 0.28 eV is not any help in confirming the flattening since values for this difference for Ag are reported to lie between 0.2 and 0.3 eV.

(3) The fact that the Drude relaxation time for this alloy is approximately the same for pure Ag indicates that this amount of alloying has not greatly affected the mean free path of conduction electrons.

(4) The shifts found in the interband transitions between pure Ag and the alloy indicate that the transition usually more sensitive to perturbation of the crystal potential ($L_{2'} \rightarrow L_1$) has a shift of about the same magnitude as the less sensitive transition ($L_3 \rightarrow L_{2'}$). This indicates that, at least in this portion of the Brillouin zone, the rigid-band model may be used to describe the interband transitions of this alloy.

dip in ε'_{1_b} would be expected near the critical point for each of them [14,15]. However, the $L_{2'}$ band is filled at the critical point, so the actual critical point transition structure for the $L_3 \rightarrow L_{2'}$ transition will not be seen. A break in the derivatives of ε_b should be seen at the energy where transitions to the Fermi level begin to occur. The minimum in ε'_{1_b} at 3.88 eV is the expected structure due to $L_{2'} \rightarrow L_1$. The associated structure in ε'_{2_b} is the peak at 3.78 eV. This places the critical point at 3.83 eV, coinciding with the peak in the energy loss function. The peak in ε'_{1_b} at 3.55 eV is due to the onset of transitions at $L_{2'}(E_F) \rightarrow L_1$. We may then conclude that the $L_{2'}$ critical point lies 0.28 eV below the Fermi level.

Ehrenreich and Phillipp [17] assigned the mean ε_2 Ag peak at 4.4 eV to the direct transition from the d-band to the Fermi surface $L_3 \rightarrow L_{2'}(E_F)$. Our data show that there is very little shift of the transition in the α-Ag$_{0.70}$Zn$_{0.30}$ alloy. The $L_3 \rightarrow L_{2'}(E_F)$ transition will produce a downward break in ε'_{1_b} with an associated break in ε'_{2_b} at the same energy, which is the energy of the onset of interband transitions. Such breaks are seen at 4.37 eV in Figure 9. This places the $L_3 \rightarrow L_{2'}$ critical point gap at 4.09 eV when the results from the data for the $L_{2'} \rightarrow L_1$ transition are used.

VI. Interband Transitions

Once the Drude effective mass and relaxation time are known, they may be used to subtract the intraband contributions to the dielectric function from the total experimental function. The resulting real and imaginary parts of the bound-electron contribution to the dielectric function are shown in Figure 8. Their derivatives are given in Figure 9. It is these derivatives of the bound part of the dielectric function which are used to assign interband transitions.

It is interesting to compare ϵ_{2_b} of Fig. 8 with the ϵ_2 results shown in Fig. 9e of [5]. The earlier work shows maxima in ϵ_2 at 3.1 and 4.9 eV with a minimum at 4.1 eV. The current work has a maximum at 2.8 eV, a minimum at 3.6 eV, and maxima at 4.0 and 4.5 eV, which are resolved here where they were not previously. We thus see that the features found in this study are at lower energies than in [5].

The current literature does not firmly fix the exact value of the Ag interband transitions of interest in this study. While the energy gap for the $L_{2'} \to L_1$ transitions ranges from 3.8 eV [7] to 4.1 eV [5], the values quoted for the $L_3 \to L_{2'}(E_F)$ transition range from 4.1 eV [7] to 4.4 eV [5]. Clearly, there is enough discrepancy in the experimental values for these energies that it will be difficult to accurately assess the effects of alloying on them.

No band structure calculation has been reported for $\alpha-Ag_{0.7}Zn_{0.3}$ but calculations do exist for $\alpha-Cu_{0.7}Zn_{0.3}$ [21,22]. In the work of Bansil, et al. [22], predictions are made for the shifts in the interband transitions of interest due to alloying. The $L_3 \to L_{2'}(E_F)$ transition is predicted to move upward by about 0.3 eV and the $L_{2'} \to L_1$ transition is to move downward in energy by 0.1 to 0.8 eV depending on the amount of lattice dilation due to alloying.

Since both transitions would be at saddle points in the Brillouin zone, a

V. Free-Electron Effects

The free and bound parts of the dielectric function have been separated by a de-convolution method which has been described elsewhere [18,19]. The Drude effective mass was found to be 1.23 free electron masses and the Drude relaxation time was found to be 1.87×10^{-14} second. These results compare well with the values found for Ag. Previous results for the effective mass of silver are $m^*/m = 1.03$ [1] and 0.97 [20]. The relaxation time in Ag was found to be 1.6×10^{-14} sec at 3 eV [17].

We thus see that the Drude part of the dielectric function predicts some flattening of the bands at the Fermi level. Although alloying will be seen to have a considerable damping effect on the interband properties of Ag, the long relaxation time found here indicates that the behavior of free electrons is not significantly changed. We may conclude that this amount of alloying has only small consequences for those electronic properties described by the Drude theory.

IV. Experimental Results

The wavelength-modulated logarithmic derivative spectrum of the reflectivity, which is the direct result of the experiment, is displayed in Figure 3. This is integrated to give the reflectivity of the sample, as shown in Figure 4. In order to perform a Kramers-Kronig analysis of the data and separate the real and imaginary parts of the dielectric function, extrapolations over all energy must be done. For the infrared region, a Hagen-Rubens extrapolation to a reflectivity of 100% at zero energy was used [16]. For the ultraviolet extrapolation, modified silver data [17] were used. Using this, the real and imaginary parts of the dielectric function, ϵ_1 and ϵ_2, are calculated. These are given in Figure 5. The dielectric function is then differentiated to give ϵ'_1 and ϵ'_2 (Figure 6).

The important point to note concerning the data is that the plasma resonance which dominates the experimental spectrum of Ag [17] is greatly damped in this alloy. In fact, ϵ_1 does not go through zero at any point in the energy range of this study, so it can be said that the amount of alloying in this sample actually eliminates the resonance. The ϵ_1 shown in Figure 5 is in excellent agreement with that of previous results [5]. Note also that the principal dip in the reflectivity is at a considerably lower energy than in pure Ag. This occurs between about 3.6 and 3.8 eV in the alloy, compared with a minimum of about 3.85 eV in pure Ag. The energy loss function, which is given in Figure 7, shows a strongly damped peak at 3.85 eV.

III. Experimental Method

Wavelength-modulated spectroscopy [10,11] was used because of the unambiguous

lineshapes obtained by this technique and the resulting ease of interpretation

of these lineshapes. The theory of wavelength-modulation spectroscopy is well

detailed elsewhere [12,13]. The theory of lineshapes near a three-dimensional

critical point was given by Batz [14,15]. It is sufficient here to give the

theoretical lineshapes for the sake of reference. All three dimensional

critical point lineshapes may be expressed in terms of a single function, $F(W)$,

which is reproduced in Figure 2. The behavior of critical points in terms of

$F(W)$ is listed in Table 1. Derivative data with a spacing of 0.02 eV between

data points were taken between 2.60 and 5.10 eV.

II. Sample Preparation

Precisely weighed amounts of 0.9999 pure Ag and 0.99999 pure Zn were sealed in quartz tubes at a pressure of less than 10^{-5} mm Hg. They were melted and thoroughly mixed by being shaken in the liquid states 5000 times and then quenched to room temperature in a water bath to form a homogeneous ingot. This ingot was, in turn, homogenized by heating to 650°C for 24 hours and then cooling slowly. After cutting and polishing, the sample was given another 24 hour anneal, this time at 225°C, and then again slow cooled. This was to relieve cold work acquired in the polishing process.

Leavings from the cutting process were assayed for Ag content by the U.S. Mint, which confirmed that the final composition was within 0.1% of $Ag_{0.70}Zn_{0.30}$.

I. Introduction

An outstanding feature of the optical properties of Ag is the sharp onset of interband transitions near 4.0 eV in the near ultraviolet, a feature which is very near the plasma resonance. This interband absorption edge is due to the overlap of contributions from d-band to Fermi level transitions and Fermi level to conduction band transitions, both in the L (111) direction in the Brillouin zone [1-3]. Optical results tend to support this interpretation [4-8], although it has been questioned by Christensen [9].

Near the absorption edge, the optical spectrum of Ag should be sensitive to alloying. Since the transitions which are involved in the absorption edge involve free electrons at either the initial or final state, alloying with Zn should shift the Fermi surface enough to separate the two transitions. In noble metals, the L_1 (s-like) level is more sensitive to the crystalline potential than the $L_{2'}$ (p-like) or the L_3 (d-like) levels [6]. (These levels are illustrated in Figure 1.) Therefore, perturbation of the potential by alloying should result in a separation of the two transitions.

Subject classification 1.3, 13.1, 20.1, 21.1, 21.6

Department of Physics, University of California, Los Angeles

Wavelength Modulated Spectra of α-$Ag_{0.7}Zn_{0.3}$ Near the Optical Absorption Edge[1]

By

R. Stearns,[2] R. Braunstein, and L. Muldawer[3]

The optical properties of α phase $Ag_{0.7}Zn_{0.3}$ have been determined near the optical absorption edge. This alloy composition eliminates the sharp Ag plasma resonance. The band shifts which are observed are in qualitative agreement with calculations which have been performed for the similar alloy, α-$Cu_{0.7}Zn_{0.3}$.

Die optischen Eigenschaften von α-Phase $Ag_{0.7}Zn_{0.3}$ wurden in der Nähe der optischen Absorptionskante bestimmt. Diese Legierungszusammensetzung eliminiert die scharfe Ag-Plasma-Resonanz. Die beobachteten Bandverschiebungen sind in qualitativer Übereinstimmung mit Berechnungen, die für die ähnliche Legierung α-$Cu_{0.7}Zn_{0.3}$ durchgeführt wurden.
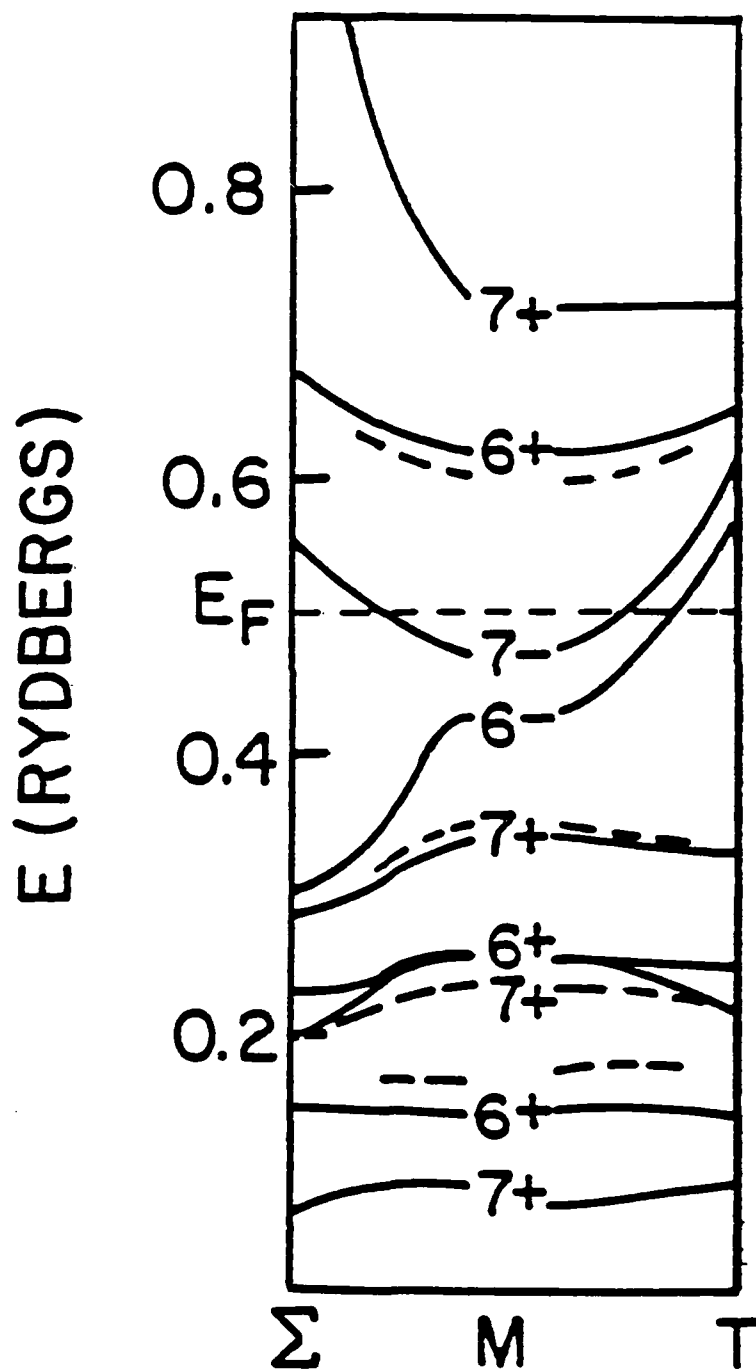
Fig. 13
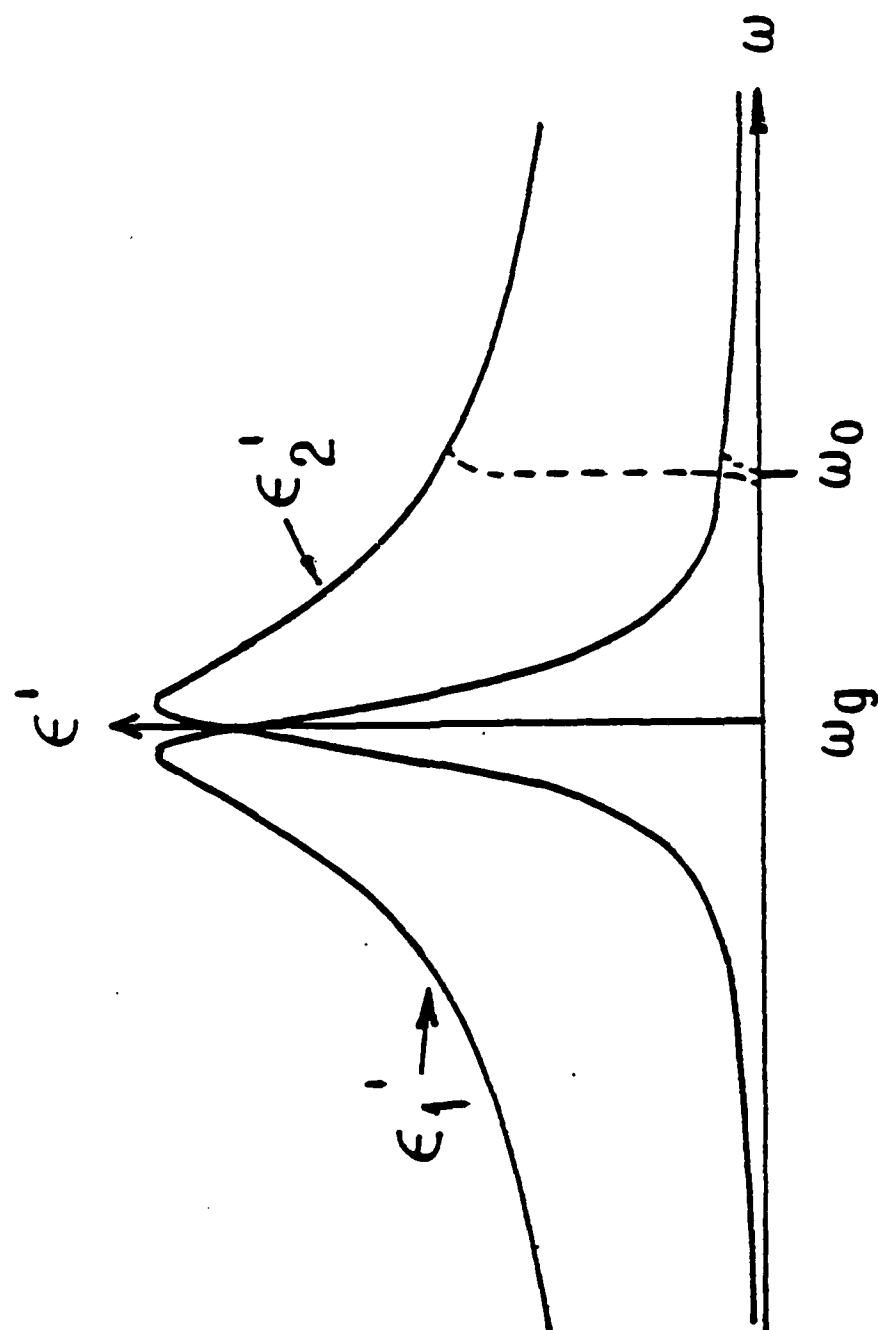
Fig. 12
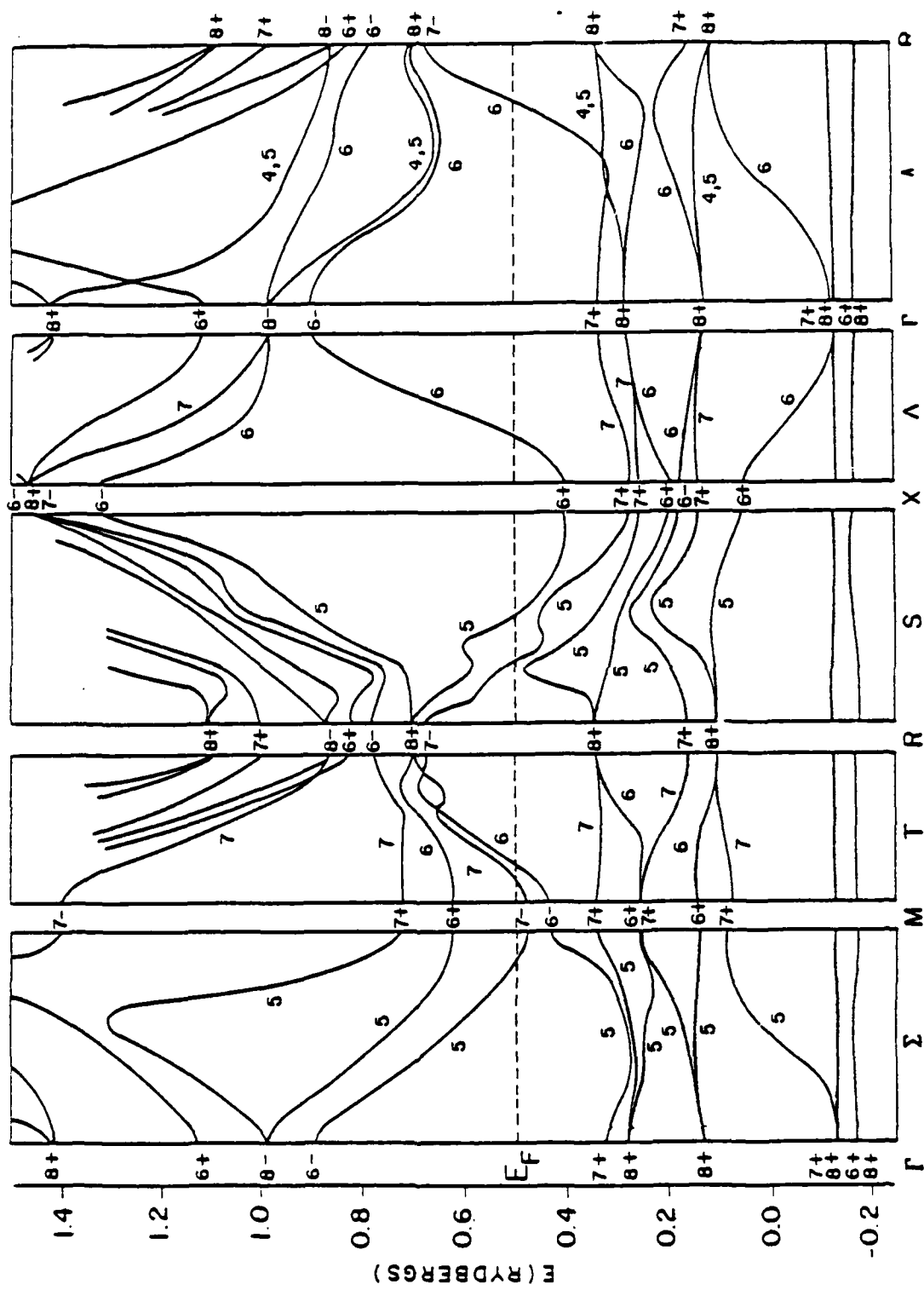
Fig. 11
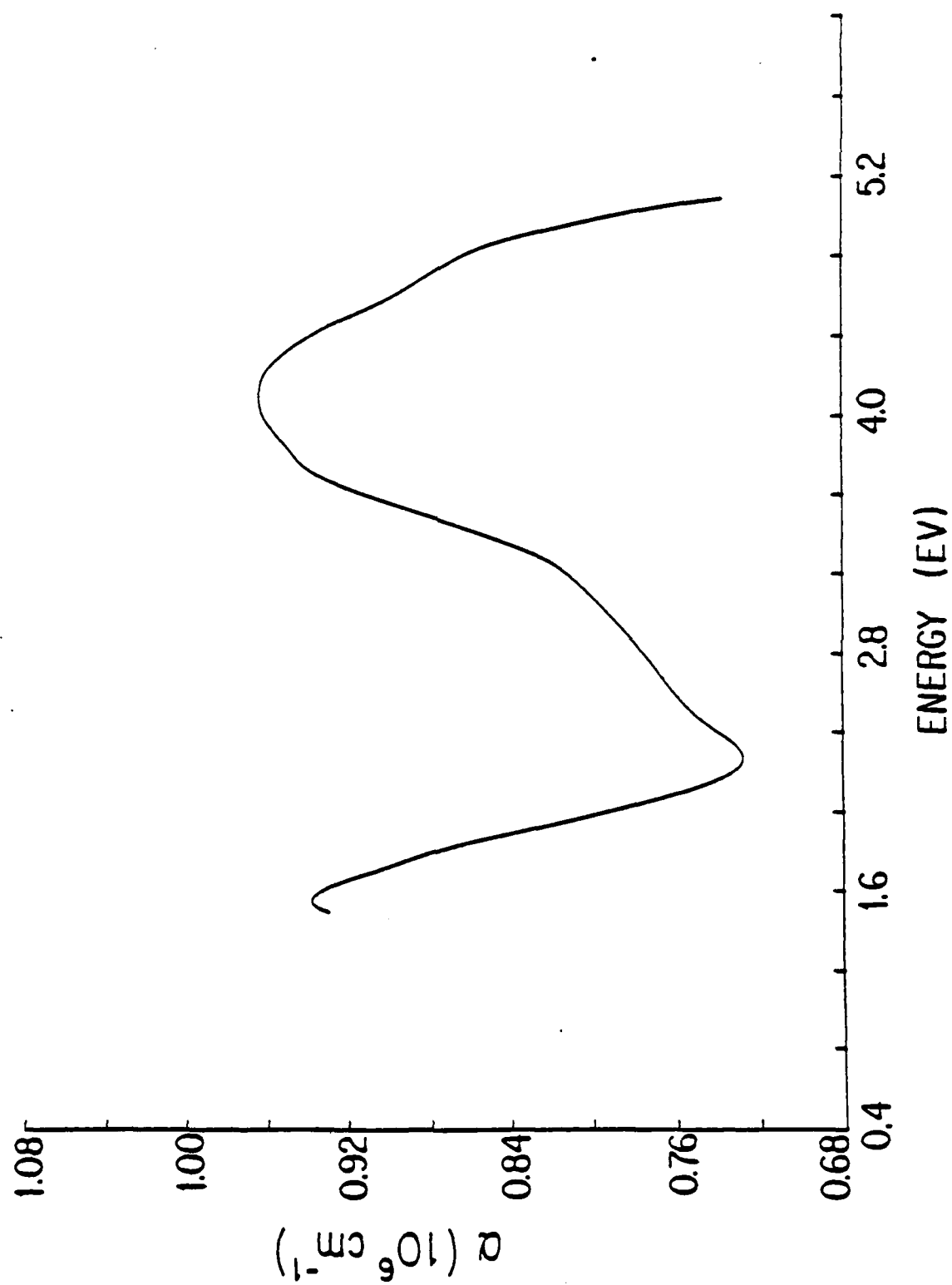
Fig. 10
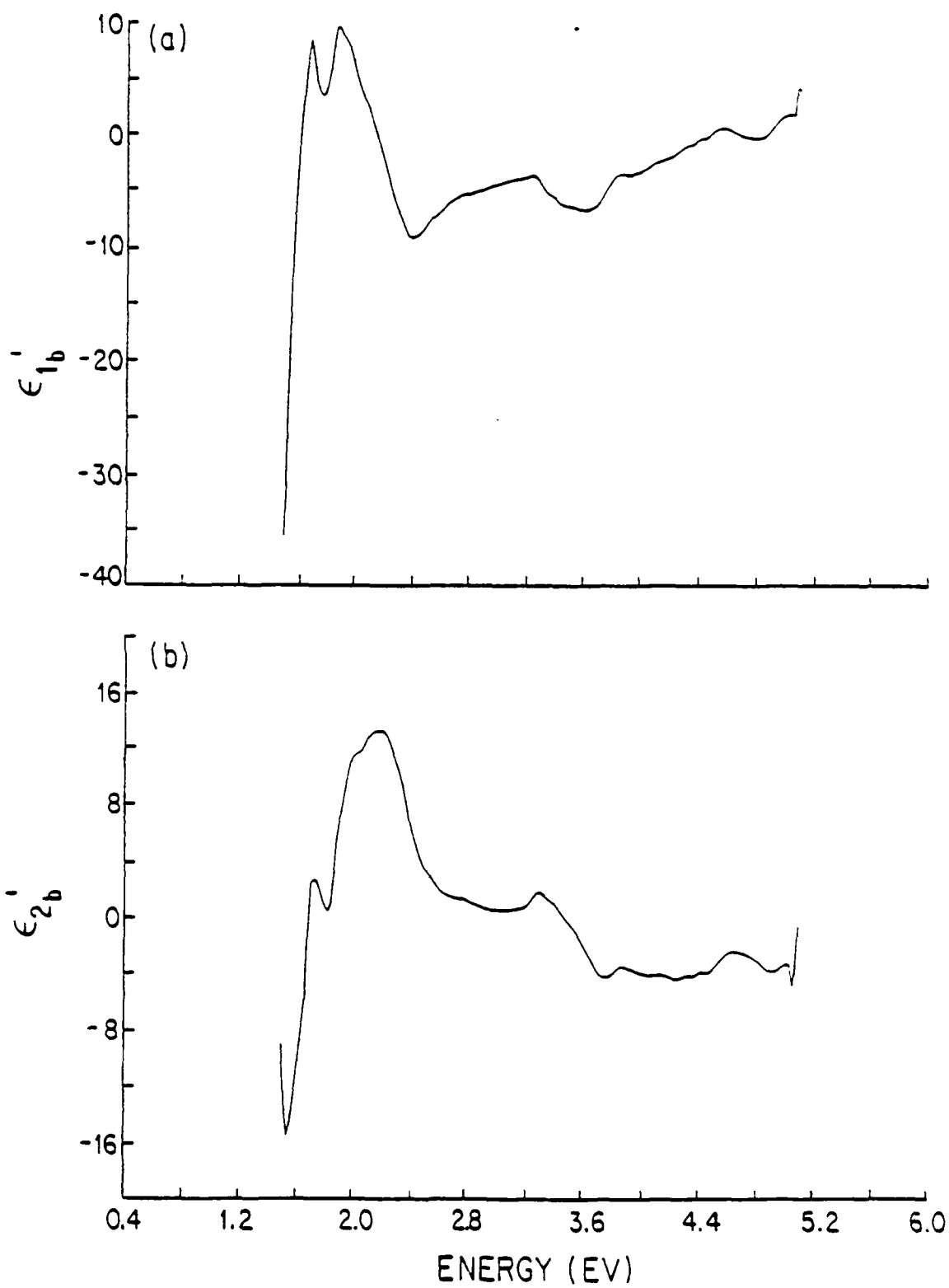
Fig. 9

References

[1] D. Beaglehole, Proc. Phys. Soc. Lond. 85, 1007 (1965); 87, 461 (1966).

[2] F. M. Mueller and J. C. Phillips, Phys. Rev. 157, 600 (1967).

[3] R. M. Morgan and D. W. Lynch, Phys. Rev. 182. 719 (1969).

[4] R. M. Morgan and D. W. Lynch, Phys. Rev. 172, 628 (1968).

[5] E. L. Green and L. Muldawer, Phys. Rev. B 2, 330 (1970).

[6] H. G. Liljenvall and A. G. Mathewson, J. Phys. C.; Suppl. Met. Phys. 3, 341 (1970).

[7] P. O. Nilsson and B. Sandell, Sol. St. Comm. 8, 721 (1970).

[8] B. F. Schmidt and D. W. Lynch, Phys. Rev. B 3, 4015 (1971).

[9] N. E. Christensen, Phys. Status Solids B 54, 551 (1972).

[10] M. Welkowsky and R. Braunstein, Rev. Sci. Instrum. 43, 399 (1972).

[11] R. Stearns, J. Steele, and R. Braunstein, Rev. Sci. Instrum. (in press).

[12] M. Cardona, Modulation Spectroscopy (Academic Press, New York, 1969).

[13] M. Welkowsky, Ph.D. Thesis, University of California at Los Angeles (1971).

[14] B. Batz, Ph.D. Thesis, Univ. Libre de Bruxelles (1967).

[15] B. Batz, Sol. St. Commun. 4, 241 (1965).

[16] N. F. Mott and H. Jones, The Theory of the Properties of Metals and Alloys (Dover Publications, New York, 1951).

[17] H. Ehrenreich and J. R. Phillipp, Phys. Rev. 128, 1622 (1962).

[18] M. Burd, R. Stearns, and R. Braunstein, Phys. Status Solidi B 117, 101 (1983).

[19] R. Stearns, Ph.D. Thesis, University of California at Los Angeles (1982).

[20] L. G. Schultz, Suppl. Phil. Mag. 6, 102 (1957).

[21] H. Amar and K. Johnson, in Optical Properties and Electronic Structure of Metals and Alloys, F. Abeles, ed. (North Holland Publ., Amsterdam, 1966),

p. 586.

[22] A. Bansil, H. Ehrenreich, L. Schwartz, and R. E. Watson, Phys. Rev. B 9, 445 (1974).

[23] M. A. Bionde and J. A. Rayne, Phys. Rev. 115, 1522 (1959).

[24] G. P. Pells and H. Montgomery, J. Phys. C 3, 5330 (1970).

Figure Captions

Fig. 1. Energy bands near the L point in pure Ag [6].

Fig. 2. Universal function, $F(W)$, derived by Batz [14,15] for lineshapes near critical points as seen in wavelength modulation spectroscopy. $F(W) = [W^2+1]^{-1/2} [(W^2+1)^{1/2} + W]^{1/2}$, where W is the reduced frequency $(\omega-\omega_g)/\eta$. $\hbar\omega_g$ is the interband energy at the critical point and η is a phenomenological broadening parameter.

Fig. 3. Wavelength-modulated logarithmic derivative of the reflectivity of α-$Ag_{0.7}Zn_{0.3}$.

Fig. 4. Reflectivity of α-$Ag_{0.7}Zn_{0.3}$, found by integrating the data from Fig. 3.

Fig. 5. Dielectric function of α-$Ag_{0.7}Zn_{0.3}$ determined by a Kramers-Kronig analysis of the reflectivity data. a) real part, ϵ_1; b) imaginary part, ϵ_2.

Fig. 6. Derivative with respect to energy of the dielectric function of α-$Ag_{0.7}Zn_{0.3}$. a) real part, ϵ'_1; b) imaginary part, ϵ'_2.

Fig. 7. Energy loss function of α-$Ag_{0.7}Zn_{0.3}$.

Fig. 8. Bound part of dielectric function α-$Ag_{0.7}Zn_{0.3}$ determined by subtracting the Drude contribution from the data of Fig. 5. a) real part, ϵ_{1_b}; b) imaginary part, ϵ_{2_b}.

Fig. 9. Derivative with respect to energy of the bound part of the dielectric function of α-$Ag_{0.7}Zn_{0.3}$. a) real part, ϵ'_{1_b}; b) imaginary part, ϵ'_{2_b}. With reference to the energy bands in Fig. 1, the following transitions are identified: $L_{2'}(E_F) \rightarrow L_1$ (3.55 eV), $L_{2'} \rightarrow L_1$ (3.83 eV), $L_3 \rightarrow L_{2'}(E_F)$ (4.37 eV).

Table 1. Derivative of Critical Points with Broadening Included in Terms of $F(W)$

$$F(W) = [(W^2+1)^{1/2} + W]^{1/2}/(W^2+1)^{1/2} , \qquad W = (\omega - \omega_g)/\eta$$

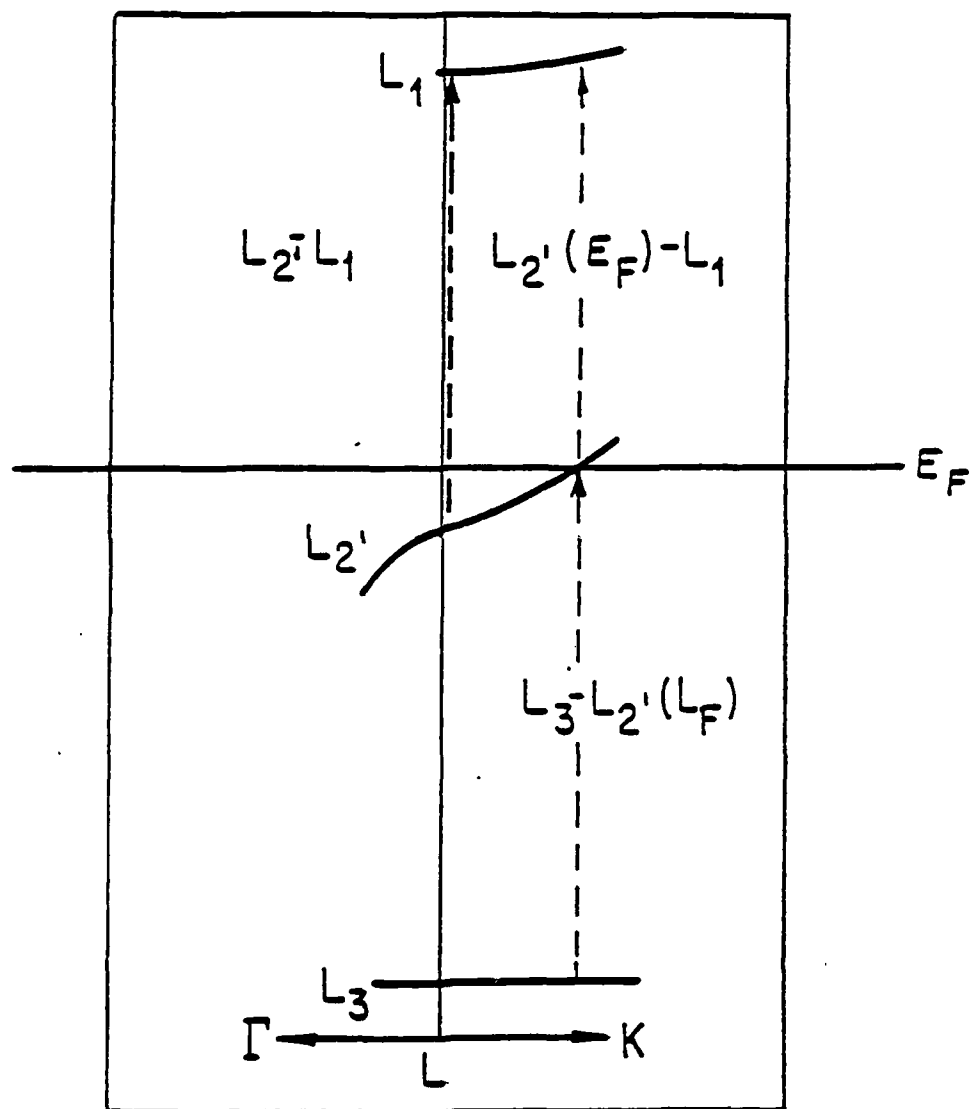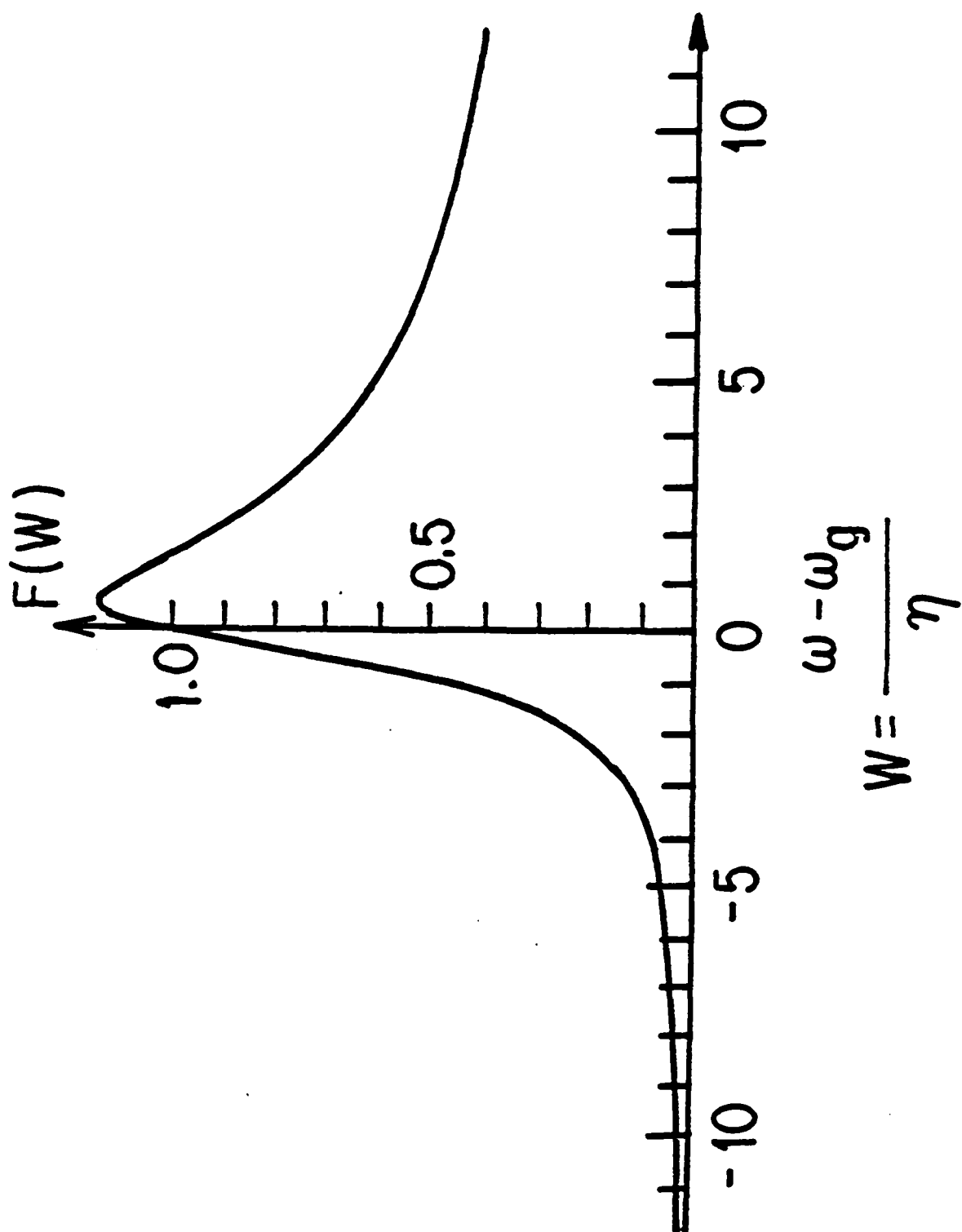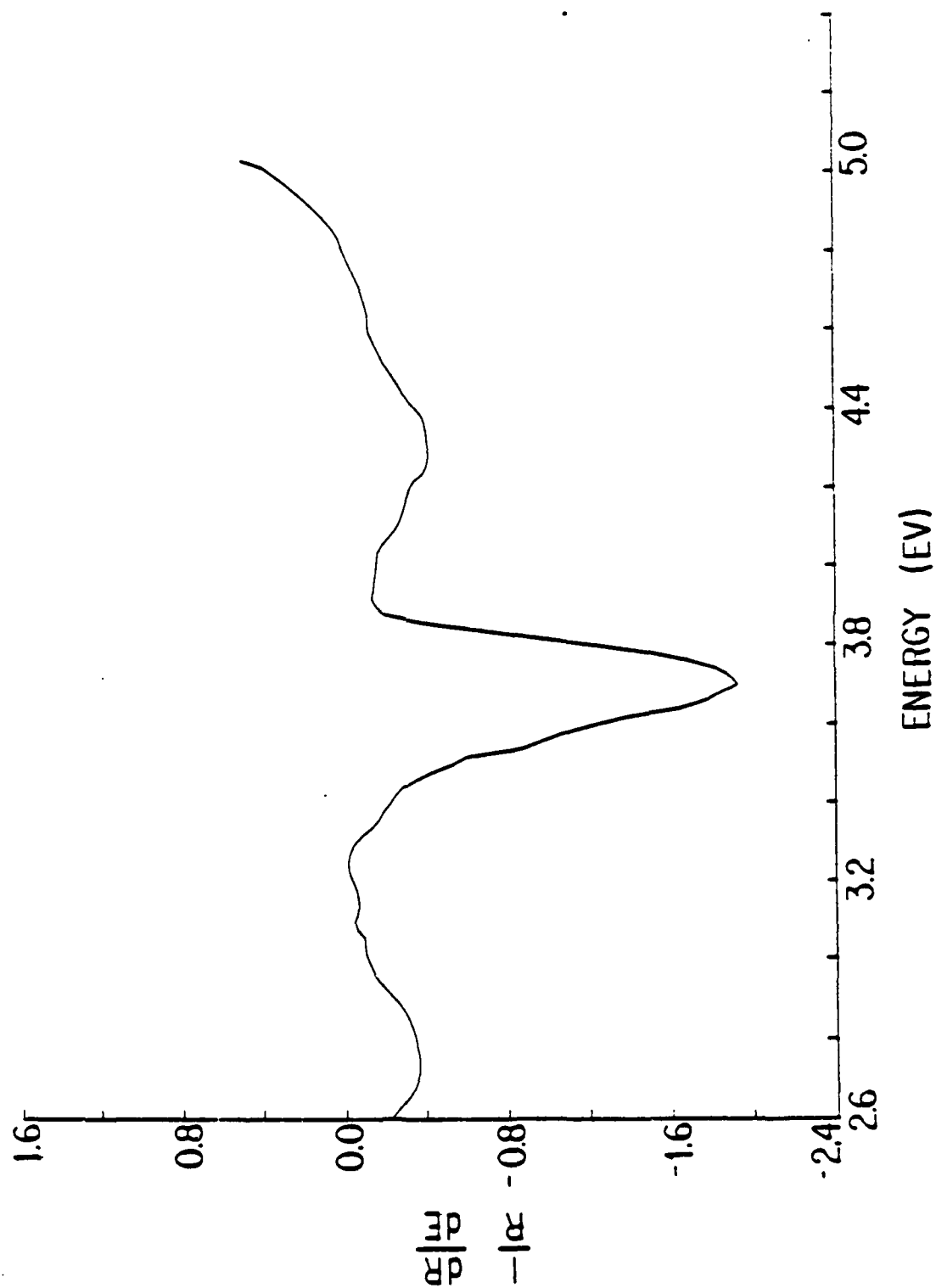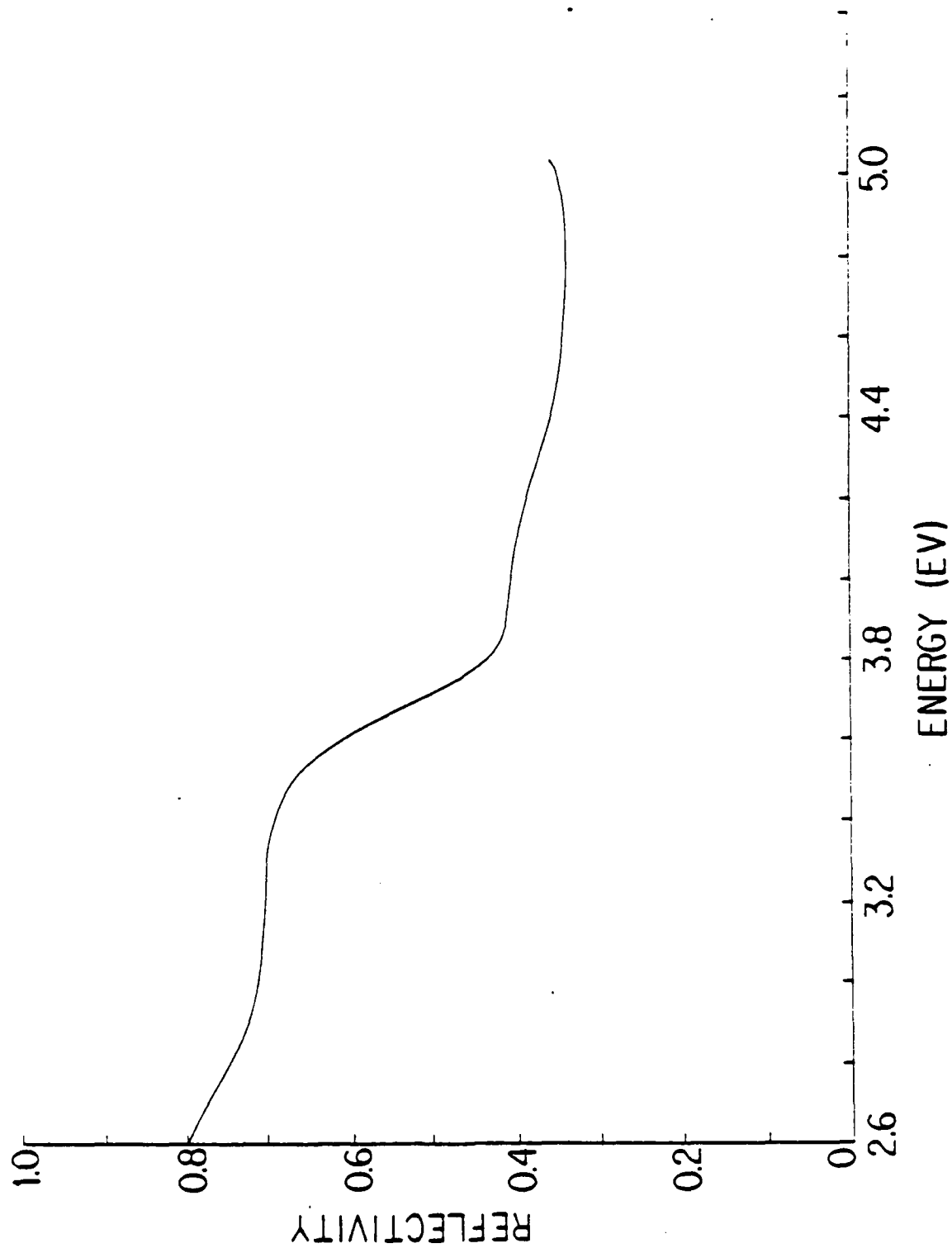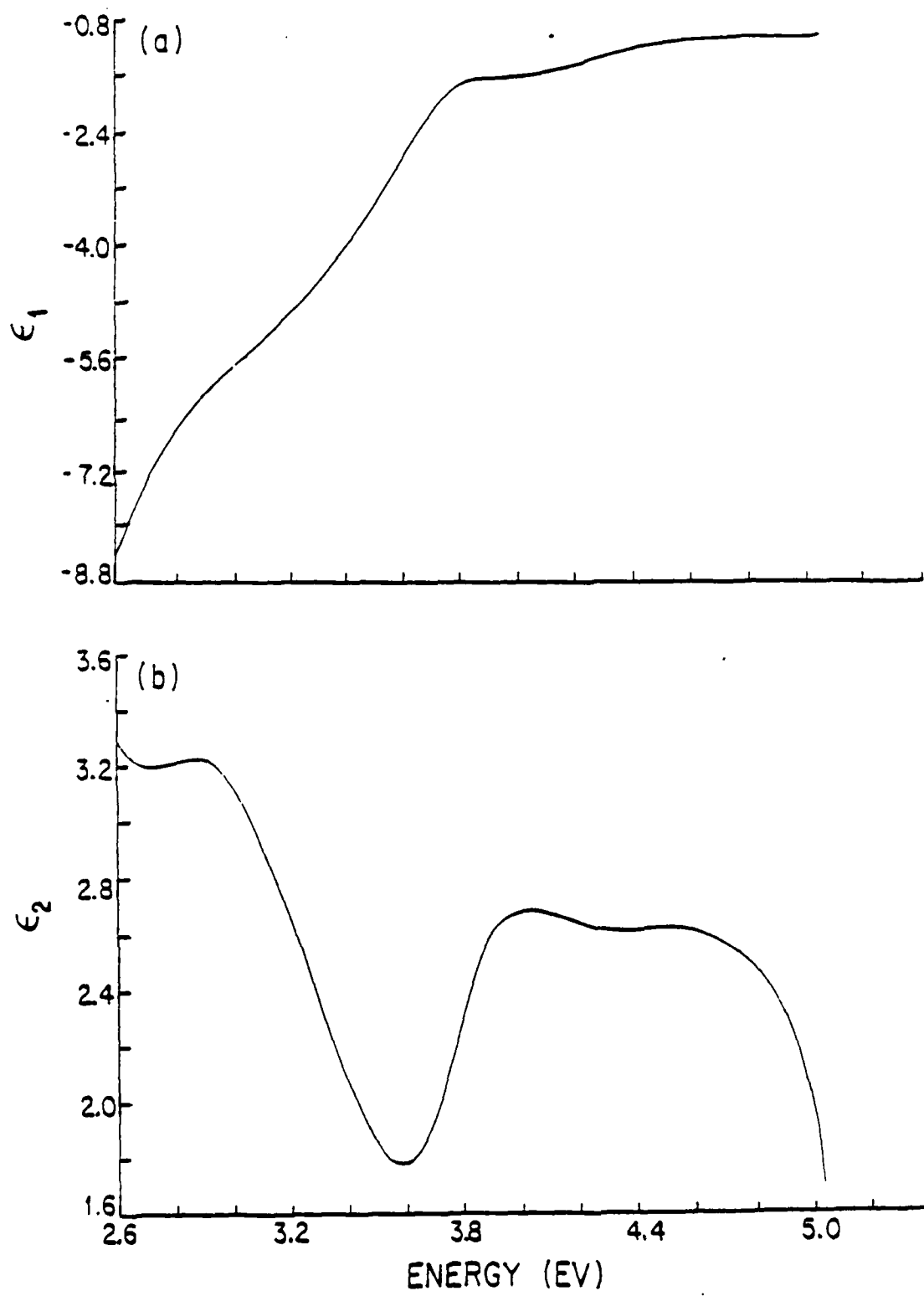| Critical Point	$2\eta^{1/2} \dfrac{d\varepsilon_1}{d\omega}$	$2\eta^{1/2} \dfrac{d\varepsilon_2}{d\omega}$
M_0	$F(-W)$	$F(W)$
M_1	$-F(W)$	$F(-W)$
M_2	$-F(-W)$	$-F(W)$
M_3	$F(W)$	$-F(-W)$

Fig. 1

Fig. 2

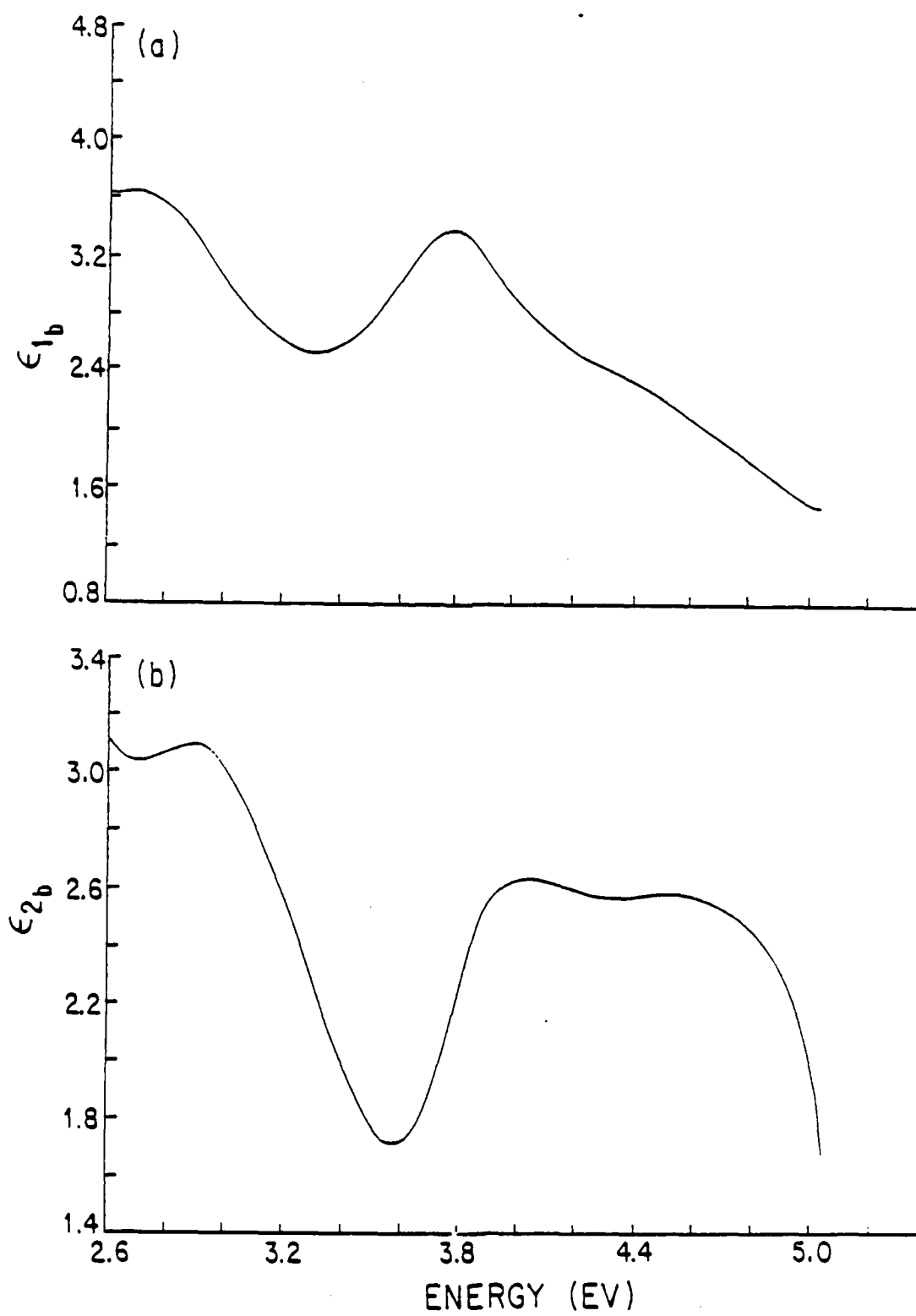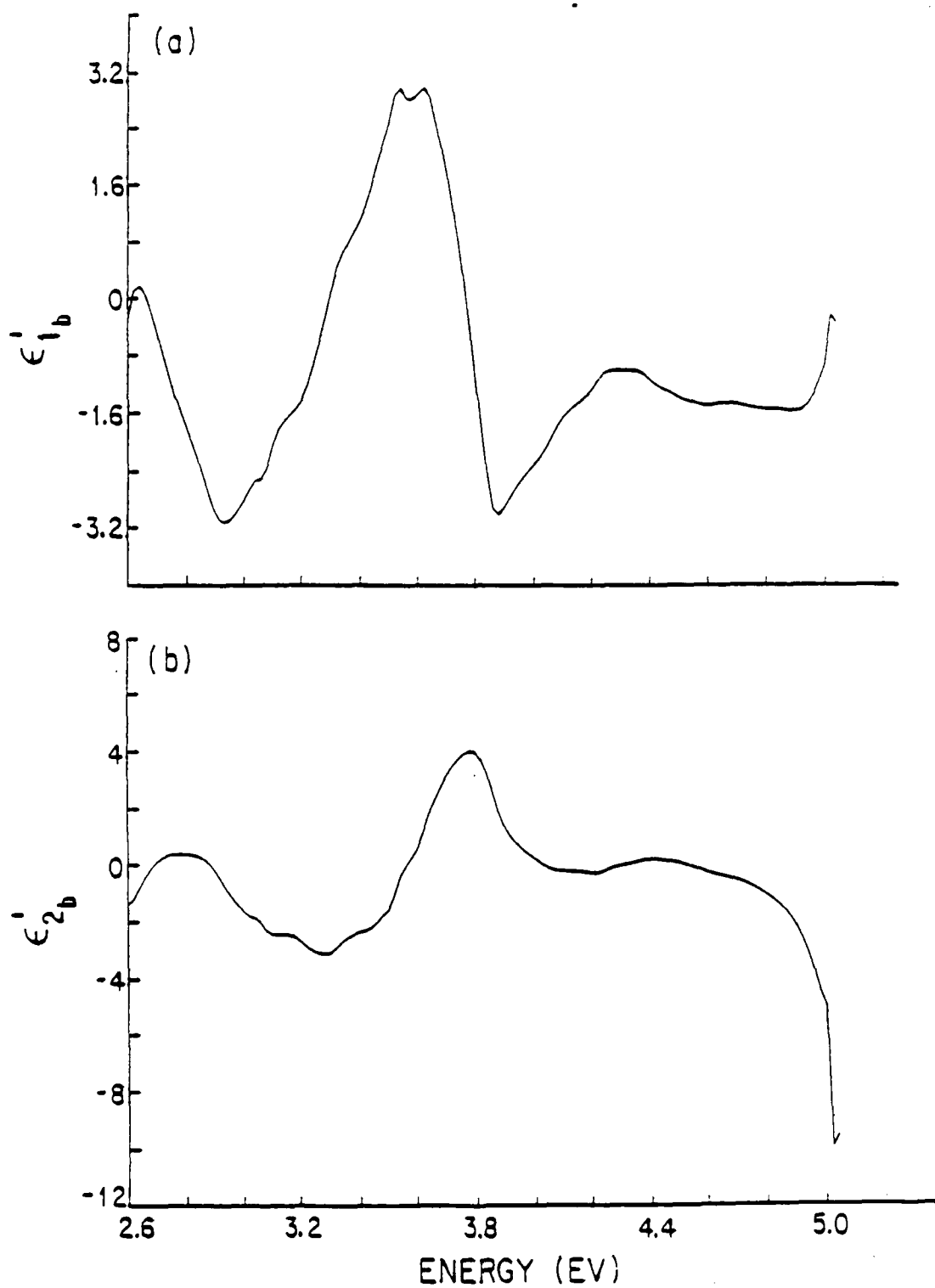Fig. 3

Fig. 4

Fig. 5
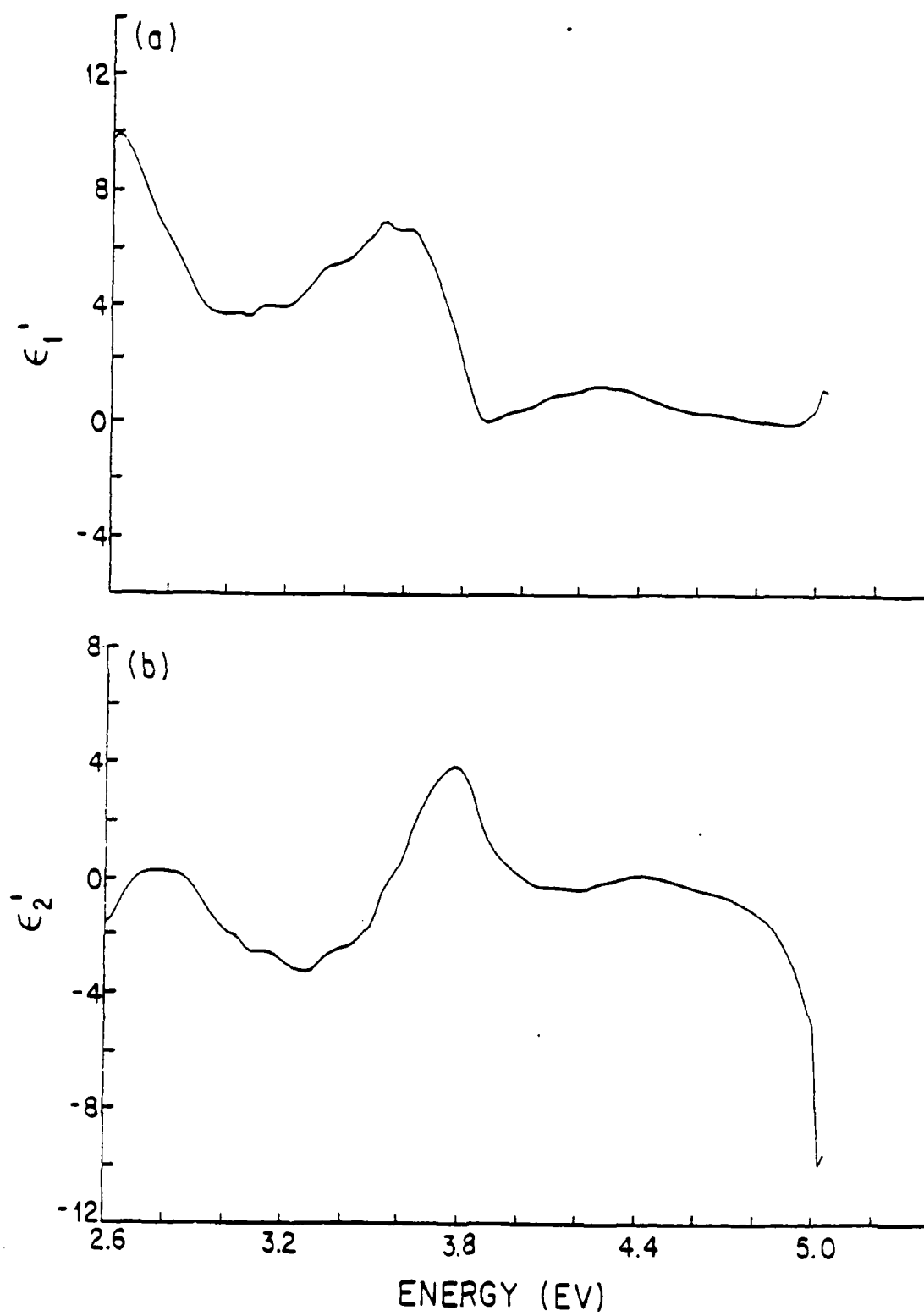
Fig. 6
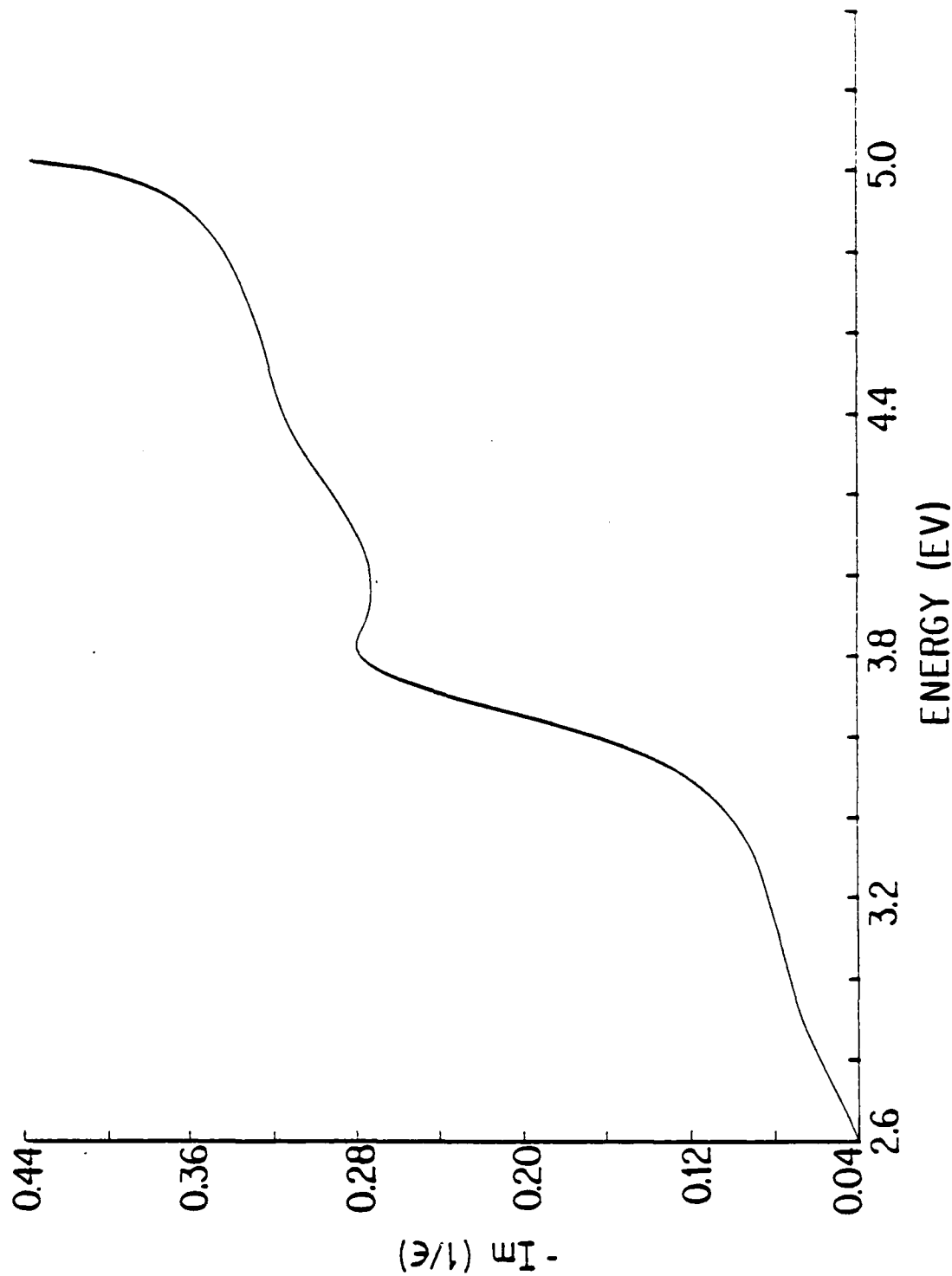
Fig. 7

Fig. 8

Fig. 9

Subject classification 1.3, 13.1, 20.1, 21.1, 21.6

Department of Physics, University of California, Los Angeles

Wavelength-Modulated Spectra of the Optical Properties of $\beta'-Cu_xZn_{1-x}$ From 1.5 to 5.1 eV at the $\beta' \rightleftarrows \alpha+\beta'$ Phase Transition[1]

By

R. Stearns,[2] R. Braunstein, and L. Muldawer[3]

Wavelength-modulated derivative spectra of the reflectivity of $\beta'-Cu_xZn_{1-x}$ have been determined between 1.5 and 5.1 eV for compositions near the $\beta \rightleftarrows \alpha+\beta'$ phase transition. The alloys have been annealed and quenched in the β' phase on both sides of the phase transition. Both the intraband and interband properties show marked changes at the transition. The Drude effective mass increases dramatically for the β' phase in the region where $\alpha+\beta'$ composition is thermodynamically preferred, indicating flattening of the bands. Shifts in interband properties also show a marked change at the phase transition, with the conduction bands showing a much greater sensitivity than the d-bands.

Wellenlängen-modulierte Ableitungsspektren des Rückstrahlvermögens von $\beta'-Cu_xZn_{1-x}$ wurden zwischen 1.5 und 5.1 eV für Zusammensetzungen nahe des $\beta' \rightleftarrows \alpha+\beta'$ Phasenübergangs bestimmt. Die Legierungen wurden in der β'-Phase auf beiden Seiten des Phasenübergangs ausgeglüht und abgeschreckt. Sowohl die Innerband- als auch die Zwischenbandeigenschaften zeigen ausgeprägte Änderungen am Übergang. Drudes effektive Masse steigt für die β'-Phase in dem Bereich, wo

IX. Conclusions

There are three major experimental facts arising from this investigation which need to be brought together to provide a unified picture of the physics of this alloy system. They are:

(1) The effective mass for intraband transitions has a sharp, large increase as we go from the β' field to the $\alpha+\beta'$ field, while maintaining a β' structure.

(2) The energy differences for the valence band-to-conduction band critical points first rise upon going to lower composition and then drop significantly upon crossing the phase boundary.

(3) The onset of d-band-to-valence band transitions moves to lower energy as the Zn concentration decreases, but the effect is much less than in (2).

We note from these observations that there is a considerable flattening of the valence bands upon crossing the phase boundary. There is also a downward shifting of both the conduction and the Cu d-bands with respect to the valence bands, although the shift of the conduction bands is much greater than the shift of the d-bands. The explanation of these results must form the basis for future band calculations in this alloy system.

VIII. d-Band Transitions

The band structure of Figure 17 shows that the Cu d-bands lie 4 to 6 eV below

the Fermi surface. There are several points in the Brillouin zone where d-band

to Fermi surface transitions are possible, with the energies of the onsets being

approximately equal. However, the critical point structure of these transitions

will not be seen because the transition at the actual extremum of the optical

band would be a filled state-to-filled state transition. For example, the band

picture shows that the transition $T_2 \rightarrow T_5$ occurs at about 4.1 eV. The critical

point of this transition is at $M_2 \rightarrow M_{5'}$. The band is filled at $M_{5'}$, so the

extreme point will not be seen.

When this kind of transition occurs, the critical structure is missing and

only relatively small breaks in the derivatives of ϵ_b are seen. In addition,

it is unlikely that these d-band to Fermi surface transitions will cause large

structures in the $\Delta R/R$ derivative data, and this is confirmed in our

experimental data. This is distinctly different from other reflectivity data

[19], where a series of structures are seen extending from 3.7 eV to higher

energies. The reason for this discrepancy is not clear.

In the 48% and 50% Zn samples, there is evidence for breaks in the

derivatives, as discussed, at about 3.7 eV. In the 46% Zn sample, the first

such break occurs at 3.6 eV. These results are slightly lower than the band

structure of Amar and Johnson [3,4] would indicate. Skriver and Christensen

[8] show that the d-bands lie 3 to 5 eV below the Fermi surface, which would

be considerably lower than our results. Thus, the d-band-to-Fermi surface energy

difference is much less affected by the crossing of the phase boundary than are

the Fermi surface-to-conducting band energy differences, in agreement with [19].

remains, but it has moved to higher energy, in agreement with [19]. The $M_5 \rightarrow M_1$ critical point is at 3.36 eV and the M_5, $\rightarrow M_3$ critical point is at 3.60 eV. This also represents a slightly greater separation between the two conduction bands. There are again breaks in the derivative spectra at 2.1, 2.2, and 2.6 eV, for this composition, which have the same interpretation as the corresponding structures seen in the 50% copper sample.

The $Cu_{0.54}Zn_{0.46}$ presents a considerably different picture of the interband transitions as measured by the derivatives of ϵ_{1_b} and ϵ_{2_b} (Figures 15c and 16c). The M_5, $\rightarrow M_1$ critical point is at 3.01 eV and the M_5, $\rightarrow M_3$ critical point is at 3.29 eV. The break at 1.9 eV is the onset of transitions to the lower conduction band and the break at 2.4 eV is due to transitions to the upper conduction band.

For each of the samples in this investigation, the derivative of ϵ_{1_b} is dominated by a large negative dip which is due to the M_5, $\rightarrow M_1$ transition. The peak due to the M_5, $\rightarrow M_3$ transition is a perturbation which is superimposed on the major dip. The critical point energies are greater for $Cu_{0.52}Zn_{0.48}$ than for $Cu_{0.50}Zn_{0.50}$, but are then again lower for the $Cu_{0.54}Zn_{0.46}$ sample. This indicates that there are competing forces whose interplay determines the transition energies.

conduction band at M_1. Therefore the transition M_5, $\to M_1$ is a maximum of the optical band, an M_3 critical point. This is not the case, however, for the M_5, $\to M_3$ transition. The conduction band rises much faster than the valence band in the Σ direction, but is again shallower than the valence band in the T direction of the Brillouin zone. Therefore, the optical band has a saddle-point type of critical point for this transition.

In the derivative of ε_{1_b} for $Cu_{0.50}Zn_{0.50}$ (Figure 15a), the critical point structure is found in the double dip structure centered at about 3.1 eV. Since an M_3 critical point has a positive derivative in ε_{1_b} at the critical point, the M_5, $\to M_1$ transition is associated with the positive peak at the center of the double structure. The associated structure in the derivative of ε_{2_b} (Figure 16a) is the local dip in the descending derivative at 3.14 eV. The centrum of these two structures is the location of the critical point, 3.16 eV. The assignment of the M_5, $\to M_3$ given to the local minimum in the derivative of ε_{1_b} at 3.26 eV. The corresponding structure in the derivative of ε_{2_b} is the minimum at 3.32 eV. The position of the critical point is thus at 3.29 eV. This is in close agreement with the calculations of Amar and Johnson [3,4], but is somewhat higher in energy than the theory of Skriver and Christensen [8] and the results of Muldawer and Goldman [19].

The onsets of these transitions are associated with breaks in the derivatives at lower energies. There are breaks in the derivatives at 2.1 and 2.2 eV which could be assigned to onsets at $T_5 \to T_1$ and $\Sigma_4 \to \Sigma_1$, respectively. The break at 2.5 eV could then be assigned to the onset at $T_5 \to T_2$, although this should be regarded as speculative.

In $Cu_{0.52}Zn_{0.48}$, the onsets of the transitions have remained at pretty much the same energies, while the critical points have moved to higher energies. Note (in Figures 15b and 16b) that the double structure at the critical points

VII. Fermi Level-to-Conduction Band Transitions

Once the Drude parameters have been determined, they may be used in the classical Drude expressions for the dielectric function to subtract the intraband contribution from the total experimentally determined dielectric function. The remaining functions are the interband parts of the dielectric function. The real parts of this, ϵ_{1_b} , are displayed in Figure 13, while the imaginary parts, ϵ_{2_b} , are given in Figure 14 for the three samples. The derivatives of these are shown in Figures 15 and 16, respectively. These results are now used to analyze and assign the interband transitions in the alloy system.

The band structure of ordered beta-brass as calculated by Amar and Johnson [3,4] is shown in Figure 17. The derivatives of interband parts of the dielectric function which have been measured may now be compared to the band calculations using the theory of Batz [16,17] for wavelength modulation data.

The onset of interband transitions has previously been identified as the Fermi level to conduction band transitions, $\Sigma_4 \rightarrow \Sigma_1$ and $T_5 \rightarrow T_1$ [2,4]. The critical point of the transition, then, is $M_{5'} \rightarrow M_1$. It would be expected that there would be a double structure due to the transition $M_{5'} \rightarrow M_3$. The above band structure shows a value of 2.0 eV for the onset of transition $T_5 \rightarrow T_1$ and 2.3 eV for the transition $\Sigma_4 \rightarrow \Sigma_1$. It shows that the $M_{5'} \rightarrow M_1$ transition has an energy of 3.3 eV. Therefore, we should expect to see a break in the derivatives of the dielectric function due to the onset at about 2.0 eV followed by an enhancement near 2.3 eV. This would then be followed by a double extreme point structure near 3.3 eV.

We can also determine from the band structure the type of three-dimensional critical point to expect. The band at $M_{5'}$ has greater curvature than the

VI. Plasma Resonance

Before making interband assignments, we need to look at the structure which dominates the experimental spectrum, the main plasma resonance which is responsible for the main dip in the reflectivity. The plasma resonance occurs when the real part of the dielectric function goes through zero. In the CuZn system this happens at a point very near to the onset of interband transition. For the 50% zinc sample, the plasma resonance is at 2.45 eV, while for the 48% and 46% zinc samples the resonance is at 2.57 and 2.59 eV. The peak in the energy loss function (Figure 12) due to the plasma resonance is greatly damped because of the relatively large values of ϵ_2 in the region. This is because of the proximity of the onset of interband transitions to the plasma resonance.

V.   Intraband Transitions

The intraband and interband contributions to the dielectric function have been separated using a method of deconvolution which was previously described [21,22]. The values of the Drude effective mass and relaxation time for each alloy composition are given in Table 2.

The relaxation times are slightly higher than others have found by optical means for this alloy system [19,20]. However, it should be noted that the relaxation times calculated from resistivity data are an order of magnitude larger than those found by optical means [19].

The most striking feature of the data in Table 2 is the change in effective mass. The values of 1.20 for 50% and 1.17 for 48% zinc are not far from the value of 1.4 reported for 50% zinc [20]. The effective mass of 1.89 free-electron masses found for the 46% zinc sample represents a significant departure from the other compositions. This means that there is a considerable flattening of the energy bands near the Fermi surface when the $\beta' \rightarrow \alpha+\beta'$ phase transition has been crossed (Figure 3) at the lower zinc concentration.

this matter, it is similar to the data which Jan and Vishnubhatla [20]

obtained for CuZn. The reasons for this will be discussed in the later section

on interband transitions.

IV. Experimental Results

The logarithmic derivatives of this series of samples, which are the direct
experimental results, are illustrated in Figure 6. These are integrated to
yield the reflectivities, shown in Figure 7. In order to analyze these results,
the dielectric function must first be calculated.

The Kramers-Krönig dispersion relation must be used to find the phase shift,
so that other optical properties may be calculated from the reflectivity and
the phase shift. To perform the integrals involved, the reflectivities must be
extrapolated over the entire energy spectrum. On the infrared side, a
Hagen-Rubens [18] extrapolation is used to match the low energy end of the
experimental spectrum and a reflectivity of 100% at zero energy. The data of
Muldawer and Goldman [19] are used from 5.1 to 18 eV. At higher energies, a
constant reflectivity was used. This brings us into consistency with the other
work [19], so results may be compared. Using this information, the real and
imaginary parts of the dielectric function, ϵ_1 and ϵ_2, are calculated. These
are found in Figures 8 and 9. Their derivatives are found numerically and are
displayed in Figures 10 and 11.

There are several points to note about the reflectivity data. The position
of the main minimum in the reflectivity moves from lower to higher energy as the
copper concentration decreases. The minima are at 2.48, 2.64, and 2.68 eV for
50, 48, and 46% zinc, respectively. This is in agreement with the results of
Muldawer and Goldman [19]. The depth of the reflectivity minimum increases as
the zinc concentration increases. At 50% zinc the minimum reflectivity is
35.2%, while at 46% zinc the minimum is at 16.9%.

The final note is that the reflectivity at higher energies is essentially
featureless and does not show the structure which has been reported [19]. In

III. Experimental Method

Wavelength-modulation spectroscopy [12,13] was used because of the unambiguous lineshapes obtained by the technique and the resulting ease of interpretation of those results. The theory of wavelength-modulation spectroscopy is well detailed elsewhere [14,15]. The theory of lineshapes near a three-dimensional critical point was given by Batz [16,17]. It is sufficient here to give the theoretical lineshapes for the sake of reference. All three-dimensional critical point lineshapes may be expressed in terms of a single function, $F(W)$, which is reproduced in Figure 5. The behavior of critical points in terms of $F(W)$ is listed in Table 1. Derivative data with a resolution of 0.02 eV were taken between 1.50 and 5.10 eV.

The ultimate limit of the wavelength modulation derivative spectrometer used in this investigation is to be able to detect a derivative signal of the order of $\Delta R/R \sim 10^{-5}$. It is important to remember that when the experimental signal is actually of this order, the signal-to-noise ratio is about 1. This will also be seen in the integral optical functions. Also, when the derivative is nearly flat, the same considerations may lead to noise in the optical functions. We may express this analytically as saying that the error bars will be larger when $\Delta R/R$ is small or when $d(\Delta R/R)/d\lambda$ is small.

This is the source of the anomalous structure which will be seen at the low energy end of these spectra. This is also the source of the noise in the high energy regions which make exact assignment of d-band-to-conduction band transitions impossible.

II. Sample Preparation

A series of samples was produced by melting high-purity copper and zinc in sealed evacuated quartz tubes. Sample composition was determined by a micro-probe analysis. The three samples were found to be $Cu_{0.54}Zn_{0.46}$, $Cu_{0.52}Zn_{0.48}$, and $Cu_{0.50}Zn_{0.50}$. The samples were cut with a string saw and polished, the final polish being with 0.3 micron alpha alumina polishing compound. They were then annealed for one hour at high temperature in the β phase, again in evacuated quartz tubes. The samples were quenched to room temperature and given a final light polish to remove any oxide layer. A final low temperature anneal at 100°C relieved any residual cold work. This temperature was low enough to prevent dezincification or precipitation of the α or γ phase.

Crystal structures of the samples were determined by x-ray diffraction analysis. Figures 4a and 4b show the scans of the $Cu_{0.54}Zn_{0.46}$ and $Cu_{0.52}Zn_{0.48}$ samples. The diffraction line at 43.3 degrees in each is due to β phase material. If there were any α phase material present, it would reveal itself by producing a line at 42.2 degrees. Thus, we may conclude that these are pure β phase samples. Figure 4c shows the first scan of the $Cu_{0.50}Zn_{0.50}$ sample, showing an additional line present at 44.7 degrees for this sample. This is due to a martensitic phase, which is a deformation of the β phase. This is caused by unrelieved thermal stresses which occur in the quenching process [11]. An additional 48-hour low temperature anneal was given to relieve these stresses. This produced the results shown in Figure 4d, which indicate that pure β phase material has again been obtained.

The phase diagram of the CuZn alloy system is given in Figure 3 [9]. The β' phase is an ordered alloy of the CsCl(B2) type. This phase exists at low temperature within a narrow range of compositions. At higher temperatures it disorders to the β phase which is a random alloy with a body-centered cubic structure. It should be noted that the $\beta \rightarrow \beta'$ transformation cannot be suppressed by quenching [10]. At lower zinc compositions the β' phase goes into an $\alpha + \beta'$ phase. Pure β' phase material may be quenched from the β phase even in the composition range where the $\alpha + \beta'$ phase is thermodynamically preferred at room temperature.

It should be instructive, then, to examine the optical properties, with their implications for band structure, as the $\beta' \rightleftarrows \alpha + \beta'$ phase boundary is crossed. If samples are obtained which have pure β' composition on both sides of the boundary, the effects of the changes in the crystal potential due to the thermodynamic stresses involved when the crystal is not in its lowest energy state may be studied. The intent of this study is to provide experimental data concerning the optical properties of this alloy system near this phase boundary, in order to stimulate continued theoretical interest in this problem.

I. Introduction

Ordered beta brass (β'-CuZn) is a traditional prototype binary alloy obeying

the Hume-Rothery rules [1]. Its theoretical electronic band structure, Fermi

surface phase stability, optical and other properties have been the subjects of

extensive study [2-8]. The wavelength-modulated spectra of the optical

properties of a series of compositions of this alloy system have been studied

in the hope that they will help lead to a better determination of the Cu and Zn

potentials.

The individual shapes of conduction and Cu d-bands are, according to

calculations [2], largely independent of small variations in crystal potential;

however, the relative position of the d-bands and conduction bands were shown

to be very sensitive to the nature of the potential. The bands originating

from the d and lower core electrons of the elements depend primarily on the

nature of the potentials within a radius of one atomic unit [3]. Self-

consistent free-atom potentials provide a reasonably accurate description of

the fields experienced by these electrons. It is the behavior of the potential

between 1 a.u. and the atomic cell boundary which is most uncertain. The

energies of the valence electrons are very sensitive to variations of the

potential in this region and to changes of the constant potential V_o between

muffin-tin spheres. The conduction bands can be shifted relative to the d-bands

simply by altering the slopes of the potentials beyond a radius of 1 a.u. or by

adjusting V_o. This is illustrated in Figure 1 for several possible potentials

chosen for Cu and Zn. The resulting band profiles for the stoichiometric alloy

along the (110) direction in the cubic Brillouin zone are shown in Figure 2.

It can be seen that the d-bands are effectively shifted with respect to the

conduction bands for various choices of potentials.

die α+β'-Zusammensetzung thermodynamisch bevorzugt ist, dramatisch an, was ein

Abflachen der Bänder anzeigt. Verschiebungen in Zwischenbandeigenschaften

bestätigen diese Deutung und weisen auf konkurrierende physikalische

Mechanismen hin, die diese Verschiebungen verursachen.

References

[1] W. Hume-Rothery, J. Inst. Metals 35, 309 (1926).

[2] K. H. Johnson and H. Amar, Phys. Rev. 139, A760 (1965).

[3] H. Amar, K. H. Johnson, and K. P. Wang, Phys. Rev. 148, 672 (1966).

[4] H. Amar and K. H. Johnson, in Optical Properties and Electronic Structure of Metals and Alloys, F. Abeles, ed. (North Holland, Amsterdam, 1966), p. 586.

[5] F. J. Arlinghaus, Phys. Rev. 157, 491 (1967).

[6] F. J. Arlinghaus, Phys. Rev. 186, 609 (1969).

[7] V. L. Moruzzi, A. R. Williams, and J. F. Janak, Phys. Rev. B 9, 3316 (1974).

[8] H. K. Skriver and N. E. Christensen, Phys. Rev. B 8, 3778 (1973).

[9] M. Hansen, Constitution of Binary Alloys (McGraw-Hill, New York, 1958).

[10] M. Hansen, Z. Physik 59, 466 (1930).

[11] F. Seitz, The Physics of Metals (McGraw-Hill, New York, 1943).

[12] M. Welkowsky and R. Braunstein, Rev. Sci. Instrum. 43, 399 (1972).

[13] R. Stearns, J. Steele, and R. Braunstein, Rev. Sci. Instrum. 54(8), 984 (1983)

[14] M. Cardona, Modulation Spectroscopy (Academic Press, New York, 1969).

[15] M. Welkowsky, Ph.D. Thesis, University of California at Los Angeles (1971).

[16] B. Batz, Ph.D. Thesis, Univ. Libre de Bruxelles (1967).

[17] B. Batz, Sol. St. Commun. 4, 241 (1965).

[18] N. F. Mott and H. Jones, The Theory of the Properties of Metals and Alloys (Dover Publications, New York, 1958).

[19] L. Muldawer and H. J. Goldman, in Optical Properties and Electronic Structure of Metals and Alloys, F. Abeles, ed. (North Holland, Amsterdam, 1966), p. 574.

[20] J. P. Jan and S. S. Vishnubhatla, Can. J. Phys. 4S, 2S0S (1967).

[21] M. Burd, R. Stearns, and R. Braunstein, Phys. Stat. Solidi (b) 117, 101 (1983).

[22] R. Stearns, Ph.D. Thesis, University of California at Los Angeles (1982).

Figure Captions .

Figure 1.   Comparison of crystal potentials for β'-CuZn based on modification
            of free atom potentials (from reference 3).

Figure 2.   Comparison of band profiles in ($\Gamma\Sigma M$) direction resulting from
            potentials of Figure 1 (from reference 3).

Figure 3.   Phase diagram of CuZn alloy system (from reference 7).

Figure 4.   X-ray diffraction scans of Cu_xZn_{1-x} samples as a function of 2θ,
            where θ is the X-ray incident angle, is evident at $2\theta = 43.3$ degrees.
            α phase would appear at 42.2 degrees. a) $x = 0.54$, b), $x = 0.52$,
            c) $x = 0.50$ showing martensite line at 44.7 degrees, d) pure β phase
            material in $x = 0.50$ sample after low temperature anneal to eliminate
            martensite.

Figure 5.   Universal function, $F(W)$, derived by Batz [14,15] for lineshapes
            near critical points as seen in wavelength modulation spectroscopy.
            $F(W) = [W^2+1]^{-1/2} [(W^2+1)^{1/2} + W]^{1/2}$, where W is the reduced
            frequency $(\omega-\omega_g)/\eta$. $\hbar\omega_g$ is the interband energy at the critical
            point and η is a phenomenological broadening parameter.

Figure 6.   Wavelength modulated derivative of the reflectivity of Cu_xZn_{1-x}.
            a) $x = 0.50$, b) $x = 0.52$, c) $x = 0.54$.

Figure 7.   Reflectivity of Cu_xZn_{1-x}, which is found by integrating the data of
            Figure 6.   a) $x = 0.50$, b) $x = 0.52$, c) $x = 0.54$.

Figure 8.   Real part of the dielectric function, ϵ_1, of Cu_xZn_{1-x}. a) $x = 0.50$,
            b) $x = 0.52$, c) $x = 0.54$.

Figure 9.   Imaginary part of the dielectric function, ϵ_2, of Cu_xZn_{1-x}.
            a) $x = 0.50$, b) $x = 0.52$, c) $x = 0.54$.

Figure 10. Derivatives with respect to energy of ϵ_1, ϵ'_1, of Cu_xZn_{1-x}.

a) $x = 0.50$, b) $x = 0.52$, c) $x = 0.54$.

Figure 11. Derivatives with respect to energy of ϵ_2, ϵ'_2, of Cu_xZn_{1-x}.

a) $x = 0.50$, b) $x = 0.52$, c) $x = 0.54$.

Figure 12. Energy loss function of Cu_xZn_{1-x}. a) $x = 0.50$, b) $x = 0.52$,

c) $x = 0.54$.

Figure 13. Real part of the bound part of the dielectric function, ϵ_{1_b}, of

Cu_xZn_{1-x}, determined by subtracting the Drude contribution from the

data of Figure 8. a) $x = 0.50$, b) $x = 0.52$, c) $x = 0.54$.

Figure 14. Imaginary part of the bound part of the dielectric function, ϵ_{2_b}, of

Cu_xZn_{1-x}, determined by subtracting the Drude contribution from the

data of Figure 9. a) $x = 0.50$, b) $x = 0.52$, c) $x = 0.54$.

Figure 15. Derivative with respect to energy of ϵ_{1_b}, ϵ'_{1_b}, of Cu_xZn_{1-x}.

a) $x = 0.50$, b) $x = 0.52$, c) $x = 0.54$. With reference to the band

structure in Fig. 17 obtained from Refs. (3,4), the following

transitions are identified for $Cu_{0.50}Zn_{0.50}$: $M_{5'} \rightarrow M_1$ (3.16 eV),

$M_{5'} \rightarrow M_3$ (3.29 eV), $T_2 \rightarrow T_5$ (3.7 eV); for $Cu_{0.52}Zn_{0.48}$: $M_5 \rightarrow M_1$

(3.36 eV), $M_{5'} \rightarrow M_3$ (3.6 eV), $T_2 \rightarrow T_5$ (3.7 eV); for $Cu_{0.54}Zn_{0.46}$:

$M_{5'} \rightarrow M_1$ (3.01 eV), $M_{5'} \rightarrow M_3$ (3.29 eV), $T_2 \rightarrow T_5$ (3.6 eV).

Figure 16. Derivative with respect to energy of ϵ_{2_b}, ϵ'_{2_b}, of Cu_xZn_{1-x}.

a) $x = 0.50$, b) $x = 0.52$, c) $x = 0.54$.

Figure 17. Band structure of β'-CuZn calculated by Amar and Johnson [3,4].

Table 1. Derivative of Critical Points with Broadening Included in Terms of $F(W)$

$$F(W) = [(W^2+1)^{1/2} + W]^{1/2}/(W^2+1)^{1/2} , \qquad W = (\omega-\omega_g)/\eta$$

Critical Point	$2\eta^{1/2} \dfrac{d\varepsilon_1}{d\omega}$	$2\eta^{1/2} \dfrac{d\varepsilon_2}{d\omega}$
M_0	$F(-W)$	$F(W)$
M_1	$-F(W)$	$F(-W)$
M_2	$-F(-W)$	$-F(W)$
M_3	$F(W)$	$-F(-W)$

Table 2.   Drude Optical Parameters

Composition (%Cu) (%Zn)		Effective Mass to Free-Electron Mass	Relaxation Time $(10^{-15}$ second)
		m^*/m_o	
54	46	1.89	2.64
52	48	1.17	2.13
50	50	1.20	3.69

Fig. 1

Fig. 2

Fig. 3

Fig. 4

F(W)

$W = \dfrac{\omega - \omega_g}{\eta}$
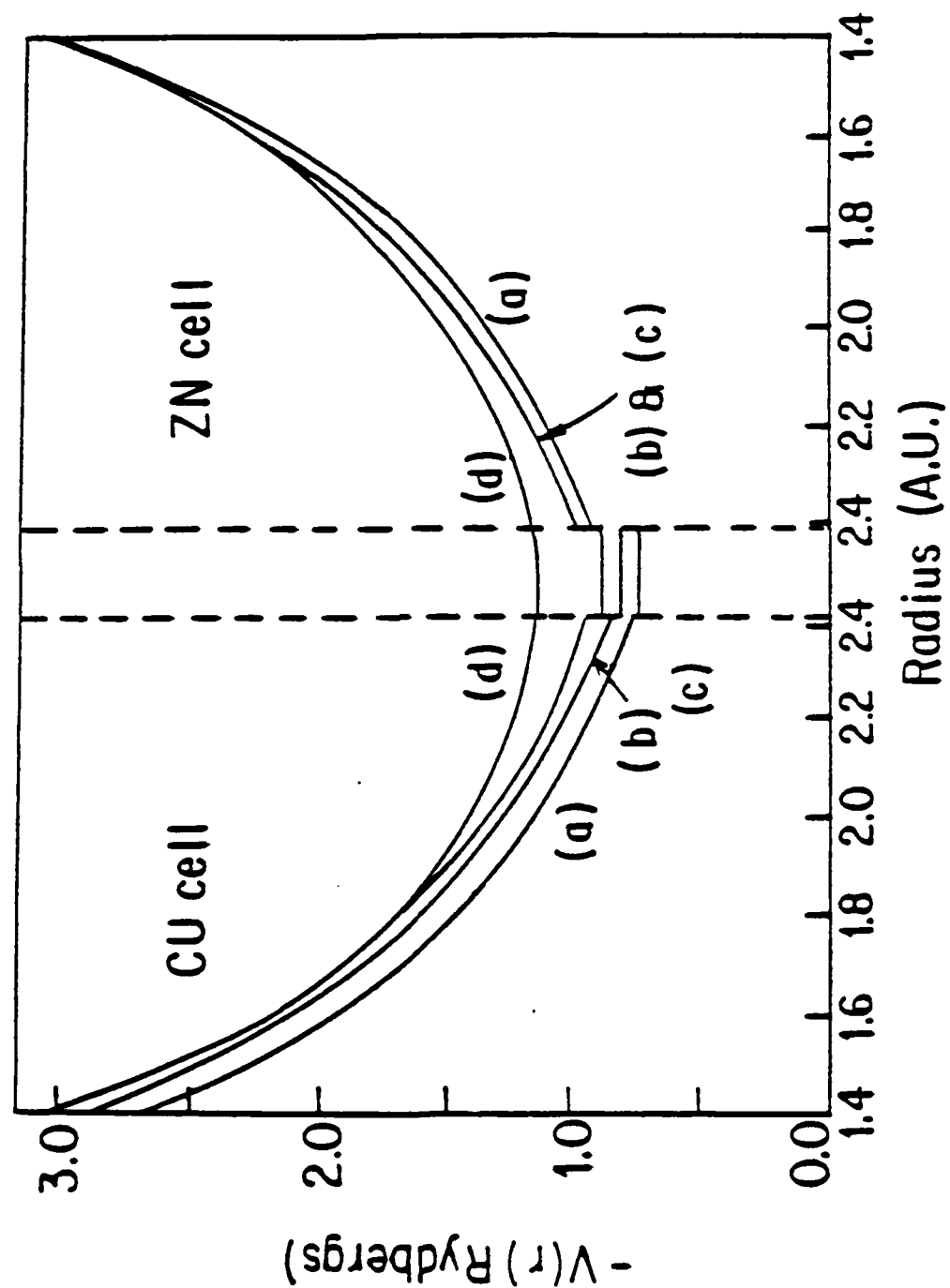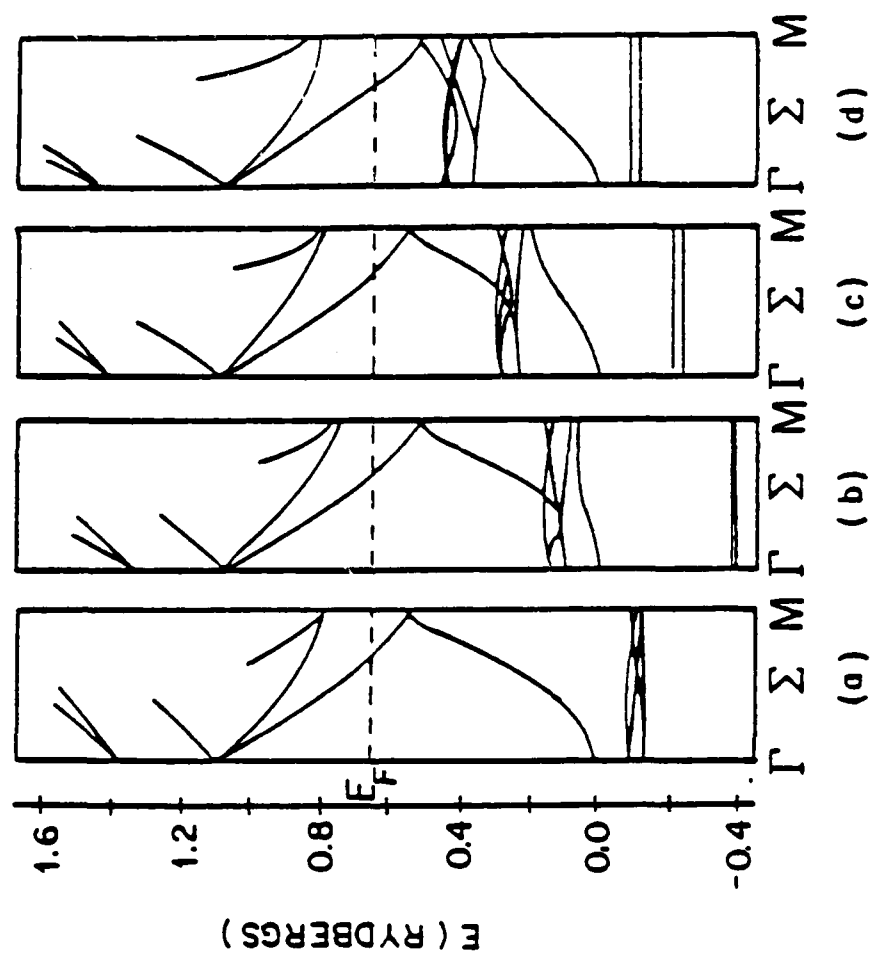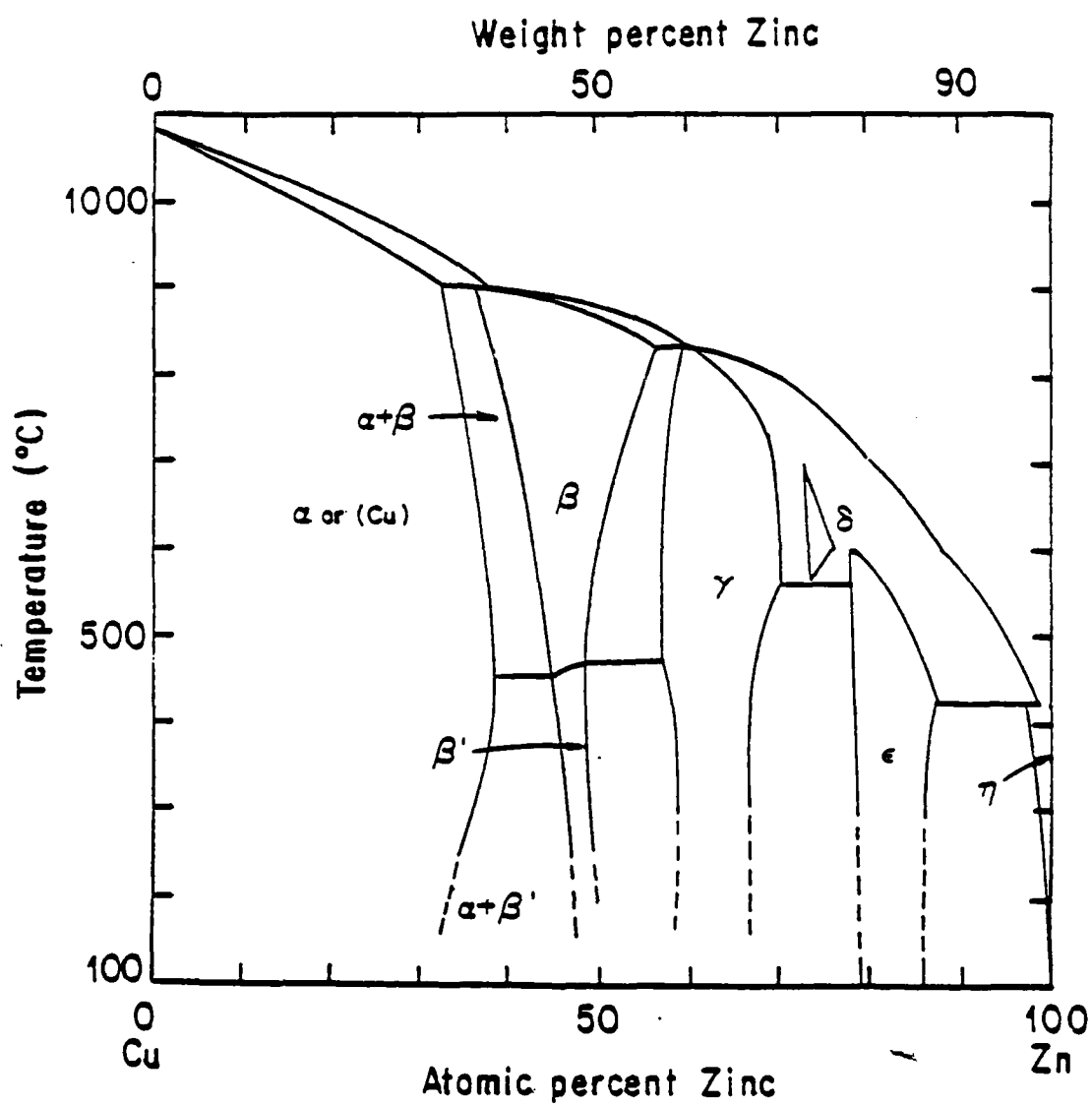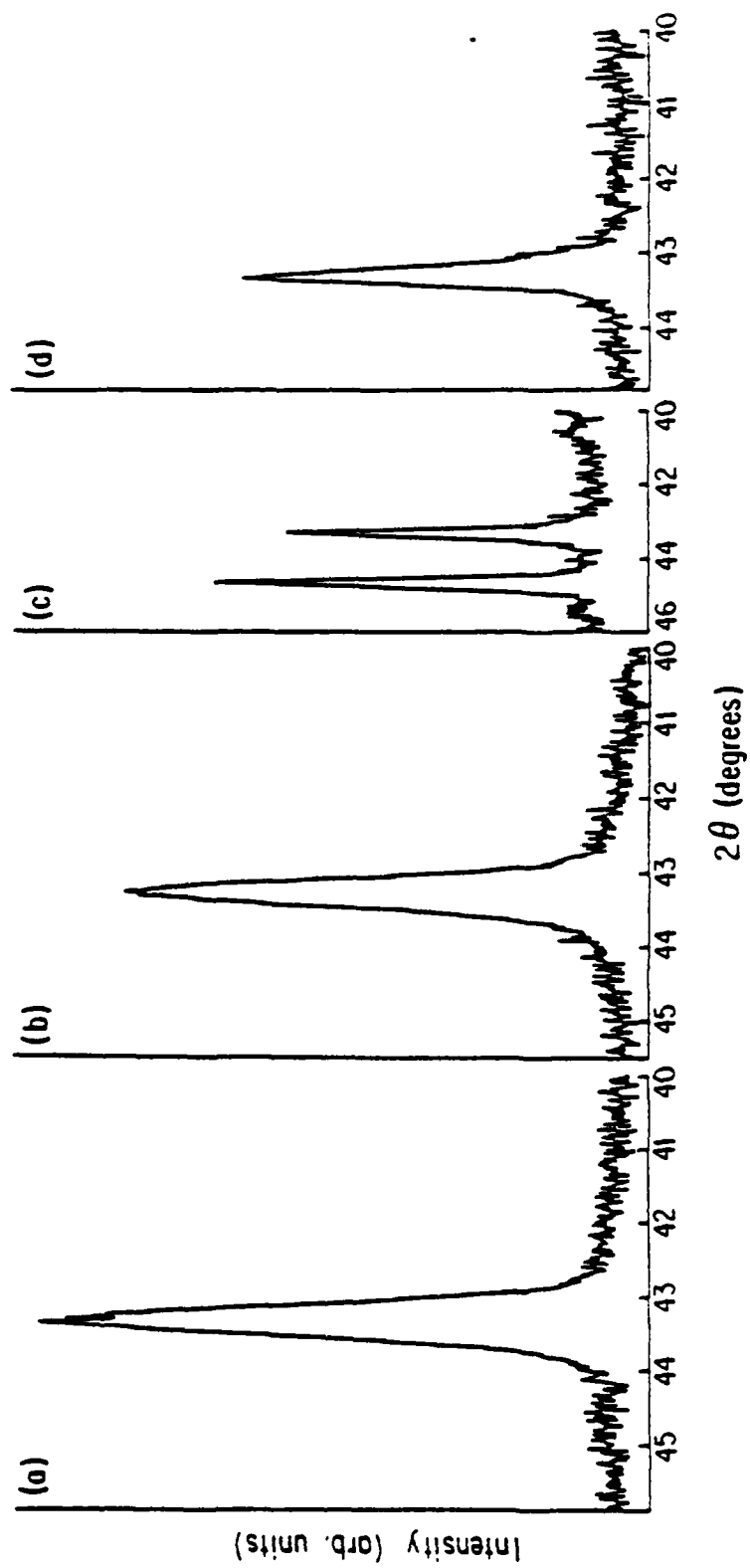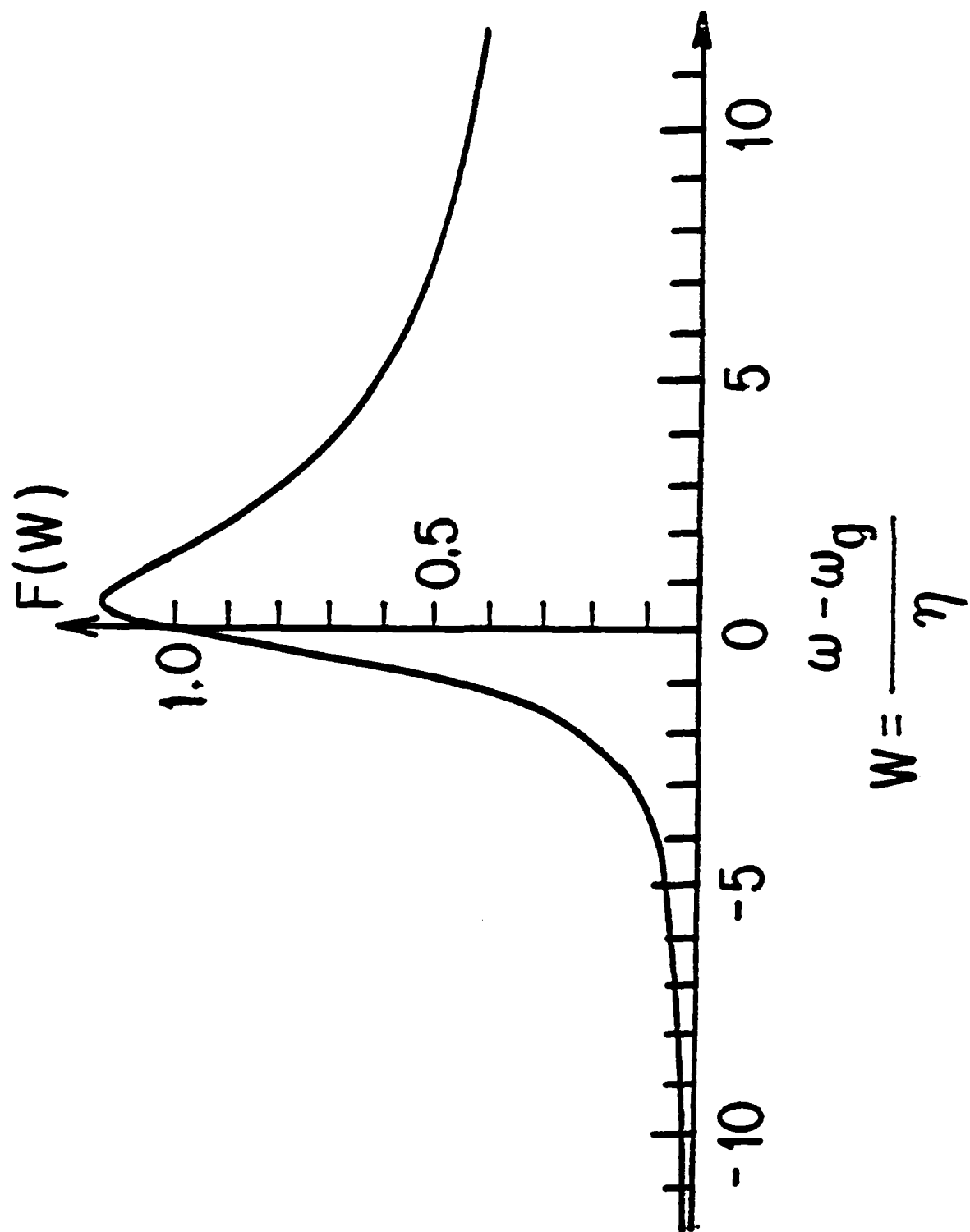
Fig. 5
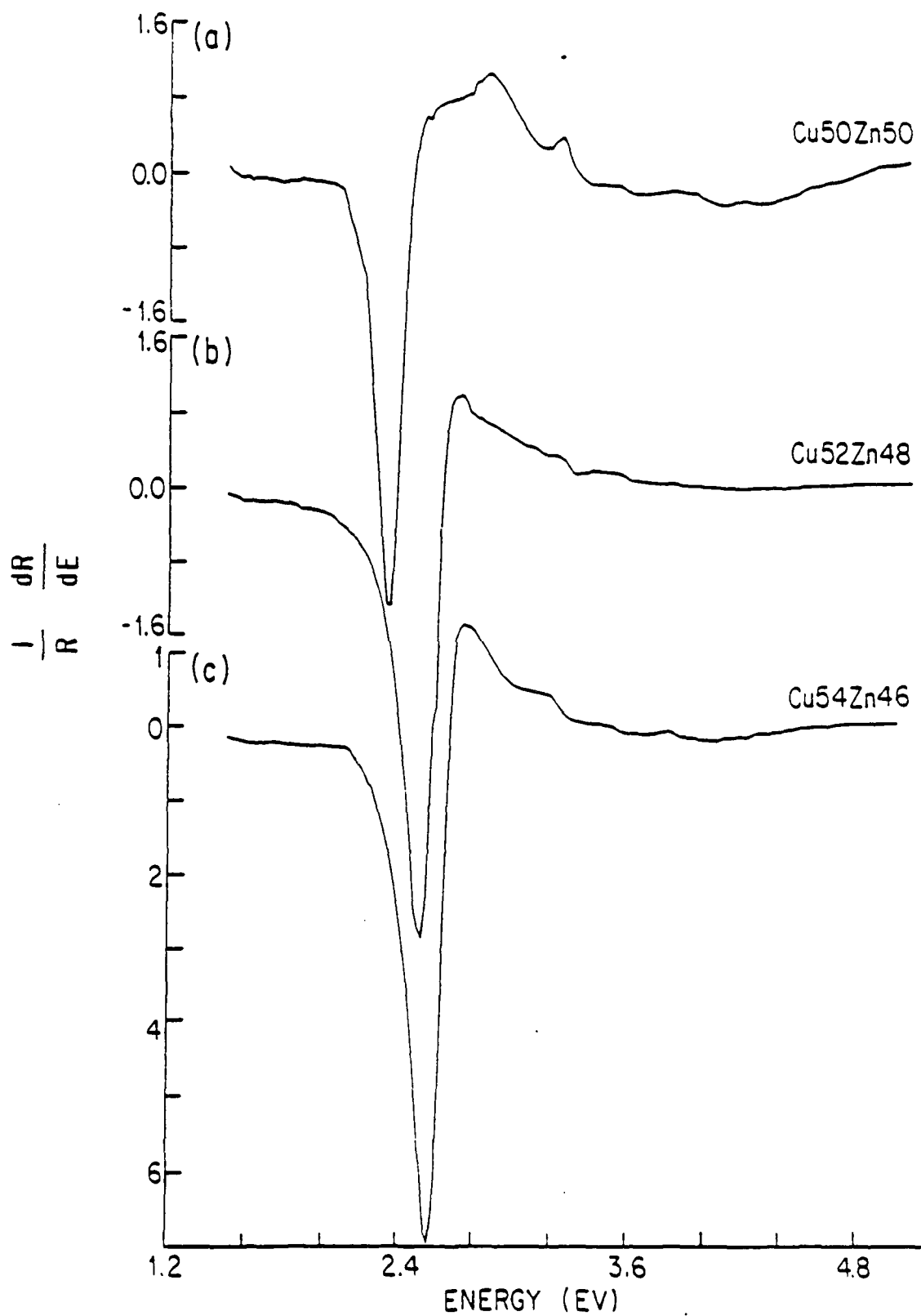
Fig. 6
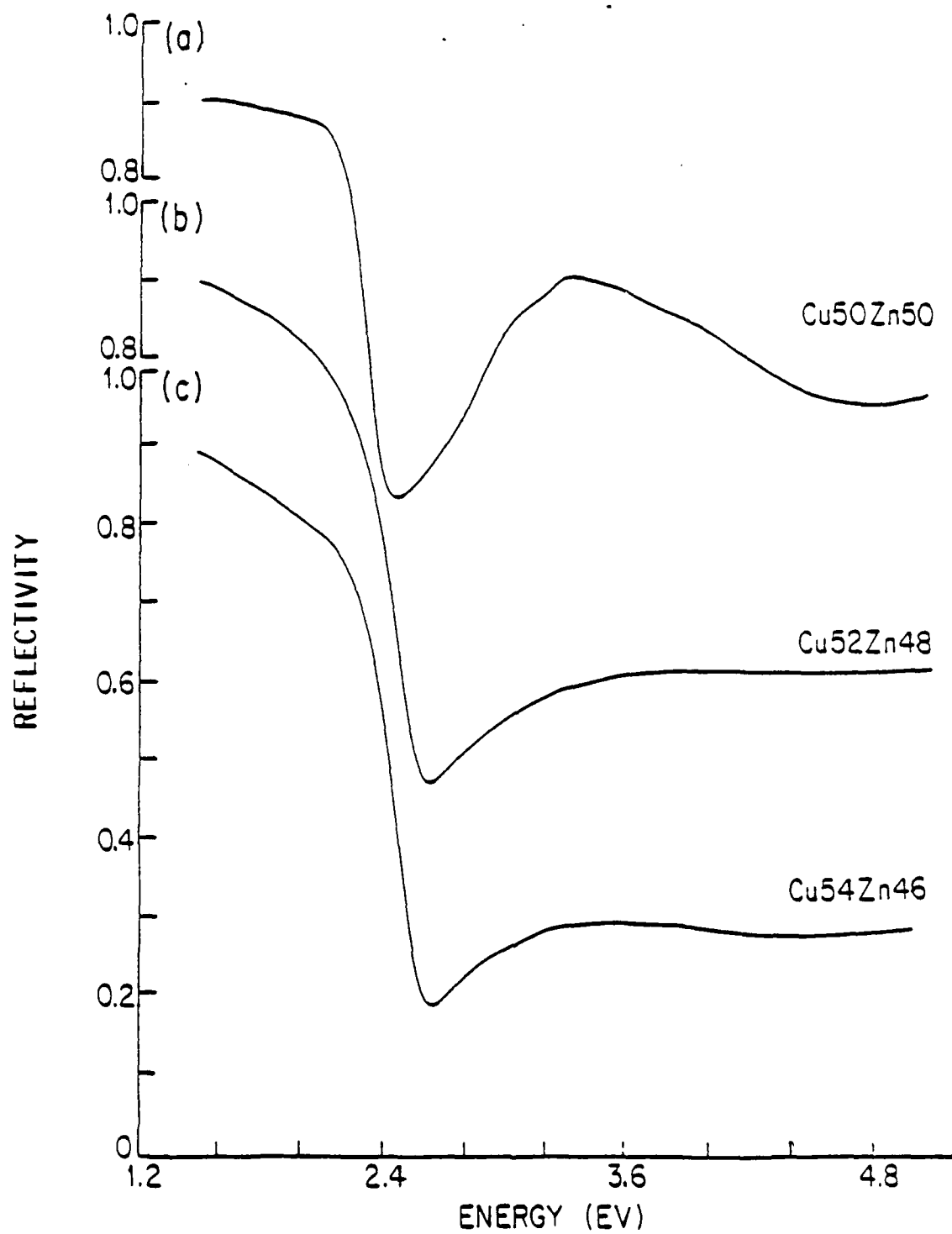
Fig. 7
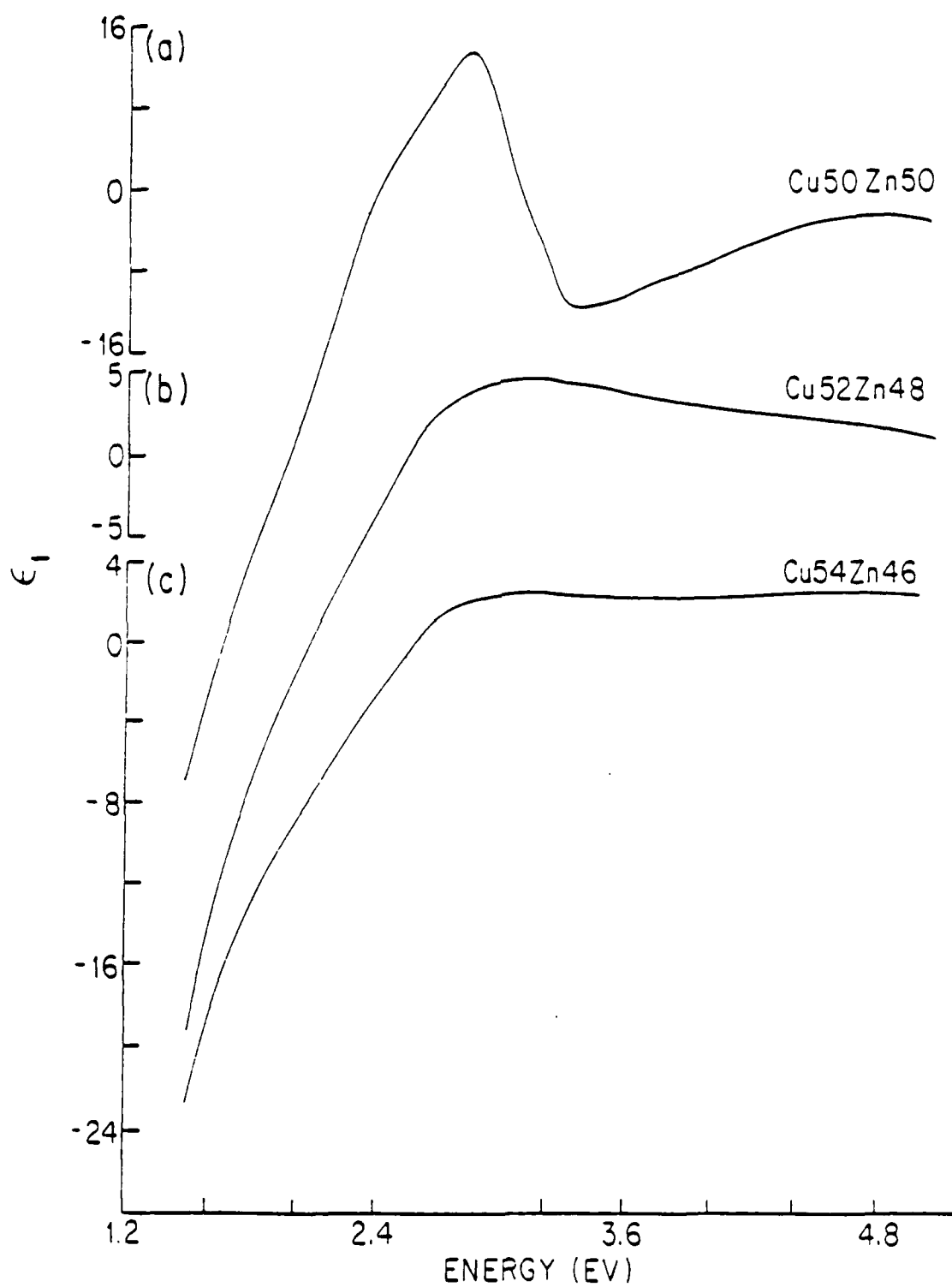
Fig. 8

heat treatment, and therefore is considered to belong to a multilevel defect complex.

The spectrum between 0.6 and 1.45 eV was identified as being due to a native defect commonly referred to as EL2.[34] Utilizing the unusual photo-quenching behavior[35] of this level we were able to re-examine the accuracy of the convertional room temperature optical absorption, commonly used in measuring the EL2 concentration, and showed that these methods typically can have up to 20% error.

II. EXPERIMENTAL TECHNIQUES

Our previously reported wavelength modulated spectrometer[31] has been modified (for the low temperature operation) by adding to it a low temperature optical dewar essential to this work. We have also improved the stability, reproducibility and control of the modulating system, as well as the signal processing. The schematic diagram of the system is shown in Fig. 1.

A liquid transfer refrigerator, with an optical window shroud and a sample holder suitable for the sample-in-sample out technique, and a digital temperature indicator/controller, were used for the low temperture operation. A tungsten/halogen light source, and quartz windows were used for the spectral range of 0.55 - 1.50 eV. For the 0.3 - 0.55 eV region, a Globar light source and Potassium Chloride windows were used. The detector throughout the spectral region was a Golay cell.

The modulation of the wavelength was accomplished by sinusoidal oscillation of a diagonal mirror located near the exit slit of the monochromator, and mounted on the shaft of an optical scanner. The internal oscillator of a lock-in amplifier was used to drive the scanner through a current amplifier driver

Wavelength modulation absorption spectroscopy, in contrast allows one to obtain the derivative spectrum by modulating the wavelength of the probing light beam, and thus has a straightforward relationship to the conventional absorption measurements with improved sensitivity.[30] The difficulty in this case is the presence of spurious structures in the spectrum due to background derivative spectra, which poses a serious problem expecially in the infrared region of spectra. This problem has been overcome by using a sample in-sample out technique and an on-line computer for collecting data and numerically decorrelating the spectra from the background.[31]

Undoped semi-insultaing (SI) GaAs substrates, grown by liquid encapsulated Czochralski (LEC) are currently being used for the fabrication of high speed GaAs MESFET and integrated circuits (IC's).[32] Deep levels play a crucial role in controlling the carrier concentration and hence the resistivity of the substrates. Therefore much attention has been focussed on detection and characterization of the deep levels in this technologically important material.

A detailed study of the derivative absorption of GaAs: Cr[33] has been reported. In the present study, we have employed a modified wavelength modulation absorption spectrometer to study the deep levels in the semi-insulating GaAs (LEC). The spectrometer was used in the spectral region of 0.3-1.45 eV and the temperature range of 80-300K, to study deep level impurities and defects in undoped semi-insulating GaAs (LEC). The measurements revealed two resonant type peaks with fine structures near 0.37 and 0.40 eV, as well as thresholds and plateaus at higher energies. The sensitivity of our measurements allows us to give credence to changes in the absorption coefficient at levels -10^{-3} cm^{-1}. The absorption band at 0.37 eV is interpreted as being due to the intra-center transition between levels of accidental iron impurity, split by the crystal field. The absorption band near 0.40 eV, annealed out as a result of

between different possible radiative and nonradiatve mechanisms.

Extrinisic optical absorption spectroscopy has been amongst the most favored techniques of studying impurity and defect levels at high level of concentrations.[23-25] These measurements are done on bulk materials and therefore are free from high electric fields and process related impurity or defects. The absorption coefficient along with its spectral and temperature dependence can give information about the photoionization energy, excited states, temperature dependence of the level, electron-phonon coupling, and the symmetry of the localized wavefunction as well as their concentration.[4] However conventional optical absorption techniques usually suffer from poor sensitivity at low levels of concentration of the order of 10^{12} - 10^{16} cm^3 usually encountered for deep levels. Consequently considerations have been given to optical derivative spectroscopies which can measure absorption coefficients at levels of 10^{-3} to 10^{-5} cm^{-1}.[26]

Several modulation schemes have been developed in optical derivative spectroscopy. Electro-modulation, peizo-modulation, thermo-modulation and wavelength modulation are examples of this technique depending on whether the modulating parameter is the applied electric field, strain, temperature or the wavelength of the probing light beam.[27,28] However, these techniques have primarily been used to study the intrinsic optical properties of materials.

The techniques of extrinsic electro-absorption has been used in some cases to study deep levels in semiconductors.[29] They have not, however, been extensively employed, since they require high resisitivity material in order that sufficiently high electric fields can be applied to obtain adequate modulation. In addition, the present knowledge of the effect of electric fields on the properties of deep levels is not sufficient for a complete interpretation of the experimental results.

I. INTRODUCTION

Deep levels in semiconductors continue to be the subject of considerable theoretical[1-6] and experimental[7-15] research as our understanding of these levels is far from complete. The presence of deep levels in semiconductors at concentrations of $10^{15}/cm^3$ or even less, can significantly affect the carrier lifetime, mobility, and the rate of radiative transitions, and thus performance of microelectronics and opto-electronics devices made from these materials.[9] The fascinating features of the physics of deep levels, coupled with great technological interest in this field has intensified searches for sensitive experimental techniques for their detection and characterization at these low levels of concentrations.

The various space charge spectroscopy techniques (such as TSC, DLTS and DLOS)[8-11] developed in recent years are commonly employed electrical measurements to detect deep levels. With very good sensitivities, they can provide thermal activation energy, carrier capture cross section and concentration of deep levels (and optical cross section in some cases). The main drawback of these techniques, however, is that measurements are carried out in space charge regions, i.e., in the presence of high electric fields (~ 10^4 – 10^5 V/cm), the effect of which on the emission rate is not thoroughly understood.[4,15-17] Furthermore, since these measurements require fabrication of p-n junctions or Schottky barriers or ohmic contacts which could result in the introduction of process related impurities and or defects into the sample. In addition, the above techniques employing essentially thermal processes usually do not yield excited states of levels. Photoluminescence type experiments, although very sensitive for shallow levels,[18-22] have limited sensitivity in the case of deep levels due to appreciable phonon coupling resulting in competition

Wavelength Modulation Absorption Spectroscopy of

Deep Levels in Semi-Insulating GaAs

S. M. Eetemadi and R. Braunstein

Department of Physics, University of California,

Los Angeles, California 90024

Infrared wavelength modulation absorption spectroscopy was used in the specral region of 0.3-1.45 eV and the temperature range of 80-300K, to study deep level impurities and defects in undoped semi-insulating GaAs grown by the liquid encapsulated Czochralski technique (LEC). The measurements revealed two resonant type peaks with fine structure near 0.37 and 0.40 eV, as well as thresholds and plateaus at higher energies. The sensitivity of the measurements allows us to give credence to changes in the absorption coefficient at levels $\sim 10^{-3}$ cm^{-1}. The absorption band at 0.37 eV is interpreted as being due to the intra-center transition between levels of accidental iron impurity, split by the crystal field. The absorption band near 0.40 eV, can be annealed out by heat treatment, and is considered to belong to a multilevel defect complex. Utilizing the photo-quenching behavior of the absorption in the spectral region of 0.6-1.4 eV, it was shown that conventional room temperature optical absorption may give erroneous results in measuring the concentration of the EL2 levels, because of appreciable absorption due to other residual deep levels in this spectral region, as revealed by the sensitivity of the wavelength modulation technique.
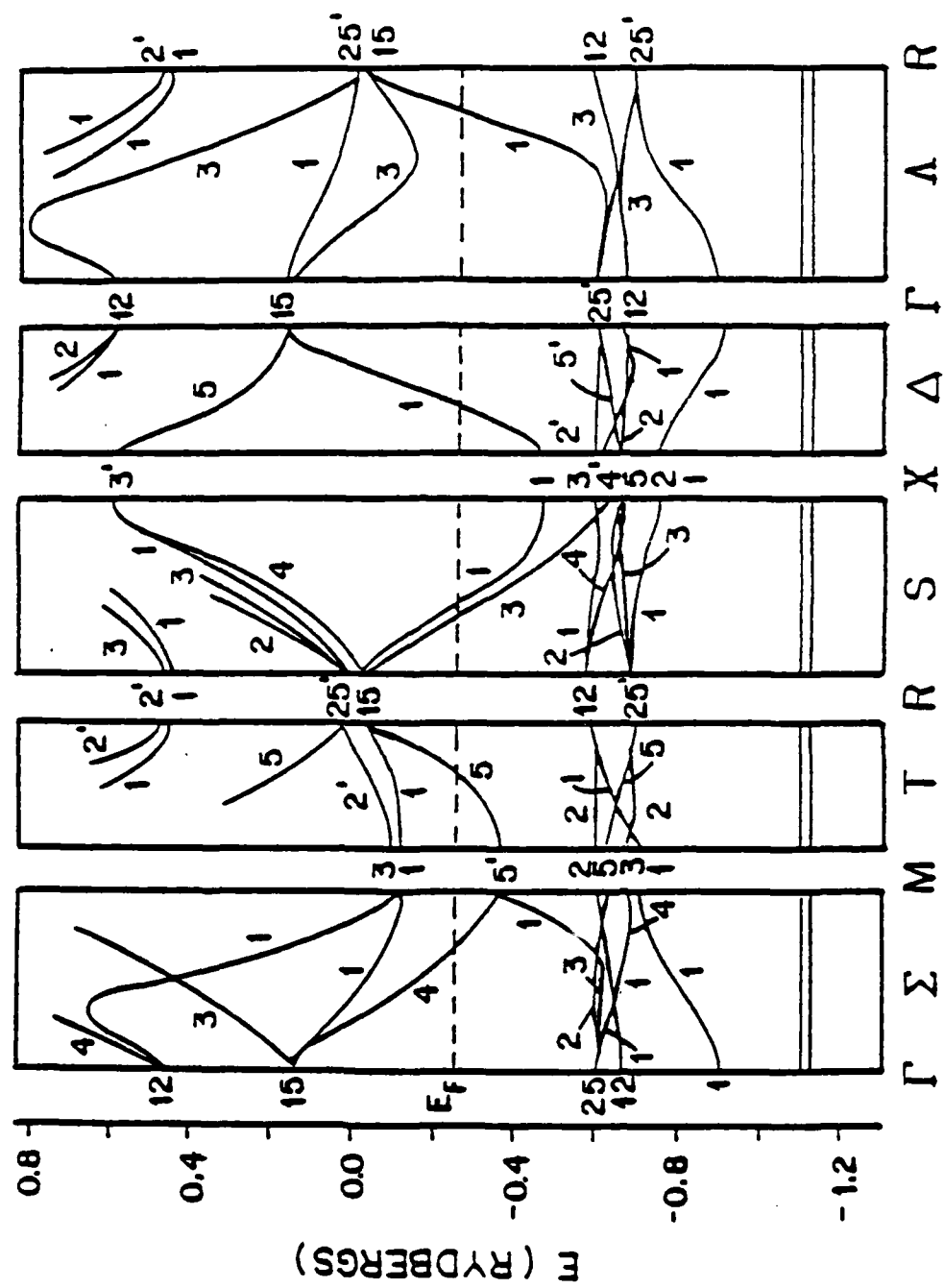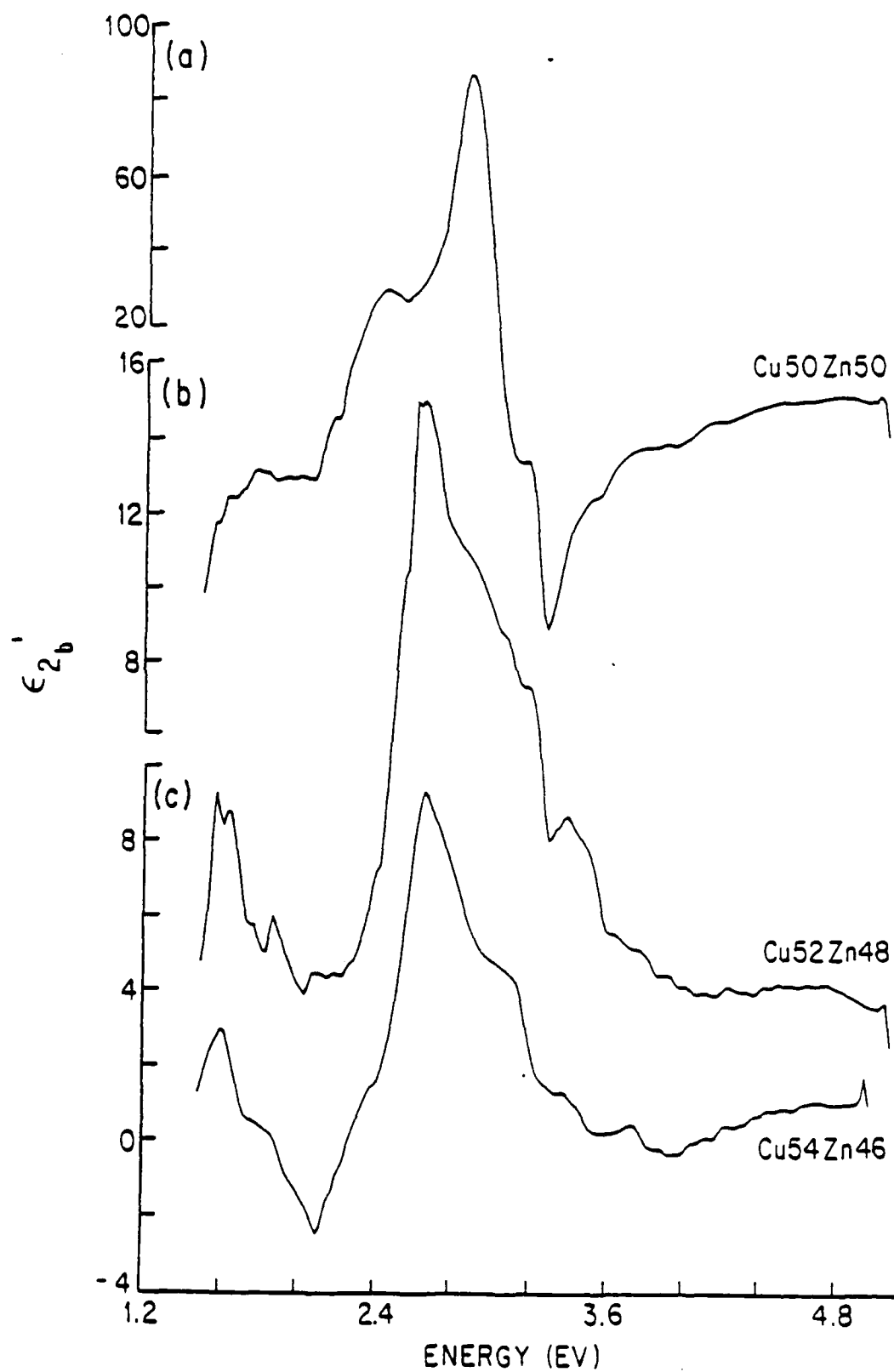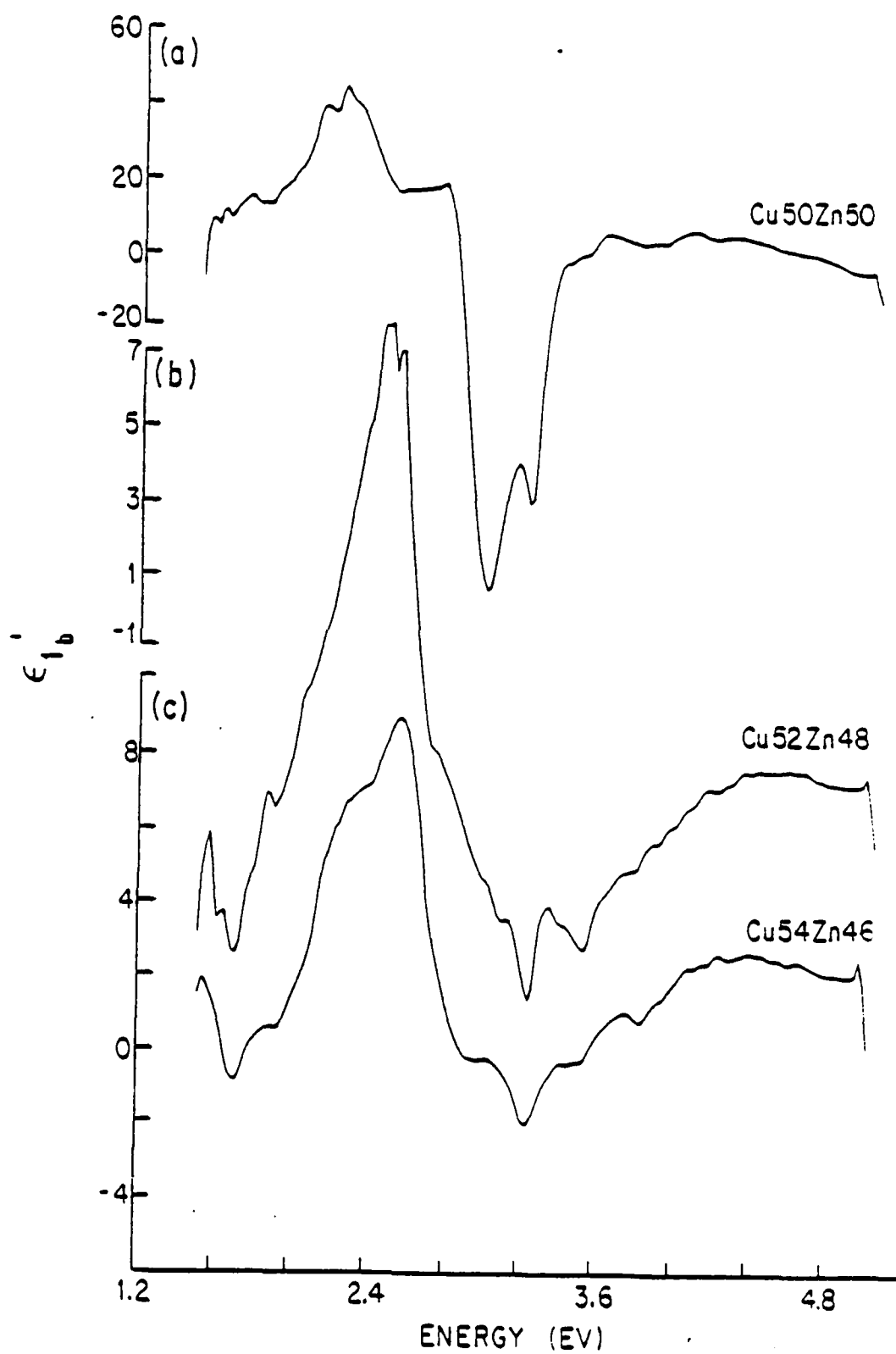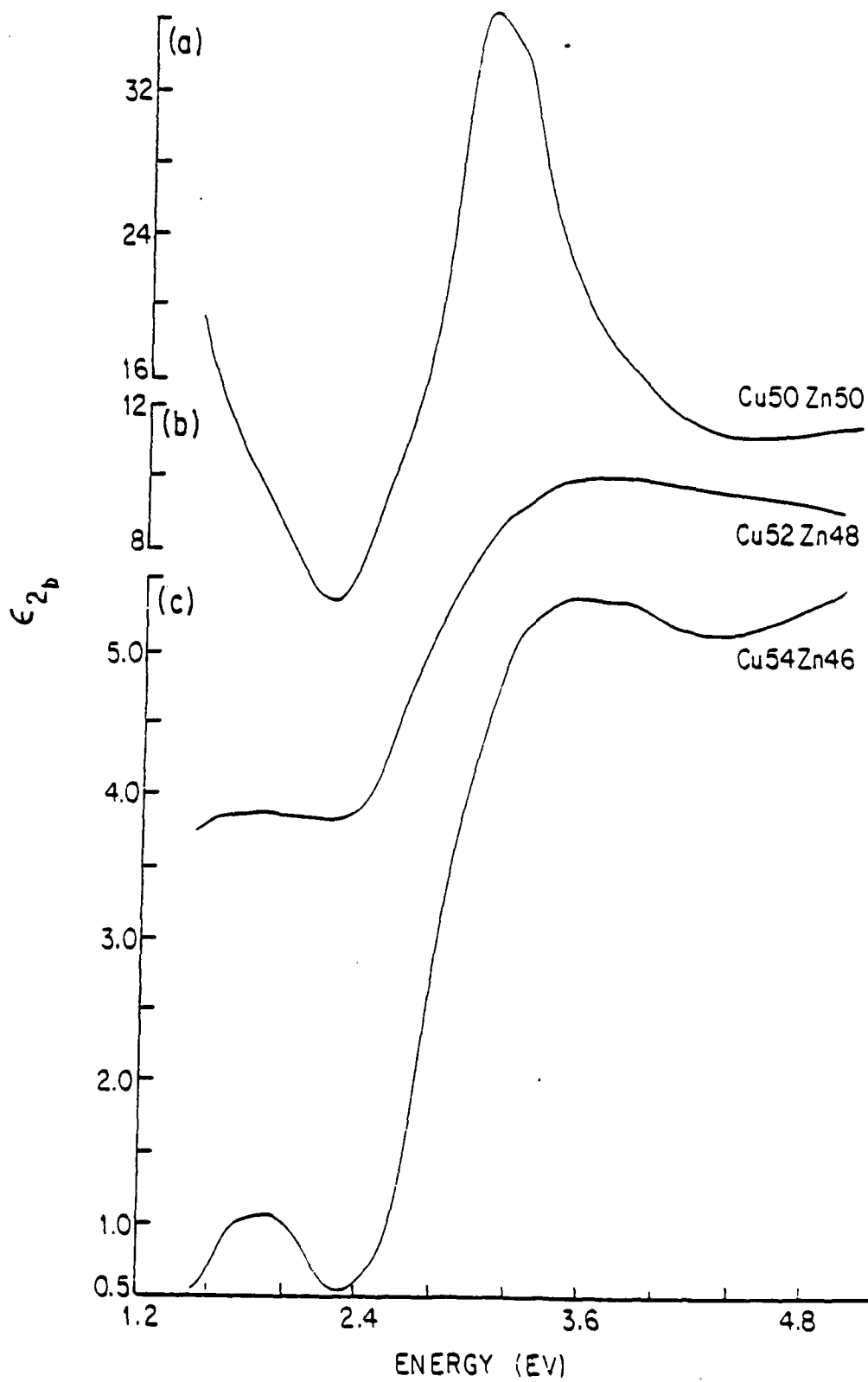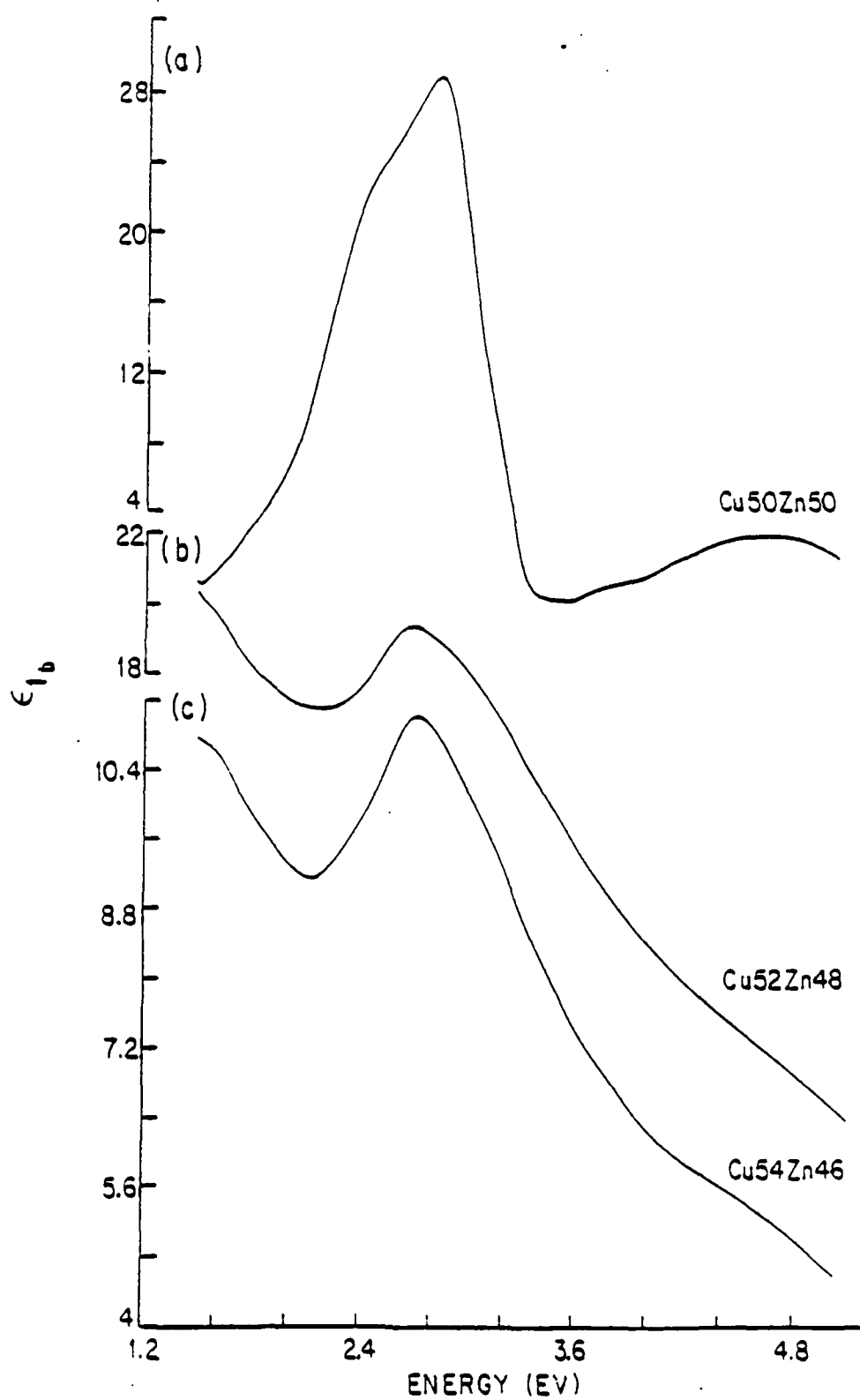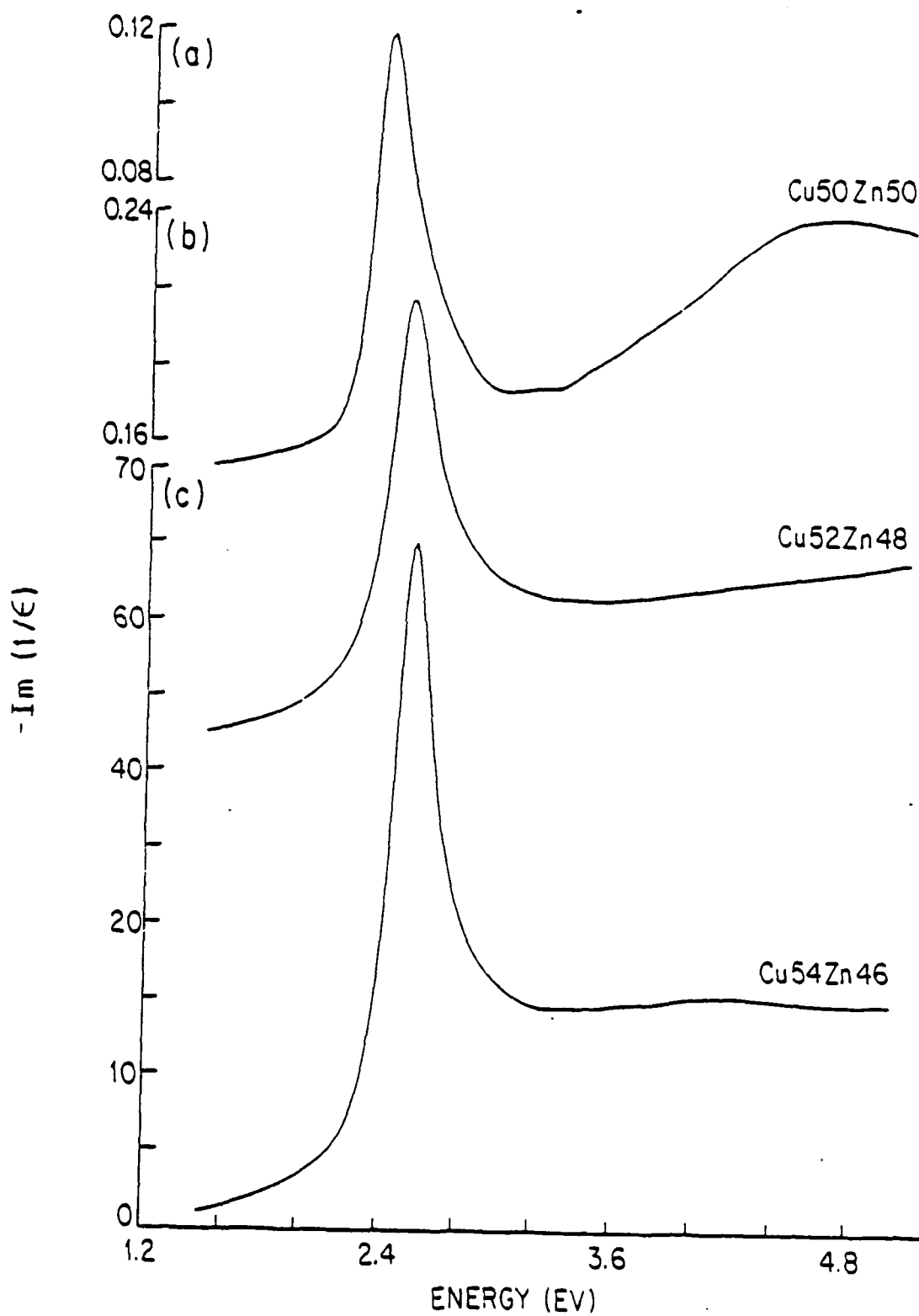
Fig. 17

Fig. 16

Fig. 15
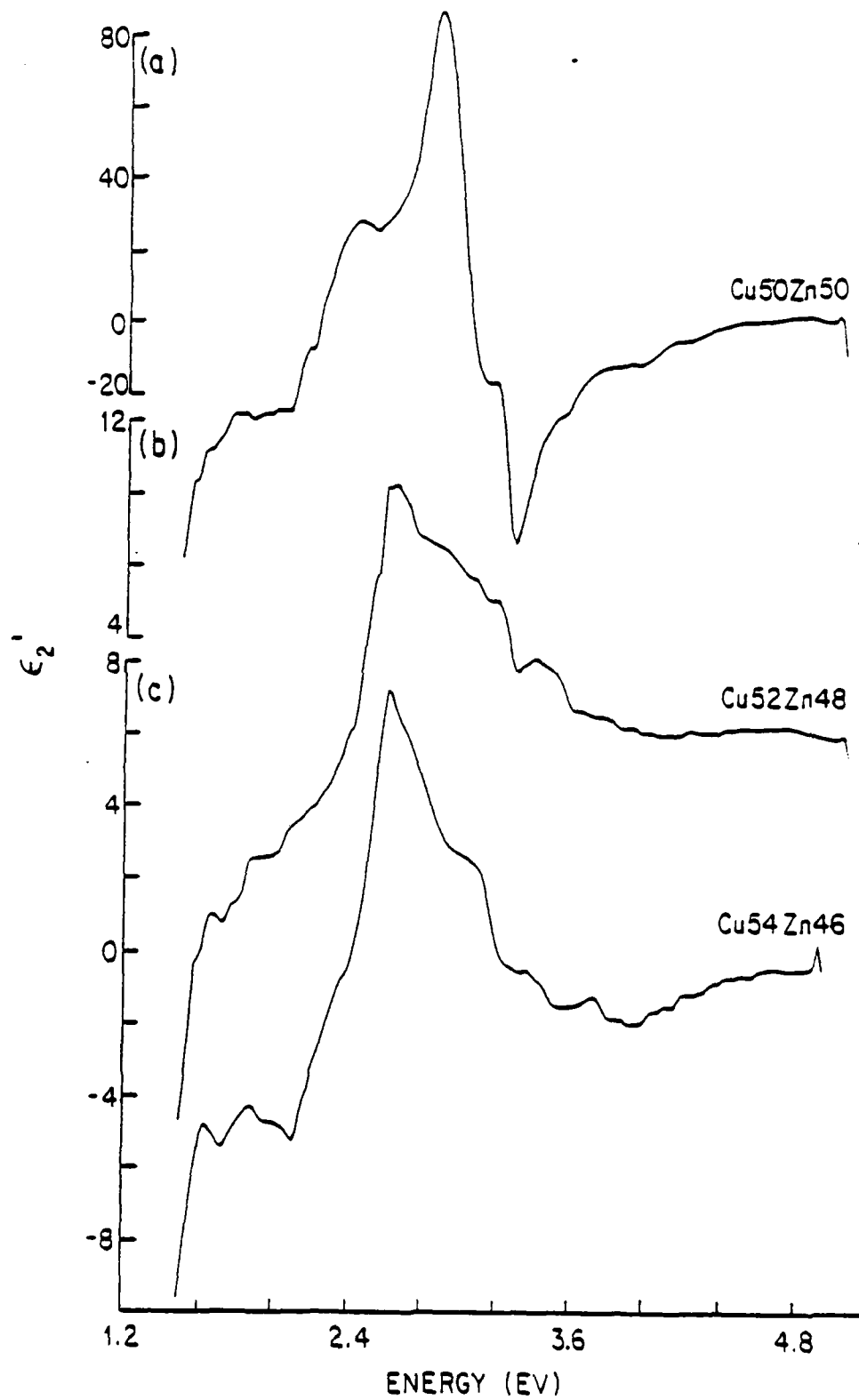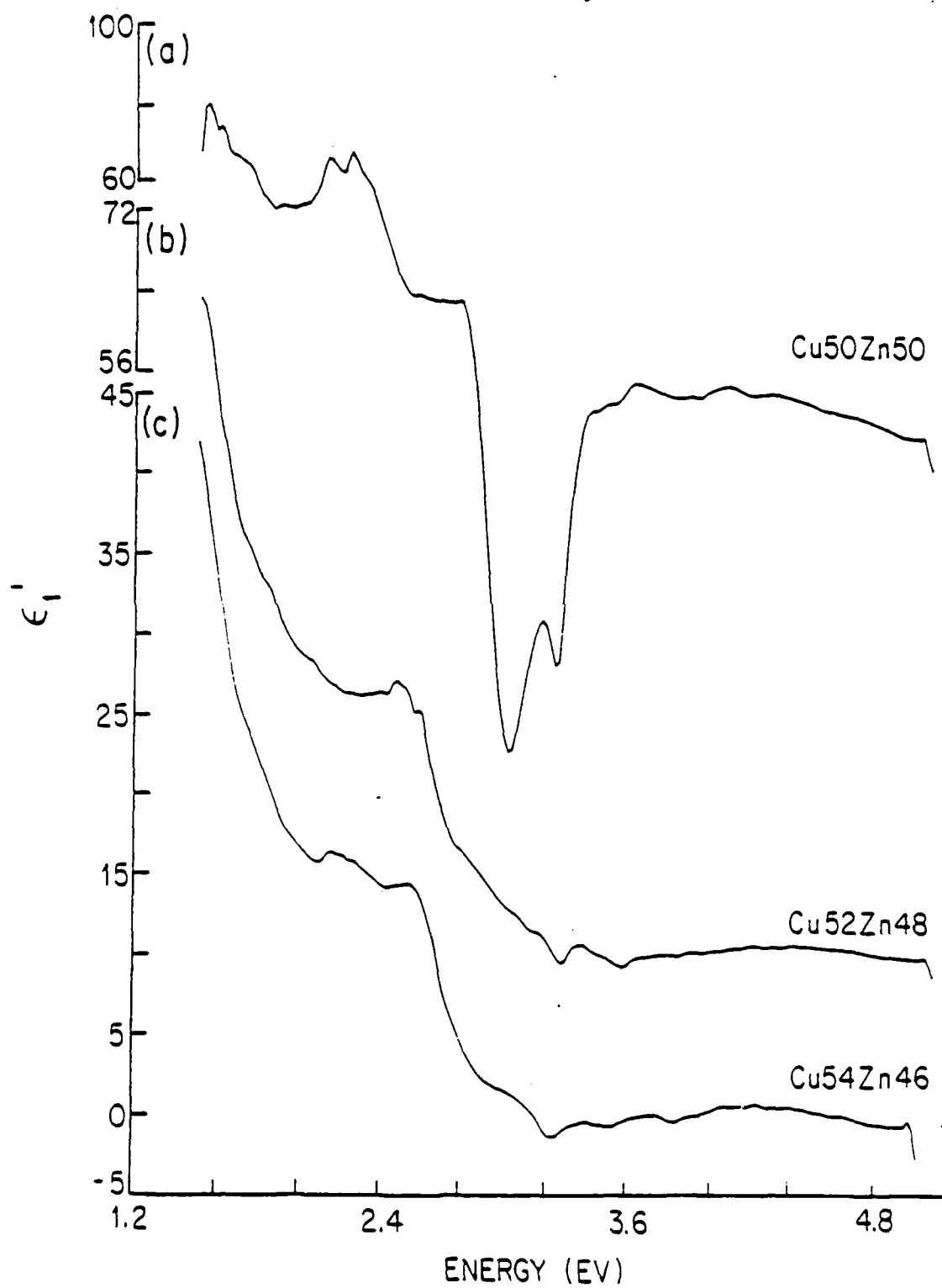
Fig. 14

Fig. 13
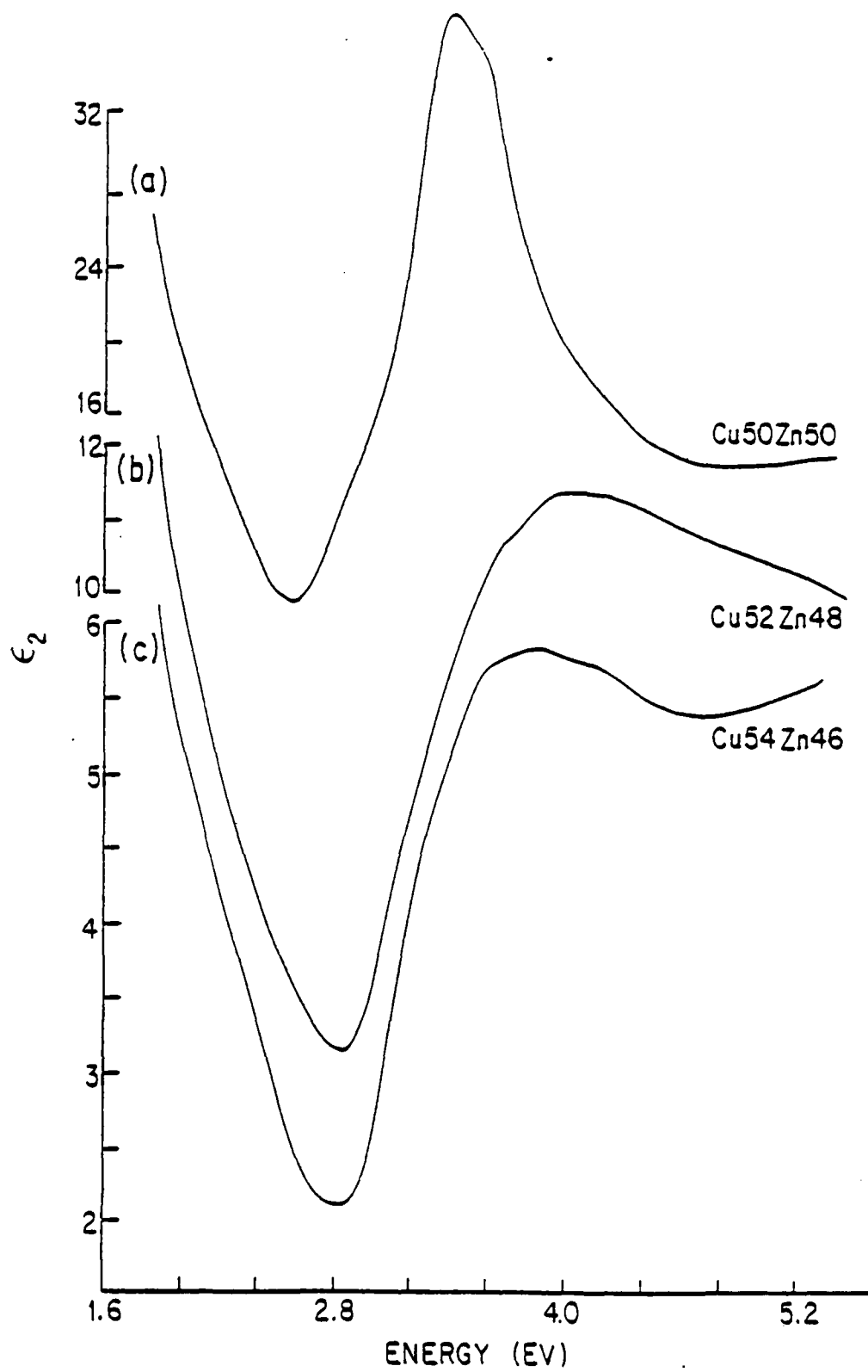
Fig. 12

Fig. 11

Fig. 10

Fig. 9

circuit. The new modulation system has several advantages over the one previously employed. It is frequency tunable (1-100 Hz), has high amplitude and frequency stability, and allow large wavelength excursions. With the new system the amplitude of modulation can be controlled from 0.2 to 150 A precision. There was no wabbling, and no crosstalk with other mechanically vibrating components. These features were desirable for reducing noise and drift, as well as optimizing the modulation frequency compatible with the detector response, and consistent with the chopper frequency to avoid harmonic or sub-harmonic pick-up. It can also be used to conveniently anu very precisely calibrate the spectral slit width, the depth of modulation, and to select these quantities for optimum resolution, signal-to-noise ratio, and minimum distortion in the derivative signal, for a given spectral region. A DC offset feature of this scanner also allows one to set the monochromator calibration electrically rather than mechanically. Data was taken at discrete energies with a resolution set by the slit width and depth of modulation which for this work was 0.00^~5 - 0.0015 eV.

An on-line computer steps the sample, in and out of the light beam, as well as steps the wavelength, and collects data from the output of lock-in amplifiers at controllable rates for additional signal averaging. These operations are conveniently done using a '.SI-11/23 computer and its peripherals in the form of a CAMAC system. The data taking cycle is shown in Fig. 2. The method of data analaysis is similar to that previously employed.[31] The wavelength modulation technique yields essentailly the energy derivative of the absorption coefficient. To obtain the value of the absorption coefficient, one numerically integrates the observed derivative spectra, and normalizes it to the absorption coefficient obtained by a direct loss measurement in the same apparatus at fixed wavelengths where the absorption coefficient can be measured with good

precision.

The undoped semi-insulating GaAs samples used in this work were cut from five different ingots, all grown in pyrolitic boron nitride (PBN) crucibles, by the liquid encapsulated Czochralski technique (LEC), with B_2O_3 as the encapsulant. They had resistivities greater than $10^7 \Omega$-cm, and Hall mobilities of 4570-6319 cm^2/V sec. They were typically 3 mm thick and the surface were polished with Br-methanol. The samples were grown by the Hughes Research Laboratory, Malibu.

III. RESULTS

Figure 3 shows the absorption spectra of an undoped SI GaAs (LEC) at 300 K. The threshold near 1.4 eV is the onset of the interband transition, while the spectra between 0.7 and 1.4 eV is the characteristic absorption of a deep level due to a presumably native defect complex, commonly referred to as the EL2 level.[35] The small structures between 0.3 and 0.5 eV, and the threshold at 0.5 eV should be noted. In conventional absorption spectroscopy these small variations would be buried in the systems noise, whereas with our technique variations as small as 10^{-3} cm^{-1} have significance. As the temperature is reduced to 160 K, we note the sharpening of the thresholds, and emergence of distinct resonance type structures, shown in Fig. 4. The structures below 0.52 eV are shown in Fig. 5 on a vastly expanded scale possible by the precision of our measurement. Upon lowering the temperature to 80 K the structures sharpen further, and some finer ones appear as seen in Fig. 6. Note should be taken of the sharp structure at 0.36 - 0.38 eV, a broad peak at 0.4 eV with side lobes, and the threshold near 0.5 eV. Figures 7-10 show the observed structures in the same spectral region and temperature for other undoped LEC GaAs samples.

It should be noted that the general shape of the resonant structure at 0.36–0.38 remains unchanged as its intensity varies from Figs. 6-9. In contrast the broad peak at 0.4 eV changes its intensity as well as the details of its shape. No distinct pattern was observed in the structures at 0.43-0.47 eV. Fig. 11 shows the spectra of the sample M039 after the sample had been annealed in a N_2 atmosphere at 450°C for four hours. The difference between this and Fig. 6 should be noted. The peak at 0.4 eV has been annealed out as a result of heat treatment.

When the temperature was lowered to below 140 K, and the sample was illuminated with a 50 W tungsten halogen lamp, the structures between 0.7 and 1.3 eV quenched (see Fig. 12) and remained in the quenched state for several hours even after the background illumination had been turned off. The magnitude and the details of the shape of the post-quenched spectra varied from sample to sample. Its magnitude at 1.2 eV was 10-20% of the total room temperature absorption coefficient at the same energy.

IV. DISCUSSION

The above results are discussed in the following subsections. In section A the resonant spectra at 0.37 is discussed and attributed to accidental iron impurities. Section B is devoted to the comparison of the spectra at 0.4 eV among the various samples, as well as its behavior under heat treatment, and is considered to be the signature of a multi-level defect complex. The results of our observation in the spectral range of 0.7-1.4 eV are discussed in Sec. C.

A. Iron in Undoped GaAs

In the spectra below 0.55 eV, the sharp peak at 0.37 eV can be attributed

to the presence of iron in these materials; a similar absorption peak has been reported in GaAs substrates intentionally doped with iron.[25] Sharp zero-phonon photoluminescence lines near 0.37 eV has also been seen in iron doped GaAs materials.[36] Similar sturctures in absorption and photoluminescence have also been observed for iron in other III-V compounds as well.[25,36] Paramagnetic resonance experiments have shown that iron is incorporated substitutionally in the Ga sublattice, and acts as a deep acceptor.[37] At the Ga site, Fe loses three electrons to the bonds, becoming Fe^{3+} in a $3d^5$ configuration, and when an electron is trapped, a Fe^{2+} in a $3d^6$ configuration is created.

The energy levels of Fe^{2+} in $3d^6$ configuration derived on the basis of the crystal field theory and up to second order term in the spin-orbit correction have been reported in the literature.[38] At a site of tetrahedral symmetry (T_d), the lowest free ion term, ^5D, of $Fe^{2+}(3d^6)$, is split by the crystal field into a ground state doublet ^5E and $^5T_2$ excited state. Allowance for the spin-orbit coupling lifts the degeneracy of the $^5T_2$ level and in the second order approximation it lifts also the degeneracy of the ^5E levels, as shown in Fig. 13. The absorption and luminescence peaks mentioned above are due to the internal transitions between ^5E and $^5T_2$ multiplets.

The central peak at 0.37 eV in Figs. 5-9 can be attributed to the zero phonon transition from the lowest ^5E multiplet to the lowest level of $^5T_2$ multiplet. The structure appearing as a weak shoulder on the low energy side of the line and about less than 2 meV away from the main peak can also be attributed to a zero-phonon transition from the second lowest level of ^5E to lowest level of $^5T_2$. This transition has been reported as well resolved into a separate peak when the measurement is done at about liquid Helium temperature.[25] From the position of the main two zero-phonon lines, and Fig. 13, we obtain a value of $\Delta \sim 3000$ cm^{-1} for the crystal field energy, in

agreement with the reported values of Δ in the III-V compounds.[4] The other side structures are harder to interpret partly because it is difficult to distinguish between vibronic and electronic levels. As for the Jahn-Teller distorion, its effect on the $^S E$ states is not pronounced but it alters the splitting of $^S T_2$ levels.[39] Such changes would be observable in transitions involving higher energy levels of $^S T_2$. Unfortunately, these transitions cannot be seen in our data, because they have much smaller oscillator strengths[23,39] and therefore are buried under the structures due to other residual impurities or defects.

A detailed analysis of iron levels is not the main concern of this work. For that, one would have to study these levels in substrates doped with iron at concentrations much above that of the residual impurities and defects. Our aim in this work was rather to make a broad survey of deep levels in the undoped SI GaAs substrates. To our knowledge this is the first observation of the distinct iron signature in the bulk of-as-grown undoped SI GaAs by optical absorption or emission techniques. Estimating the value of the oscillator strength, the lowest detected concentration of Fe^{2+} was 5×10^{15} cm^{-3} in our work. Although Fe^{2+} in GaAs does have a distinct photoluminescence signature at 0.37 eV, to our knowledge no such emission band has been reported in the undoped-as-grown materials. Emission lines, however, do appear after the substrates are heated to about 700^oC because of accumulation of iron in the near surface region at concentrations of 10^{17} to 10^{18} cm^{-3}.[40] Therefore it is significant that we have been able to detect Fe at levels of 10^{15} cm^{-3}. It should also be noted that in the absence of absorption bands due to other residual deep levels - interfering with the iron absorption spectra - the sensitivity of our present measurement would allow detection of iron at an order of magnitude below the above concentration level.

The threshold near 0.5 eV whose intensity scales with the intra-center transition at 0.37 eV can be identified with a transition from the valence band to the lower multiplet of Fe^{2+}. This is further substantiated by the fact that the position of this threshold moves with a temperature coefficient of $-(5.0 \pm 0.5) \times 10^{-4}$ eV/K, which is similar to the temperature coefficient of the GaAs band gap; a similar observation has been made from Hall measurements.[41] A deep acceptor level at aobuc 0.5 eV from the valence band, due to iron impurity has also been reported by several investigators.[42,43]

One might also expect to observe thresholds at higher energies due to the photoionization of electrons from Fe^{2+} levels to the conduction band. Figs. 3 and 4 show absorption thresholds in the range of 0.7 to 1.4 eV. However, in Sec. C it will be shown that these thresholds bear no relation to the presence of iron. They are rather attributed to another level commonly referred to as EL2,[35] which is believed to originate from a native defect sample. The absorption spectra due to EL2 can be quenched out at 80 K if the sample is illuminated by band gap light (see Sec. C). The remaining spectra shown in Fig. 12 does not contain any strong photoionization threshold. We therefore conclude that the magnitude of the photoionization cross section for electronic transition from the Fe^{2+} levels to the conduction band is very small. It can be argued that since the site symmetry of iron is tetrahedral, transitions from d-orbitals to conduction band s-like orbitals may be strongly prohibited by the selection rules.

B. Multilevel Defect Complex

Another dominant absorption band common to all the substrates we studied is the resonant spectra whose peak is near 0.4 eV, with a peak absorption coefficient typically below 0.4 cm^{-1}, a half width of about 30 meV, and usually

with two sides lobes. Being a peak rather than a threshold it can be interpreted as being due to an electronic transition between levels associated with the same center. The peak magnitude, and the detail shape of this structure as well as its sidebands varied from sample to sample as seen from Fig. 5 to 10, indicating that it is not associated with a simple multilevel impurity. It is more likely that this structure is due to a complex defect formed during the crystal growth or in the cooling period following the growth; whose exact structure is sensitively dependent upon the thermal history of the sample. To explore the possible origin of this level, sample M039 was cleaned, etched and annealed in a nitrogen atmosphere for four hours, at a temperature of 450 C. In contrast to the spectra of M039 shown in Fig. 6, the post-annealed spectra, shown in Fig. 11, indicated that the spectra at 0.4 eV has been annealed out. We thus conclude that i) the structure is a defect or defect complex; ii) this defect introduces two main levels into the gap separated by 0.4 eV; iii) these levels may split into more levels depending on the exact nature of the defect's immediate surrounding or additional complexing. These additional complexes could vary from sample to sample if they do not have identical thermal history. This would account for variations of the fine structures of the spectra among the samples. To our knowledge this is the first observation of this multilevel defect in SI LEC GaAs by optical techniques. A possibly related level has been observed by the photo-induced-transient spectroscopy (P.I.T.S.) in these samples.[44] However, an exact correlation between the levels observed by the wavelength modulation absorption and the level detected by P.I.T.S. must take into account the fact that the latter essentially yields information on the thermal emission from the level to the band, where as the former gives information about the intra-center transitions.

C. The EL2 in SI GaAs

The absorption spectra in the 0.6-1.4 eV shown in Figs. 3 and 4, are due to a deep level known as the EL2 which is associated with a native defect.[34] This defect is responsible for producing undoped semi-insulating GaAs by compensating the shallow impurities.[45,46] The exact origin and microscopic structure of this defect is still subject to considerable debate. Many of the investigations on this defect have involved studies of the correlation between the distribution pattern across the wafer, of the EL2 concentration, dislocation density, resistivity, as well as their relation to the stoichiometry of the melt, and conditions of the crystal growth.[47-50] Central to many of these studies is the precise measurement of the EL2 concentration and its distribution. Optical absorption spectroscopy, at room temperature, nas commonly been used for this purpose, since it provides a convenient and nondestructive way of measuring the local concentration of the EL2 with good spatial resolution.[35] In this method the value of the absorption coefficient at about 1.2 eV is taken to be a measure of the EL2 concentration. However, we have shown that the presence of other residual deep levels, even at low concentratiors, may give rise to appreciable absorption spectra in the neighborhood of the EL2 spectra.[51] Hence the apparent near-infrared absorption spectra cannot be a priori attributed to the EL2 levels alone.

The EL2 level has been shown to exhibit unusual properties, among them, the quenching of photoluminescence,[52] photocapacitance,[53] and optical absorption,[35] at low temperature (T ≤ 140 K). In particular, the near-infrared absorption spectra due to EL2 quenches out at low temperature after the sample is illuminated with light of 0.9 ≤ hV ≤ 1.35 eV and remains in the quenched state for many hours, even after the background illumination has been

turned off. The sensitivity of the wavelength modulation absorption spectroscopy together with the photo-quenching behavior of the EL2 allowed us to separate the EL2 spectra in the total absorption spectra and to observe the absorption spectra due to all other residual deep levels. Figure 12 shows the absorption due to all the deep levels other than the EL2 in the spectral region of 0.3 - 1.5 eV. The spectra of another SI GaAs sample in the spectral region of 0.5 - 1.5 eV is also shown in Fig. 14, in which the solid curve is the room temperature spectra and the dotted curve is the post-quenching spectra (at 80 K) due to residual absorption. As is seen from these figures, the post-quenching spectra do not exhibit any strong threshold associated with the photoionization of electrons from the iron impurity levels. In surveying several samples of undoped SI GaAs (LEC) we found that in a typical sample up to 20% of the room temperature optical absorption coefficient may be due to residual deep levels other than the EL2.[31]

Therefore in cases where the EL2 concentration and distribution must be measured with better than 10% accuracy,[49] room temperature optical absorption is not adequate. In such cases, the use of infrared wavelength modulation absorption in conjunction with the photo-quenching[31] represent a more accurate method of measuring the EL2 concentration.

V. CONCLUSIONS

In summary, wavelength modulation absorption was used to investigate the deep levels in the undoped SI GaAs (LEC) which is currently of high technological interest. Extensive low temperature measurements permitted observation of structures with fine details in the spectra of the SI GaAs at 0.37 eV and 0.4 eV. The structures near 0.37 eV were identified as intra-center transitions between the levels of accidental iron impurities incorporated in the Ga sublattice. To our knowledge this was the first observation of the iron absorption spectra in the SI GaAs at such low levels of concentration. The structure at 0.4 eV was considered as being due to an intra-center transition associated with a growth related multi-level defect complex. The fine details of this structure were found to be sensitive to the thermal history of the sample, and the whole structure was annealed out at about 450 C. Such a level and its characeristics have not been previously reported.

Measurements at liquid nitrogen temperature also allowed us to utilize the photo-quenching behavior of the absorption bands in the spectral region of 0.7 - 1.45 eV to assess the accuracy of the conventional room temperature optical absorption spectroscopies in measuring the deep level concentrations. It was demonstrated that the non-selectivity of such measurements may give erroneous results in measuring the concentration of specific deep levels, because of appreciable absorption due to the collective contribution of other residual deep levels. This result holds special significance in the current investigations on the origin of the non-uniform distribution of the main electron trap, the EL2 level, in the undoped SI GaAs (LEC).

ACKNOWLEDGMENTS

REFERENCES

1. A. G. Milnes, Deep Impurities in Semiconductors (Wiley, New York, 1973).

2. S. T. Pantelides, Rev. Mod. Phys. 50, 797 (1978).

3. M. Scheffler, in Festkorperprobleme XXII, ed. by A. P. Grosse (Vieweg, Braunschweig, 1984), p. 115.

4. M. Jaros, Deep Levels in Semiconductors (Adam Hilger Ltd., Bristol, U.K., 1982).

5. V. F. Masterov, Sov. Phys. Semicond. 18, 1 (1984).

6. P. Vogl, Adv. Electron. Electron Phys. 62, 101 (1984).

7. R. K. Watt, Point Defects in Crystals (Wiley, New York, 1977).

8. C. T. Sah, Solid State Electron. 19, 975 (1976).

9. H. G. Grimmeiss, Ann. Rev. Mater. Sci. 7, 341 (1977).

10. G. L. Miller, D. V. Lang, and L. C. Kimerling, Ann. Rev. Mater. Sci. 7, 377 (1977).

11. A. Chantre, G. Vincent, and D. Bois, Phys. Rev. B 23, 5335 (1981)

12. A. Mircea and D. Bois, Inst. Phys. Conf. Ser. 46, 82 (1979).

13. G. M. Martin, in Semi-Insulating III-V Materials, Nottingham 1980, ed. by G. J. Rees (Shiva Publ., Orpington, U.K.), p. 13.

14. U. Kaufmann and J. Schneider, Adv. Electron. Electron Phys. 60, 81 (1982).

15. G. Vincent, A. Chantre, and D. Bois, J. Appl. Phys. 50, 5484 (1979).

16. A. Mircea and R. Mitonneau, J. Phys. Lett. (Orsay, Fr.) 40, L-31 (1979).

17. D. Pons and S. Makram-Ebeid, J. Phys. (Orsay, Fr.) 40, 1161 (1979).

18. J. J. Hopfield, G. D. Thomas, and M. Gershenzon, Phys. Rev. Lett. 10, 162 (1963).

19. P. J. Dean, J. D. Cuthbert, G. D. Thomas, and R. T. Lynch, Phys. Rev. Lett. 18, 122 (1967).

20. R. A. Street and W. Senske, Phys. Rev. Lett. 37, 1292 (1976).

21. E. Cohen and M. D. Sturge, Phys. Rev. B 15, 4020 (1977).

22. A. C. Carter, P. J. Dean, M. S. Skolnick, and R. A. Stradling, J. Phys. C 10, 5111 (1977).

23. E. Burstein, G. S. Picus, B. Henvis, and R. Wallis, J. Phys. Chem. Solids 1, 65 (1956).

24. W. H. Kleiner and W. E. Kragg, Phys. Rev. Lett. 25, 1490 (1970).

25. J. M. Baranowski, J. W. Allen, and G. L. Pearson, Phys. Rev. 160, 627 (1967).

26. R. Braunstein, R. K. Kim, and M. Braunstein, in Proceedings of the Symposium on "Laser Induced Damage in Optical Materials" (NBS-SP-620), Boulder, CO, USA, 1980 (Washington D.C., USA: NBS 1981), pp. 29-43.

27. M. Cardona, Modulation Spectroscopy (Academic Press, New York, 1969).

28. R. K. Willardson and A. C. Beer, editors, Semiconductors and Semimetals, Vol. 9, Modulation Techniques (Academic Press, New York, 1977).

29. A. D. Jonath, E. Voronkov, and R. H. Bube, J. Appl. Phys. 46, 1754 (1975).

30. M. Welkowsky and R. Braunstein, Rev. Sci. Instrum 43, 399 (1972).

31. R. K. Kim and R. Braunstein, Appl. Opt. 23, 1166 (1984).

32. R. Zucca, B. M. Wehch, P. M. Asbeck, R. C. Eden, and S. I. Long, in Proceedings of the Semi-Insulating II-V Materials Conference, Nottingham 1980, edited by G. J. Rees (Shiva, Orpington, U.K., 1980), p. 335.

33. R. Braunstein, R. K. Kim, D. Matthews, and M. Braunstein, Physica 117B and 118B (1983).

34. G. M. Martin, A. Mitonneau, and A. Mircea, Electron. Lett. 13, 191 (1977).

35. G. M. Martin, Appl. Phys. Lett. 39, 747 (1981).

36. W. H. Koschel, S. G. Bishop, and B. D. McCombe, in Proceedings of the 13th Internat'l Conference on Physics of Semiconductors, Rome, 1976, p. 1065.

37. E. M. Ganapol'skii, Sov. Phys. Solid State 15, 269 (1973).

38. W. Low and M. Weger, Phys. Rev. 118, 1119 (1960).

39. G. A. Slack, F. S. Ham, and R. M. Chrenko, Phys. Rev. 152, 376 (1966).

40. P. E. R. Nordquist, P. B. Klein, S. G. Bishop, and P. G. Siebermann, Inst. Phys. Conf. Ser. 56, 569 (1981).

41. R. W. Haisty, Appl. Phys. Lett. 7, 208 (1965).

42. V. I. Fistul, L. Ya. Pervova, E. M. Omelyanovskii, and E. P. Rashevskaya, Sov. Phys. Semicond. 8, 311 (1974).

43. D. V. Lang and R. A. Logan, J. Electron. Mater. 4, 1053 (1975).

44. M. R. Burd, Private Communication.

45. D. E. Holmes, R. T. Chen, K. R. Elliott, and C. G. Kirkpatrick, Appl. Phys. Lett. 40, 46 (1982).

46. H. Winston, Solid State Technol. 26, 145 (1983).

47. G. M. Martin, G. Jacob, G. Poilbaldu, A. Goltzone, and C. Schwab, Inst. Phys. Conf. Ser. 59, 281 (1981).

48. M. R. Brozel, I. Grant, R. M. Ware, and D. J. Stirland, Appl. Phys. Lett. 42, 610 (1983).

49. D. E. Holmes, R. T. Chen, K. R. Elliott, and C. G. Kirkpatrick, Appl. Phys. Lett. 43, 305 (1983).

50. S. Miyazawa, Y. Ishii, S. Ishida, and Y. Nanishi, Appl. Phys. Lett. 41, 853 (1983).

51. S. M. Eetemadi and R. Braunstein, to be published.

52. P. W. Yu, Appl. Phys. Lett. 44, 330 (1984).

53. G. Vincent and D. Bois, Solid State Commun. 27, 431 (1978).

END

FILMED

DTIC
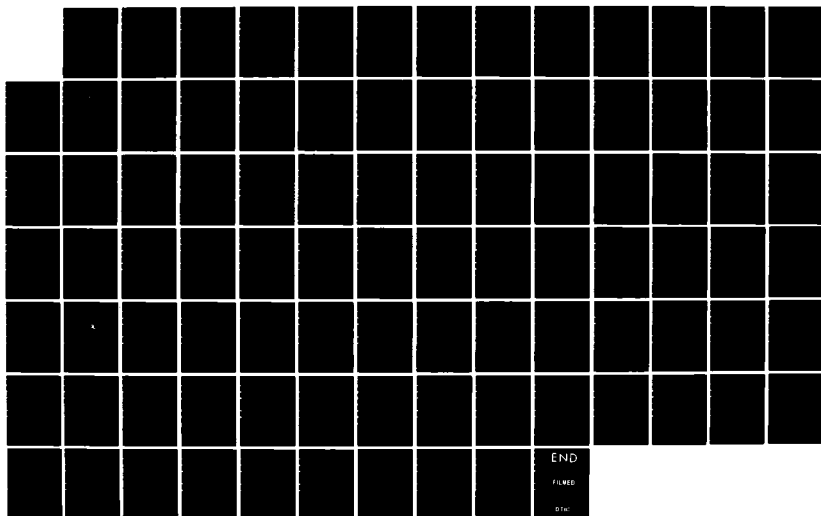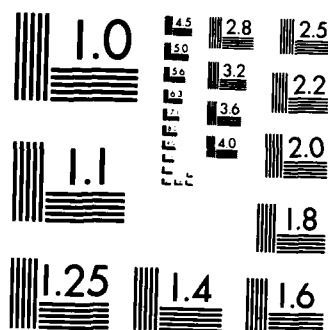
MICROCOPY RESOLUTION TEST CHART

NATIONAL BUREAU OF STANDARDS-1963-A

FIGURE CAPTIONS

Fig. 1.   Block diagram of the wavelength modulation absorption system.

Fig. 2.   Block diagram of the data taking cycle.

Fig. 3.   Absorption spectra of the MO39T SI GaAs (LEC) sample; T = 300 K,
           spectral range: 0.3 - 1.5 eV.

Fig. 4.   Absorption spectra of the MO39T SI GaAs (LEC) sample; T = 160 K,
           spectral range: 0.3 - 1.5 eV.

Fig. 5.   Absorption spectra of the MO39T SI GaAs (LEC) sample; T = 160 K,
           spectral range: 0.3 - 0.52 eV.

Fig. 6.   Absorption spectra of the MO39T SI GaAs (LEC) sample; T = 80 K,
           spectral range: 0.3 - 0.52 eV.

Fig. 7.   Absorption spectra of the MO43T SI GaAs (LEC) sample; T = 80 K,
           spectral range: 0.3 - 0.52 eV.

Fig. 8.   Absorption spectra of the MO32T SI GaAs (LEC) sample; T = 80 K,
           spectral range: 0.3 - 0.52 eV.

Fig. 9.   Absorption spectra of the MO40T SI GaAs (LEC) sample; T = 80 K,
           spectral range: 0.3 - 0.52 eV.

Fig. 10.   Absorption spectra of the MO47T SI GaAs (LEC) sample; T = 80 K,
           spectral range: 0.3 - 0.52 eV.

Fig. 11.   The post-annealed absorption spectra of the MO39T SI GaAs (LEC)
           sample: T = 80 K, spectral range: 0.3 - 0.52 eV.

Fig. 12.   The post-illumination absorption spectra of the MO39T SI GaAs (LEC)
           samples; T = 80 K, spectral range: 0.3 - 0.52 eV.

Fig. 13.   Energy level scheme of the ^5D level of Fe^{2+} $(3d^6)$ in GaAs.

Fig. 14.   The total absorption spectra at 300 K (solid curve) and the residual
           absorption spectra after photo-quenching at 80 K (dotted curve) of
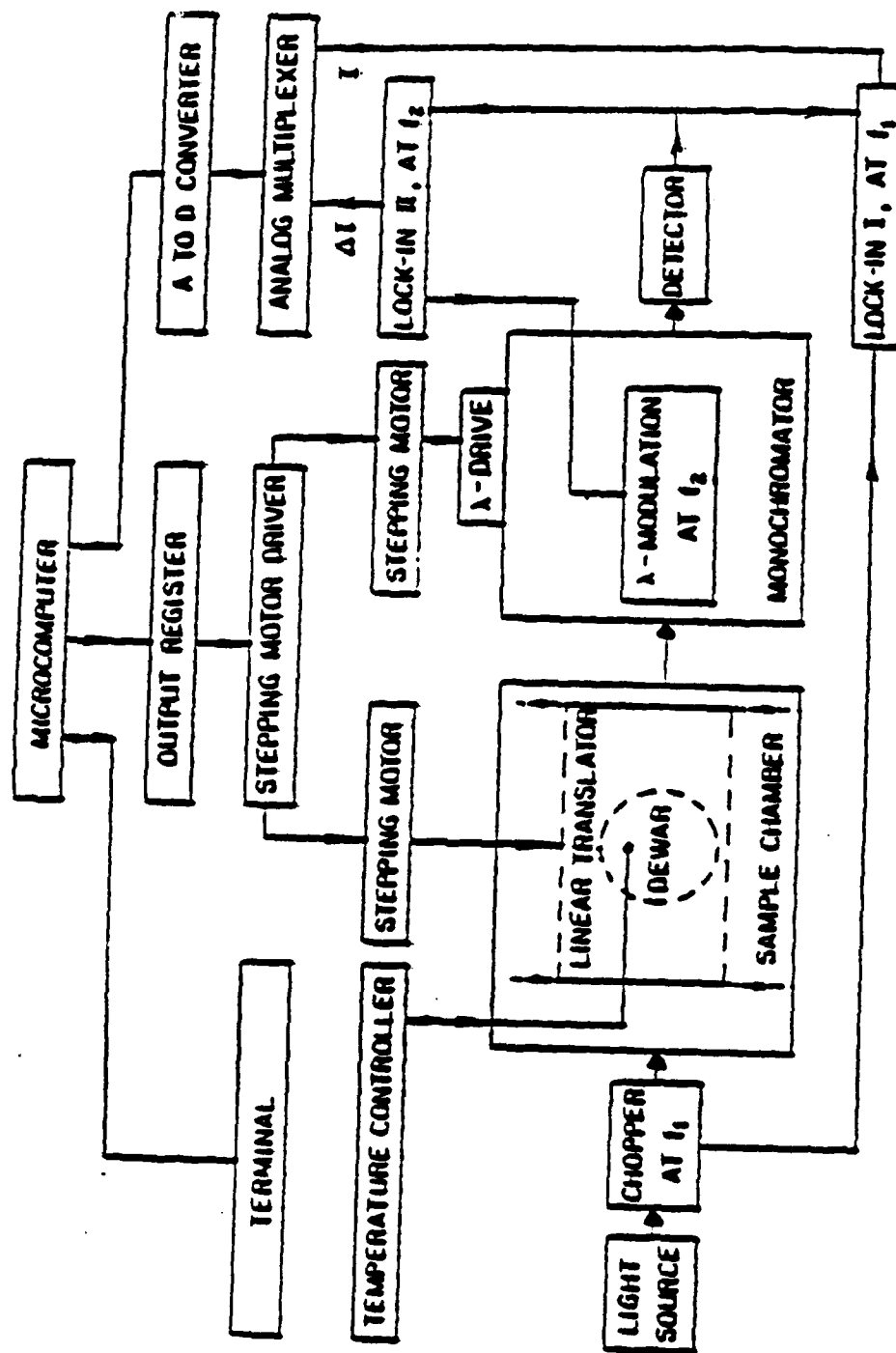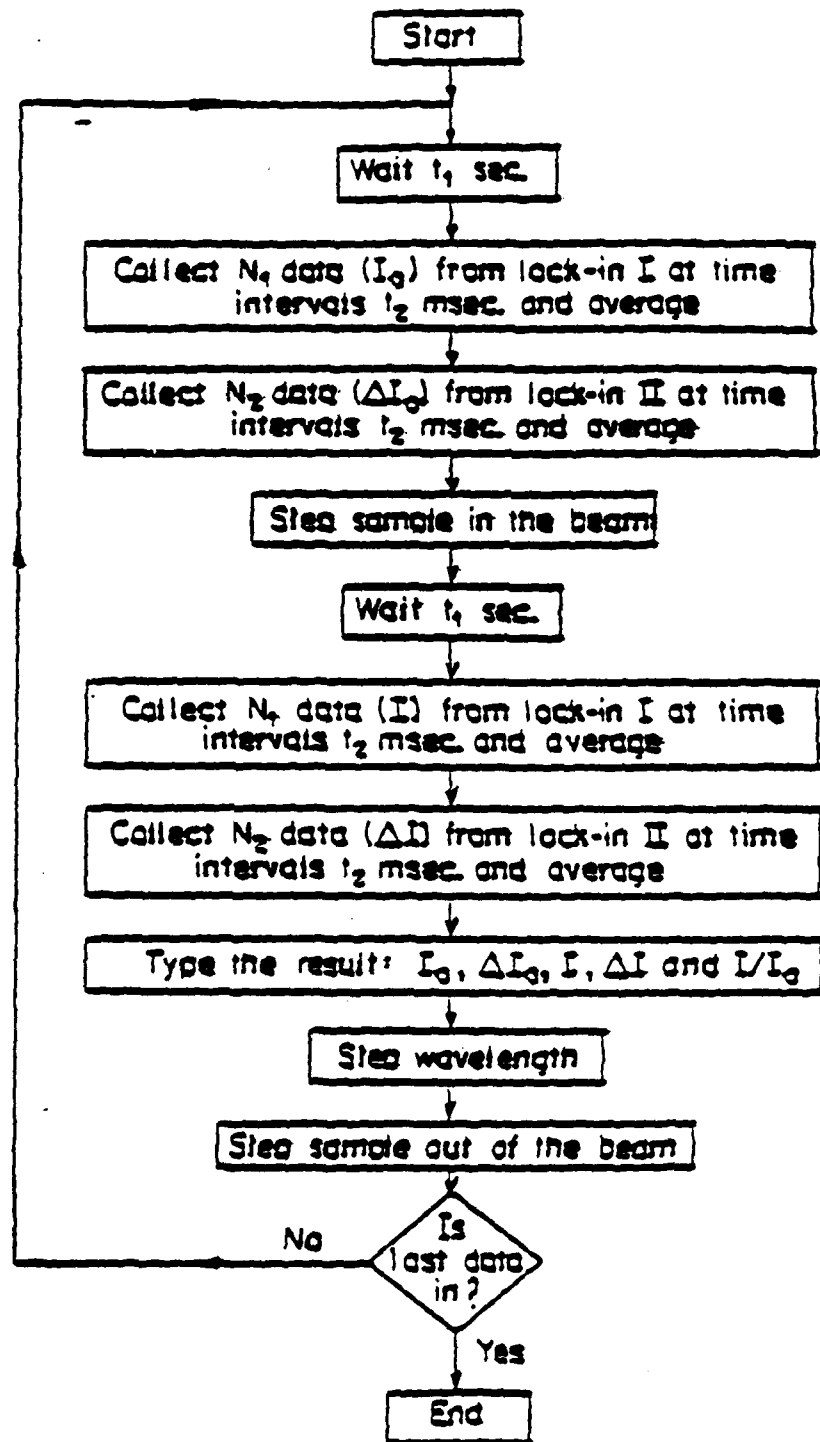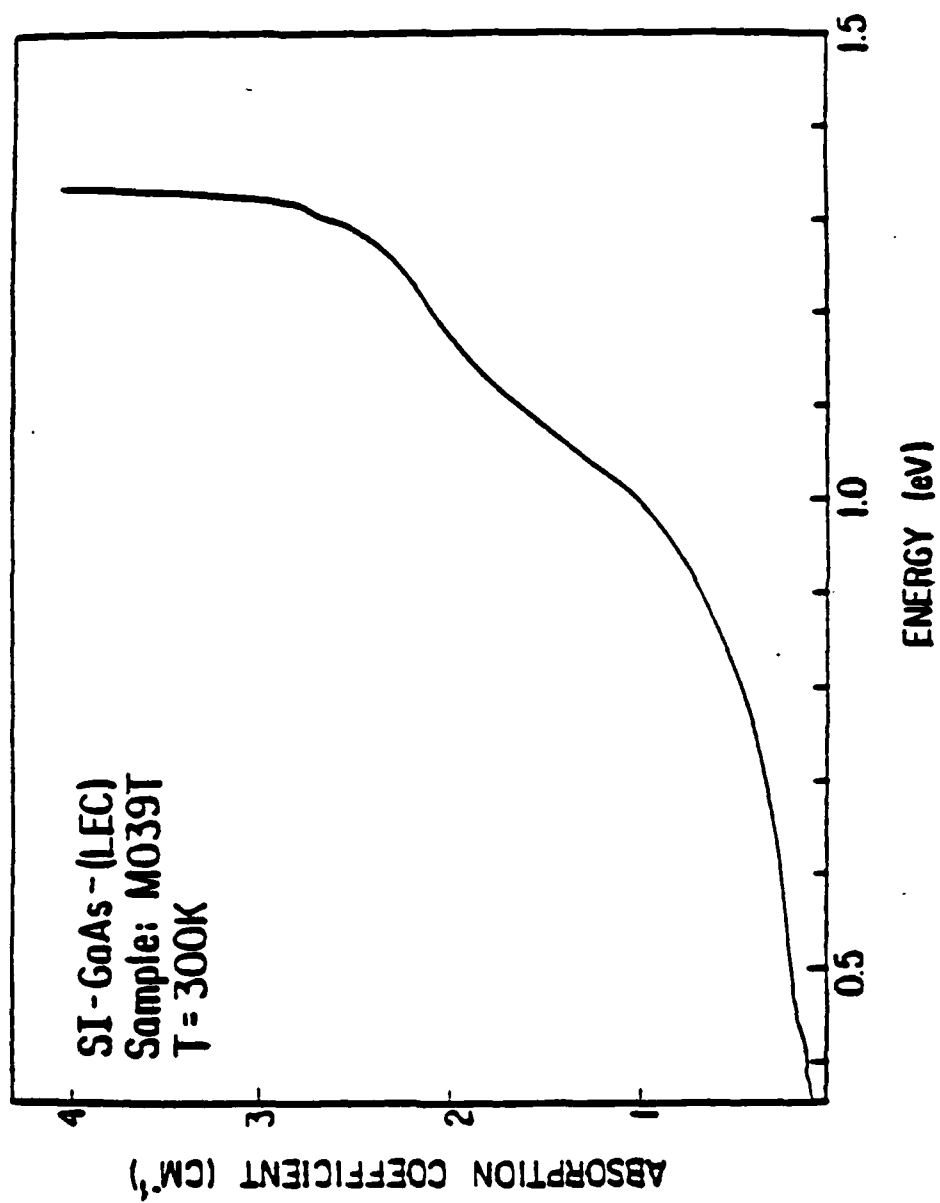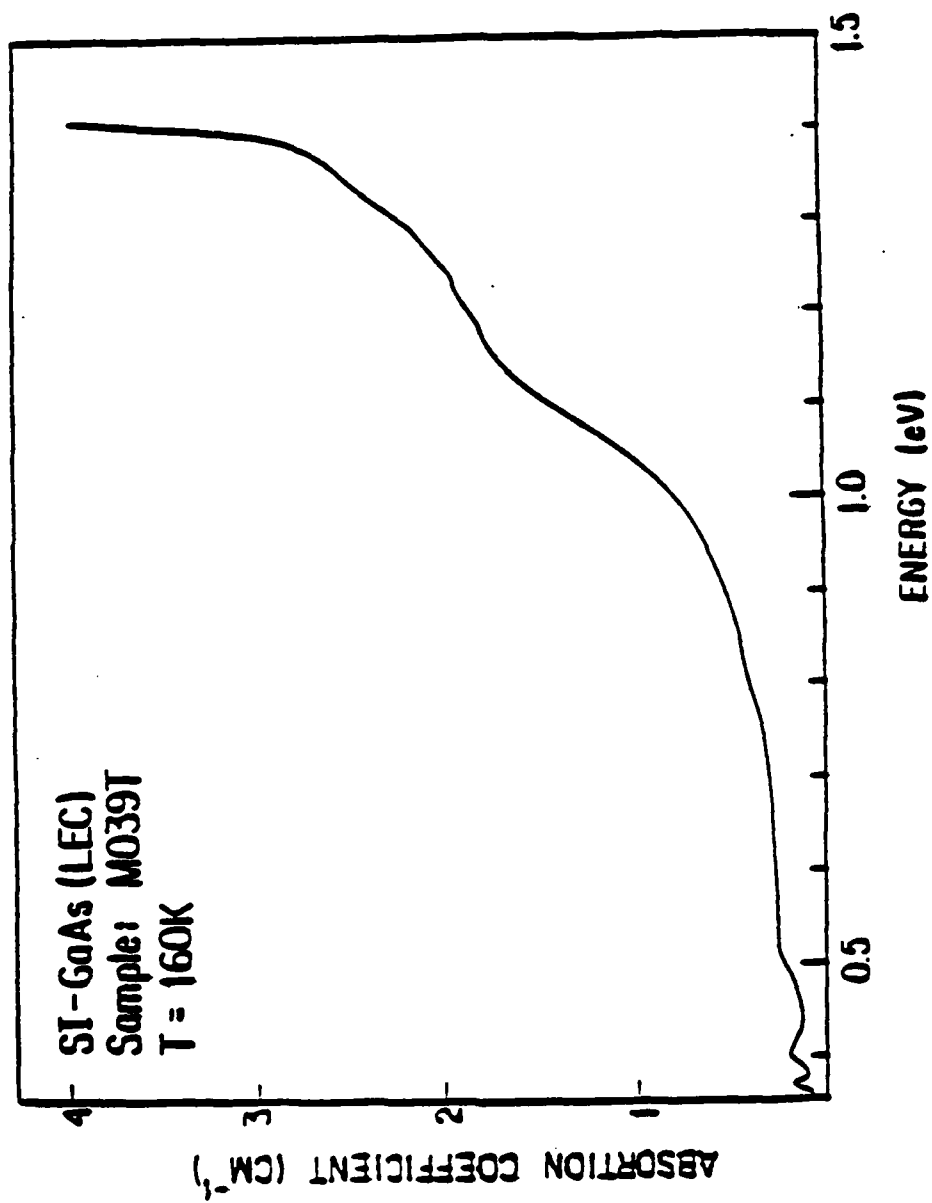   the MO43T SI GaAs (LEC) sample.

Fig. 1

Fig. 2

SI - GaAs - (LEC)
Sample: M039T
T = 300K

ABSORPTION COEFFICIENT (CM⁻¹)

ENERGY (eV)

Fig. 3

SI-GaAs (LEC)
Sample: M039T
T = 160K

ABSORPTION COEFFICIENT (CM⁻¹)
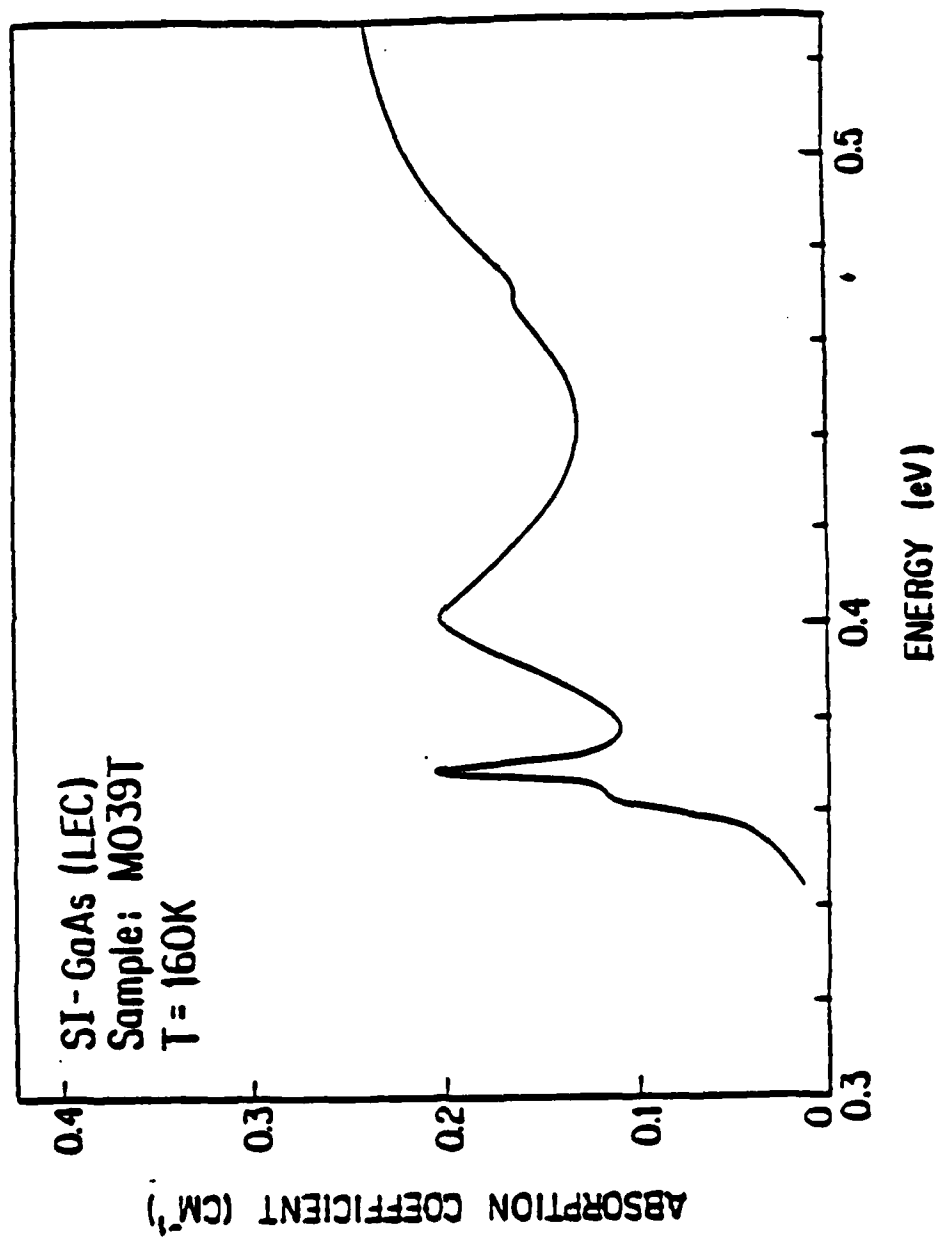
ENERGY (eV)

Fig. 4

SI-GaAs (LEC)
Sample: MO39T
T = 160K

ABSORPTION COEFFICIENT (CM⁻¹)

ENERGY (eV)

Fig. 5

Fig. 6

Fig. 7

SI-GaAs
Sample: MO32T
T = 80K

ABSORPTION COEFFICIENT (CM⁻¹)
ENERGY (eV)

Fig. 8

SI-GaAs(LEC)
Sample: MQ40T
T = 80K

ABSORPTION COEFFICIENT (CM⁻¹)

ENERGY (eV)

Fig. 9

SI - GaAs (LEC)
Sample: M047T
T = 80K

ABSORPTION COEFFICIENT (CM⁻¹)

ENERGY (eV)

Fig. 10

SI-GaAs(LEC)
Sample: MO39T Annealed
T = 80K

ABSORPTION COEFFICIENT (CM⁻¹)

ENERGY (eV)

Fig. 11

Table 1. Description of sample preparations

SAMPLE	DESCRIPTION OF SAMPLE PREPARATION
D9 MO2S M2S-2I	LEC-grown GaAs with ion-implanted contacts (note: there is extensive annealing as part of the ion-implantation process)
M177	LEC-grown with MBE layer, ion-implanted contacts (note: there is extensive heat treatment during both the MBE and ion- implantation processes)
MO39 MO43 M2S-2	LEC-grown with In soldered contacts
MO39 ann MO43 ann M2S-2 ann	LEC-grown and annealed at 700K for four hours with a one hour cool off, In- soldered contacts
MO39 que	LEC-grown and heat treated at 700K for three hours with a fast cool off, In- soldered contacts

Figure Captions

Fig. 1 Block diagram of the photo-induced transient spectroscopy apparatus.

Fig. 2 Flow diagram of the computer program which operates the photo-
induced transient spectroscopy apparatus.

Fig. 3 Plots of $\log(T_m^2 t)$ versus $1/T$ for all deep levels seen by photo-
induced transient spectroscopy.

Fig. 4 Transient current vs. T for sample MO39 t=40 msec, He-Ne laser
light source.

Fig. 5 Transient current vs. T for sample MO39 ann t=40 msec, He-Ne
laser light source.

References

1. C.T. Sah, L. Forbes, L.L. Rosier, and A.F. Tasch, Jr., Solid State Elect. 13, 759 (1970).

2. R. Thyagarajan, R.C. Narula, and T.R. Parashar, Ind. J. Pure and Appl. Phys. 17, 650 (1979).

3. Ch. Gurtes, M. Boulou, A. Mitonneau, and D. Bois, Appl. Phys. Lett. 32, 821 (1978).

4. M.R. Burd, doctoral thesis, University of California, Los Angeles (1984).

5. A. Mitonneau, G.M. Martin, and A. Mircea, Electron. Lett. 13, 666 (1977).

6. G.M. Martin, A. Mitonneau, and A. Mircea, Electron. Lett. 13, 191 (1977).

7. P.E.R. Nordquist, P.B. Klein, S.G. Bishop, and P.G. Siebenmann, Inst. Phys. Conf. Ser. 56, 569 (1981).

8. A. Mircea and D. Bois, Inst. Phys. Conf. Ser. 46, 82 (1979).

9. G.M. Martin, P. Secordel, and C. Venger, J. Appl. Phys. 53, 8706 (1982).

10. R.N. Thomas, H.M. Hobgood, D.L. Barret, and G. Eldridge, Proceedings of the Conference on Semi-Insulating III-IV Materials, Shiva, Nottingham, p. 76 (1980).

11. A. Mircea, A. Mitonneau, and J. Vannemenus, J. Physique (Lett.) 38, L41 (1977).

produced in the boron-implantation process might be what caused this level to be broadened into a band. This damage would not be present in the samples where the boron was introduced during the growth process. Since it is not possible to determine whether the level is hole-like or electron-like with P.I.T.S. both a σ_{pa} and a σ_{na} are reported for it in Table 3.

III. Conclusions

Several deep levels were seen in samples of semi-insulating liquid encapsulated Czochralski grown GaAs by photo-induced transient spectroscopy. Two of the levels one at 0.56 eV and the other at 0.27 eV appear in all of the LEC samples regardless of the heat treatment they received and seem to be related to the presence of iron and zinc impurities respectively. These are most probably due to accidental introduction during the growth process since there was no intentional doping of the GaAs used in this study. Most of the other deep levels seen were correlated with levels seen by other investigators. Very good agreement between the signatures of the levels made the identifications certain. One particular deep level seen with an energy of 0.52 eV seems to be related to a complex defect involving boron present in the samples. It appears to ba a non-broadened version of the band seen in boron-implanted GaAs and probably appears as a single level rather than a band because the boron was introduced during the growth process instead of being ion-implanted.

level with the activation energy of 0.42 eV is HBS which is believed to be the same level as HLS.[5] This particular level is thought to be associated with a native defect in the crystal. This is supported in this study by the fact that it is readily annealed, as can be seen in Table 2 since it does not appear in any of the heat treated samples except MO39 que. The fact that it reappears in the quenched sample means that it can be easily reintroduced by "freezing in" the high temperature concentration of these imperfections.

There is some difficulty in assigning a designation to the 0.27 eV level in that its signature lies almost halfway between the signatures of EL8 and HL12.[5] Assuming it is one of the two and not a newly seen level, the feature which lends more weight toward identifying it as HL12 is that the level appears in all of the samples except the MBE samples. HL12 has been seen in samples which contain zinc, a chemical impurity, and is, therefore, not as likely to be affected by annealing. As can be seen in Table 3 this identification results in σ_{pa} being equal to 3.8×10^{-15} cm^2.

The best candidate for the identification of the deep level seen at an energy of 0.52 eV is a somewhat unconventional band seen in samples which have undergone ion-implantation using boron as the bombarding ions.[9] This boron-implantation produced defect structures which were annealable and the energy band associated with them has a peak at temperatures which agree with those seen for the level in this work. Since there is most likely boron present in the samples used in this study,[10] and since the band is associated with boron the evidence for associating the level seen in this work with the so-called U-band seen in Ref. 9 seems strong. The reason that this defect produced a clear level in the samples studied here while a band was seen in the samples which were boron-implanted would seem to be due to the difference in the manner in which the boron was introduced into the samples. The associated damage

of behavior can be seen with regard to the heat treatment given the various samples. As can be seen by comparing Fig. 4 to Fig. 5, the difference between an as-grown sample and the same sample after being subjected to heat treatment is quite significant. Table 3 shows a listing of all the observed deep levels' activation energies and emission sections.

The level with an activation energy of 0.18 eV has a signature which matches that of the deep level designated as EL10 and observed in other studies.[6] As can be seen in Table 3 it has a σ_{na} equal to 1.5×10^{-15} cm^2. The best identification for the level with the activation energy of 0.22 eV is EL17.[8] The level being an electron level means σ_{na} is equal to 1.5×10^{-14} cm^2. The best fit to the signature of 0.36 eV level occurs for the deep level designated as HL7.[5] The hole nature of the level means σ_{pa} is equal to 5.6×10^{-13} cm^2.

The deep level listed in Table 3 with an activation energy of 0.56 eV has a signature which is an excellent fit to that of the level designated in other studies as HL3[5] yielding a σ_{pa} equal to 1.4×10^{-15} cm^2. This particular deep level has been found to correspond to the presence of iron in the samples tested in other works. This is supported here by the fact that this level appears in all of the samples used in this study which gives greater weight to the level being associated with a chemical impurity rather than just a crystal imperfection. Another feature which supports this identification is the presence of this level in the MBE sample M177. It is known that iron is a fast diffuser in GaAs[7] and tends to migrate toward the surfaces of a sample. The presence of the 0.56 eV deep level in the MBE sample would imply that the iron-associated defect had migrated from the LEC substrate into the MBE layer during either the MBE process or the ion-implantation of the electrical contacts.

The deep level with a signature which most closely matches that of the

line graph. The value for γ_n has been determined to be $(4\sqrt{6}\ \pi^{3/2}\ h^{-3}\ m_n^* \ k^2).$[11]

For electrons this equals $2.28\times10^{20}\ cm^{-2}s^{-1}K^{-2}.$[6] Putting in the effective mass

term for holes yields a value of $1.7\times10^{21}\ cm^{-2}s^{-1}K^{-2}.$[5] This straight line

graph or the combination of E_A and σ_{na} (σ_{pa} for holes) is called the signature

of the deep level and is preferred method for identifying a deep level.

The photo-induced-transient spectroscopy (P.I.T.S.) apparatus[4] consisted of

a dewar in which the samples could be cooled to liquid nitrogen temperatures.

There were windows in the dewar to allow the light pulses from the two light

sources used for this experiment to strike the samples. The light sources used

were a He-Ne laser and a GaAs light emitting diode which gave light at energies

greater than and less than the band gap respectively. The temperatue of the

sample was monitored by a thermocouple. The current through the sample was

measured as a voltage across a resistor which was placed in series with the

sample and the dc power supply which provided the bias voltage to the sample.

The apparatus was controlled and the temperature and transient current were

read by a CAMAC data acquisition system under the control of an LSI-11/23

computer. A representation of the transient current was obtained at each point

in temperature by having the computer read the voltage across the series

resistor at several regularly spaced times following each pulse of light. This

allowed a complete set of data to be obtained in only one temperature scan.

Figure 1 shows a block diagram of the P.I.T.S. apparatus while Fig. 2 shows the

flow diagram for the computer program which controls the system.

The signatures of all the deep levels seen in all of the samples tested are

compiled in Fig. 3, while a tabulation of which level was present in a given

sample is diplayed in Table 2. As can be seen there is a rich spectrum of deep

levels in the samples which were not subjected to any heat treatment, those

being M039, M043, and M2S-2. For several of the deep levels definite patterns

The method used to detect the presence of the deep levels in the samples was photo-induced-transient spectroscopy.[3] This technique involves pulsing a monochromatic light source at a sample of GaAs which has a bias voltage applied across contacts on its surface. The transient current which follows the termination of the light pulse is then measured. If the trap being seen is an electron-like trap and the intensity of the light pulse is such that a saturated condition is achieved for the photo-current then the form of the transient current becomes:

$$\delta i(t) = CN_T \, e_n \, \exp(-e_n t) \qquad (1)$$

where e_n is the emission rate, N_T is the trap concentration, and C is a constant. When this equation is differentiated with respect to temperature the following results:

$$\frac{d\delta i(t)}{dT} = C \, N_T \, (1-e_n t) \, \exp(-e_n t) \, \frac{de_n}{dT} \quad . \qquad (2)$$

It can be seen that an extremum occurs when $t = 1/e_n$. Therefore, by choosing a time after the termination of the light pulse and plotting the magnitude of the transient current as a function of temperature, a series of peaks are obtained. Each peak corresponds to a different deep level with the position of the peak occurring at a temperature, T_m, where the level's emission rate is equal to the reciprocal of the time chosen. By graphing the transient current's value at different times as a function of temperature, several values of T_m can be obtained for the different values of the time, t. Assuming the form for e_n is[6]:

$$e_n = \gamma_n \, T^2 \, (\sigma_{n\infty} \, g_n \, \exp(\alpha/k)) \, \exp(-E_A/kT). \qquad (3)$$

where E_A is called the activation energy and $\sigma_{na} = (\sigma_{n\infty} \, g_n \, \exp(\alpha/k))$ is the apparent cross section. A plot of $\log(T^2 t)$ versus $1/T$ will yield a straight

II. Experimental Techniques

All of the samples used in this study were LEC grown[2] GaAs and were semi-insulating because of the deep levels which were caused by the growth process as opposed to being deliberately introduced into the samples by doping with materials such as Cr. One sample, M177, however, did have a layer of GaAs grown on it by molecular beam epitaxy. A summary of the treatment of the samples is presented in Table 1.

Samples MO39, MO43, and M2S-2 had no heat treatment performed on them until they had first been tested for deep levels; then the same samples were annealed and redesignated MO39 ann, MO43 ann, and M2S-2 ann. The annealing process involved raising their temperature in a nitrogen atmosphere over a period of one hour from room temperature to 700K. They were left at this temperature for four hours and then, over a period of one hour, their temperature was lowered back to room temperature. After being tested for deep levels sample MO39 ann was given another heat treatment and redesignated MO39 que. This particular heat treatment involved raising its temperature to 700K over a period of one hour. The sample was left at this temperature for a period of three hours and then was cooled back down to room temperature in approximately ten seconds.

Samples M2S-2I, D9, MO2S, and M177 had ion-implanted electrical contacts. This process involves masking the samples and implanting Si ions into the surface at extremely high concentrations such that the conductivity becomes very large in the implanted regions. The samples are then given a high temperature anneal to drive in the Si and remove some of the damage caused by the implantation process. The electrical contacts on all of the other samples were made by soldering In to the surfaces of the samples with an ultrasonic soldering iron. The soldering process was performed as quickly as possible in order to minimize the amount of heating the samples would be subjected to.

I. Introduction

It is important to fully understand the deep levels present in GaAs samples which have been prepared by various growth techniques. Unfortunately, in many of the studies done on samples produced by a particular growth method the measurement techniques used tended to obscure some of the deep levels which may have been present at the time of growth. For instance, the use of deep level transient spectroscopy[1] requires the construction of a diode structure from the sample to be studied causing the sample to be subjected to relatively high temperature annealing. Such temperature treatment can remove defects that give rise to certain deep levels, thus, making them impossible to study.

The purpose of this study is to investigate the deep levels present in samples of liquid encapsulated Czochralski (LEC) grown, semi-insulating GaAs. To accomplish this, photo-induced-transient spectroscopy was used as the measurement technique for detecting deep levels in the sample. This method was chosen for two reasons: first, it is one of the preferred methods for detecting deep levels in semi-insulating GaAs, and, second, the preparation of the samples for this technique involves only a small amount of heat treatment allowing study of annealable deep levels which may have been introduced during the growth process.

Measurements were made on samples which had been subjected to a variety of heat treatments with the purpose of giving some evidence for possible defect structures which may be causing the deep levels. Using these methods seven deep levels were observed with most of them being readily identified with deep levels seen in other works.

Deep Levels in Semi-Insulating, Liquid-

Encapsulated-Czochralski-Grown GaAs

M.R. Burd and R. Braunstein

Department of Physics, University of California

Los Angeles, California 90024

Using photo-induced-transient spectroscopy on variously heat-treated samples of semi-insulating LEC-grown GaAs, we detected seven deep levels. Six of these levels were matched with previously catalogued levels, four of them being hole-like and two being electron-like. The seventh level appears to be associated with a boron-related defect which has previously been seen only as a band in boron-implanted GaAs.
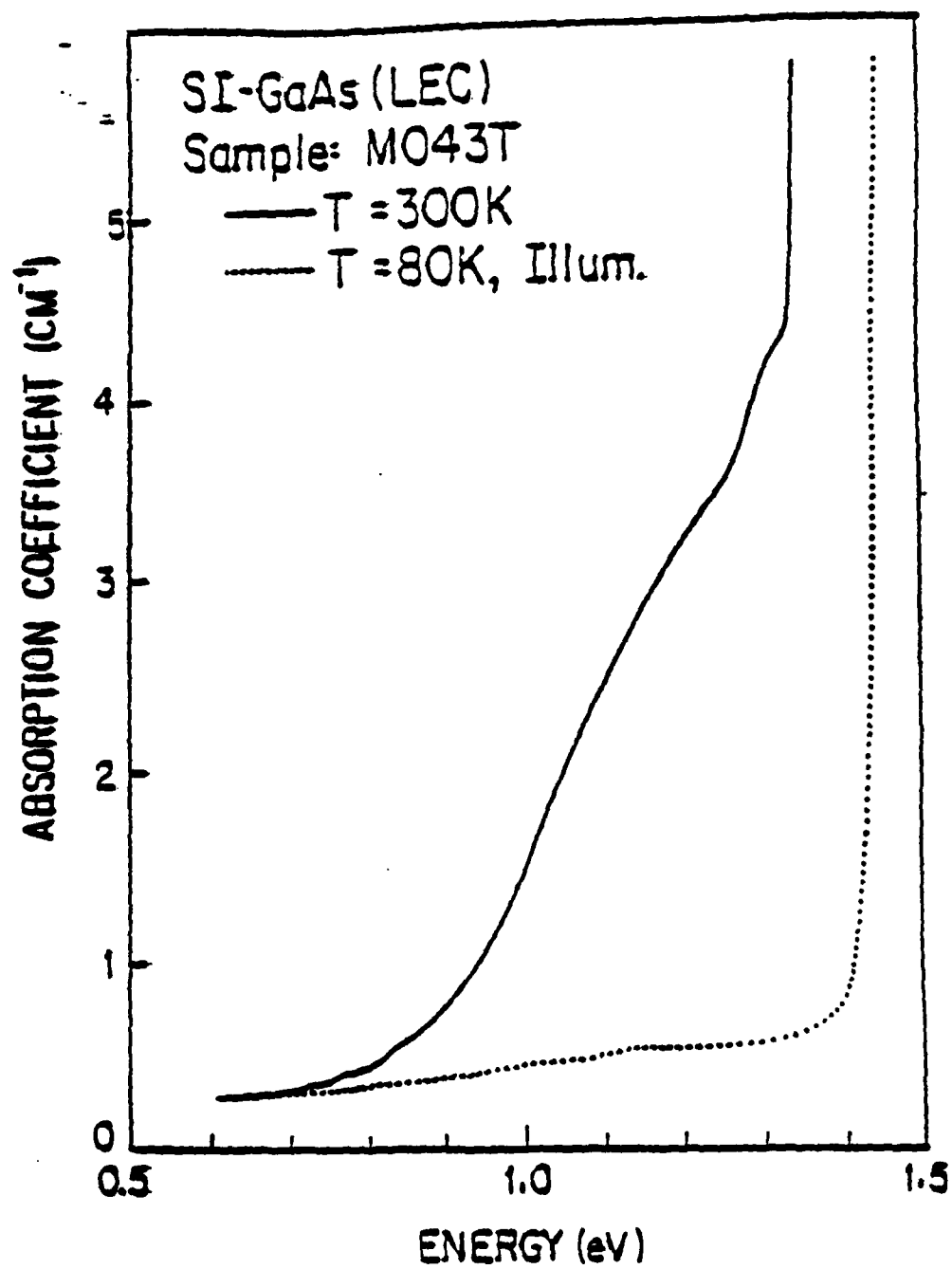
SI-GaAs (LEC)
Sample: MO43T
——— T = 300K
······ T = 80K, Illum.

Fig. 14

Fig. 13

SI-GaAs(LEC)
Sample: M039T
T = 80K

ENERGY (eV)

ABSORPTION COEFFICIENT (CM⁻¹)
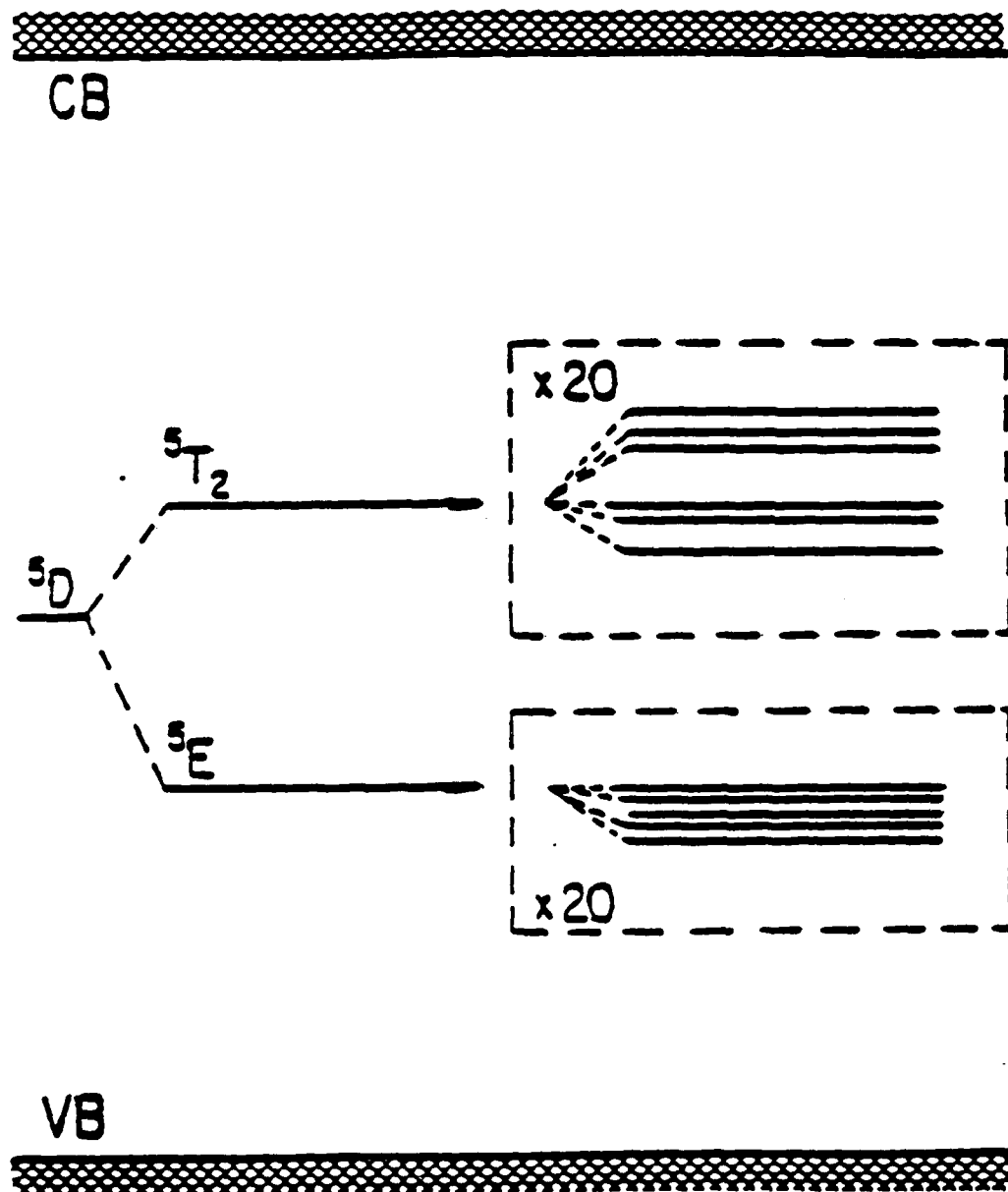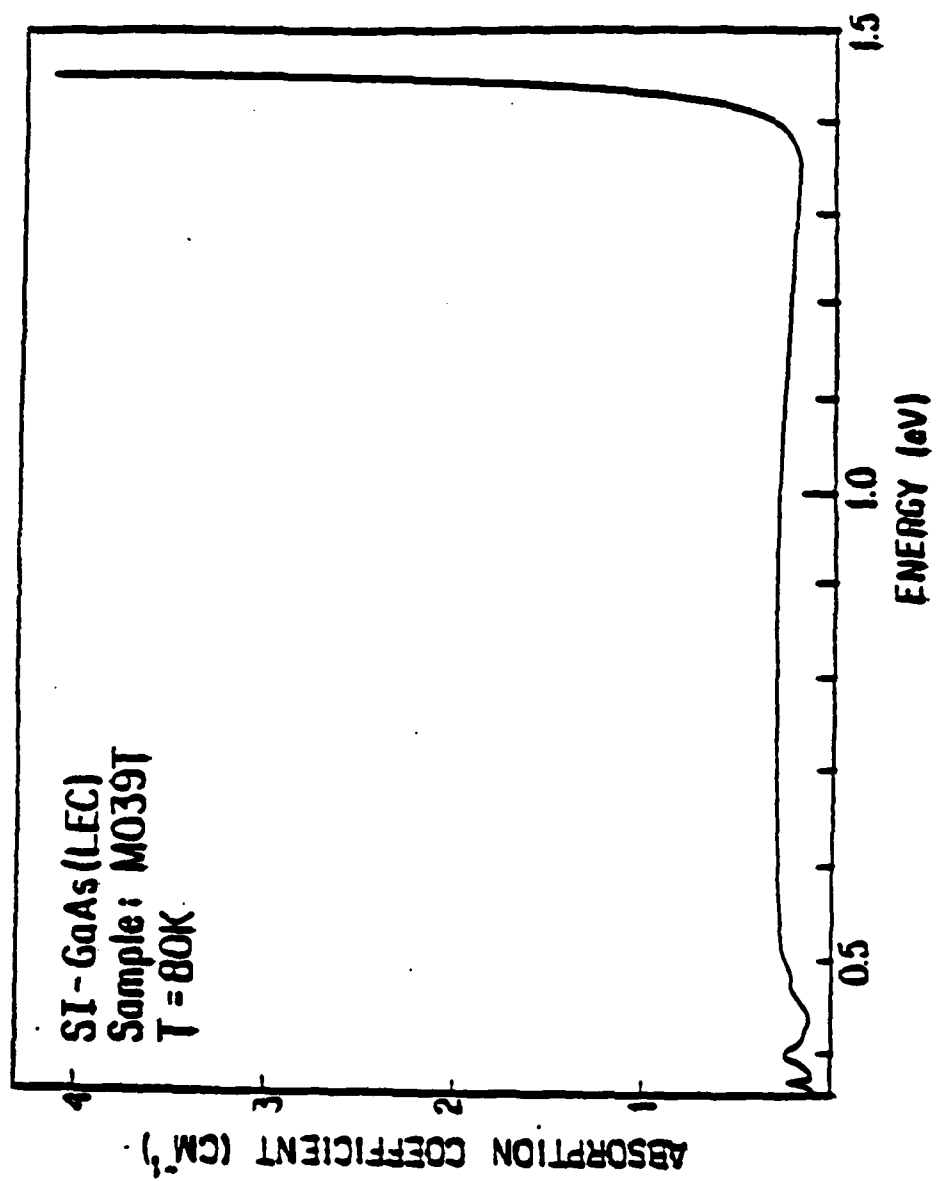
Fig. 12

Table 2. <u>Activation energies of deep levels detected by photo-induced transient spectrscopy measurements</u>

SAMPLE	ACTIVATION ENERGY OF THE LEVEL (eV)						
M2S-2I	0.57			0.36	0.27		0.18
D9	0.56			0.36	0.28	0.22	
MO2S	0.55			0.36	0.27	0.22	0.18
M177	0.56						
M2S-2	0.56	0.52	0.42	0.36	0.27		0.18
MO39	0.56	0.52	0.42	0.36	0.27	0.22	0.18
MO43	0.56	0.52	0.42	0.36	0.27		0.18
M2S-2 ann	0.56				0.27		0.18
MO39 ann	0.56				0.27	0.22	
MO43 ann	0.57				0.27		
MO39 que	0.56		0.42		0.27	0.22	

Table 3. Activation energies and emission sections for the deep levels
          seen in this study

LEVEL IDENTIFIED	ACTIVATION ENERGY (eV)	EMISSION SECTION (cm^2)
HL3	0.56	$\sigma_{pa} = 1.4 \times 10^{-15}$
Boron defect	0.52	$\sigma_{pa} = 1.7 \times 10^{-14}$ $\sigma_{na} = 1.3 \times 10^{-13}$
HBS or HLS	0.42	$\sigma_{pa} = 2.2 \times 10^{-13}$
HL7	0.36	$\sigma_{pa} = 5.6 \times 10^{-13}$
HL12	0.27	$\sigma_{pa} = 3.8 \times 10^{-15}$
EL17	0.22	$\sigma_{na} = 1.5 \times 10^{-14}$
EL10	0.18	$\sigma_{na} = 1.5 \times 10^{-15}$

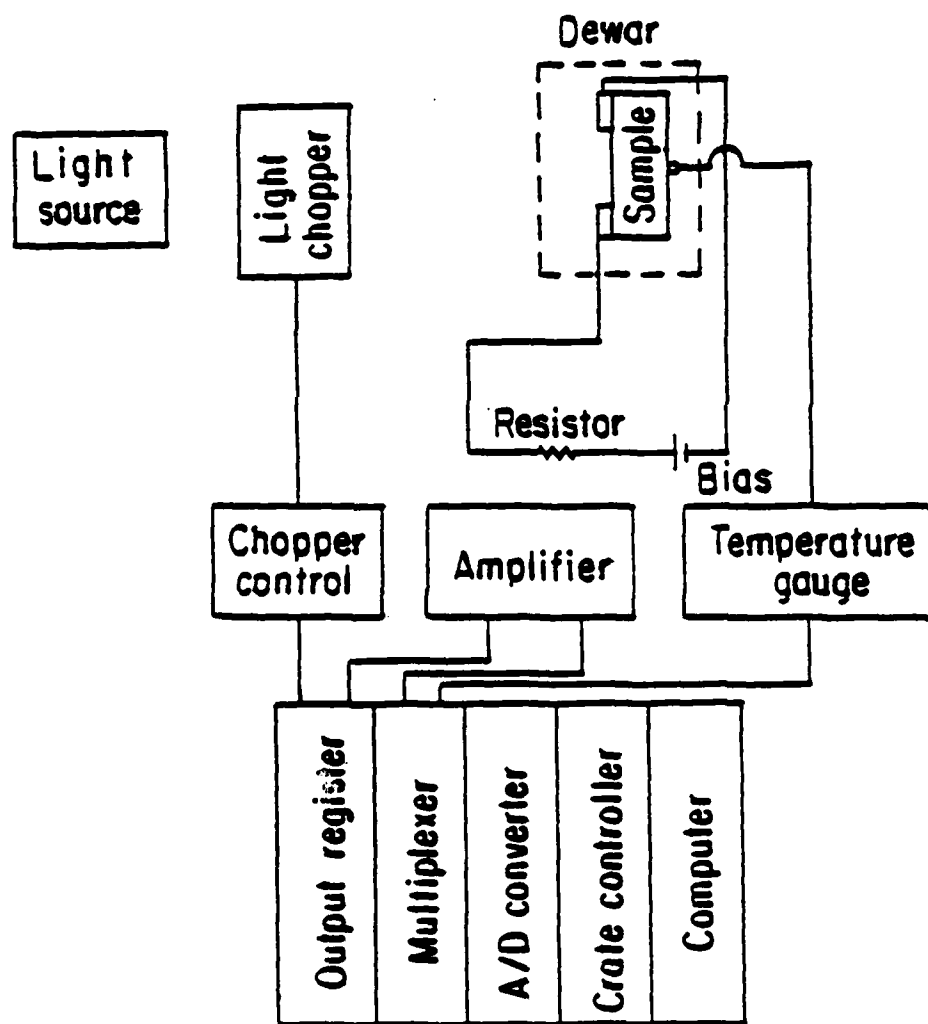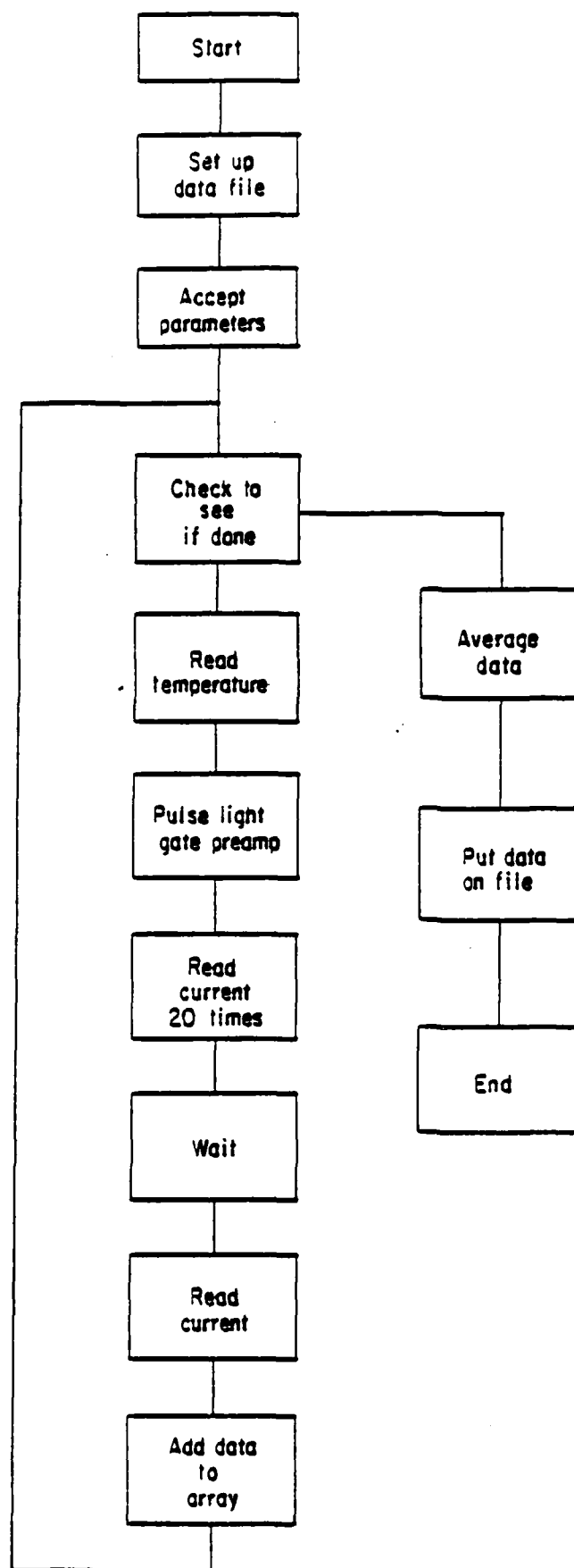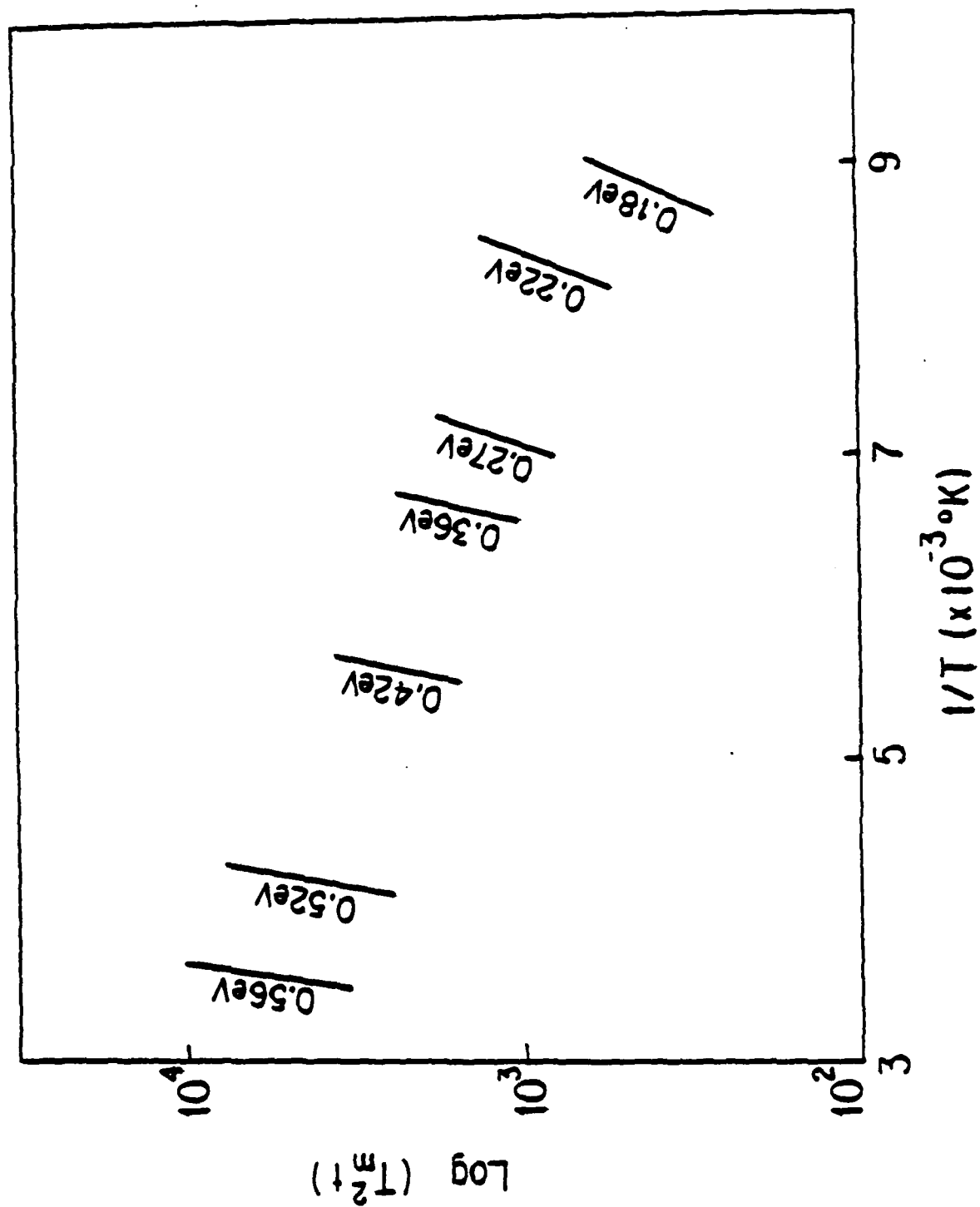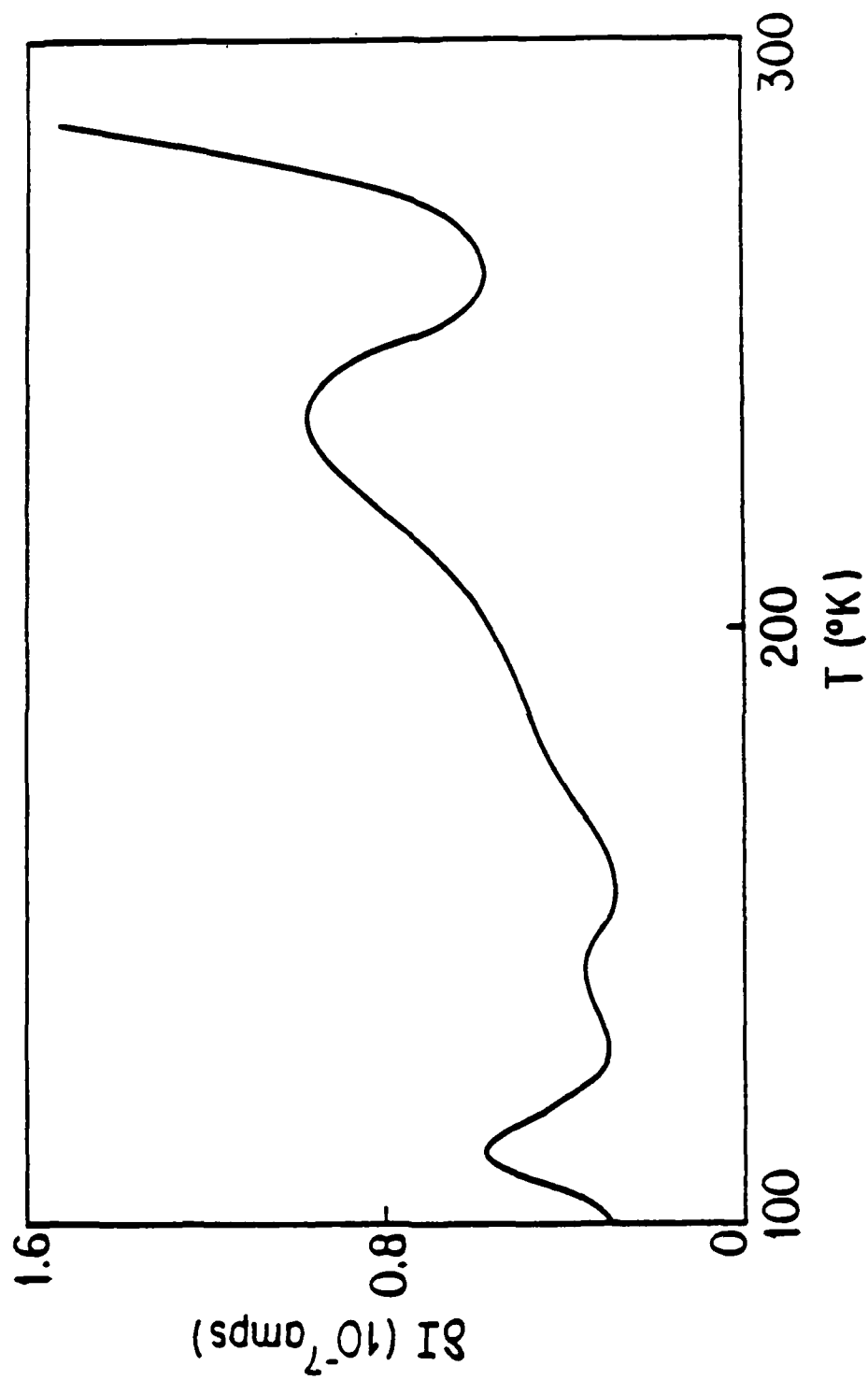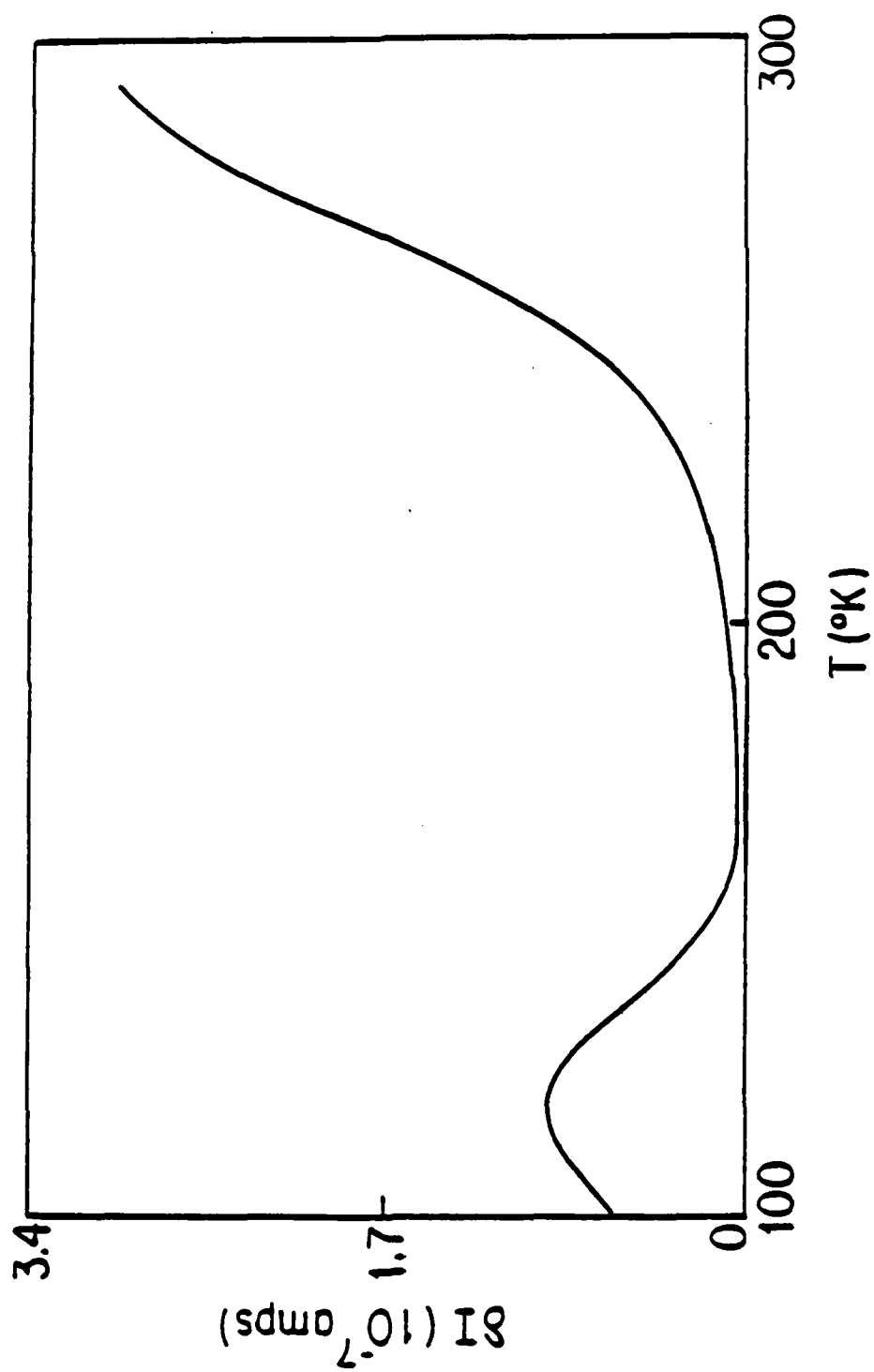Fig. 1

Fig. 2

Fig. 3

δI $(10^{-7}$amps)

T (°K)

-Fig. 4

Fig. 5

Re-examination of the Wavelength

Modulation Photoresponse Spectroscopies

S. M. Eetemadi and R. Braunstein

Department of Physics, University of California,

Los Angeles, California 90024

Re-examination of the wavelength modulation photoresponse

spectroscopies showed that the line shapes obtained by these methods

are subject to distortions from several sources of spurious interference

spectra. Limitations of these methods in studies of the deep levels

and the interband transitions in semiconductors are discussed and a

practical method for removal of the distortions due to the background

spectra is suggested. Finally, a comparison is made between the

wavelength modulation absorption/reflection and the wavelength modulation

photoresponse spectroscopies. It is concluded that the former are the

most suitable modulation techniques for the above studies since they

yield unambiguous line shapes.

I. INTRODUCTION

To measure low level absorption, wavelength modulation techniques are employed. In one form, direct wavelength modulation absorption is utilized,[1] while in other implementations the wavelength modulation photoresponse of the sample is used to infer the absorption.[2-4] In this report we present a re-examination of the wavelength modulation photoresponse spectroscopies in general, and their application to the studies of the deep levels and interband transitions in semiconductors. Some of the limitations of these techniques, as well as the necessary precautions in interpreting the experimental results, are also discussed. A comparison was made between wavelength modulation absorption/refraction and wavelength modulation photoresponse spectroscopies.

Optical modulation spectroscopy has been extensively used in the past to study the optical absorption and reflection of materials.[5] Being a derivative technique in nature, it is far more sensitive than conventional spectroscopic methods for detecting small structures out of a broad background.[6] Various modulation parameters such as applied electric field, stress, temperature, and wavelength of the probing light beam have been combined with absorption and refelction spectroscopy to form a whole family of derivative spectroscopy techniques.[7] More recently, other derivative techniques combining the wavelength modulation and the photoresponse (photo-induced changes in voltage, capacitance, and current) spectroscopies have been introduced as a new approach to the study of absorption in semiconductors. Wavelength modulation photoconductivity,[2] photovoltage,[3] and photocapacitance,[4] are some examples. Such techniques have been used to study the interband transitions as well as transition involving the photoionization of the deep levels in some semiconducting materials.

In these methods, samples are prepared in the form of a p-n junction,[2] a

metal-insulator-semiconductor (MIS),[3] or a Schottky barrier[4] with semi-transparent electrodes. The changes in the photoresponse induced in the space-charge region, by wavelength modulation of the incident light beam, are measured using a phase-locked amplifier synchronous with the wavelength modulator. The derivative photoresponse spectrum thus obtained is interpreted as being proportional to the derivative of the absorption coefficient, and thus to the derivative of the photoionization cross section.[3] In particular, for the transitions involving photoionization of the deep levels, the derivative surface photovoltage (DSPV) is given by[4]:

$$\frac{dV_s}{d\lambda} = - V_s \, I_o \, A \, \frac{n_t}{N_D - N_A} \frac{d\sigma}{d\lambda} \quad , \tag{1}$$

where V_s is the surface photovoltage, I_o is the incident photon flux, n_t is the concentration of the occupied traps being probed, and $N_D - N_A$ is the net doping concentration. The constant, A, depends on the thermal generation and recombination of the traps, and σ is the photoionization cross section.

Wavelength modulation reflection and transmission spectroscopies have a serious experimental difficulty because the spectra contain substantial spurious structures originating from the derivative of the background spectra which must be properly removed in order to obtain the true spectra of the sample itself.[8] The structures in the background spectrum are due to the spectral dependence of the light source intensity, various optical components of the experimental system, and the atmospheric absorption, especially in the infrared region of the spectra. These structures have been successfully removed by various ingenious methods of background derivative subtractions,[5] including double beam-single detector[9] and single beam sample-in sample-out techniques.[1] However, the question of the effect of the background spectra on

the derivative photoresponse results has not yet been addressed in the previous theoretical and experimental works on this subject.

To investigate the possible effects of the background spectra, a preliminary derivative surface photovoltage (DSPV) experiment was conducted on a silicon sample prepared in the form of a semi-transparent MOS structure, and the result was compared with the derivative of the incident photon flux spectrum. Similarities between changes in the structures observed in both spectra were taken as an indication of possible superposition of the derivative of the background spectra on the DSPV spectra, and prompted us to re-examine the theory of the wavelength modulation surface photovoltage spectroscopy.

The result of our investigation showed that the proportionality relationship, eq. (1), between the DSPV and the derivative of the absorption coefficient is not valid in general. the DSPV spectra are rather a superposition of several terms, one of which includes 'he derivative of the background spectra; these additional terms are the various sources of distortions depend on the spectral region under investigation. Important implications of this result in the DSPV studies of the deep levels and the interband transitions are further explored below and modifications of the experimental technique for the removal of the major portions of the background spectra are suggested. The following discussion is focused primarily on the wavelength modulation surface photovoltage. The analysis, however, applies equally to other modulation photoresponse spectroscopies as well.

II. EXPERIMENTAL RESULTS

The derivative surface photovoltage measurements were performed on n-type silicon substrates (100) utilizing MOS structures. The experimental system used is described elsewhere.[10] The MOS structures were made by evaporating a 400 Å semi-transparent gold electrode on an oxide layer (1000 Å thick) grown on silicon by a standard dry oxidation technique.[11]

Typical sub-band-gap derivative surface photovoltage spectra (dV_s/dE) obtained at 83 K are shown in Figs. 1(a) and 2(a). To obtain a good signal-to-noise ratio it was necessary to keep the modulation amplitude and the spectral slit width of the monochromator fairly large: $\Delta\lambda/\lambda \sim 10^{-2}$. The derivatives of the incident photon flux spectra for the same instrument and spectral region with comparable amplitude of modulation were obtained using a PbS detector. These are shown for comparison in Figs. 1(b) and 2(b). With the sensitivity of the PbS detector a much better resolution, $\Delta\lambda/\lambda \sim 2\times10^{-3}$ is also possible, as shown in Fig. 3.

The dominant structure in Fig. 1(a) is due to the interband transition near the indirect band gap of silicon with emission and absorption of phonons. It is similar to other reported DSPV results.[12] The smaller structures below 1.15 eV may in principle be associated with the multi-phonon absorption. However, they can also be considered to be a manifestation of similar structures in the derivative of the background spectra dI_o/dE, shown in Fig. 1(b). Comparison of Fig. 2(a) and 2(b) also suggests a strong correlation between the structures in the DSPV and the derivative of the background spectra near 0.65 and 0.9 eV. In fact, signatures of the derivative of the background spectra are quite commonly observed in the wavelength modulated spectra of the reflected and transmitted light beam as predicted by the theory of the corresponding wavelength modulation spectroscopy.[8] These can be

corrected for by subtraction of the experimentally determined background.[8,9] In contrast, the theory of the DSPV, as formulated in Eq. (1), is not consistent ~~with~~ the above observation. In the next section we present our analysis of the theory of the DSPV spectroscopy, which clearly shows that the DSPV spectra can contain signatures of the derivative of the background spectra as well as other possible sources of distortions in the various regions of spectra.

III. DERIVATIVE OF SURFACE PHOTOVOLTAGE (DSPV)

The theory of surface photovoltage has been treated by a number of authors.[13] For the purpose of this study, the changes in the surface potential of a semiconductor, V_s, induced by the light of intensity I_o and wavelength λ may be written, for small signals (surface photovoltage $\ll$ surface potential), in the form[13]:

$$V_s(\lambda) = I(\lambda)\ \alpha(\lambda)\ F(\lambda) \quad , \tag{2}$$

where

$$F = F(L_o, \alpha, T, E_f;\ \tau_b, n_b, p_b;\ E_t, n_t, \sigma_{ph}{}^n, \sigma_{ph}{}^p, e_n e_p, S) \quad .$$

F is a complicated function of diffusion length L_o, absorption coefficient α, temperature T, Fermi energy E_f, bulk carrier lifetime for electrons and holes and concentrations τ_b, n_b, p_b, respectively, deep levels energy E_t, concentration n_t, photoionization cross sections $\sigma_{ph}{}^n$, $\sigma_{ph}{}^p$ for electrons and holes, respectively, and their thermal emission rates e_n and e_p, in the semiconductor as well as the effective surface recombination velocity S. The exact functional dependence of F on these parameters is not needed for our

discussion; however, it is rather important to note its implicit wavelength dependence through $\alpha(\lambda)$, $\sigma_{ph}^{n}(\lambda)$, and $\sigma_{ph}^{p}(\lambda)$. $I(\lambda)$ is the actual photon flux entering the space charge region of the semiconductor. Quite often in the past, $I_o(\lambda)$, which is the incident photon flux illuminating the MOS structure has been used instead of $I(\lambda)$, thus ignoring the spectral dependence of the transmittance through the metal and the insulating layers $I(\lambda)$ and $I_o(\lambda)$ are related by[14]:

$$I(\lambda) = I_o(\lambda) \, T(\lambda) \qquad (3)$$

with

$$T(\lambda) = n_3 \left| \frac{(1+r_1)(1+r_2)(1+r_3) \, \exp(\delta_1+\delta_2)}{1 + r_1 r_2 \, \exp2\delta_1 + r_1 r_3 \, \exp2(\delta_1+\delta_2) + r_2 r_3 \, \exp2\delta_2} \right|^2 \qquad (4)$$

where r_i are the Fresnel reflection coefficients at the interfaces and are defined in terms of the complex refractive indices ($N = n+ik$) of the media involved as follows:

$$r_1 = \frac{1-N_1}{1+N_1} \, , \qquad r_2 = \frac{N_1-N_2}{N_1+N_2} \, , \qquad r_3 = \frac{N_2-N_3}{N_2+N_3} \, . \qquad (5)$$

The phase factors for normal incidence are written

$$\delta_1 = -i\left(\frac{2\pi}{\lambda}\right) N_1 d_1 \, , \qquad \delta_2 = -i\left(\frac{2\pi}{\lambda}\right) N_2 d_2 \, . \qquad (6)$$

For the MOS structure considered here, N_1 and d_1 are respectively the complex refractive index and thickness of the semi-transparent gold electrode, N_2 and d_2 apply to the SiO_2 film, and N_3 to the silicon substrate. In essence the wavelength dependence of $T(\lambda)$ is due to the spectral dependence of: the absorption coefficient of the light in the metal and insulator layers, the reflection coefficients at the interfaces, and the interference pattern due to
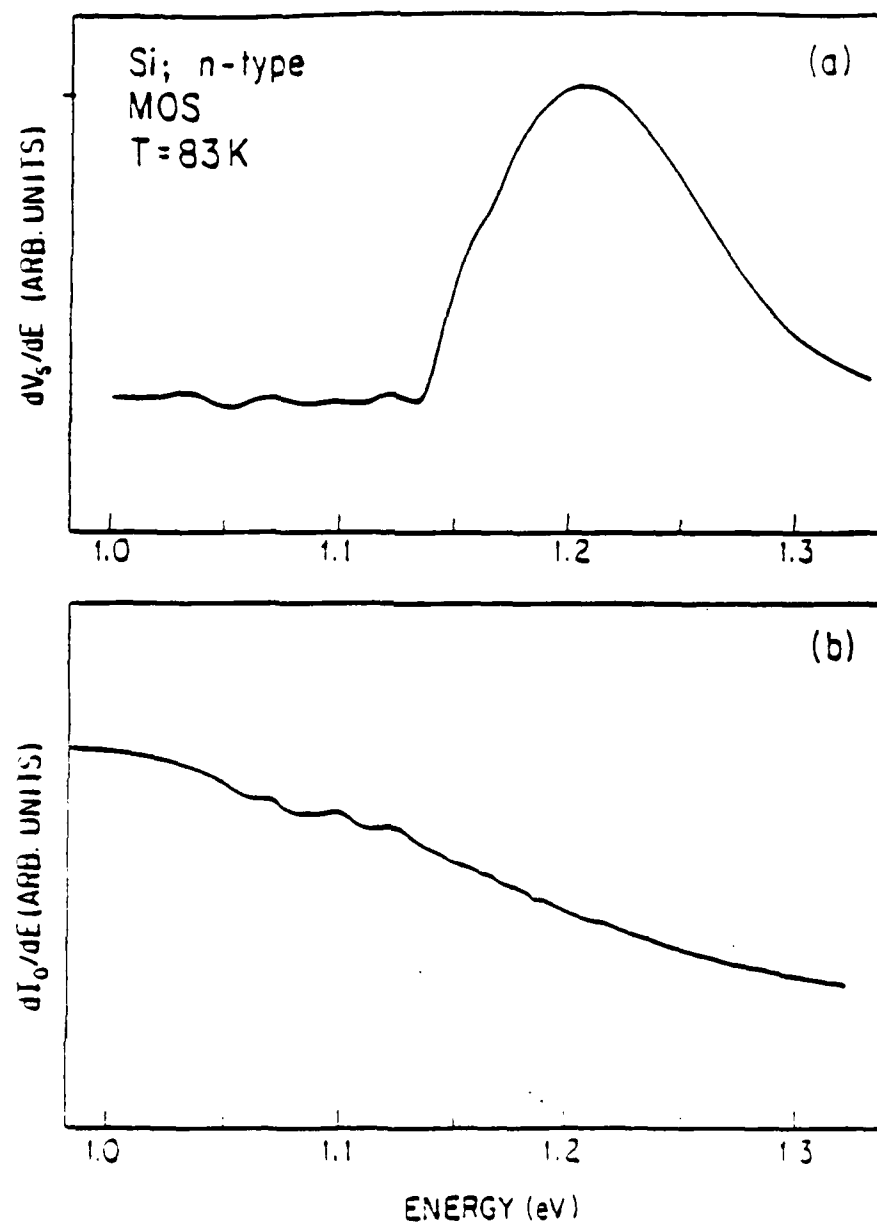
Fig. 1

FIGURE CAPTIONS

Fig. 1. (a) The derivative surface photovoltage spectra of silicon (T = 83 K);

(b) the derivation of the background spectra in the spectral range of

1.0 - 1.35 eV; amplitude of modulation $(\Delta\lambda/\lambda) = 10^{-2}$.

Fig. 2. (a) The derivative surface photovoltage spectra of silicon (T = 83 K);

(b) the derivative of the background spectra in the spectral range of

0.6 - 1.0 eV; amplitude of modulation $(\Delta\lambda/\lambda) = 10^{-2}$.

Fig. 3. Derivative of the background spectra in the spectral range of

0.76 - 1.0 eV; amplitude of modulation $(\Delta\lambda/\lambda) = 2\times10^{-3}$.

Fig. 4. Derivative of the background spectra in the spectral range of

4400 - 3400 A using a xenon arc source; derive from reference 8.

Fig. 5. (a) Normal reflectivity spectrum, and (b) logarithmic derivative

spectrum of the reflectivity of Au at 80 K; derived from ref. 19.

Fig. 6. Logarithmic derivative spectrum of the reflectivity of silicon at 80

K and 300 K and the normal reflectivity spectrum at 80 K; derived

from reference 18.

17. S. M. Eetenmadi and R. Braunstein, to be published.

18. M. Welkowsky and R. Braunstein, Phys. Rev. B 5, 497 (1972).

19. K. L. Shaklee and J. E. Rowe, Appl. Opt. 9, 627 (1970).

20. M. Welkowsky, Ph.D. Thesis, University of California, Los Angeles (1971).

21. R. Rosei, R. Antonangeli, and U. M. Grassano, Surf. Sci. 37, 689 (1973).

22. W. L. Wolfe, in Handbook of Optics, ed. by W. G. Driscol and W. Vaughan
    (McGraw-Hill, 1973), Ch. 7.

23. R. J. Powell, J. Appl. Phys. 40, 5093 (1969).

24. J. Lagowski, L. Jastrzebski, and G. W. Cullen, J. Electrochem. Soc. 128,
    2669 (1981).

25. R. Zucca and Y. R. Shen, Appl. Opt. 12, 1293 (1973).

REFERENCES

1. R. K. Kim and R. Braunstein, Appl. Opt. 23, 1166 (1984).

2. T. Nishino and Y. Hamakawa, Phys. Stat. Sol. (b) 50, 345 (1972).

3. J. Lagowski, W. Walukiewicz, M. M. G. Slusarczuk, and H. C. Gatos, J. Appl. Phys. 50, 5059 (1979).

4. E. Kamieniecki, J. Lagowski, and H. C. Gatos, J. Appl. Phys. 51, 1863 (1980).

5. M. Cardona, Modulation Spectroscopy (Academic Press, New York, 1969).

6. G. Bonfiglioli, P. Brovetto, G. Busca, S. Levialdi, G. Palmieri, and E. Wanke, Appl. Opt. 6, 447 (1967).

7. R. K. Willardson and A. C. Beer, editors, Semiconductors and Semimetals - Vol. 9, Modulation Techniques (Academic Press, New York, 1977).

8. M. Welkowsky and R. Braunstein, Rev. Sci. Instrum. 43, 399 (1972).

9. R. Stearns, J. Steele, and R. Braunstein, Rev. Sci. Instrum. 54, 984 (1983).

10. S. M. Eetemadi, Ph.D. Thesis, University of California at Los Angeles (1984).

11. A. S. Grove, Physics and Technology of Semiconductor Devices (John Wiley and Sons, New York, 1967).

12. L. L. Jastrzebski and J. Lagowski, RCA Review 41, 181 (1980).

13. D. L. Lile, Surf. Sci. 34, 337 (1973), and reference therein.

14. O. S. Heavens, Optical Properties of Thin Solid Films (Academic Press, New York, 1955).

15. S. M. Ryvkin, Photoelectric Effects in Semiconductors (Consultants Bureau, New York, 1964), Ch. III.

16. M. Jaros, Deep Levels in Semiconductors (Adam Hilger Ltd., Bristol, U.K., 1982).

VI. CONCLUSIONS

We have shown that contrary to the previous assumptions, the DSPV in general is not-proportional to the derivative of the absorption coefficient. A general formulation of the DSPV was derived which revealed the various possible sources of spurious interference spectra. The effects of these interferences on the line shapes of the optical transitions were studied and their impact on the identification of the deep levels and the critical poings in the band structures were discussed. A practical method for removal of the main source of the disortions, i.e., the background, was suggested.

ACKNOWLEDGMENTS

wavelength is scanned. The output of the lock-in amplifier II can be used in another negative feedback loop to regulate an intensity modulator to keep $dI_o/d\lambda$ equal to zero. The intensity modulator can be placed anywhere in the light path before the beam splitter. Its modulation frequency should be the same as the wavelength modulator and its amplitude can be controlled by the negative feedback loop from the lock-in amplifier II. One such intensity modulator has been used in a wavelength modulation reflectance spectrometer for the same purpose.[25] The two feedback loop systems eliminate $dI_o/d\lambda$ and the spectral changes of the background $I_o(\lambda)$ to the extent that it is smooth in the spectra region of interest. This is not possible in the absolute sense nor the entire region of the spectrum. However, what is needed in practice is to have detectors whose spectral responsivity are flat and smooth compared to the line shapes of the optical transitions under investigation.

Finally, in comparing the wavelength modulation techniques, the wavelength modulation absorption/reflection (WMA/R) spectroscopy has several advantages over the wavelength modulation photoresponse spectroscopy (WMPR). Firsty and foremost, the WMA/R method yields unambiguous line shapes for the optical transitions, which are therefore easier to interpret. This is also true of the temperature dependence of the line shapes. Second, the intra-center transitions involving the deep levels can be observed by the WMA but not with the DSPV spectroscopy. Third, in the WMA/R, the only source of spurious signals is the background spectrum which can be completely removed in a systematic way, independent of the spectral responsivity of the detector. Finally, the WMA/R is a nondestructive method which can be applied directly to the bulk of the materials. In contrast, the WMPR measurements often require fabrication of devices in the form of MIC, p-n junction, of Schottky barriers which could result in the introduction of process related impurities or defects into the samples.

V. COMPARISON OF WAVELENGTH MODULATION PHOTORESPONSE AND WAVELENGTH MODULATION ABSORPTION/REFLECTION SPECTROSCOPIES

It is therefore clear that the spectra of $T(\lambda)$ and $dT/d\lambda$ contain substantial structures that could significantly change the line shapes of the absorption obtained from the wavelength modulation surface photovoltage, as well as other forms of wavelength modulation photoresponse spectroscopies.

In contrast to the wavelength modulation absorption/reflection spectroscopy, removal of the background interferences $I_0(\lambda)$ and $dI_0/d\lambda$ from the DSPV spectra is very difficult. To date no systematic method for its subtraction has been suggested. We present a technique utilizing a double-beam system in combination with a reference optical detector and feedback loops to suppress the spectral changes of $I_0(\lambda)$ and $dI_0/d\lambda$. Its success, hwoever, depends on the relative smoothness of the spectral responsivity of the detector in the spectral region of interest.

To suppress the spectral changes of $I_0(\lambda)$ and $dI_0/d\lambda$, a double-beam system is needed. For this purpose, the light beam from the exit slit of the monochromator in a DSPV spectrometer needs to be split by a beam splitter. Both beams can therefore be wavelength modulated at frequency ω_2. One of the beams can be used to illuminate the DSPV sample while the other beam can be chopped at frequency ω_1 and then incident upon an optical detector. The output of the detector is fed into two lock-in amplifiers. One of the lock-in amplifiers (I) is tuned to ω_1 to measured the light intensity, and the other one is turned to ω_2 to measured $dI_0/d\lambda$. Except for the beam splitter and the DSPV sample, this is similar to the infrared wavelength modulation spectrometer described elsewhere.[1] The output of the lock-in amplifier I can be used in a negative feedback loop to regulate the power supply of the light source. This arrangement will keep the light intensity constant as the

light sources, in the visible region of spectra, also have structures as reported in the literature.[19] The structures in the $dI_o/d\lambda$ spectrum at longer wavelength are primarily due to the atmospheric absorption as discussed before.

The structure in the spectra of the transmittance $T(\lambda)$ and its derivative $dT/d\lambda$ are caused by the spectral changes of the optical constants in the metal and the insulating layers and the reflection coefficient of the semiconductor, as well as the interference patterns generated because of the interfaces [see Eqs. (4)-(7)]. These factors are separately discussed below:

a) The spectral changes of the reflectivity of gold $R(\lambda)$ as well as its logarithmic derivative $dR/d\lambda$,[20] are shown in Fig. 5. These spectral changes occur in the 2.0 - 5.0 eV region of the spectra and are primarily due to the d-band to Fermi level transitions. Structural changes in the spectrum of the derivative of its transmission coefficient in the 2.0 - 3.5 eV region have also been observed.[21]

b) The optical constants of the insulating layer, SiO_2, are fairly smooth in the 0.5 - 4.5 eV region of the spectrum,[22] and therefore are not expected to influence the line shapes of the interband transitions.

c) The spectral changes caused by the interference pattern depend on the thickness of the layers, their index of refraction, and the spectral region of interest. Optical interference patterns have been studied for the MIS structures with various thicknesses of Au and SiO_2 layers on silicon substrates.[23] The signatures of such interference patterns have also been observed in the surface photovoltage spectra.[24]

d) Finally, the spectral changes in the $R(\lambda)$ and $dR/d\lambda$ of the semiconductor substrate contribute significantly to the spectra of $T(\lambda)$ and $dT/d\lambda$, and hence to the DSPV spectra. Figure 6 shows the reflectivity of Si and its logarithmic derivative obtained by the wavelength modulation reflectance spectroscopy.[18]

3. Interband Transitions.

Optical modulation spectroscopy has been a powerful tool in studies of the interband transitions in solids.[5] These techniques have allowed small structures immersed in a large but relatively smooth background spectrum to be observed and correlated with the critical points in the band structures.[18] In order to identify the types of critical points involved in the optical transitions and correlate them with the existing band structure calculations, experimentally unambiguous line shapes are necessary. Amongst the various modulation spectroscopies, the wavelength modulation reflectance has the unique advantage of having a straightforward relationship to the normal reflectance and other optical constants.[18] This allows one to obtain experimentally unambiguous line shapes which is the basis of the semi-empirical energy band calculations.

Wavelength modulation surface photovoltage spectroscopy is the youngest member of the family of modulation techniques which have been used to study the interband transitions of semiconducting materials. However, the main advantage of the wavelength modulation technique is lost in the DSPV spectroscopy, since it no longer has a direct or simple relationship with the optical constants. It is seen from Eq. (11) that the DSPV line shapes are distorted by the interference of the various spurious spectra. We discuss below the effects of the various terms of Eq. (11) on the line shapes of the interband transitions.

The effect of the I_o and $dI_o/d\lambda$ terms on the interband transitions depends, primarily, on the light source used in that particular region of the spectrum. Xenon arc lamps are commonly used for the ultraviolet region of spectra. The derivative of its spectrum,[8] shown in Fig. 4, contains sharp structures and therefore poses a serious problem in this region. Tungsten

2. Temperature Dependence of the DSPV Spectra.

The temperature dependence of the absorption spectra, $\alpha(\lambda, T)$, is very valuable in studies of the deep centers and their electron-lattice relaxation. It is also an important parameter for comparing the theoretical results to those of experiments.[16] Unfortunately, the relationship between the temperature dependence of the DSPV and that of $\alpha(\lambda, T)$ is not a simple one, which makes it rather difficult to interpret the results.

The temperature dependence of the DSPV comes from that of $G(\omega,T)$, $\alpha(\lambda,T)$, $F(\lambda,T)$, as well as $dF/d\lambda$ and $d\alpha/d\lambda$ [see Eq. (11) and the paragraph following it]. The temperature dependence of the frequency response function, $G(\omega,T)$, is similar to that of the ac photoconductivity,[13] and since $G(\omega,T)$ stands as a proportionality factor, it can be treated in a similar way. But $F(\lambda,T)$ is in general a complicated function of temperature through its arguments, and appears in a nontrivial way in the expression for $dV_s/d\lambda$, Eq. (11). In some rather simple cases,[13] $F(\lambda,T)$ can be written:

$$F(\lambda,T) \propto \frac{L(T)\tau_b(T)S(T)}{[\alpha(\lambda,T)L(T) + 1][L(T) + S(T)\tau_b(T)]} \quad , \tag{12}$$

where S is the effective surface recombination velocity. Therefore

$$\frac{dF}{d\lambda} \propto \frac{L^2(T)\tau_b(T)S(T)}{[\alpha(\lambda,T)L(T) + 1]^2[L(T) + S(T)\tau_b(T)]} \times \frac{d\alpha(\lambda,T)}{d\lambda} \quad . \tag{13}$$

It is clear from Eqs. (11), (12), and (13) that even when $F(\lambda,T)$ has a fairly simple form, it is by no means trivial to extract the temperature dependence of $\alpha(\lambda,T)$ from the DSPV data. Therefore extreme care must be taken in order to arrive at an accurate interpretation of the temperature dependence of the DSPV spectra in relation to the parameters characterizing the deep levels involved. Such difficulties are not usually encountered in the wavelength modulation absorption spectroscopy which directly measures $d\alpha(\lambda,T)/d\lambda$.

rate depends exponentially on E_i/kT, where E_i is the photoionization energy of the shallow level.[12] Hence, temperature and frequency scans of the DSPV spectra may be useful in detection and identification of such transitions.

ii) <u>Deep Level to Band Transitions</u>: In contrast to intra-center transitions, the deep level to band transitions have characteristically broad and often featureless absorption spectra, resulting in broad peaks and shoulders in the derivative of the absorption coefficient, $d\alpha/d\lambda$. Furthermore, to obtain accurate information on the parameters which characterize the deep levels such as photoionization energy, concentrations, site symmetry, local potential and electron-lattice relaxation, one often needs to analyze the line shape of the absorption spectra as well as its temperature dependence.[16] Hence any spurious line shape due to the various possible sources of distortions would lead to inaccurate information about the parameters of interest and, consequently, the cross correlations between the experimental results and the theoretical predictions. The effects of the last three terms of Eq. (11) on the DSPV spectra are therefore especially significant in the case of the deep levels and cannot be <u>a priori</u> ignored. In particular, the spectrum of $dI_o/d\lambda$ in the near infrared contains numerous structures, as seen in Figs. 2(b) and 3, which may dominate the DSPV spectra. Although some previous reports have cautioned about distortions from the background, $I_o(\lambda)$,[2,3] no systematic method has been used or suggested for their removal. Hence the DSPV spectroscopy as it stands appears to have limited usefulness in studies of the deep levels in semiconductors. In a later section we will suggest a practical method for systematic removal of the background contributions from the DSPV spectra.

IV. DISCUSSION

1. Sub-Band-Gap Transitions.

Sub-band-gap electronic transitions associated with the deep levels are categorized as: i) the intra-center transitions between different levels of the same impurity or defect, and ii) photoionization of the electrons or holes into the conduction or valence bands.

i) Intra-Center Transitions: The intra-center transitions often produce sharp zero-phonon lines in the optical absorption and photoluminescence spectra at low temperature. For example, transition metal impurities at high and moderate concentrations in the III-V compounds have been extensively studied using these methods, yielding a great deal of information regarding the impurity's site symmetry, concentrations, and crystal field strength.[16] At lower concentrations these transitions were observed by wavelength modulation absorption spectroscopy.[17] Generally the positions of the sharp zero-phonon lines are the best signatures of the centers involved. However, intra-center transitions between the deep levels generally do not delocalize the carriers and so no spatial charge separation occurs. Consequently such transitions cannot be detected by the wavelength modulation surface photovolage spectroscopy. This is one of the disadvantages of the DSPV as compared to the wavelength modulation absorption spectroscopy.

If, however, one of the levels involved is a shallow level, then a photo-thermal ionization may occur, in which the carrier is first optically excited into the shallow level and subsequently ionized to the conduction or valence band by thermal excitation, producing a change in the surface potential. Whether this produces a wavelength modulation surface photovoltage depends on the temperature as well as the incident frequency, since the thermal emission

obtain:

$$\frac{dV_s}{d\lambda} = I_o(\lambda)\ T(\lambda)\ F(\lambda)\ \frac{d\alpha(\lambda)}{d\lambda} + T(\lambda)\ F(\lambda)\ \alpha(\lambda)\ \frac{dI_o}{d\lambda}$$

$$+ I_o(\lambda)\ F(\lambda)\ \alpha(\lambda)\ \frac{dT(\lambda)}{d\lambda} + I_o(\lambda)\ T(\lambda)\ F(\lambda)\ \frac{dF(\lambda)}{d\lambda} \quad . \tag{11}$$

It must be added that, in order to incorporate the response of the system to a time varying incident light intensity, the above equation must be multiplied by a frequency response function $G(\omega)$.[13] However, since this factor is to first order independence of the wavelength, it is treated here as a constant of proportionality. Its effect on the temperature dependence of the DSPV spectra is discussed in a later section.

In contrast to Eq. (1), Eq. (11) shows that the DSPV signal is not in general proportional to $d\alpha/d\lambda$ and therefore its various terms introduce different degrees of distortion which depend on the relative size of their spectral changes in the spectral region of interest. The most notorious source of the distortion is the spectral changes of $I_o(\lambda)$, the background. The distortion introduced by I_o is present in all four terms of Eq. (11), but its effect is most dramatic in the second term which contains $dI_o/d\lambda$. This term affects the DSPV spectra in the near infrared region of spectra which corresponds to the sub-band-gap transitions in some semiconductors (e.g., Si, GaAs), as well as in the ultraviolet region of the spectra where the interband transitions occur. The spectral dependence of $dt(\lambda)/d\lambda$, however, is more pronounced in the region of the interband transition. Hence, in what follows, the sub-band-gap transitions which involve the impurity and defect levels are discussed separately from the inter-band transitions.

the internal multiple reflections from the interfaces; to simplify the discussion we write:

$$T(\lambda) = T[N_1(\lambda), N_2(\lambda), N_3(\lambda), g(\lambda)] \quad , \qquad (7)$$

where $g(\lambda)$ symbolizes the interference phenomena. Combining Eqs. (2) and (3), we have:

$$V_s = I_0(\lambda) \, T(\lambda) \, \alpha(\lambda) \, F(\lambda) \quad , \qquad (8)$$

which together with Eq. (7) form the basis of our analysis of the wavelength modulation surface photovoltage.

If the wavelength of the incident light beam is modulated as:

$$\lambda = \lambda_0 + \Delta\lambda \cos \omega t \quad , \qquad (9)$$

where $\Delta\lambda$ and ω are the amplitude and the frequency of modulation, respectively, then the surface photovoltage, $V_s(\lambda)$, becomes a periodic function of time, V_s $(\lambda_0 + \Delta\lambda \cos \omega t)$. For small $\Delta\lambda$, the modulated surface photovoltage can be expanded in powers of $\Delta\lambda$, or:

$$V_s(\lambda_0 + \Delta\lambda \cos \omega t) = V_s(\lambda_0) + \Delta\lambda \frac{dV_s}{d\lambda_0} \cos \omega t + O(\Delta\lambda)^2 + \cdots \quad . \qquad (10)$$

The modulated surface photovoltage is detected by a standard lock-in amplifier tuned to the reference frequency ω. Hence, the output voltage of the lock-in amplifer is proportional to the amplitude of the first harmonic, i.e., $\Delta\lambda(dV_s/d\lambda)$. Similarly, the right-hand side of Eq. (8) can be expanded in powers of $(\Delta\lambda)$. By comparing the first harmonic terms on both sides, we
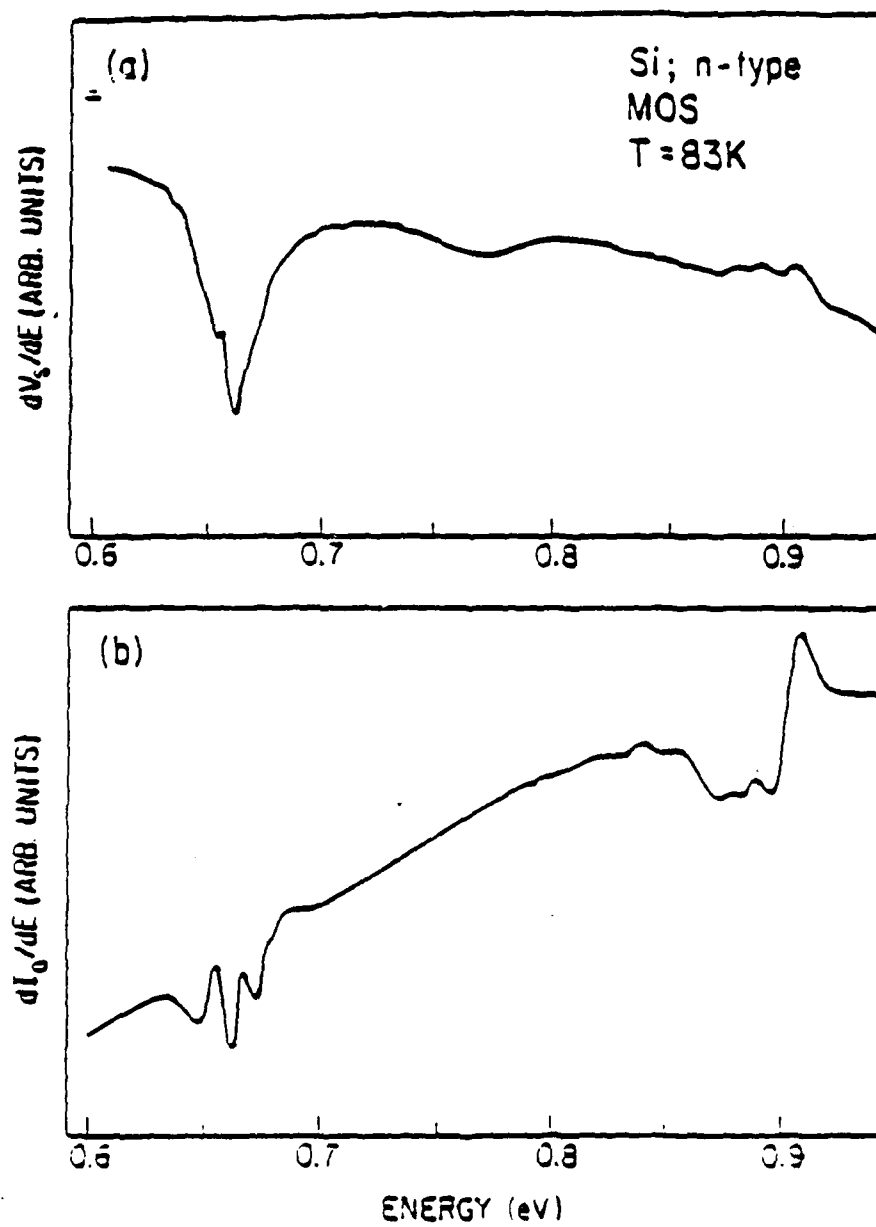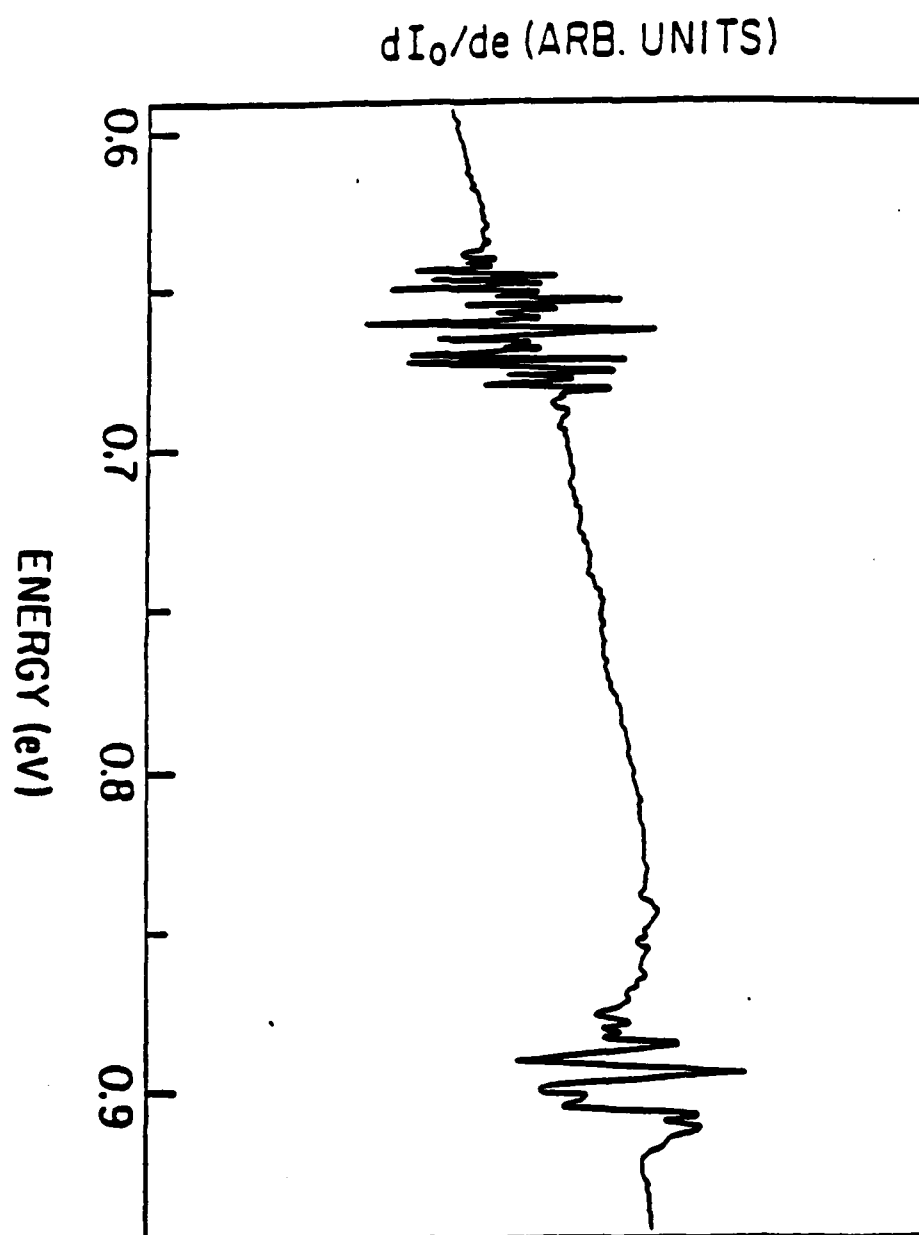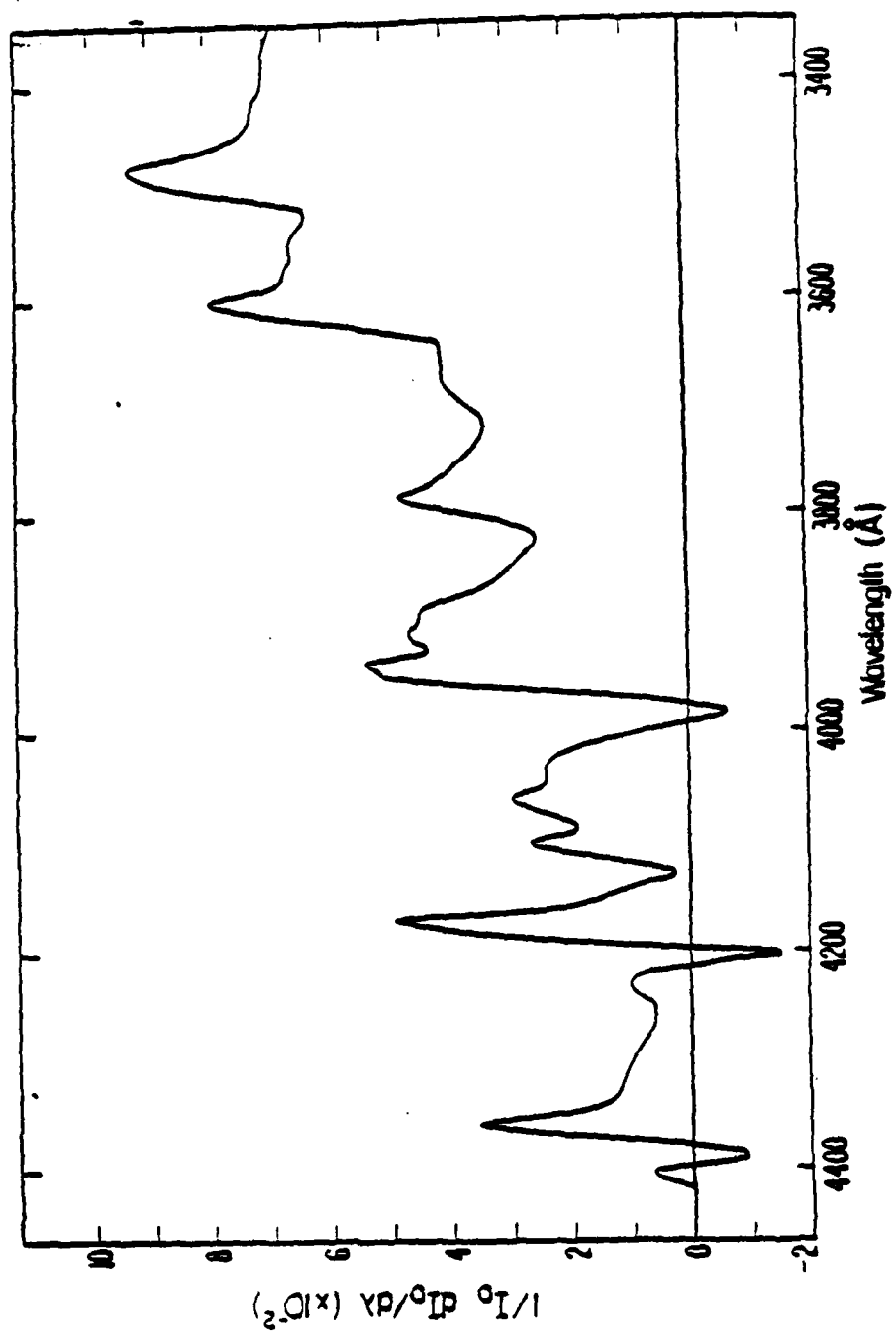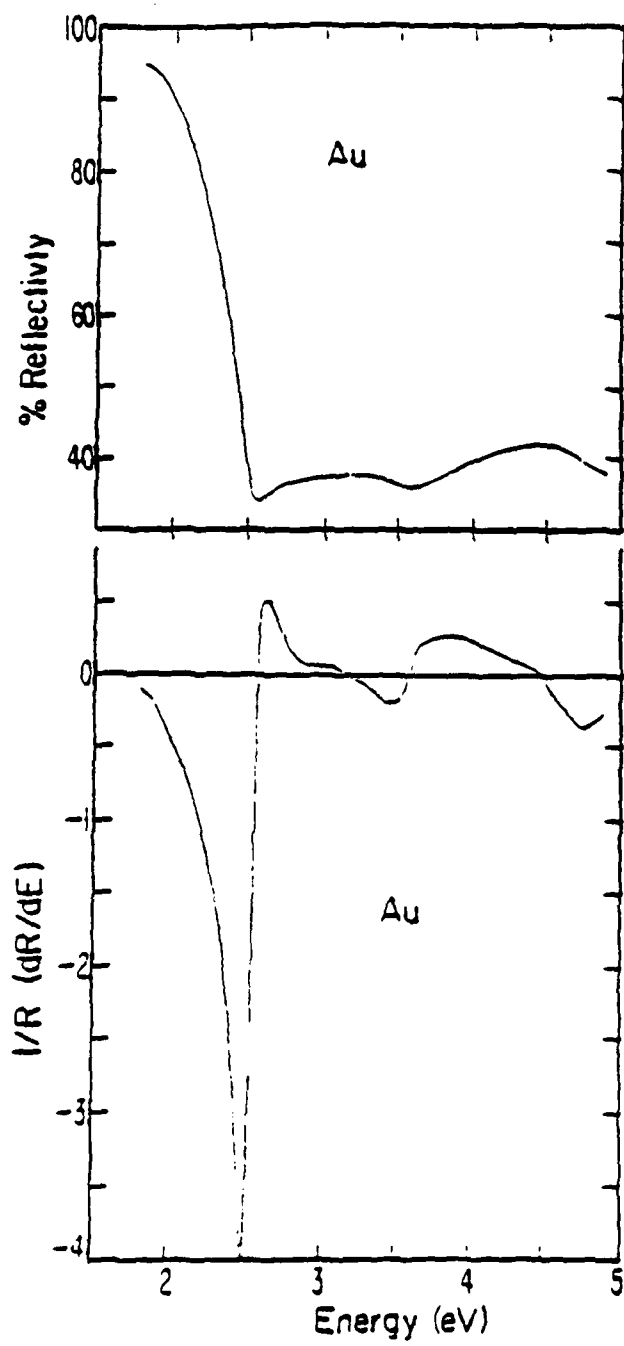
Si; n-type
MOS
T = 83K

ENERGY (eV)

Fig. 2

Fig. 3

Fig. 4

Fig. 5
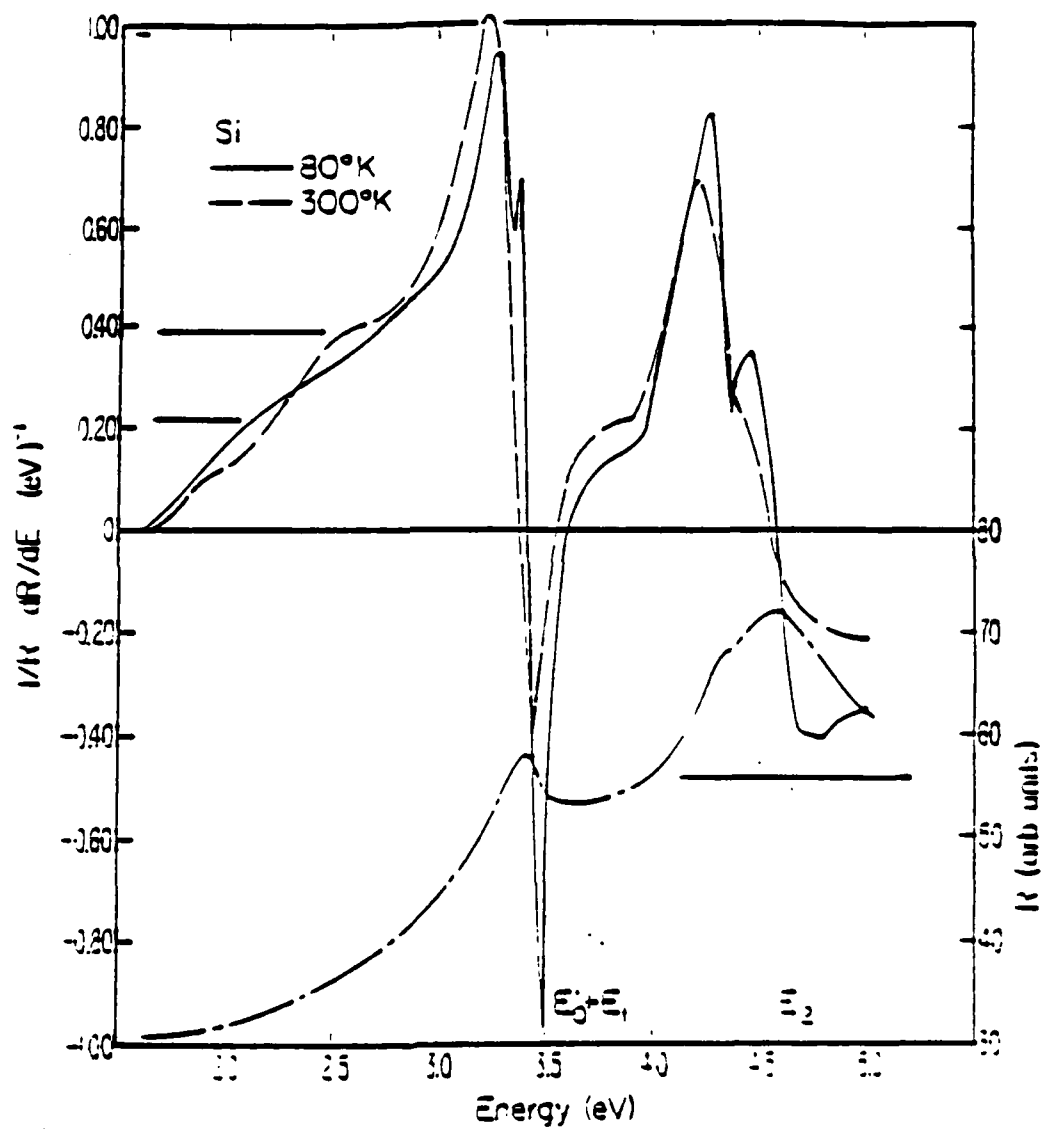
Fig. 6

Measurement of the EL2 and Chromium Concentration

in the Semi-Insulating GaAs

S. M. Eetemadi and R. Braunstein

Department of Physics, University of California,

Los Angeles, California 90024

Low temperature infrared wavelength modulation was performed on
GaAs in conjunction with the photo-quenching of the absorption in
the spectral region of 0.7-1.4 eV, due to the EL2 levels, to assess
the accuracy of the conventional room temperature optical absorption
spectroscopy in measuring EL2 and chromium concentrations; an
accurate method for such measurements was suggested.

The deep chromium acceptor level at $E_v + 0.73$ eV, and the deep donor level, commonly referred to as EL2, at $E_c - 0.74$ eV are responsible for controlling the compensation mechanism of semi-insulating (SI) GaAs, grown by the liquid encapsulated Czochralski (LEC) technique.[1-6] Non-uniformities in the concentration of deep levels could adversely affect the yield, reliability, and performance of the devices made from these substrates. The correlation between the distribution pattern across the wafer, of the concentration of the deep levels, resistivity, dislocation density, as well as their relation to the stoichiometry of the melt and conditions of the crystal growth, are essential in understanding the origin and nature of these nonuniformities.[6-9] Central to many of these studies is the measurement of the concentration and the distribution of the deep levels, especially EL2 and chromium. However, many of the standard methods of measuring deep level concentration are either not suitable or not easily applicable to the semi-insulating materials. Optical absorption spectroscopy at room temperature in the near infrared spectral region is considered a convenient, rapid, and nondestructive way of measuring the local concentration of deep levels with good spatial resolution,[2] and is used in the above reference studies, for EL2 and chromium concentration profiles in SI GaAs. However, for low concentration of impurities or defects, conventional optical absorption lacks sensitivity, and the improved sensitivity of infrared wavelength modulation must be employed.[10] The purpose of the present work was to make an assessment of the accuracy of the room temperature optical absorption method in measuring the EL2 and chromium concentrations.

In undoped SI GaAs, EL2 seems to be the dominant deep level. The total absorption coefficient of this defect and other residual impurities can be

written as

$$\alpha(E) = N_{EL2} \, \sigma^e(E) f_{EL2} + N_{EL2} \, \sigma^h(1 - f_{EL2})$$

$$+ \sum_j N_j [\sigma_j^{\,e} \, f_j + \sigma_j^{\,h} (1-f_j)] \qquad (1)$$

where N_{EL2} is the EL2 concentration, σ^e and σ^h are the photo-ionization cross section for electrons and holes respectively, f_{EL2} is the occupancy of the EL2 level which depends on the relative position of the Fermi energy and the EL2 level. The last term represents the absorption coefficient due to all other residual impurity and defect levels present in the material. It is commonly assumed that the EL2 levels are almost completely filled (f_{EL2} close to unity) if the Hall measurements indicate strongly n-type character for the SI GaAs. Thus the second term in Eq. (1) can be omitted and the first term becomes $N_{EL2}\sigma^e$. Furthermore, if independent measurements such as secondary ion mass spectroscopy (SIMS) indicate very low concentration of other deep levels compared to the EL2, the magnitude of the last term in Eq. (1) is assumed to be negligible. The above two assumptions simplify Eq. (1) to $\alpha(E) = N_{EL2}\sigma^e$. This is the form commonly used in conjunction with the reported values of the photo-ionization cross section to obtain the concentration of EL2 levels in the SI GaAs.

The validity of the first assumption regarding the occupancy of the EL2 level has been discussed.[11] It is shown that in the typical SI GaAs, the occupancy of the EL2 level changes most noticeably in the region where the Hall mobility is still high, and the sign of the Hall constant indicates a dominant contribution from electrons. Therefore, changes in the optical absorption coefficient cannot be a priori attributed to the changes in the EL2

concentration. However, the validity of the second assumption regarding the smallness of the collective contribution of all the other residual deep levels (hereafter referred to as residual absorption coefficient), to the total absorption coefficient, has not been studied, and no estimate of its magnitude is available.

The following arguments suggest that, even if the concentration of residual deep levels is individually small compared to the EL2, the magnitude of the residual absorption coefficient may still be appreciable, and therefore cannot be a priori ignored. Firstly, the photoionization spectra of deep levels are broad and often featureless, extending beyond $2E_j$, where E_j is the threshold energy of the j-th deep level.[12] Thus the photoionization cross section of all other deep levels present in the material may have appreciable values in the 1.1 - 1.2 eV region, in the neighborhood of the EL2 spectra. Secondly, even though the concentration of the individual residual deep levels are small compared to the EL2, the number of different types of such levels in SI GaAs is usually large. And lastly, the values of the photoionization cross section of deep levels span several orders of magnitude, and some of the less dominant levels, in concentration, may have a much larger photoionization cross section, making $N_j\sigma_j$ appreciable.

The object of the present work was to make an estimate of the magnitude of the residual absorption coefficient, and thus, of the error that results in ignoring its contribution when the room temperature optical absorption coefficient is used to measure the EL2 concentration in the undoped SI GaAs.

Low temperature wavelength modulation absorption, with and without background illumination, made it possible to separate the absorption coefficient of EL2 from other residual deep levels. The experiment showed that, in the typical undoped SI GaAs, with EL2 as the dominant deep level,

about 10-20% of the absorption coefficient was due to residual deep levels. The significance of this error is discussed, and an appropriate method which completely eliminates this error is suggested. Special problems which arise in the case of the chromium doped SI GaAs (LEC) are also discussed.

The EL2 level has been shown to exhibit unusual properties—among them, the quenching of photoluminescence,[13] photocapacitance,[14] and optical absorption,[2] at low temperature (T < 140 K). In particular, the near-infrared absorption spectra due to EL2 quench out at low temperature after the sample is illuminated with light of 0.9 < hυ < 1.35 eV and remains in the quenched state for many hours, even after the background illumination has been turned off. These properties have been explained by postulating the existence of a metastable state of the EL2, accessible at low temperature with background illumination,[15] or by a charge-state-controlled structural relaxation model.[16] Taking advantage of the quenching of the absorption coefficient, we studied the near infrared absorption spectra of undoped SI GaAs samples of different ingots, all grown in pyrolitic boron nitride (PBN) crucibles, by the liquid encapsulated Czochralski (LEC), and B_2O_3 as the encapsulant. They had resistivity greater than 10^7 Ω-cm, Hall effect mobilities of 4570-6319 cm^2/V sec, electron concentrations in the range (1.3 - 2.4) × 10^7 cm^{-3}, and EL2 levels virtually 100% occupied. The samples were typically 3 mm thick with the surfaces polished with Br-methanol.

These studies were performed using a wavelength-modulated spectrometer described elsewhere,[10] with sensitivity of 10^{-4} cm^{-1} in the near infrared spectral region. The spectra were first taken at room temperature from 0.6 eV to 1.45 eV; a typical result is shown in Fig. 1 (solid curve). The samples were then cooled down, while in the dark, to 80 K. The values of the absorption coefficients at 1.2 eV were recorded, and while monitoring its

value at this energy, the samples were illuminated with a 50 W tungsten/halogen
lamp, until complete quenching of the absorption was reached in 10-20 minutes,
and no further change in the absorption coefficients was observed. The
illumination was then turned off, and the samples were left in darkness for
another 20 minutes. This last step was done to avoid a possible non-equilibrium
population of other deep levels present, as will be explained in connection
with the dependence of the chromium level population on illumination. The
post-illumination and relaxation spectra thus obtained are also shown in Fig.
1 (dotted curve). The resulting spectra, except for finer details revealed
in our experiments due to better sensitivity, were in general agreement with
other reported spectra.[2] As the samples were warmed up, the absorption
coefficient monitored at 1.2 eV recovered in the manner shown in Fig. 2.

The shape of the residual absorption spectra at 80 K, from 0.6 eV to 1.45
eV, varied in detail from sample to sample but was generally a small and
rather flat plateau. Its magnitude also varied from sample to sample, and at
1.2 eV the variation was typically 10-20% of the total absorption coefficient
for a given temperature prior to the quenching by illumination.

The above result indicates that in typical LEC SI GaAs, only 80-90% of the
absorption coefficient measured as 80 K may be attributed to the EL2, and the
rest is due to the presence of other deep levels. The following argument
shows that this result is also true for measurements performed at room
temperature. At 1.2 eV the value of the absorption coefficient at 300 K was
nearly equal to that measured at 80 K. Furthermore, since near 1.2 eV the
residual absorption spectra are quite flat and featureless (dotted curve in
Fig. 1), the magnitude of the residual absorption coefficient at room
temperature is not expected to be appreciably different from its value at 80 K.
Hence, the ratio of the residual and total absorption coefficient at room

temperature and 80 K should be nearly the same. Therefore in typical undoped SI GaAs (LEC), up to 20% of the apparent room temperature spectra of the EL2 might be due to the spectra of other residual deep levels.

The significance of the above result can be appreciated in the context of the following reported observations:

Fabrication of high-performance GaAs IC's makes stringent demands on the uniformity of the substrate materials. Very marked non-uniformities in the electrical properties across the wafers of SI GaAs (LEC) has been reported.[9,17] Since the semi-insulating properties of this material are achieved by the compensation of residual shallow impurities by deep levels,[3,18] much attention has been focused on the distribution of deep levels in the starting substrate material. The deep donor EL2, which is thought to be an "antisite defect," is the dominant deep level in the melt grown GaAs. Optical absorption and photoluminescence experiments have shown that the distribution of the EL2 levels follows a characteristic "W" or "U" shaped pattern along the diameter of the SI GaAs wafers.[7,19-21] The variations in the concentration of the EL2, as measured by room temperature optical absorption, have been reported to be up to ± 10% of the average EL2 concentration.[8] Similar patterns have also been observed in the distribution of dislocation densities.[7,20,22] However, some uncertainty remains about the quantitative correlation between the profiles of the dislocation density and the EL2 concentration,[8,22] and hence the association of "antisite defects" to the dislocation climb processes.[23] It must also be added that there have been reports of precipitation of some impurities around the dislocation centers, and hence the impurity concentration might be high in regions of high dislocation density.[24,25]

As mentioned, the EL2 concentration profile has been obtained primarily by room temperature optical measurements. In the light of our results regarding

the percent contribution of residual deep levels to the apparent measured spectra of EL2, it is quite conceivable that an increase in the absorption coefficient in regions of high dislocation density is due to the increase in the concentration of precipiate impurities rather than the EL2. Therefore studies of the quantitative correlation between the distribution of EL2 and dislocation density require techniques which can selectively measure the EL2 concentration with accuracies much better than 10%. The low temperature method suggested below completely separates the EL2 contribution from other deep levels and thus provides an accurate measure of the EL2 concentration.

The method is to first measure the pre-illumination spectra at a temperature below ~ 120 K by a very low intensity and quasi-chromatic light to avoid any partial quenching of the absorption coefficient. The absorption spectra due to EL2 are subsequently quenched out by illuminating the sample with intense light of hv > 1.1 eV and the remaining spectra are recorded after a period of relaxation in the dark for about 20 minutes. The difference between the pre-illumination and the post-relaxation spectra, thus obtained, would belong to EL2 levels, and their concentration can be obtained from the value of the photoionization cross section[2] and the occupancy of the level.[11] This is in contrast to the commonly used method, in which the room temperature absorption coefficient at ~ 1.2 eV is attributed to the EL2 level alone, and is used as a measure of the EL2 concentration. As we showed above, in LEC SI GaAs substrates, even if the precise occupancy of the EL2 is known, the room temperature measurement of the EL2 concentration could still be in error by up to 20%, because of the collective contribution of other deep levels present in the material. It should also be mentioned that the reported values of the photoionization cross section, which have been obtained by calibrating the room temperature absorption coefficient with independently measured

concentration, are subject to the same error. However, the newly suggested low temperature method can be used in the same manner to obtain a more accurate value of the EL2's photoionization cross section.

The low temperature pre- and post-quenching absorption (LTPPQA) method suggested above can also be used to obtain concentration of chromium or other level impurities and defects. In GaAs:Cr materials it has been established that Cr centers can be in any of the various stable charged states, Cr^{2+}, Cr^{3+}, and Cr^{4+} (Cr^{4+} is seen primarily in p-type materials) depending on the position of the Fermi level.[26-30] Furthermore, it is believed that it is the $(Cr^{3+})/(Cr^{2+})$ ratio, which plays the dominant role in the compensation mechanism.[6,31] However, direct measurement of $(Cr^{3+})/(Cr^{2+})$ by optical absorption of room temperature is difficult because of the presence of the EL2 levels in appreciable amounts in the melt grown materials and hence the total absorption coefficient is due to the Cr as well as the EL2 spectra. An indirect method of obtaining the $(Cr^{3+})/(Cr^{2+})$ ratio has been to estimate the EL2 contribution by taking it to be equal to the spectra of an undoped SI GaAs multiplied by a constant factor.[6] The EL2 spectra thus found are subtracted from the total absorption spectra, to obtain the spectra due to Cr levels alone, from which the $(Cr^{3+})/(Cr^{2+})$ ratio is estimated.

The present LTPPQA method has the distinct advantage that it directly eliminates the EL2 contribution, revealing the remaining spectra. Figure 3 shows the spectra of another undoped SI GaAs (LEC) sample before and after quenching of the EL2. The residual absorption coefficient is about 70% of the total absorption coefficient at 1.2 eV, and consists of several thresholds. Although the post-quenching spectra still have some of the structures reminiscent of the unquenched EL2 spectra (at 10 K),[2] additional illumination and recycling of the quenching procedure did not change the spectra, thus

and can contribute an electron for the reduction of the tungsten atom. This is supported by the observation that the permanent blue coloration is most efficient if the $WO_{3-\delta}$ used has an oxygen deficit: $\delta \approx 0.1$ is obtained by chemical analysis of various purchases of WO_3. So the coloration mechanism involved in our borate-tungstate-glass could be the same as in the electrochromatic experiments with WO_3-films in Li^+-electrolytes. That means, that the intervalence-transfer-obsorption-model /8/ and Fig. 5 can also be used here to explain the optical absorption. This model yields activation energies for thermally activated hopping of electrons of the order of 0-3 eV /2/. A logarithmic plot of the measured loss factor $\tan\delta$ versus $1/T$ (Fig. 6) gives the following activation energies for the conductivities of the glasses:

Activation energies of the conductivity $\sigma(T) = \sigma_0 \exp(-E/kT)$

$X = 0$: $E = 0.19$ eV $\quad \sigma_0 = 4,4 \cdot 10^{-5}$ $1/\Omega$ m

$X = 0,41$: $E = 0,16$ eV $\quad \sigma_0 = 2,5 \cdot 10^{5}$ $1/\Omega$ m

$X = 0,5$: $E = 0,12$ eV $\quad \sigma_0 = 3,8 \cdot 10^{-5}$ $1/\Omega$ m

These results support the use of thermally activated hopping models here. In summary, the blue coloration is a good indicator for the existence of intact WO_6-octahedra in the $(Li_2B_4O_7)_{1-x}(WO_3)_x$-glasses. Therefore, further measurements of the dielectric properties in the compositional region $0.44 \leq x \leq 0.55$ might be most rewarding.

Acknowledgements:

Discussion:

Studies of Raman- and luminescence-spectra /13/ showed a similar threshold concentration as found in our experiments. Above the threshold the measured spectra changed fundamentally. This behavior was explained by a change in the borate structure at greater WO_3-concentrations, called "borate-anomaly".

Based on our results we suggest a percolation model /14/ for the solubility of WO_3 in $Li_2B_4O_7$. This is indicated by our dielectric measurements shown in fig. 4, which show an abrupt increase of the static dielectric constant in the region $X = 0.41$ to 0.5. We assume, that the distorted WO_6-octahedra, which are responsible for the ferroelectric behaviour of WO_3, are totally destroyed when they are dissolved in $Li_2B_4O_7$ up to the concentration $X = 0.44$ and only above this percolation-threshold are the WO_6-octahedra near their crystalline state. This reconstruction might be related to the formation of O-W-O-chains according to the percolation model. This would also explain the increase of the dielectric constant. Our measurements of the maximum optical absorption and the fundamental edge show a great similarity to those on electrochromically colored WO_3-films. Both systems show a shift of fundamental absorption edge to lower energies with an increase of the coloration and also of the relative maximum of optical absorption at 1,4 eV /7/. This correspondence we explain as follows: Simultaneous with the existence of complete WO_6-octahedra the formation of lithium-tungsten-bronzes becomes possible. During the cooling the Li-atoms move to an intact WO_6-octahedron by diffusion, for instance through oxygen vacancies,

For the identification of the blue coloration obsorption spectra were taken in the energy range between 1,3 eV and 4,0 eV. For this the samples were polished with an abrasive with a grain-size of 1 μm. For the evaluation of the absorption coefficient the reflectivity of the specimens was estimated to be 10 %. The results for different WO_3-concentrations X are shown in fig. 1. From the absorption curves the coloration of the glasses with increasing WO_3-content can be traced. In order to exclude impurities as the reason for the blue coloration, measurements were carried out on cobalt-doped lithium-borate-glasses. The results of these measurements are shown in fig. 2.

Results:

We can take from the comparative measurements that for conventional color centers the shape of the absorption spectra remains constant with increasing concentration, while its amplitude is increasing by a factor which scales with the concentration. Furthermore the location of the fundamental absorption edge E_0 is constant, too.

All this is different with the WO_3-doped borate-glasses. The energy range of the strong absorption increases with the WO_3-concentration and its value at E = 1.4 eV shows a large increase when the concentration exceeds X = 0.44 (Fig. 3a). Also, the fundamental absorption edge, (fig. 1) shifts abruptly to lower energy values (Fig. 3b). The maximum of the optical absorption lies at 1.4 eV, which is the same value as found for the electrochromic coloration of WO_3-films.

than one, the tungsten atoms are in different valence states.
The theory of the intervalence-transfer-absorption /8/ describes
the transfer   of electrons between two transition metal ions
of different valence. This theory is in good agreement with
the experimentally observed absorption at 1.4 eV. Aside from
these electrochromatic experiments many investigations have
been done on alkali-borate-tungstate-glasses /9-12/ in the
search for ferroelectric glasses.
In this work we describe the onset of a permanent blue colora-
tion   of the $(Li_2B_4O_7)_{1-X}(WO_3)_X$-glasses with increasing X
and   explain it in terms of the formation of lithium-
tungsten-bronzes in a glass matrix.

Experimental:

The specimens were prepared as follows: Lithium-tetraborate
and tungsten-oxide powders were weighed and mixed and sub-
sequently were heated and melted at 920° C in Al_2O_3-crucibles.
The melts were casted and chilled on a ceramic disc. The colora-
tion of the glasses could be observed during the solidifi-
cation of the initially colorless melt. Up to the WO_3-concen-
tration X = 0,55 the glasses were   clear and
their structure was proved to be amorphous by X-ray diffraction
and differential-thermo-analysis. For concentrations X > 0,55
we obtained polycrystalline ceramics. The glassy specimens
were colorless up to X = 0.33. From X = 0.33 to X = 0.47 they
were reddish brown, and from X = 0.47 to X = 0.55 blue, with
decreasing transparency.

Introduction:

Since S.K. Deb first reported about the optical and photo-
electric properties of thin tungsten oxide films /1/, many
workers investigated the coloration of WO_3-layers in electro-
chromatic experiments /2-6/ with regard to possible applica-
tions in displays. In these experiments the evaporated WO_3-
film serves as one electrode of the electrochemical cell,
while a platinum wire forms the other one. Both of them are
immersed in the electrolyte, which mostly consists of H_2SO_4
in H_2O or $LiClO_4$ in an organic solvent. When for a certain
time interval a negative potential is applied to the WO_3-
electrode, there is a current pulse through the cell and if
H^+ - or Li^+-electrolytes are used the film color turns to
blue. The amount of optical absorption measured thereafter
depends on the value of the applied field, while the shape
of the spectrum remains unchanged with a maximum at 1,4 eV/2/.
In addition to this maximum the fundamental absorption edge
of WO_3 was investigated, which is situated at about 3,8 eV
for WO_3-films in Li^+-electrolytes /7/. Many attempts were made
to explain the electrocoloration of WO_3-films /1,4,6/. The
currently most favoured model /8/ proposes the formation of
tungsten bronzes of the form A_xWO_3, where A = H,Li,Na. The
A^+-ions originate from the electrolyte, while the electrons
are injected from the metal contact on the other side of the
cell. Where the charge carries combine, A_xWO_3 is formed. The
A_xWO_3-unit has an electron localized at the tungsten atom,
i.e. W^{5+}, while the A^+-ion remains ionized. When X is smaller

Permanent Blue Coloration of $(Li_2B_4O_7)_{1-x}(WO_3)_x$-Glasses

by

Ch. Ruf and K. Bärner

IV. Physikalisches Institut der Universität Göttingen,
Göttingen, W.-Germany

and

R. Braunstein[+]

University of California, Los Angeles, CA 90024

Abstract

A permanent blue coloration is found in $(Li_2B_4O_7)_{1-x}(WO_3)_x$-glasses for $X \geqslant 0.44$. Since this concentration limit looks like a percolation threshold and since the blue coloration is conventionally ascribed to the formation of Lithium-tungsten-bronzes A_xWO_3 (A = H,Li,Na), we assume fast diffusion of Lithium to decorate the WO_6-tree once it forms in the glass matrix.

Zusammenfassung

$(Li_2B_4O_7)_{1-x}(WO_3)_x$-Gläser zeigen eine spontane Blaufärbung für Konzentrationen oberhalb $X = 0.44$. Diese Grenze zeigt Eigenschaften einer Perkolationsschwelle. Daher und weil eine solche Blaufärbung üblicherweise der Bildung von A_xWO_3-Molekülen zugeschrieben wird (A = H,Li,Na) nehmen wir an, daß sich bei $X = 0.44$ ein Baum von WO_6-Oktaedern bildet, der mit schnell diffundierten Lithiumatomen dekoriert ist.

SI-GaAs(LEC)
Sample: M047
——— T=300K
·········· T=80K, Illum.

Fig. 3

Fig. 2

SI-GaAs (LEC)
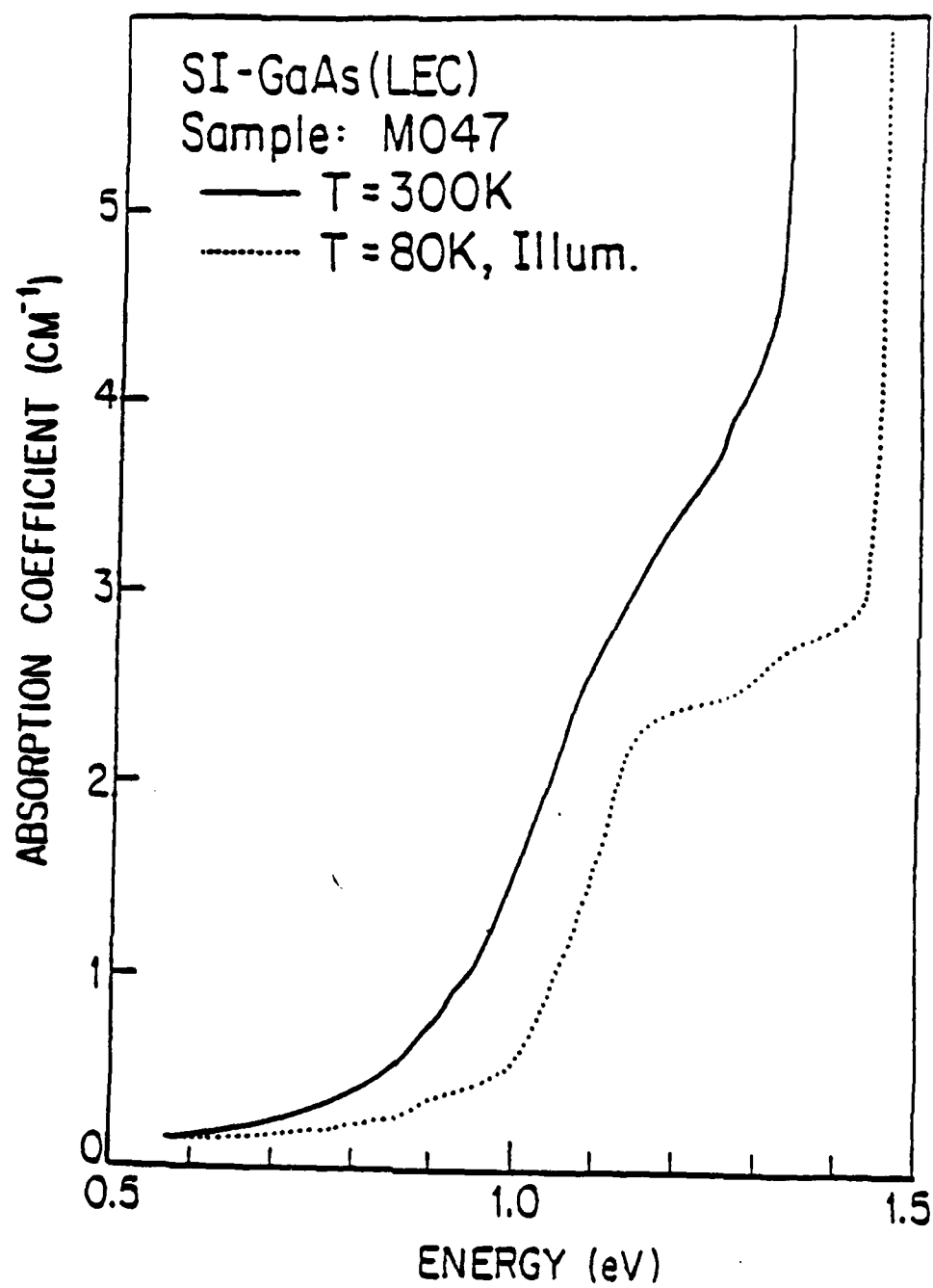Sample: MO43T
——— T = 300K
·········· T = 80K, Illum.
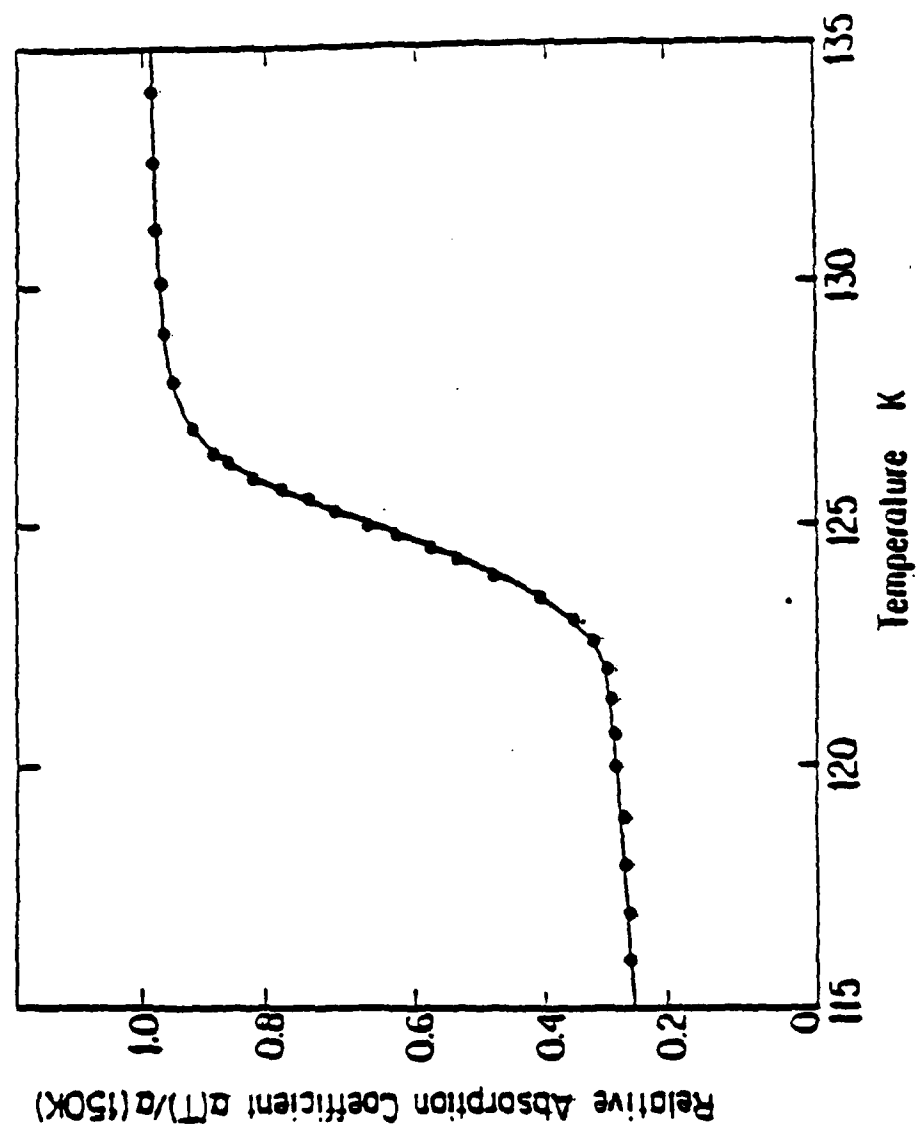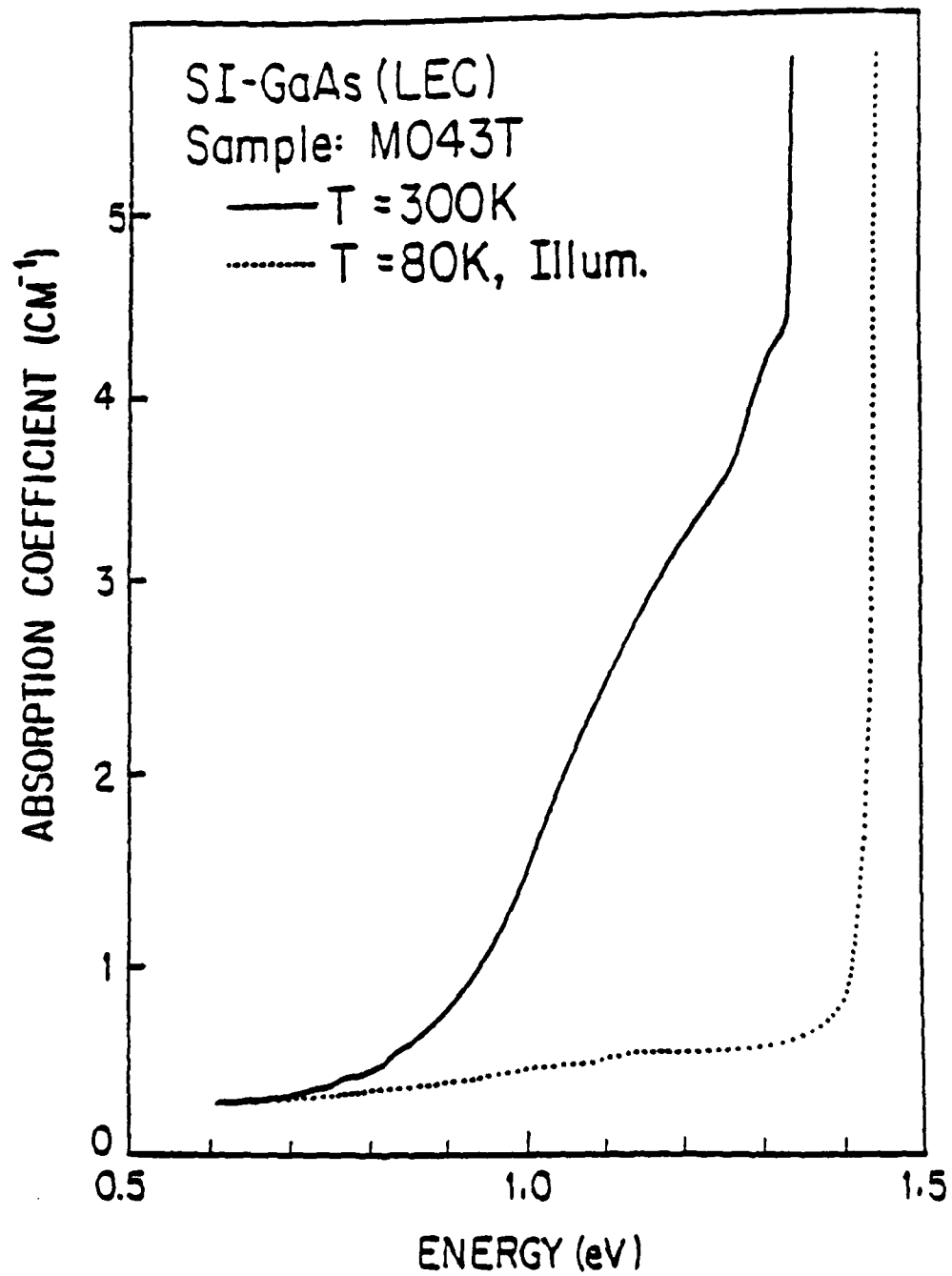
Fig. 1

Figure Captions

Fig. 1.   The total absorption spectra at 300 K (solid curve), and the residual
          absorption spectra at 80 K (dotted curve) of the M043T SI GaAs (LEC)
          sample.

Fig. 2.   Typical thermal regeneration of the absorption coefficient (measured
          at 1.2 eV).

Fig. 3.   The total absorption spectra at 300 K (solid curve), and the residual
          absorption spectra at 80 K (dotted curve) of the M047T SI GaAs (LEC)
          sample.

17. Y. Nanishi, H. Yamazaki, T. Mizutani, and S. Miyazawa, Inst. Phys. Conf. Ser. 63, 7 (1982).

18. H. Winston, Solid State Technol. 26, 145 (1983).

19. M. Tajima, Japan J. Appl. Phys. 21, L227 (1982).

20. D. E. Holmes, R. T. Chen, and J. Yang, Appl. Phys. Lett. 42, 420 (1983).

21. Y. Mita, S. Sugata, and N. Tsukada, Appl. Phys. Lett. 43, 842 (1983).

22. F. Haegawa, N. Iwata, N. Yamamoto, and Y. Nannichi, Japan J. Appl. Phys. 22, L502 (1983).

23. E. R. Weber, H. Ennen, U. Kaufmann, J. Windschief, and J. Schneider, J. Appl. Phys. 53, 6140 (1982).

24. A. V. Markov, S. S. Shirifin, and L. M. Morgvlis, Sov. Phys. Crystallogr. 27, 620 (1982).

25. D. V. Klyachko and V. G. Krigel, Sov. Phys. Solid State 25, 676 (1983).

26. A. M. White, in Proceedings of the Semi-Insulating Materials Conference, Nottingham 1980, edited by G. J. Rees (Shiva, Orpington, U.K., 1980), p. 3.

27. U. Kaufmann and J. Schneider, Appl. Phys. Lett. 36, 747 (1980).

28. G. H. Strauss, J. J. Kerbs, S. H. Lee, and E. M. Swiggard, Phys. Rev. B 22, 3141 (1980).

29. A. M. Hennel, W. Szuszkiewicz, M. Blanski, and G. Martinez, Phys. Rev. B 23, 3933 (1981).

30. D. C. Look, S. Chaudhuri, and L. Eaves, Phys. Rev. Lett. 49, 1729 (1982).

31. A. Goltzene, C. Schwab, G. M. Martin, G. Jacob, and J. Poiblaud, Inst. Phys. Conf. Ser. 56, 557 (1981).

32. G. H. Strauss and J. J. Krebs, Inst. Phys. Conf. Ser. 33a, 84 (1977).

33. A. M. White, J. J. Krebs, and G. H. Strauss, J. Appl. Phys. 51, 419 (1980).

34. A. L. Lin and R. H. Bube, J. Appl. Phys. 47, 1859 (1976).

35. O. V. Vakulenko, G. D. Melnikov, and V. A. Skryshevskii, Sov. Phys. Semicond. 16, 1239 (1982).

References

1. G. M. Martin, in <u>Semi-Insulating III-V Materials, Nottingham 1980</u>, ed. by G. J. Res (Shiva Publ., Orpington, U.K.), p. 13.

2. G. M. Martin, Appl. Phys. Lett. <u>39</u>, 747 (1981).

3. D. E. Holmes, R. T. Chen, K. R. Elliott, and C. G. Kirkpatrick, Appl. Phys. Lett. <u>40</u>, 46 (1982).

4. G. M. Martin, J. P. Farges, G. Jacob, and J. P. Hallais, J. Appl. Phys. <u>51</u>, 2840 (1980).

5. G. M. Martin, A. Mitonneau, D. Pons, A. Mircea, and D. W. Woodard, J. Phys. C <u>13</u> (1980).

6. G. M. Martin, G. Jacob, G. Poilblaud, A. Goltzone, and C. Schwab, Inst. Phys. Conf. Ser. <u>59</u>, 281 (1981).

7. M. R. Brozel, I. Grant, R. M. Ware, and D. J. Stirland, Appl. Phys. Lett. <u>42</u>, 610 (1983).

8. D. E. Holmes, R. T. Chen, K. R. Elliott, and C. G. Kirkpatrick, Appl. Phys. Lett. <u>43</u>, 305 (1983).

9. S. Miyazawa, Y. Ishii, S. Ishida, and Y. Nanishi, Appl. Phys. Lett. <u>43</u>, 853 (1983).

10. R. K. Kim and R. Braunstein, Appl. Opt. <u>23</u>, 1166 (1984).

11. W. Walukiewicz, J. Lagowski, and H.C. Gatos, Appl. Phys. Lett. <u>43</u>, 192 (1983).

12. M. Jaros, <u>Deep Levels in Semiconductors</u> (Adam Hilger Ltd., Bristol, U.K., 1982).

13. P. W. Yu, Appl. Phys. Lett. <u>44</u>, 330 (1984).

14. G. Vincent and D. Bois, Solid State Commun. <u>27</u>, 431 (1978).

15. D. Bois and G. Vincent, J. Phys. (Paris) <u>38</u>, L351 (1977).

16. M. Levinston, Phys. Rev. B <u>28</u>, 3660 (1983).

of the remaining spectra can still be due to residual impurities or defects other than EL2 and Cr, which in contrast to EL2 in SI GaAs can no longer be directly measured and remains as the error of the measurement. This error would, however, be small if the material under study has relatively high Cr concentration. The LTPPQA method can be similarly used for other impurities or defects besides Cr in GaAs materials.

In summary, we have shown that, using the magnitude of the near infrared absorption coefficient as a measure of the EL2 concentration requires, in addition to the position of the Fermi energy, knowledge of the magnitude of the residual absorption due to the photoionization of all other deep levels, even if they are individually present in small concentration. The use of infrared wavelength modulation absorption and photoquenching represents a practical method for measuring the magnitude of this residual absorption.

Acknowledgments

ruling out contribution to the remaining spectra of a possible partially quenched state of EL2 level. The various thresholds of the residual absorption coefficient in Fig. 3 (dashed curve) resembled the photoionization thresholds of the various reported charged states of Cr,[6] indicating that chromium is perhaps the dominant accidental deep level impurity in this sample.

As it was pointed out earlier, in using the LTPPQA method, especially in obtaining Cr spectra and after the EL2 has been quenched out, it is necessary to keep the sample in darkness for several minutes before the remaining spectra are recorded. This step is required for the following reason. It has been demonstrated in experiments such as low temperature EPR,[28,32,33] ESR,[27] and photoconductivity,[34] that in GaAs:Cr, the occupancy of the various change states of Cr can be changed by illuminating the sample with light. Illumination of the Cr^{3+} centers with light of hv > 0.75 eV increases the concentration of Cr^{2+} and Cr^{4+} while decreasing the number of Cr^{3+} states.[35] The system, however, has been observed to return to the equilibrium population in minutes after the light is turned off.[33] This relaxation time is characteristically much less than the time (several hours) that the EL2 remains in its "metastable stabe," if the measurement is done at temperature well below the quenching temperature (< 40 K). Therefore, following the quenching out of the EL2 spectra, if the background illumination is turned off, the Cr charged states would reach their equilibrium population (in minutes), while the metastable of the EL2 remains effectively unaltered. The remaining spectra thus obtained are primarily due to the appropriate equilibrium concentration of Cr charged states. Although the dependence of charged states population on the background illumination has been most extensively studied for Cr in GaAs, other multilevel impurity and defects are prone to the same phenomena and thus are subject to the above considerations. It must also be pointed out that a portion

References

/1/ S.K. Deb, Philos. Mag. 27, 801 (1973)

/2/ B.W. Faughnan, R.S. Crandall, P.M. Heyman, RCA Review 36, 177 (1975)

/3/ H.N. Hersh, W.E. Kramer, J.H. McGee, Appl.Phys.Lett. 27, 646 (1975)

/4/ O.F. Schirmer, V. Wittwer, G. Baur, G. Brandt,
     J. Electrochem. Soc. 124, 749 (1977)   --

/5/ H.R. Zeller, H.U. Beyeler, Appl.Phys. 13, 231 (1977)

/6/ R. Hurditch, Electr.Letters 11, 142 (1975)

/7/ A. Nakamura, S. Yamada, Appl.Phys. 24, 55 (1981)

/8/ N.S. Hush, Progr. Inorg. Chem. 8, 391 (1967)

/9/ R. Braunstein, Solid State Comm. 28, 839 (1978)

/10/ R. Braunstein, K. Bärner, Solid State Comm. 28, 847 (1978)

/11/ R. Braunstein, K. Bärner, Solid State Comm. 33, 941 (1980)

/12/ R. Braunstein, I. Lefkowitz, Ferroelectrics 27, 225 (1980)

/13/ D. Deal, M. Burd, R. Braunstein, J.Non-Cryst. Solids 52, 207 (1983)

/14/ J.M. Ziman, Models of disorder, Cambridge 1979, p. 370

Figure captions

Fig. 1: Absorption spectra of the $(Li_2B_4O_7)_{1-x}(WO_3)_x$-glasses for different concentrations X.

Fig. 2: Absorption spectra of $(Li_2B_4O_7)$ glasses doped with two different concentrations of cobalt. $c_1 = 10^{-5}$; $c_2 = 2 \cdot 10^{-3}$ $[molCo/mol\ Li_2B_4O_7]$.

Fig. 3(a) Change of the absorption coefficient at $E = 1,4$ eV;
    (b) the location of the fundamental absorption edge for different WO_3-concentrations.

Fig. 4: Static dielectric constant as a function of the temperature for three borate-tungstate-glasses.

Fig. 5: Lattice-model for the formation of the lithium-tungsten-bronzes according to /4/.

Fig. 6: Arrhenius-plot of loss factor $\tan\delta$ for the pure lithium-borate-glass (X = 0).
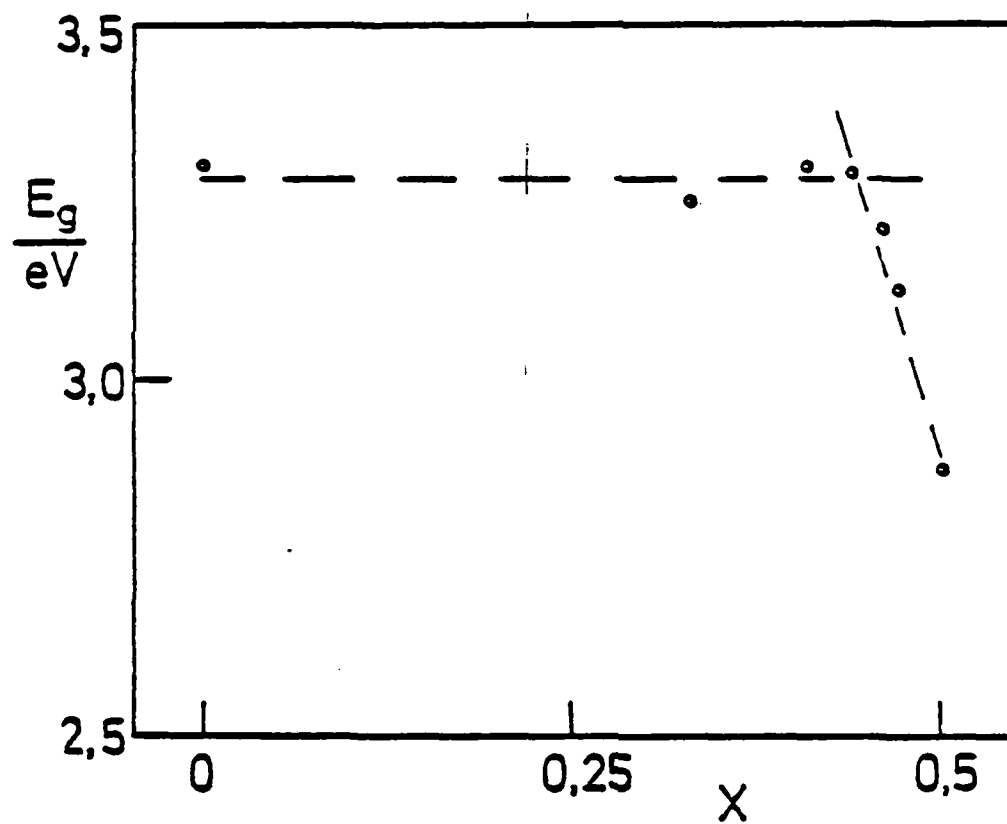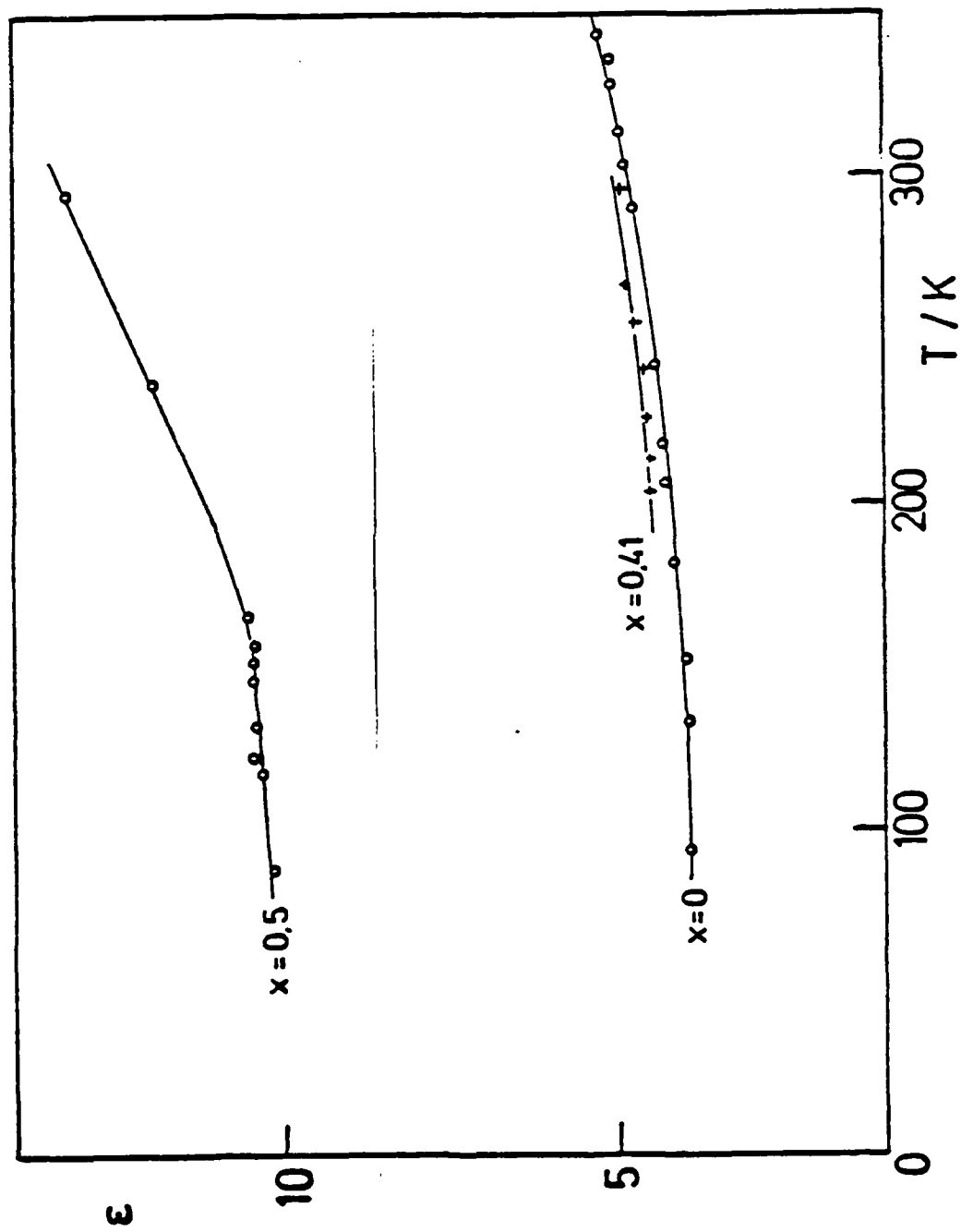
Fig.
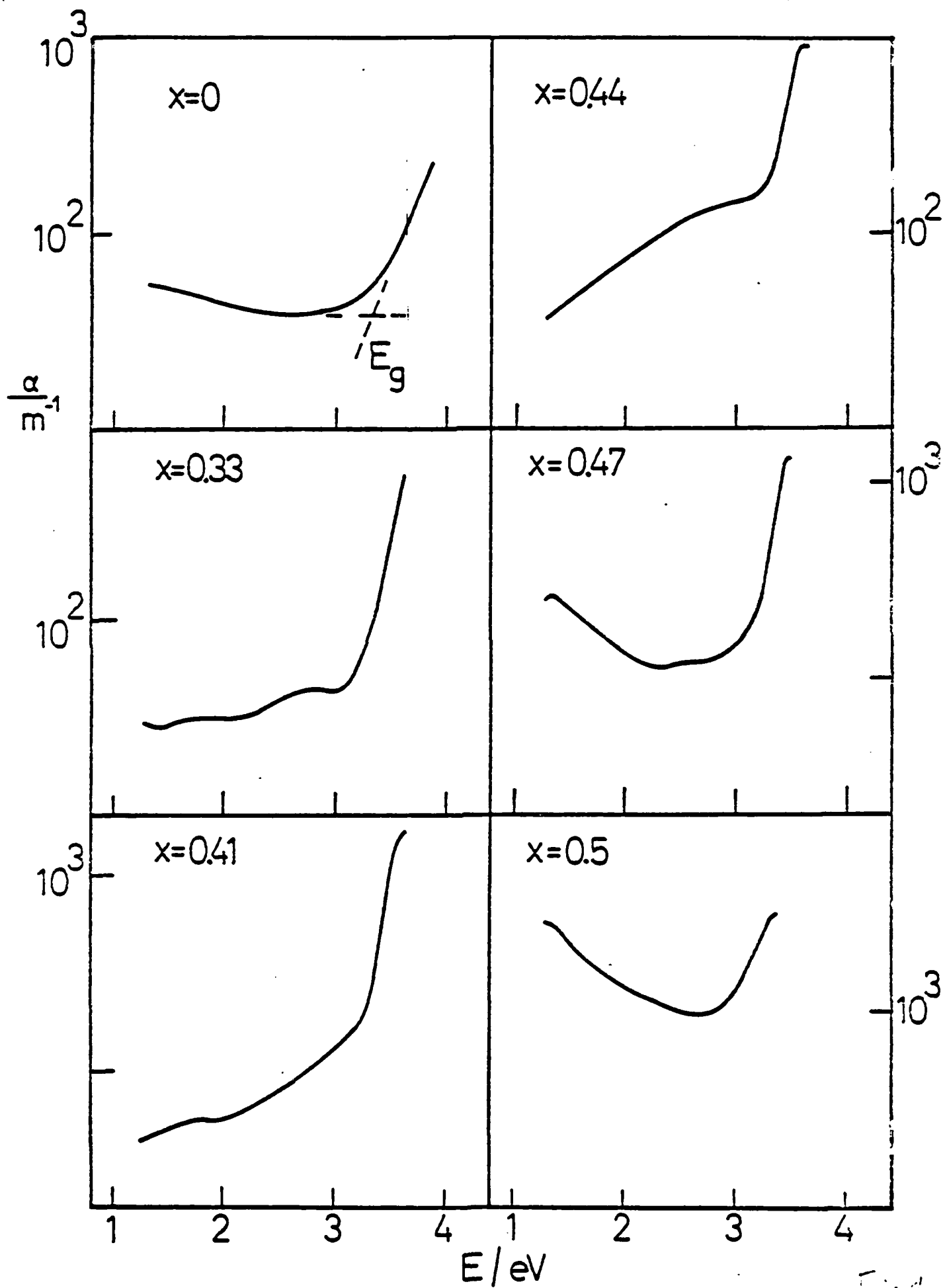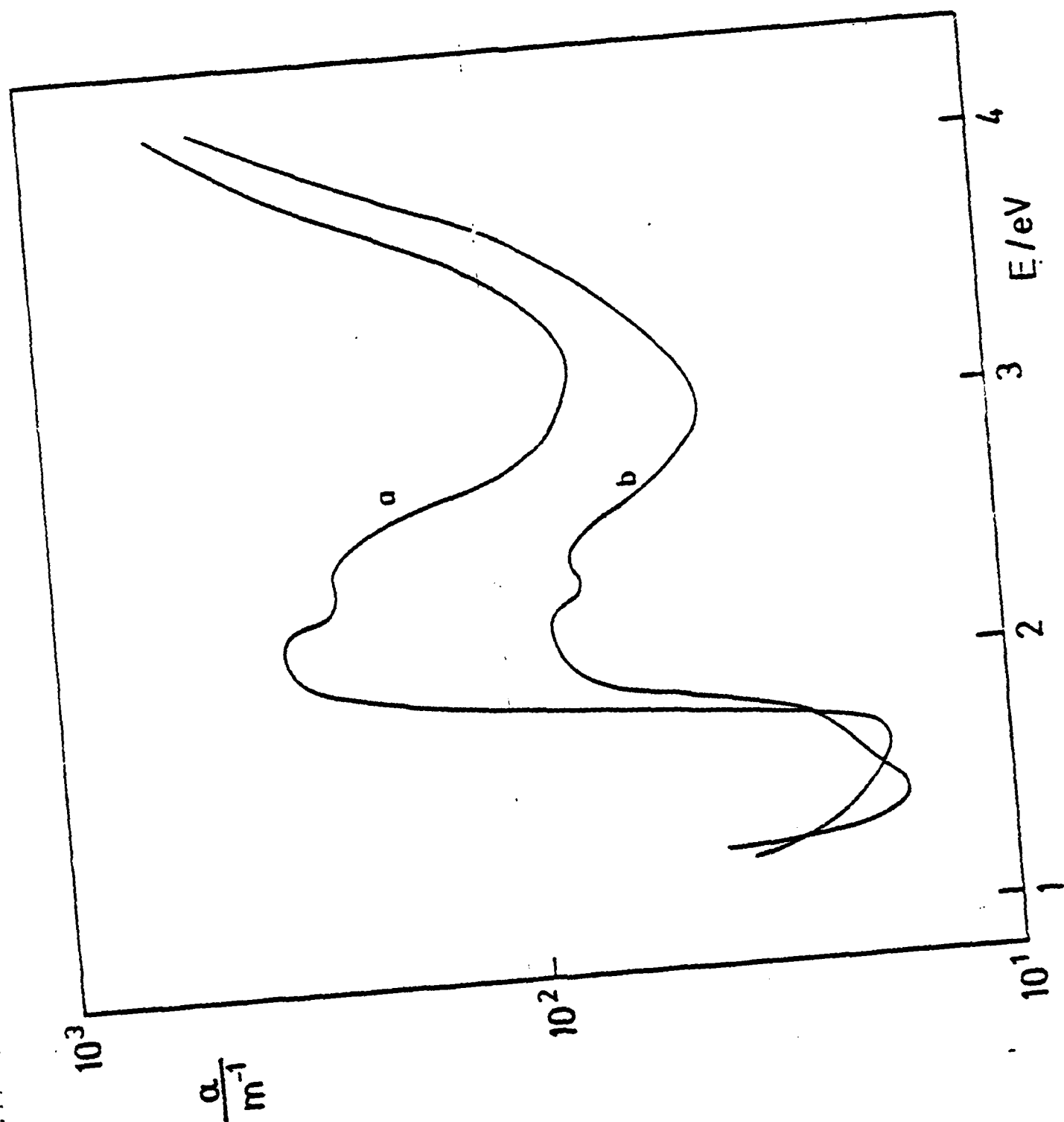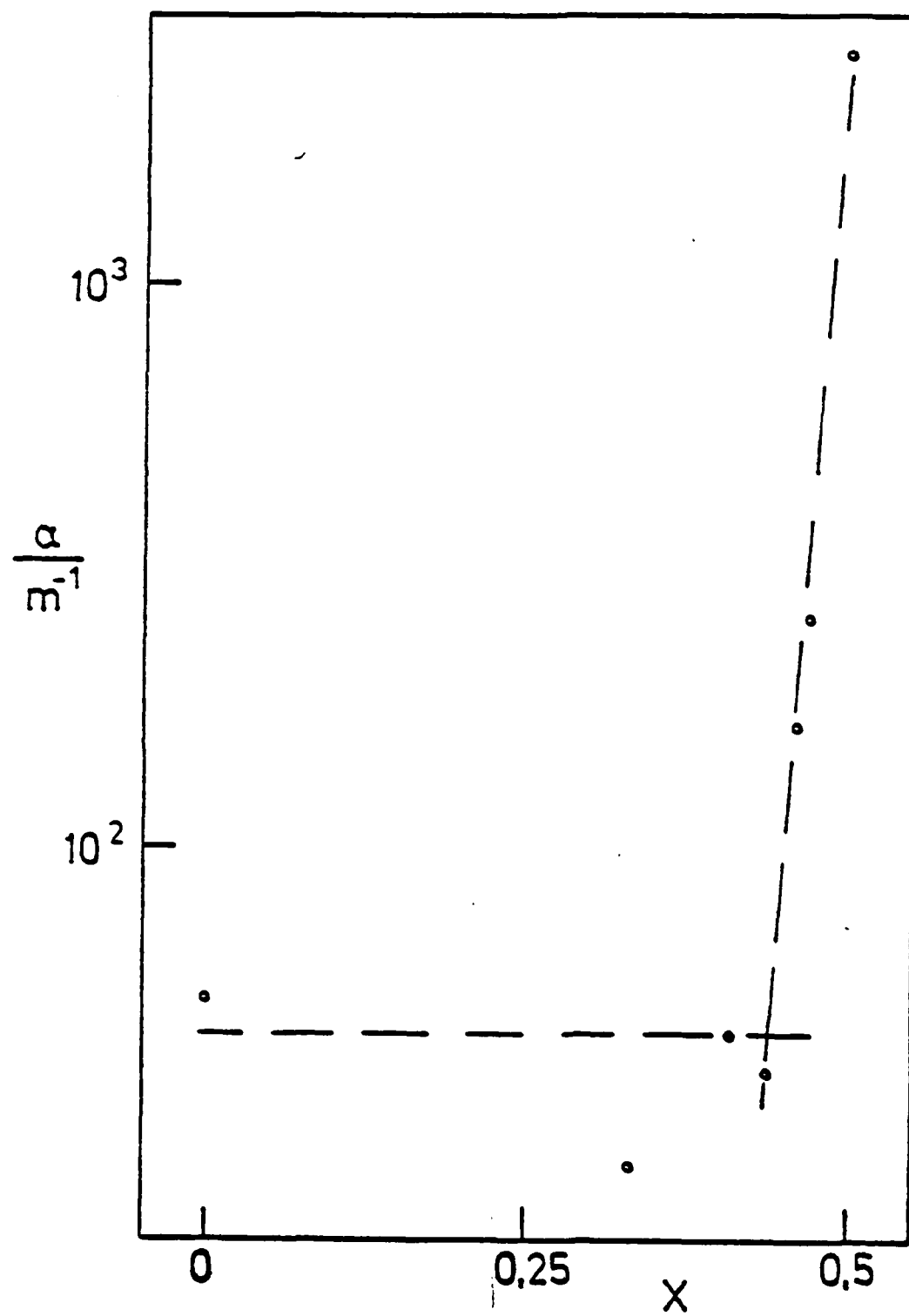
Fig 3a

Fig 3b-

Fig. 4
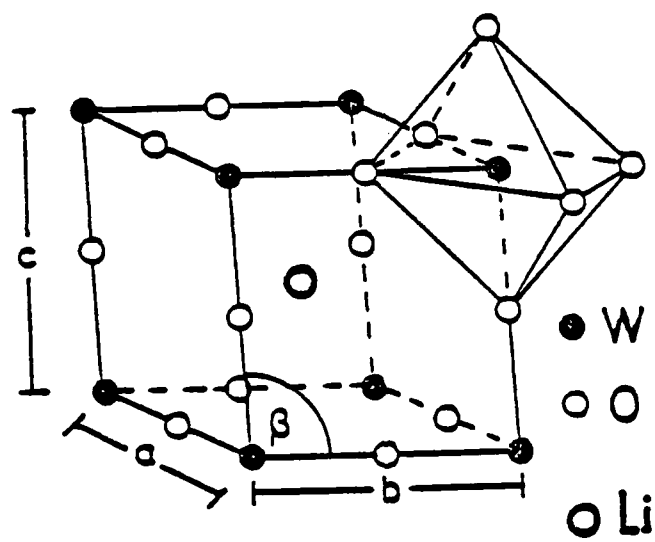
Fig 5

Fig 6

END

FILMED

8-85

DTIC